# $LaFeO_3$ as a Base Material for Cathode Applications in Intermediate Temperature Solid Oxide Fuel Cells

*Felicity H. Taylor*

A thesis submitted to

University College London

in partial fulfilment of the requirements for the degree of

Doctor of Philosophy

Supervised by Professor C. Richard A. Catlow

March 2019

Department of Chemistry

20 Gordon Street

London WC1H 0AJ

United Kingdom

*For Paul Taylor*

# Declaration

I, Felicity H. Taylor, confirm that the work presented in this thesis is my own. Where information has been derived from other sources, I confirm that this has been indicated in the work.

Felicity H. Taylor

# Abstract

Computational techniques have been employed to perform an in-depth study into the defect chemistry of $LaFeO_3$, a mixed ionic electronic conductor and a promising candidate for intermediate temperature solid oxide fuel cell cathode applications. Initially, a range of isolated point defects and disorder schemes were considered, from which we established the favourable formation of cation and oxygen vacancies, under oxygen rich and oxygen poor conditions respectively. Schottky disorder also plays an important role in the defect chemistry of $LaFeO_3$ and the defect model we propose was verified through comparison with experimental work on the oxygen non-stoichiometry of $LaFeO_3$. Work on the activation energy of oxide ion migration through $LaFeO_3$ considered three pathways, due to two inequivalent oxygen sites being present in orthorhombic $LaFeO_3$. The pathways between the O1 and O2 and O2 and O2 sites were found to be the most favourable, having low activation energies in line with experimental results. A range of divalent dopants were then considered, for both the A- and B-sites, with strontium, calcium and manganese showing promising results as A-site dopants, due to low solution and binding energies, while cobalt and nickel showed promising results as B-site dopants. We finished by considering two terminations of the (001) surface of $LaFeO_3$: $FeO_2$ and LaO. We found that although the LaO terminated surface has the lowest surface energy, the $FeO_2$ terminated surface is most defective, with cation vacancies and oxygen vacancies having low formation energies. The $FeO_2$ terminated surface, therefore, is likely to be more catalytically active than the LaO terminated surface. Two techniques have been used throughout this work, interatomic potential-based methods and DFT-based methods, the results from each are compared throughout.

# Impact Statement

The issues of fuel security and environmental impact that surround energy generation via current, non-renewable routes have increased the demand for clean, renewable alternatives. One such alternative for electricity generation is the use of fuel cells, particularly solid oxide fuel cells (SOFCs). SOFCs have historically been considered as a clean alternative to the combustion engine based power stations for large-scale electricity generation. However, current technologies require extreme temperatures to operate efficiently, limiting both their lifetime and their range of uses. An aim in the field of SOFCs is to lower the operating temperature into the range of 500 - 800°C, the intermediate temperature range. In the work of this thesis we have considered a promising material for intermediate temperature solid oxide fuel cell cathode applications: $LaFeO_3$. The cathode, the site of the oxygen reduction reaction, becomes the limiting component in a SOFC as temperatures are lowered, and thus new materials for this component, that are active at reduced temperatures, must be identified. $LaFeO_3$ is a mixed ionic electronic conductor, a property that increases its activity as a cathode, by increasing the area within which the oxygen reduction reaction can occur. By studying the defect chemistry of $LaFeO_3$ we are able to gain a better understanding of the source of the conductivity observed in this material, and thus suggest ways to enhance it. Our work has established the prominent defects in bulk $LaFeO_3$, the favoured pathways for oxide ion migration, identified dopants that should enhance the mixed ionic electronic properties of $LaFeO_3$ and identified the most defective, and therefore catalytically active, surface termination of the (001) surface. The benefit of this work within academia is the insight it has provided into the defect chemistry of $LaFeO_3$, providing an enhanced

understanding of the conductivity regime observed in this material. Additionally, as the majority of calculations were performed using both interatomic potentials and DFT+$U$ we were able to identify the shortcomings of the former when modelling $LaFeO_3$ and how these could be compensated for, which will aid future modelling of $LaFeO_3$ using interatomic potential-based methods. Our work has identified a number of areas for further research, using both computational and experimental techniques. In particular, we have found possible alternatives to the traditional doping strategy of $LaFeO_3$ (strontium on the A-site and cobalt on the B-site), most notably the use of manganese as either an A- or B-site dopant, which is worth further investigation, including an assessment of its impact on the thermal expansion coefficient of $LaFeO_3$, and the effect of manganese on the electronic conductivity of $LaFeO_3$. Outside academia, work on the development of SOFCs is vital to make these technologies more commercially viable, thus increasing the amount of clean electricity we are generating and therefore reducing our reliance on non-renewable fuels. In this work we have gained greater understanding in the chemistry of a promising intermediate temperature SOFC cathode material and identified potential routes to increase its activity for cathode applications, thus bringing this field of research closer to commercially available intermediate temperature solid oxide fuel cells.

# Acknowledgements

First and foremost, thanks must be given to my supervisors Prof. Richard Catlow and Dr John Buckeridge, your help, advice and guidance has been invaluable throughout my time at UCL. The project was challenging but fascinating, and it has been a real pleasure to work with both of you.

I would like to thank David Scanlon, the Catlow group and the members of the 'Energy Materials: Computational Solutions' grant, whose discussions and knowledge have greatly enriched my experience at UCL and contributed significantly to the work presented here.

I am grateful to the UCL Chemistry Department for the financial support of this work and the Materials Chemistry Consortium for providing computational resources.

Thank you to Alex, Ben, Chris, Dougal, Ian, Mia, Rachel and Susanne, for your friendship and ever interesting conversations throughout my time at UCL, it would not have been the same without you all.

To Dan, Lisa, Louise, Rose, Beth, Laura, Jess, Ana, Emma, Jon and Sami, a massive thank you for keeping me sane, particularly in the last year. Writing while working was always going to be difficult, but your patience, encouragement and good humour made this process bearable, sorry it took so long.

Finally, a big thank you to my family and to Jack, your love and support has always kept me going, and I would not be here without you.

# Publications

The following publications resulted from the work of this thesis.

- F. H. Taylor, J. Buckeridge, and C. R. A. Catlow. Defects and Oxide Ion Migration in the Solid Oxide Fuel Cell Cathode Material $LaFeO_3$. *Chemistry of Materials*, 28(22):8210–8220, 2016.

- F. H. Taylor, J. Buckeridge, and C. R. A. Catlow. Screening Divalent Metals for A- and B-Site Dopants in $LaFeO_3$. *Chemistry of Materials*, 29(19):8147–8157, 2017.

- J. Buckeridge, F. H. Taylor, and C. R. A. Catlow. Efficient and Accurate Approach to Modeling the Microstructure and Defect Properties of $LaCoO_3$. *Physical Review B - Condensed Matter and Materials Physics*, 93:155123, 2016.

# Contents

# List of Figures

# List of Tables

# List of Abbreviations

TPB: Triple Phase Boundary

MIEC: Mixed Ionic Electronic Conductor

FM: Ferromagnetic

AFM: Antiferromagnetic

LDA: Local Density Approximation

GGA: Generalised Gradient Approximation

PBE: Perdew-Burke-Ernzerhof

PBEsol: Perdew-Burke-Ernzerhof for solids

VBM: Valence Band Maximum

CBM: Conduction Band Minimum

SOFC: Solid Oxide Fuel Cells

DFT: Density Functional Theory

NEB: Nudged Elastic Band

LSM: $La_{1-x}Sr_xMnO_{3-\delta}$

LSCF: $La_{1-x}Sr_xCo_{1-y}Fe_{y3-\delta}$

GSC: (Gd, Sr)$CoO_3$

YSZ: Yttria Stabilised Zirconia

GDC/GCO: Gadolinium Doped Ceria

LSGM: Magnesium Doped Lanthanum Gallate

IT-SOFC: Intermediate Temperature Solid Oxide Fuel Cell

TEC: Thermal Expansion Coefficient

ORR: Oxygen Reduction Reaction

LSC: $La_{1-x}Sr_xCoO_{3-\delta}$

BSCF: $Ba_{1-x}Sr_xCo_{1-y}Fe_yO_{3-\delta}$

SDC: Samarium Doped Ceria

LSCF6428: $La_{0.6}Sr_{0.4}Co_{0.2}Fe_{0.8}O_{3-\delta}$

IP: Interatomic Potentials

HF: Hartree-Fock

MP: Many-Body Perturbation

CI: Configuration Interaction

LSDFT: Local Spin Density Functional Theory

RPA: Random Phase Analysis

PW91: Perdew-Wang 1991

LDSA: Local Density Spin Approximation

PAW: Projector Augmented Wave

VASP: Vienna *ab initio* Simulation Package

DFP: Davidon-Fletcher-Powell

BFGS: Broyden-Fletcher-Goldfarb-Shanno

DIIS: Direct Inversion in Iterative Subspace

GULP: General Utility Lattice Program

HPC: High Performance Computing

CPLAP: Chemical Potential Limits Analysis Program

MEP: Minimum Energy Pathway

CI-NEB: Climbing Image-Nudged Elastic Band

SOD: Site Occupancy Disorder

LSNF: $La_xSr_{1-x}Fe_yNi_{1-y}O_{3-\delta}$

# Chapter 1

# Introduction

In this chapter, we will introduce fuel cell technologies, with an emphasis on solid oxide fuel cells (SOFC), along with $LaFeO_3$ and its role in SOFC cathode applications. We will discuss relevant research, that has been carried out previously, on which the work presented here has been built. We begin by discussing the motivation behind this work, followed by introducing solid oxide fuel cells, their components and current state-of-the-art cathode materials. Perovskite oxides, the class of materials $LaFeO_3$ belongs to, will be introduced before presenting more specific accounts of the topics covered in the subsequent chapters: defects, dopants and surface studies.

## 1.1 Motivation

The growing demand for energy, due in part to economic growth and an increasing population size, is putting a large amount of pressure on our planet, through both the consumption of limited non-renewable resources, such as oil and natural gas, and the environmental impact of generating energy by combustion of such resources. These issues of fuel security and environmental impact that surround energy generation via current, non-renewable routes have increased the demand for clean, renewable alternatives. There are many technologies available for generating energy using renewable resources; examples include solar panels and wind turbines, but the work of this thesis focuses on fuel cells, particularly solid oxide fuel cells (SOFCs). SOFCs have historically been considered as having the potential to be a direct, clean

replacement for current combustion engine based power plants, as large static units for generating electricity.[34–36] The predominant obstacle to the implementation of these devices is the necessary operating conditions, as current SOFC technologies require high temperatures to operate efficiently, limiting the lifetime of each cell which increases the expense of electricity generation via this route.[35, 37–39] Therefore, a key need in the field of SOFC research is to find new materials for each of the SOFC components, with the aim of lowering operating temperatures to the intermediate temperature region (500 - 800°C), while maintaining, or ideally improving, current efficiencies to make these technologies more viable for widespread use. With this in mind, our aim is to understand the defect chemistry of promising new materials at a fundamental level. The defect chemistry of a material is key to understanding properties, such as conductivity and reactivity, that govern its performance for fuel cell applications; it can, therefore, guide the design of more efficient fuel cells.

### 1.1.1 Solid Oxide Fuel Cells

Fuel cells are able to convert a variety of fuels, including hydrogen, hydrocarbons and methanol,[34, 40] directly to electricity, without a combustion step, making them more efficient than the combustion engine used to convert oil or gas into electricity; another key benefit is that fuel cells are cleaner and quieter than the traditional combustion engine.[34, 40–43]

There are a number of different types of fuel cell, which all work on the same principles: the movement of electrons around an external circuit is balanced by the movement of charged ions through an internal circuit. All fuel cells have the same three base components; a cathode, an electrolyte and an anode. Their differences originate from the material used for the electrolyte component and, by extension, the ions that migrate through the electrolyte to form the internal circuit. For example, alkali fuel cells have an aqueous alkaline electrolyte, such as KOH, and $OH^-$ is the migrating species, whereas phosphorous acid fuel cells have a phosphoric acid electrolyte, and the migrating species is $H^+$.[40, 44] One of the advantages of solid oxide fuel cells over both these types, and other types, of fuel cell is that they

contain a solid oxide electrolyte which is significantly safer than the corrosive liquid electrolytes used in the above systems.[40, 44]

Additional advantages of using SOFCs include their higher efficiency compared to many other types of fuel cell,[37, 43, 44] and the good fuel flexibility they offer.[34, 45] Potential fuels include hydrocarbon based fuels, which can be used directly with no need for complex fuel preprocessing, due to the tolerance of SOFCs to CO coking.[44] Low temperature fuel cells, such as polymer electrolyte membrane cells, require hydrocarbon fuels to be preprocessed before use, adding further complication and cost to production. SOFCs can also utilise hydrogen as a fuel, meaning they could play a vital part in any future hydrogen economy.[40]

However, current technologies require high temperatures: in the region of 800 to 1000°C, to operate efficiently.[35, 46] These temperatures make solid oxide fuel cells costly to run as expensive materials that can withstand these conditions are necessary, in addition to the cells' limited lifetimes under such extreme conditions.[39, 47] Therefore, to increase the widespread use of this technology, operating temperatures need to be reduced while maintaining, or improving, current efficiencies.

A key strategy is thus the exploration of new materials for each fuel cell component; our work focuses on the cathode. The current material commonly used for SOFC cathode applications is $La_{1-x}Sr_xMnO_3$ (LSM). However, LSM only performs efficiently at high temperatures, meaning a different cathode material is required if the operating temperatures are to be reduced. Our work considers perovskite oxides based on $LaFeO_3$, which are a promising alternative for the cathode component of solid oxide fuel cells operating in the intermediate temperature region; between 500 and 800°C.

### 1.1.2 $LaFeO_3$-based Materials

Our work explores the use of $LaFeO_3$-based perovskites as potential cathode materials for solid oxide fuel cell applications. $LaFeO_3$ is a mixed ionic electronic conductor (MIEC)[27, 48, 49] and it is the conduction properties of $LaFeO_3$ that makes it a promising candidate for cathode applications. Cathode materials need

to be efficient electronic conductors,[46] to transport electrons from the external circuit to the cathode surface where they react with an oxidant to form the internal migrating species: oxygen gets reduced at the cathode surface in solid oxide fuel cells, forming oxide ions, $O^{2-}$, that migrate through the electrolyte. If the cathode is also an efficient ionic conductor, the activity of the oxygen reduction reaction on the cathode will increase;[37, 41] this point is be discussed in more detail in Section 1.3.

Lanthanum ferrite is also a parent material of $La_{1-x}Sr_xFe_{1-y}Co_yO_{3-\delta}$ (LSCF), another MIEC that has shown great promise for SOFC cathode applications at intermediate temperatures: between 500 and 800°C.[46, 50–53] The origin of the strong performance of LSCF is not well known,[54] and the aim of this work is to study the parent materials of this double doped perovskite oxide, to understand how the atomic level structure of this material may contribute to its performance. Knowledge of what factors help or hinder the conductivity of $LaFeO_3$ and related materials may allow us to formulate design strategies to optimise these materials further, thus moving closer to wide spread use of intermediate temperature SOFCs.

### 1.1.3 Summary

The motivation behind this work stems from the obvious need for clean, renewable energy generation technologies and the knowledge that solid oxide fuel cells hold great promise in delivering this need, particularly for static, large scale electricity generation. However, the implementation of such technologies commercially is hindered by the high costs associated with running such fuel cells, caused by the high operating temperatures required and the limited lifetimes of cells under such extreme conditions. Therefore, these operating temperatures need to be reduced, while maintaining current efficiencies. A promising strategy to reduce temperatures is to develop new, or existing materials, for each fuel cell component that are active at reduced temperatures. Our work focuses on studying materials based on $LaFeO_3$ which have the potential to improve on the efficiencies of current intermediate temperature cathode materials due to their mixed ionic and electronic conductivity properties.

In the rest of this chapter, more details will be given on the topics introduced briefly here, starting with solid oxide fuel cells, followed by materials of interest for cathode applications, including $LaFeO_3$.

## 1.2 Solid Oxide Fuel Cells

Fuel cells generate electricity from fuel and an oxidant in one step with minimal by-products; the by-products can be limited to just water if hydrogen is used as the fuel.[40, 55] All fuel cells have three main components: the cathode, electrolyte and anode. The fuel is brought into the anode site, the oxidant brought into the cathode site, and the electrolyte is present to stop direct chemical combustion. In a simplistic example, with hydrogen as the fuel and oxygen as the oxidant, the overall reaction is:

$$\frac{1}{2}O_2 + H_2 \leftrightarrow H_2O \tag{1.1}$$

This can be broken down into two half equations; a reduction reaction which occurs at the cathode and an oxidation reaction that occurs at the anode.

The cathode is the site of the oxygen reduction reaction in which an oxidant, $O_2$ in our example, is reduced:

$$\frac{1}{2}O_2 + 2e^- \leftrightarrow O^{2-} \tag{1.2}$$

therefore cathode materials need to be efficient electronic conductors, stable under oxidising conditions and be catalytically active towards the oxygen reduction reaction. As discussed above, typical cathode materials for SOFCs include (La, Sr)$MnO_3$ (LSM), while (Gd, Sr)$CoO_3$ (GSC) is another common example.[46]

At the anode, the fuel, hydrogen in our example, is oxidised and electrons are released back into the external circuit, while water is produced as a by-product:

$$H_2 + O^{2-} \leftrightarrow H_2O + 2e^- \tag{1.3}$$

As with the cathode material, electronic conductivity is a key property for an anode

material, along with high catalytically active towards fuel oxidation.[46] Typical anode materials are composites of the electrolyte material and a metal, known as a cermet. A common anode material for SOFC use is a YSZ and nickel metal cermet; nickel is an excellent fuel oxidation catalyst while the electrolyte material, YSZ, aids compatibility with the electrolyte component.[37, 46]

The role of the electrolyte is to transport the migrating species, $O^{2-}$ ions for SOFCs, from the cathode to the anode. Therefore, the main property required for an electrolyte material is high ionic conductivity, but it also must be highly stable in both oxidising and reducing conditions, unreactive towards the migrating species and have low electronic conductivity.[56] Typical electrolyte materials include yttria stablised zirconia (YSZ), gadalinium doped ceria (GDC) and strontium and magnesium doped lanthanum gallate (LSGM).[37, 57, 59–61]

The cathode, electrolyte and anode form a single fuel cell unit, seen in Figure 1.1. Multiple fuel cell units are connected together to form larger units, the size of which depends on how much power is to be generated. Fuel cell units are linked by an interconnect material, which must be stable under high operating temperatures and in both oxidising and reducing environments, in addition to being unreactive towards the other components. Ferric steel or alkali earth doped $LaCrO_3$[40] are commonly used interconnect materials in solid oxide fuel cells, selected because they have a similar thermal expansion coefficient to the other common component materials of fuel cells.[21, 40]

The thermal expansion coefficient (TEC), is not only an important property to consider when choosing an interconnect material, but is important for all components of the fuel cell. It is necessary for all materials to have a similar TEC to those components with which it is in contact, e.g. the cathode must have a similar TEC to both the electrolyte and the interconnect material. If the TECs of connected materials differ significantly, thermal stresses occur during heating and cooling cycles when the cell is in operation, which can shorten the lifetime of a cell significantly.[21] It is therefore vital that this property is appropriately considered when choosing materials for each of the components.

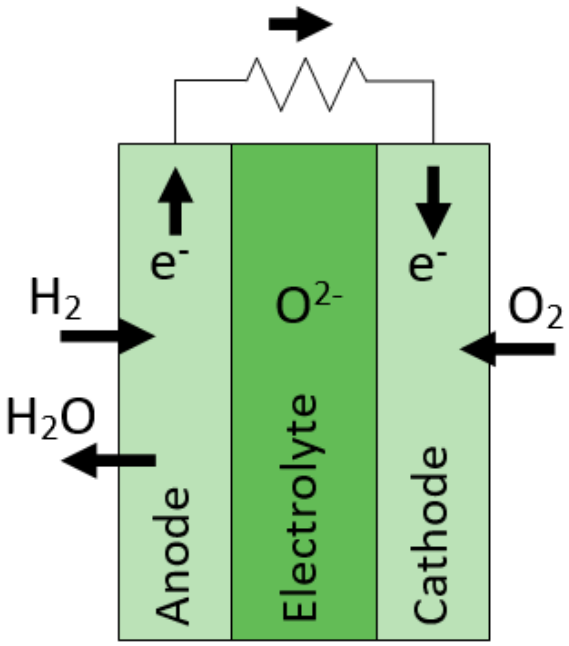


**Figure 1.1:** A simplistic schematic of a solid oxide fuel cell; an oxidant (oxygen gas in this case) reacts at the cathode sites to form $O^{2-}$ ions which migrate across the electrolyte to the anode where they react with a fuel, for example hydrogen. If hydrogen is used as fuel the only by-product is water.

In our description of solid oxide fuel cells so far, we have focused on SOFCs that use $O^{2-}$ as the species that migrates through the electrolyte. An alternative type of SOFC conducts protons, $H^+$, which are created at the anode site, meaning the cell works in the opposite direction compared to a fuel cell based on oxide ions.[40] The focus of our work is on fuel cells that use oxide ions as the migrating species and therefore proton conducting SOFCs will not be mentioned further.

Current standard operating temperatures for solid oxide fuel cells are between 800 and 1000°C.[35, 46] The high temperatures are required to allow the thermally activated conduction of ions, through the electrolyte, to occur at an efficient rate.[40, 62] However, these operating conditions mean expensive materials, that can withstand such extreme conditions, are required, and the high temperatures will also lead to an increase in the degradation rate of each component, shortening the lifetime of the fuel cells.[34] A crucial aim is then to bring the operating temperatures of these cells down, to between 500 and 800°C, (referred to as the intermedi-

ate temperature region), which would not only increase the lifetimes of the fuel cell components, but could also extend their range of applications; lower operating temperatures mean shorter start up times, which opens up the possibility of automotive and other portable uses.[34, 44]

Lowering the operating temperatures, however, decreases the rate of ionic conductivity across the cell,[37, 56] decreasing their efficiency. There are a number of ways to try and maximise the efficiency of a solid oxide fuel cell at lower temperatures, including cell design and choice of component materials, the latter of which is the focus of our work: investigating intermediate temperature solid oxide fuel cell (IT-SOFC) cathode materials based on $LaFeO_3$.

While the main focus of this work is on cathode materials for IT-SOFCs, it is worth briefly mentioning materials of interest for the other two components: the electrolyte and the anode. The desired properties for each component have already been covered: high ionic conductivity for the electrolyte and high electronic conductivity and catalytic activity towards fuel oxidation for the anode. The commonly employed YSZ electrolyte can perform poorly under intermediate temperatures due to the strong dependence of its ionic conductivity on temperature; generally requiring temperatures between 800 and 1000°C to perform optimally.[61] A number of new materials for IT-SOFC electrolyte components have been considered which have higher ionic conductivities at low temperatures compared to YSZ, including GDC,[55, 61] LSGM[55, 61] and apatites[56, 61, 63] with the general formula $Ln_{10}(XO_4)_6O_2$. However, each new material has drawbacks that need addressing including the presence of electronic conductivity (GDC),[61] and stability issues surrounding compatibility with the other fuel cell components (LSGM and apatites).[61] An alternative avenue of investigation is the introduction of strain at the interface between the electrolyte and electrode, which may increase the ionic conductivity of the conventional fluorite-based electrolyte materials so that they could be used at intermediate temperatures.[56] However, the effectiveness of this technique is still a matter for further research.

For anode materials, Ni/YSZ-based cermets have proved very successful, even at

reduced temperatures. The main issues to address for the anode site are: the redox stability of Ni, as nickel expands during redox cycles,[46] and the coking intolerance of Ni, which becomes a major issue if fuels other than hydrogen, e.g. hydrocarbons, are to be used.[37] Perovskite oxides, such as $La_{0.75}Sr_{0.25}Cr_{0.5}Mn_{0.5}O_3$, have been considered to address the redox stability issues. However, these materials only perform well at higher temperatures, making them inappropriate for IT-SOFC use.[37, 46]

Our decision to investigate new materials for the cathode component stems from the cathode being the site of the oxygen reduction reaction (ORR). The ORR has a high activation energy[34] and a limited area within which it can take place in conventional cathodes: the triple phase boundary (TPB), where the electrode, electrolyte and electrochemical gas meet, shown schematically in Figure 1.2.[55] Both these features lead to the ORR becoming the limiting factor for fuel cell efficiency at intermediate temperatures.[41, 46]

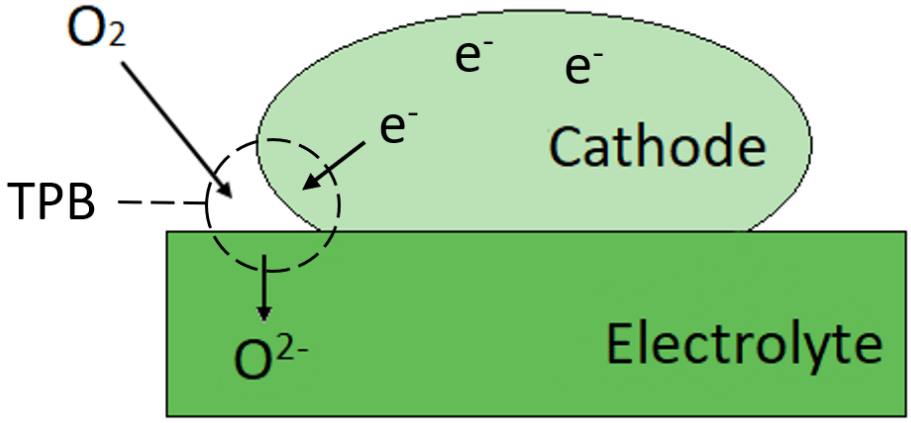


**Figure 1.2:** The triple phase boundary (TPB) point is the point where the cathode, electrolyte and oxidant (oxygen gas in this case) meet. In fuel cells where the cathode is purely an electronic conductor, the oxygen reduction reaction can only occur at this site.

We, therefore, wish to find cathode materials that are active in the intermediate temperature range. For a cathode material to be active in this region, it needs high electronic conductivity, to be catalytically active towards the oxygen reduction reaction within the intermediate temperature region, and have high ionic conductivity. If the cathode material is able to conduct ions, the area within which the oxygen reduc-

tion reaction can occur is increased beyond the TPB, which increases the rate of this reaction and therefore the activity of the cell.[37, 41, 46, 55] Consequently, mixed ionic electronic conductors, such as $LaFeO_3$ are being considered as cathode materials for solid oxide fuel cells. Before considering $LaFeO_3$ in more detail, we will first review previous materials that have been considered as potential SOFC cathode materials, including the current material favoured for high temperature SOFC cathodes, LSM.

## 1.3 SOFC Cathode Materials

In the following section, previous materials that have been used as SOFC cathode materials are discussed, including the traditional cathode material $La_{1-x}Sr_xMnO_3$. Following this, $LaFeO_3$ will be introduced and current progress on investigations into its use as a cathode material outlined.

### 1.3.1 Perovskite Oxides

Perovskite oxides, of the formula $ABO_3$, have a vast array of potential applications due to their tunable properties. Through controlling the A- and B-site cations, for example by choice of oxidation state or cation size, the properties of the perovskite oxide can be varied to suit the desired application.[46] The choice of cation will also affect the crystal structure of the perovskite - another way to control the properties of the final material. Figure 1.3 shows the generic structure of a cubic perovskite oxide.

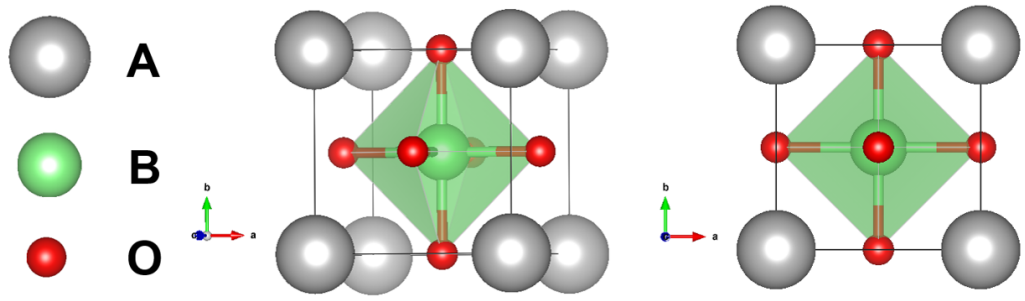


**Figure 1.3:** Example structure of a cubic perovskite oxide, of the form $ABO_3$ where A and B are cations. The larger cation, A, occupies lattice sites at the eight corners of a cube, while the smaller cation, B, will occupy the site in the centre of the cube, surrounded by a polyhedron of 6 oxide ions.

It is, therefore, not surprising that these materials have been considered as candidates for fuel cell applications, as fuel cell materials have a well defined list of desired properties to which perovskites can be tuned. One of the most popular, commercial SOFC cathode materials is based on a cubic perovskite: $LaMnO_3$. Lanthanum manganate has an $A^{III}B^{III}O_3$ formula; both the A- and B-site cations are in a 3+ oxidation state. The presence of manganese, a transition metal that is stable in several oxidation states, means that $LaMnO_3$ is an excellent electronic conductor, a property which is further improved when introducing dopants, usually on the A-site, forming $La_{1-x}M_xMnO_{3-\delta}$, a popular example being $La_{1-x}Sr_xMnO_{3-\delta}$.

#### 1.3.1.1 $La_{1-x}Sr_xMnO_3$

$La_{1-x}Sr_xMnO_{3-\delta}$ (LSM) has received a large amount of interest as a SOFC cathode material and is the traditional cathode material used in high temperature SOFCs; operating at temperatures around 800 to 1000°C.[37, 46, 56] Key properties of LSM that make it so successful in this area include high electrochemical activity towards the oxygen reduction reaction, high thermal and chemical stability, and good compatibility with other SOFC components, e.g. common electrolytes such as YSZ and GDC, at operating temperatures.[57, 64]

The introduction of Sr as a dopant on the A-site enhances both the electrical conductivity and catalytic activity of $LaMnO_3$.[34] The charge imbalance caused by substituting a $La^{3+}$ ion with a $Sr^{2+}$ ion, is compensated for by the formation of a hole on the B-site. The increase in hole concentration on Sr doping leads to the observed electrical conductivity, which increases as Sr content is increased up to a maximum value at x = 0.5.[34] The choice of mole fraction of Sr, x, to include in LSM is made by considering the balance between maximising the electrical conductivity of the material while maintaining stability; increasing Sr content leads to an increased formation of $SrZrO_3$ at the interface of LSM with YSZ.[64, 65] $SrZrO_3$ is a poor conductor and detrimentally effects the efficiency of the fuel cell; therefore minimising its formation is important for maximising the activity of LSM as a cathode material.[65]

However, as successful as this material is at high temperatures, it does not per-

form well under intermediate temperatures. The main reason for this failing is the poor ionic conductivity exhibited by LSM,[34] which limits the reaction area of the oxygen reduction reaction to the triple phase boundary point, see Figure 1.2, where oxygen gas, cathode and electrolyte meet, which severely limits the cathode's performance at lower temperatures.[46, 66, 67] Various techniques have been employed to enhance the ionic conductivity of LSM materials, predominantly creating composite cathodes of LSM and YSZ.

YSZ has a high ionic conductivity and the incorporation of this material into LSM as a composite cathode increases the ionic conductivity of the material, leading to an extended TPB area and a higher rate for the oxygen reduction reaction.[34] However, the introduction of YSZ can have a detrimental effect on the electronic conductivity of LSM, and the different sintering needs of each material can add complications during fabrication.[34]

An additional critical downside to LSM as a cathode material is its incompatibility with interconnect materials. It is common to use metallic interconnect materials in SOFCs, such as stainless steel, containing Cr species which become volatile at operating temperatures.[34, 68] Chromium species interact with the surface of LSM, poisoning the material and causing a significant decrease in the activity of the fuel cell.[68–70]

These issues outline a requirement for alternative materials to LSM for intermediate temperature cathode applications. The need for materials with both ionic and electronic conductivity has led to an interest in mixed ionic electronic conductors (MIECs) which display both properties without the processing complications introduced by composite materials. In addition, $La_{1-x}Sr_xCo_{1-y}Fe_yO_{3-\delta}$ (LSCF), a promising MIEC material, has demonstrated a resistance to poisoning from Cr-species compared to LSM, increasing the interest in this material as a potential alternative.[71]

#### 1.3.1.2 Mixed Ionic Electronic Conductors

Mixed ionic electronic conductors (MIECs), as mentioned previously, are a class of materials that have high ionic and electronic conductivity properties. They have

attracted a great deal of interest for IT-SOFC cathode applications as the addition of ionic conductivity, on top of the electronic conductivity of traditional cathode materials, extends the area within which the oxygen reduction reaction can occur to beyond the TPB. Increasing this area naturally increases the rate of this reaction, thus increasing the activity of the whole cell.

Figure 1.4 is a schematic representation of the active site for the oxygen reduction reaction in a mixed ionic electronic conductor, compared to the active site in a purely electronic conductor, shown in Figure 1.2.

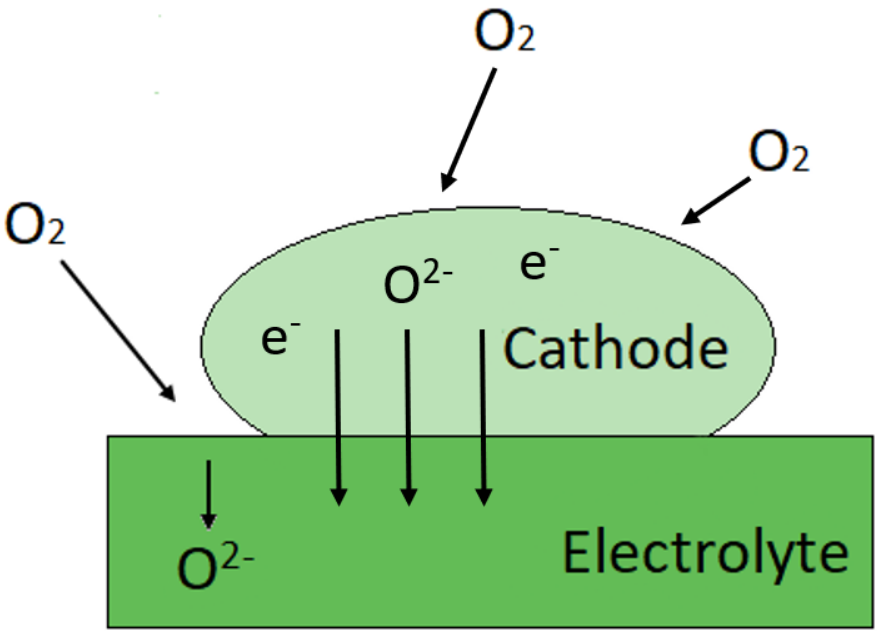


**Figure 1.4:** A simplistic representation of the active area within which the oxygen reduction reaction can occur in a mixed ionic electronic conductor (MIEC). In a purely electronic conductor, the oxygen reduction reaction is limited to the triple phase boundary point, where electrode, electrolyte and $O_2$ gas meet. In MIECs the oxygen reduction reaction can occur anywhere on the surface of the cathode, the reduced $O^{2-}$ is then transported to the electrolyte through the cathode.

Perovskite oxides have provided the basis for many MIEC cathode materials, including $La_{1-x}Sr_xCoO_3$, $La_{1-x}Sr_xFeO_3$, $La_{1-x}Sr_xCo_{1-y}Fe_yO_{3-\delta}$ and $Ba_{1-x}Sr_xCo_{1-y}Fe_yO_{3-\delta}$. As the main topic of this thesis, $LaFeO_3$-based materials will be introduced in detail in Section 1.4; here we will give a brief overview of previous work on other perovskite oxide based MIEC materials; predominantly Sr-doped $LaCoO_3$ and $Ba_{1-x}Sr_xCo_{1-y}Fe_yO_{3-\delta}$.

In $LaCoO_3$, as in $LaMnO_3$, the A- and B-site cations are in a 3+ oxidation state, with Co also able to stably occupy the 2+ and 4+ oxidation states, enabling electronic conductivity. The substitution of a divalent ion, for example $Sr^{2+}$, on the A-site creates a charge imbalance that is compensated through both oxygen vacancies and the creation of holes localised on Co (creating $Co^{4+}$), enhancing both ionic and electronic conductivity.[72]

The ground state structure of $LaCoO_3$ is rhombohedral, as shown in Figure 1.5. $LaCoO_3$ exhibits a structural phase transition to cubic at around 900°C.[73] Introducing strontium as a dopant on the A-site affects this phase transition; an X-ray diffraction study of $La_{0.6}Sr_{0.4}CoO_{3-\delta}$ at ambient temperatures showed that LSC contains a rhombohedral distortion for $x \leq 0.5$, while displayed a cubic structure for x = 0.6 to 0.8.[35, 73]

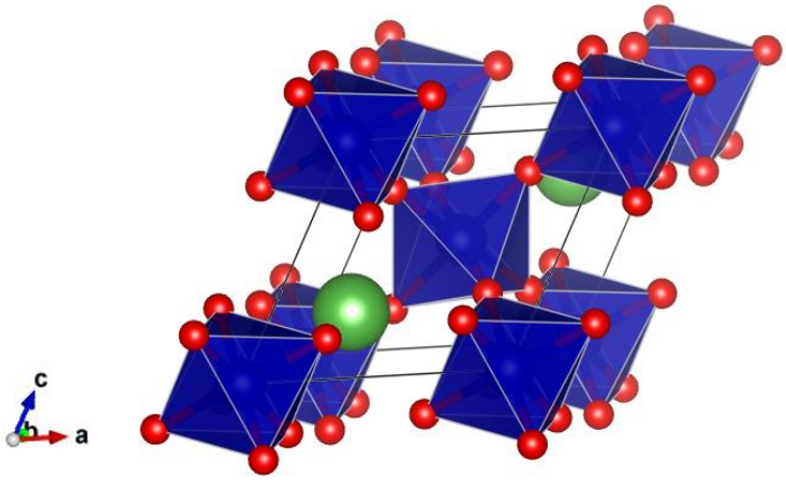


**Figure 1.5:** Rhombohedral $LaCoO_3$, lanthanum is shown in green, cobalt in blue and oxygen in red.

$La_{1-x}Sr_xCoO_{3-\delta}$-based materials have demonstrated an excellent combination of high electronic conductivity, good ionic conductivity and excellent catalytic activity towards the oxygen reduction reaction, along with being highly stable in high temperature oxidising environments making them very popular candidates for SOFC cathode applications.[35, 74–80] However, the issues associated with LSC present themselves during practical application of the material within a fuel cell. Firstly, LSC-based materials have a tendency to react with YSZ,[35, 55, 81] a common

electrolyte material, at 1000°C - the minimum sintering temperature of YSZ - to form insulating $La_2Zr_2O_7$ and $SrZrO_3$ phases.[79, 80, 82] Methods used to address this reactivity include introducing layers of doped ceria between the LSC and YSZ layers,[83–85] although this approach has had mixed success.[86] The use of alternative electrolyte materials, such as gadolinium doped ceria (GDC) has also been investigated,[87] and although the reactivity issue is removed, thermal incompatibilities still remain.

The second key issue with LSC-based materials is that they have high thermal expansion coefficients; for example $La_{0.6}Sr_{0.4}CoO_{3-\delta}$ has a TEC of $21.3\times10^{-6}$ [17] much higher than other common fuel cell component materials, a number of which are listed in Table 1.1.

**Table 1.1:** The thermal expansion coefficients of $LaCoO_3$-based materials along with other common materials used in other SOFC components. [a]Ref[17], [b]Ref[18], [c]Ref[19], [d]Ref[20], [e]Ref[21].

| Component | Material | TEC / $K^{-1}$ |
|---|---|---|
| Cathode | $La_{0.6}Sr_{0.4}CoO_{3-\delta}$[a] | $21.3\times10^{-6}$ |
| Cathode | BSCF ($Ba_{0.5}Sr_{0.5}Co_{0.8}Fe_{0.2}O_{3-\delta}$)[b] | $24.3\times10^{-6}$ |
| Cathode | LSCF ($La_{0.6}Sr_{0.4}Co_{0.2}Fe_{0.8}O_{3-\delta}$)[c] | $15.3\times10^{-6}$ |
| Anode | Ni + YSZ Cermet[d] | $12.6\times10^{-6}$ |
| Electrolyte | YSZ ($Zr_{0.85}Y_{0.15}O_{2-x}$)[d] | $10.6 - 11.1\times10^{-6}$ |
| Electrolyte | GDC ($Ce_{0.8}Gd_{0.2}O_{1.9}$)[e] | $12.7\times10^{-6}$ |
| Interconnect | Ferritic Steel[e] | $13.9\times10^{-6}$ |

A mismatch in TECs causes stress on the fuel cell during operation and significantly shortens the lifetime of the cell. The TEC of $LaCoO_3$-based materials can be tuned by substituting a fraction of the Co ions with alternative transition metals. Substituting nickel onto the B-site has been shown to bring the TEC of $LaCoO_3$ closer to those of the other components; however, the ionic conductivity decreases.[88, 89] Chromium has also been considered as a B-site dopant for $LaCoO_3$ and was shown to decrease the TEC; however, it also reduced electrical conductivity, making it inappropriate for cathode applications. [55, 88]

The lack of success from doping exclusively the A- or B-site of $LaCoO_3$, and related MIEC materials, has led to an interest in doping both sites. Two common examples

of this are $La_{1-x}Sr_xCo_{1-y}Fe_yO_{3-\delta}$ and $Ba_{1-x}Sr_xCo_{1-y}Fe_yO_{3-\delta}$. The former will be discussed in more detail in Section 1.3.1.3.

$Ba_{1-x}Sr_xCo_{1-y}Fe_yO_{3-\delta}$ (BSCF) has been widely studied for IT-SOFC cathode applications due to its high oxygen vacancy concentration and high ionic conductivity.[46, 55, 90, 91] BSCF can remain stable while containing a large concentration of oxygen vacancies due to the large size mismatch between the two A-site cations.[92, 93] However, this large size mismatch is also the source of a number of detrimental properties. Firstly, it causes thermal instabilities; below 850°C BSCF degrades over time from a cubic structure to a mixture of cubic and hexagonal phases;[94–99] the degradation is accompanied by a decrease in electrical conductivity[94, 96–101] and slower oxygen transport properties.[102]

In addition to this thermal instability, BSCF also has a number of decomposition routes, due to the large number of Ba-based oxides. Kuklja *et al.*[103] determined, using electronic structure calculations, that full and partial Schottky disorder, as well as new phase growth, have relatively low energies in BSCF, lower than other related perovskites, making them likely to decompose, even at low temperatures.

Furthermore, BSCF-based cathode materials, are susceptible to $CO_2$ poisoning, forming carbonate $BaCO_3$ at temperatures below 900°C.[104–107]

Finally, there are issues surrounding the use of BSCF within a fuel cell stack. BSCF has been shown to react with common electrolyte and barrier materials; such as YSZ[46] and samarium doped ceria (SDC),[108] forming layers with lower conductivity and therefore limiting the activity of the cell. In addition, BSCF materials have high TECs compared with common electrolyte materials, due to the presence of cobalt, which will cause thermal stresses during operation.

Research into BSCF for IT-SOFC cathode applications is still ongoing, to find methods of reducing the stability issues discussed above. One such method is to introduce A-site deficiency,[109] which has been reported to lower the TEC of BSCF, particularly in the 450 to 750°C temperature range. The use of composite cathodes of BSCF with alternative electrolyte materials to YSZ, for example LSGM[110] and $BaZr_{0.1}Ce_{0.7}Y_{0.2}O_3$,[111] has also been considered as a method to improve the

stability and electronic conductivity of BSCF. However, Švarcová *et al.*[94] studied the transition of cubic BSCF to the hexagonal phase and concluded that the simplest method to avoid degradation was to substitute Ba or Sr with La, suggesting that lanthanum-based materials, such as LSCF, are more promising candidates for IT-SOFC cathode applications due to their higher stability,[92] even though they have higher oxygen vacancy formation energies and therefore a smaller concentration of these defects, vital for ionic conductivity. The degradation into hexagonal phases is not observed in cubic LSCF and there are fewer lanthanum-based oxides meaning less degradation routes.[92] For this reason, LSCF and its parent materials have become the focus of our research into potential SOFC cathode materials.

#### 1.3.1.3 $La_{1-x}Sr_xCo_{1-y}Fe_yO_{3-\delta}$

Of the class of doubly doped perovskite oxide materials, $La_{1-x}Sr_xCo_{1-y}Fe_yO_{3-}$ (LSCF) is a stand out candidate for IT-SOFC applications. LSCF-based materials have shown high electronic and ionic conductivities along with high catalytic activity and low thermal expansion coefficients, see Table 1.1, making them more compatible with common electrolytes.[50–53] It is, therefore, not surprising LSCF has received a large amount of attention as a promising IT-SOFC cathode candidate.

The chosen ratios of cations on both the A and B-sites are of vital importance for the success of LSCF-based materials as IT-SOFC cathodes. Increasing the Sr content on the A-site, x, increases the oxygen non-stoichiometry and ionic conductivities.[112] Electrical conductivity also increases with increasing Sr content but only up to a maximum of x = 0.5,[112] after which it decreases again with higher Sr content. However, the TEC of the material increases with increasing Sr content, making it less compatible with common electrolyte materials.[112, 113]

When doping on the B-site, one must consider the balance between electrochemical activity and stability. Cobalt is responsible for the catalytic activity of the material, meaning a higher proportion of Co leads to an increased activity towards the oxygen reduction reaction. Cobalt also has less tendency to bind oxygen, compared to iron, and therefore oxygen vacancies are formed more readily in a material with higher cobalt content, leading to a higher ionic conductivity.[19, 35, 114] However,

increasing the Co content substantially increases the TEC of the material, and also decreases the materials stability in oxidising atmospheres,[112] meaning a low Co content is often required for a stable performance.

The relative proportions of the cations present in $La_{0.6}Sr_{0.4}Co_{0.2}Fe_{0.8}O_{3-\delta}$ (LSCF6428) are commonly used to optimise electronic conductivity and catalytic activity with stability and compatibility with electrolyte materials.[46] LSCF6428 has proved very successful, demonstrating similar power densities to LSM, but at operating temperatures of 100°C lower,[113] while also showing a higher resilience towards Cr poisoning.[50]

However, as with all potential cathode materials discussed so far, LSCF-based materials are not without drawbacks. Although LSCF tends to be more thermally stable than BSCF, with the degradation to hexagonal phases not observed for this doubly doped pervoskite, it does suffer from other degradation issues.[115, 116] Most notable is their reactivity with YSZ,[50] which causes $La_2Zr_2O_2$ or $SrZrO_3$ insulating layers to form, significantly reducing the activity of the cathode,[90] although long term performance can be improved by using alternative electrolytes, such as GDC or a GDC barrier layer between the cathode and electrolyte.[79, 117, 118] Other potential causes of degradation include strontium segregation to the electrolyte surface,[46, 52] coarsening of the LSCF micro-structure and sulphur poisoning.[46]

The defect chemistry of this material is expected to play an important role in both the successful electrochemical properties and the degradation mechanisms of the LSCF-based materials.[113] We wish, therefore, to understand this material at an atomic scale. Through understanding the effect of the dopants on both sites, and the defects that can form in compensation, we hope to identify the fundamental factors controlling performance and approaches that could address the degradation issues. However, this doubly doped perovskite, containing two transition metals, is difficult to model accurately, with order parameters on both the A- and B-site lattices as well as dopant stoichiometries to consider.

Previous computational investigations of LSCF have employed various assumptions in order to model this material, including: 1) Periodically ordered A- and B-site

lattices,[119] 2) Treating the two cation lattices separately,[120] 3) Restricting the magnetic ordering of the transition metals to FM ordering,[119, 120] 4) Using the same Hubbard *U* parameter[121, 122] (See Chapter 2, section 2.3.3.3) for each transition metal,[120] or using no Hubbard *U* parameter at all.[119] With some assumptions, e.g. FM ordering of the transition metals, there is experimental evidence that this is an acceptable assumption to make, considering the operational temperatures of these materials.[120] However, some assumptions are an over simplification and will limit the accuracy of the information gained from such models.

Therefore, an alternative strategy is to model dopants and defects in the parent materials of LSCF; $LaFeO_3$ and $LaCoO_3$. The work of this thesis will focus on $LaFeO_3$; for work on $LaCoO_3$ see Ref[123].

### 1.3.2 Ruddlesden-Popper Phases

Before moving on to our discussion of $LaFeO_3$ in more detail, it is worth mentioning an alternative class of materials that has been considered for IT-SOFC cathode applications. Although related to conventional cubic perovskites discussed so far, such as $LaMnO_3$ and $LaCoO_3$, Ruddlesden-Popper phases have a layered structure, made up of $ABO_3$ layers sandwiched between AO rock salt layers, see Figure 1.6, giving a general formula of $A_{n+1}B_nO_{3n+1}$ where n refers to the order of the Ruddlesden-Popper phase; n = 1, 2, 3, etc.

As with the related class of conventional perovskites discussed so far, Ruddlesden-Popper materials offer the ability to fine tune properties such as conductivity and electrochemical properties through careful selection of the A- and B-site cations.[124–135] A predominant reason for the interest in members of the Ruddlesden-Popper series for IT-SOFC cathode applications is their ability to accommodate both oxygen deficient and oxygen excess stoichiometries, for example $La_2NiO_{4-\delta}$ and $La_2NiO_{4+\delta}$, allowing oxygen ion migration to be mediated via either vacancies or interstitials.[46, 124–135] It is the oxygen excess materials that have gained the most interest for SOFC cathode applications, as they tend to have a simpler structure - Ruddlesden-Popper materials need to be doped with divalent cations to form a significant concentration of oxygen vacancies - and show very high

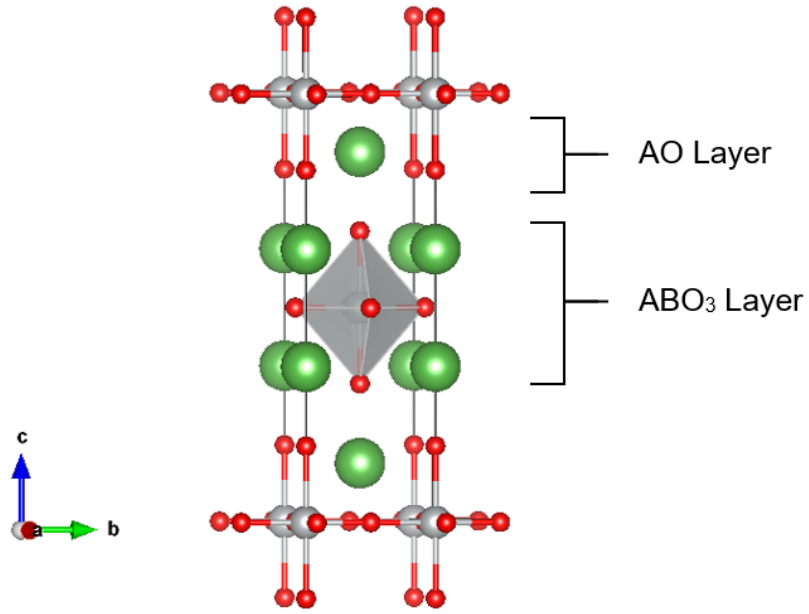


**Figure 1.6:** The structure of Ruddlesden-Popper materials using $La_2NiO_4$, a first order Ruddlesden-Popper material, as an example; $LaNiO_3$ layers are sandwiched between two LaO layers.

oxygen transport rates.[55, 136, 137] Of the oxygen excess Ruddlesden-Popper materials, it is those based on nickel that have been the main focus of research into this class of materials for IT-SOFC applications, such as $La_2NiO_{4+\delta}$.[41, 46, 55, 90] Investigations into the nickelate family of Ruddlesden-Popper phases tend to focus on La and Pr as the A-site cations, as these materials display fast oxygen ion conduction, good electrocatalytic properties and relatively low TECs.[46] $La_2NiO_4$ exhibits the tetragonal symmetry, seen in Figure 1.6, between 423 - 1073K, covering the temperature range for IT-SOFC applications. Skinner[138], using molecular dynamics, found that oxygen diffusion in both $La_2NiO_4$ and $Pr_2NiO_4$ is highly anisotropic, with almost all diffusion occurring in the a-b plane via an interstitialcy mechanism,[139–142] where an interstitial oxygen displaces an oxygen ion on a lattice site, causing the displaced ion to become an interstitial. The diffusion coefficients calculated by Skinner matched well with reported experimental values. The anisotropic diffusion of oxygen interstitials in Ruddlesden-Popper materials has since been confirmed by a number of groups using both computational[56, 140, 143, 144] and experimental techniques.[135, 136, 145–149]

The migration of oxygen interstitials along the a-b plane is aided by the lattice flexibility of these materials; i.e. cooperative tilting and un-tilting of the $NiO_6$ octahedra.[56] This dependence on lattice flexibility causes a dependence of the oxygen diffusivity on hyper-stoichiometry (oxygen excess). Initially diffusion increases rapidly with $\delta$, due to increasing concentrations of oxygen interstitials but levels off, at around $\delta = 0.02$ for $Pr_2NiO_{4+\delta}$, due, it is suggested, to the increased concentration of oxygen interstitials stiffening the lattice making it difficult of the $NiO_6$ octahdra to tilt.[56] Unfortunately, the nickelates, both $La_2NiO_4$ and $Pr_2NiO_4$, have stability issues below 1000°C[62, 150–153] and have been observed as being reactive towards common electrolyte materials, with Sayer *et al*.[154] reporting significant activity between $La_2NiO_{4+\delta}$ and gadolinium doped ceria oxide (GDC) at high temperatures (above 900°C), while $Pr_2NiO_{4+\delta}$ has been shown to react with YSZ.[155] However, $La_2NiO_{4+\delta}$ is unreactive towards LSGM,[154] and using barrier layers between electrode and electrolyte, to prevent reaction, has proved successful in a number of cases.[156, 157]

Alternative n = 1 Ruddlesden-Popper based materials that have been considered for IT-SOFC cathode applications include $La_2CoO_{4+\delta}$,[56] $La_2CuO_{4+\delta}$,[41] and $Pr_2CuO_{4+\delta}$.[90] All three can accommodate excess oxygen as interstitials and have displayed fast oxygen migration via an interstitalcy mechanism along the a-b plane, with limited mobility seen along the c-direction, as with the nickelate material.[139–142, 158]

In addition to the n = 1 series of RP materials, higher order phases have also been considered for IT-SOFC cathode applications.[124] $La_3Ni_2O_{6.95}$ and $La_4Ni_3O_{9.78}$ were shown to have higher electronic conductivities than $La_2NiO_4$, and display long term stability and compatibility with common electrolytes.[124, 125, 159–162] However, the mechanism of ionic transport is not as clearly understood as in the n = 1 materials; also, catalytic activity tends to be higher in materials with lower values of n.[161]

The main issue with all Ruddlesden-Popper materials is their low electronic conductivity particularly when compared to the conventional perovskites.[46, 90] So

although Ruddlesden-Popper phases offer an interesting alternative for cathode applications, materials based on cubic perovskites, such as LSCF, currently display higher performances and are therefore the focus of this work.

## 1.4 $LaFeO_3$

$LaFeO_3$ exhibits high stability in both oxidising and reducing atmospheres,[163, 164] while having reasonable ionic and electronic conductivities which can be improved on doping. These properties make it of great interest for SOFC cathode applications.

In this final section of the current chapter, we shall introduce $LaFeO_3$, discuss its crystal, electronic and magnetic structure and review previous work on $LaFeO_3$-based materials for SOFC applications.

The properties of $LaFeO_3$ strongly depend on its defect chemistry, potential dopants and surface chemistry. These three topics will be discussed in greater detail in Chapters 4, 6 and 7; however, we shall briefly describe previous work in these areas which have provided the basis for the work we have carried out.

### 1.4.1 Crystal Structure and Morphology

At low and ambient temperatures, $LaFeO_3$ adopts the orthorhombic perovskite form, with space group *Pbnm* (no. 62).[165] $LaFeO_3$ goes through a phase transition from orthorhombic to rhombohedral, between 980 and 1005°C dependent on stoichiometry, thermal history and dopant content,[166, 167] with a further phase transition from rhombohedral to cubic observed in doped samples.[166]

Due to the orthorhombic structure of $LaFeO_3$ at ambient conditions and the rhombohedral phase transition occurring at temperatures higher than the desired temperature range for IT-SOFC applications, the orthorhombic structure is used throughout our work. It is shown in Figure 1.7.

The orthorhombic perovskite structure is a distorted form of the cubic perovskite, with neighbouring octahedra tilted in alternate directions, described in Glazer notation as $a^+b^-b^-$.[168–170] The tilting of the octahedra leads to a larger unit cell and inequivalent lattice parameters, listed in Table 1.2.

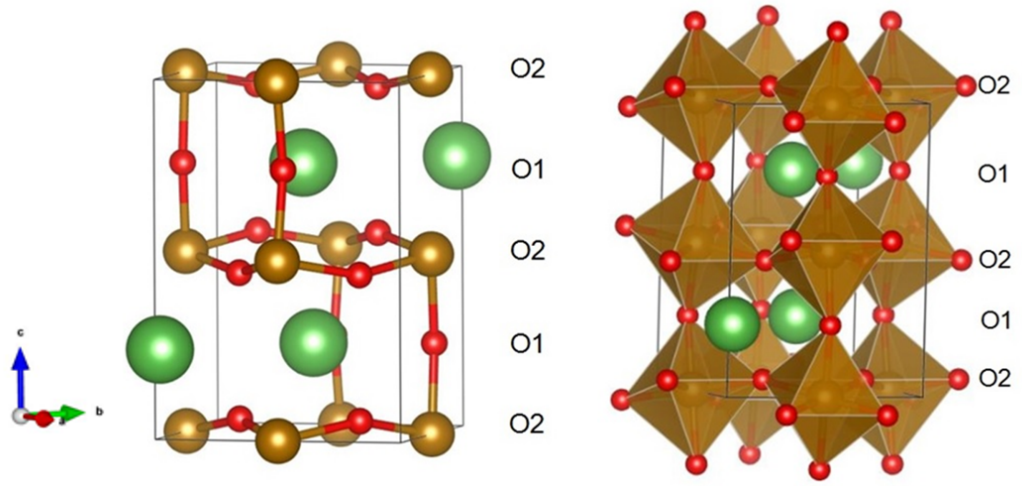


**Figure 1.7:** Orthorhombic form of $LaFeO_3$; lanthanum is shown in green, iron in gold and oxygen in red. Labels, O1 and O2, to the right of the structure show the two oxygen environments.

**Table 1.2:** Experimental[2] lattice parameters of orthorhombic $LaFeO_3$.

| Direction | Lattice Parameter / Å |
|---|---|
| a | 5.553 |
| b | 5.563 |
| c | 7.862 |

Another structural feature caused by the tilting octahedra is a change in the six Fe-O bond lengths away from uniformity into two groups: four equatorial Fe-O bonds with a bond length of 2.019 Å while the two axial bonds have a bond length of 2.005 Å.[165] The two different Fe-O bond lengths create two inequivalent oxygen environments, referred to as O1 and O2 throughout this work. The O2 oxygen ions are equatorial to $Fe^{3+}$, while the O1 oxygen ions are axial, see Figure 1.7 where the oxygen environments are labelled to the right of each structure.

### 1.4.2 Electronic and Magnetic Structure

Lanthanum and iron are both in 3+ charge states in $LaFeO_3$, meaning iron has a $d^5$ electronic configuration. Iron in $LaFeO_3$ is in an octahedral environment and favours a high spin formation, so each $t_{2g}$ and $e_g$ $d$-orbital is occupied by a single electron, leading to a maximum theoretical magnetic moment of 5 $\mu_B$ for each $Fe^{3+}$ ion.

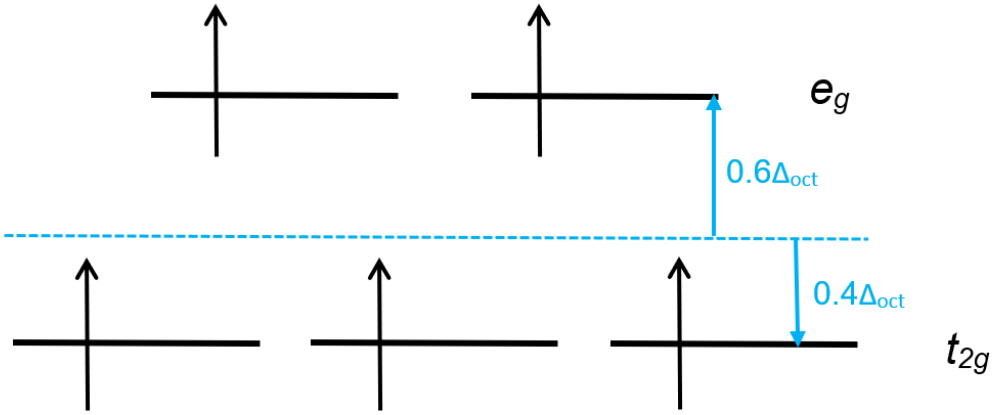


**Figure 1.8:** The octahedral split and band filling for the $d^5$ transition metal ion, $Fe^{3+}$, where $e_g$ and $t_{2g}$ are $d$-band orbitals and $\Delta_{oct}$ is crystal field splitting energy, the energy difference between the $d_{z^2}$ and $d_{x^2-y^2}$ (the $e_g$ orbitals), and the $d_{xy}$, $d_{xz}$ and $d_{yz}$ (the $t_{2g}$ orbitals).

There are a number of possible magnetic arrangements for the $Fe^{3+}$ ions in the $LaFeO_3$ lattice: ferromagnetic (FM), in which the magnetic dipole of all $Fe^{3+}$ ions are aligned, and antiferromagnetic (AFM), where the magnetic moment of neighbouring $Fe^{3+}$ ions are opposed. The antiferromangetic arrangement has three subcategories; AFM-C, AFM-A and AFM-G which differ in the arrangement of neighbouring spins. The four possible magnetic arrangements are shown in Figure 1.9.

Experimentally, the ground state magnetic arrangement of $LaFeO_3$ is AFM-G, where every $Fe^{3+}$ ion is aligned in the opposite direction to all its neighbouring $Fe^{3+}$ ions. The Néel temperature of $LaFeO_3$ is roughly 450°C[166, 167, 171] so that at IT-SOFC operating conditions $LaFeO_3$ is likely to be paramagnetic. However, because the modelling methods employed in this work do not take entropic effects into account, and does not include dynamic effects, we chose to model $LaFeO_3$ using AFM-G ordering of the $Fe^{3+}$ ions, as opposed to paramagnetic ordering.

### 1.4.3 Defects in $LaFeO_3$

Several key materials properties, including structure and conductivity, are dependent on the material's defect chemistry and an understanding of the defect properties of a material is necessary to optimise them for specific applications.

Although doped $LaFeO_3$ displays superior performance as a cathode material, com-

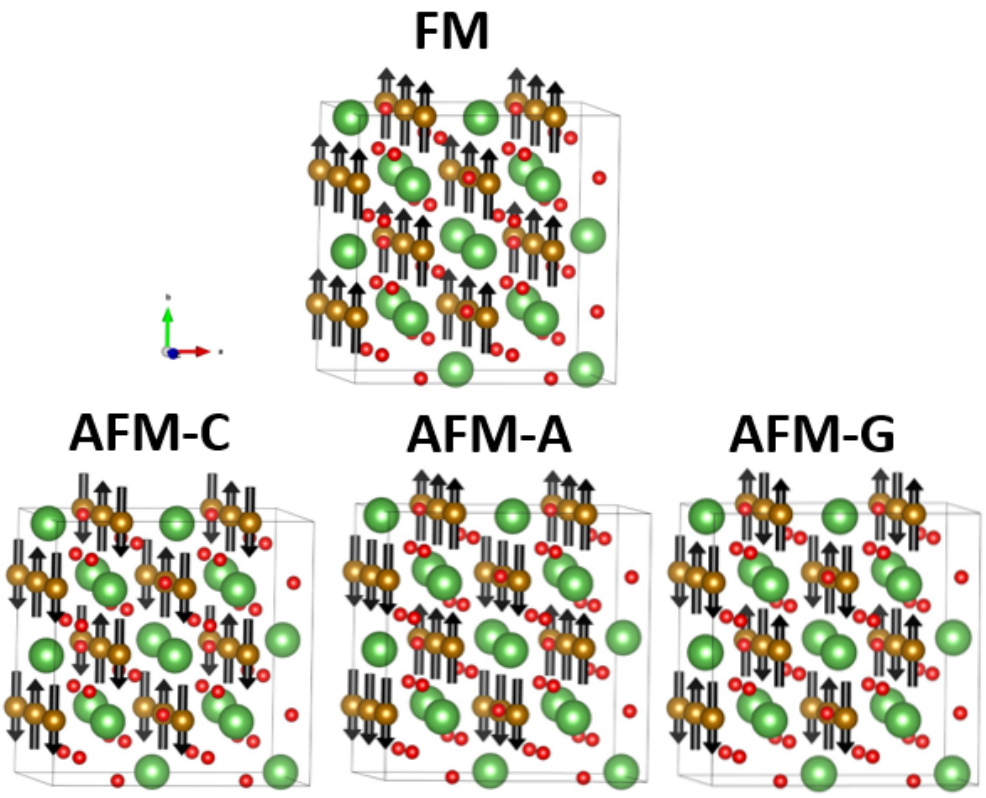


**Figure 1.9:** Possible spin arrangements for $Fe^{3+}$ in $LaFeO_3$: Ferromagnetic (FM), and antiferromagentic C, A and G (AFM-C. AFM-A and AFM-G respectively). AFM-G is the experimental ground state spin arrangement in $LaFeO_3$.

pared to the stoichiometric material, it is important to understand the defect chemistry of the stoichiometric material initially, before external dopants are introduced. Having a complete picture of the intrinsic defects present in the system is essential in understanding the effect of dopants on the properties of $LaFeO_3$.

For such atomic scale insight, computational techniques are invaluable, as studying particular point defects using experimental techniques is highly challenging. In Chapter 4, we will investigate a range of point defects in $LaFeO_3$, using two different computational methods, to establish the defects most likely to be present and their relative concentrations. Here, an overview of previous studies on defects in $LaFeO_3$ will be given, including both computational and experimental work.

There are two predominant computational techniques that have been used to study point defects in perovskite-type materials: interatomic potential-based methods[27,

172–174] and density functional theory (DFT).[54, 119, 120, 123, 174–177]

Using interatomic potentials, Jones and Islam,[27] calculated the energies of isolated point defects in orthorhombic $LaFeO_3$ and presented them in terms of Frenkel and Schottky disorder energies, see Chapter 4 Section 4.1.1. They found that Frenkel disorder was highly unfavourable, in line with the expected difficulty of forming interstitials in closely packed materials such as perovskites. The energies of Schottky disorder, although lower, were also considered too high to contribute significantly to the defect chemistry of stoichiometric $LaFeO_3$, leading them to conclude that dopants were required for $LaFeO_3$ to exhibit *p*-type conductivity.[27]

DFT studies of defects in $LaFeO_3$ have focused mainly on oxygen vacancies rather than considering a range of defects. Ritzmann *et al.*[175] investigated the formation energies of oxygen vacancies in $La_{1-x}Sr_xFeO_3$ at increasing Sr content: x = 0, 0.25 and 0.5. They found that the formation energy of an oxygen vacancy was high in $LaFeO_3$ compared to the doped samples because the electrons released from the formation of the oxygen vacancy localised on $Fe^{3+}$, reducing it to $Fe^{2+}$, whereas, in the doped material, the electrons compensate holes introduced by strontium. Following the work on $La_{1-x}Sr_xFeO_3$, they considered the effect of lanthanum vacancies on the formation energies of oxygen vacancies in unsubstituted $LaFeO_3$, after observing that the computational reaction enthalpies for oxygen vacancy formation matched well with experimental results whereas the predicted concentrations of oxygen vacancies did not.[54] They found that introducing a small number of lanthanum vacancies reduced the formation energy of oxygen vacancies significantly and they argue that the holes created from a lanthanum vacancy compensate for the electrons formed from an oxygen vacancy. They noted that the formation of an isolated lanthanum vacancy is high; 4.33 eV, but did not consider how lanthanum vacancies would be incorporated into $LaFeO_3$.

Experimentally, defect models have been proposed through investigations into the electronic conductivity of $LaFeO_3$ by Mizusaki *et al.*[48] and Wærnhus *et al.*[49, 167] Mizusaki *et al.*[48] studied electronic conductivity and Seebeck coefficients under varying temperatures and oxygen partial pressures. They found that

at the highest oxygen partial pressures, conductivity was independent of the partial pressure, in the mid-range of partial pressures the conductivity decreased with decreasing partial pressure and at the lowest range of partial pressures, conductivity increased with decreasing partial pressure. Combining these observations with the Seebeck coefficient being positive at high partial pressures and negative at low partial pressures (representing *p*-type and *n*-type conduction respectively) they constructed a defect model and conclude that *n*-type conductivity is caused by hopping between $Fe^{3+}$ and $Fe^{2+}$, while *p*-type conduction is caused by hopping between $Fe^{3+}$ and $Fe^{4+}$. They proposed that the electronic properties of $LaFeO_3$ may be effected by lanthanum vacancies as well as oxygen vacancies. More recently, Wærnhus *et al.*[49, 167] found a similar trend in electrical conductivity: *n*-type conductivity at low oxygen partial pressures and *p*-type at high partial pressures, when investigating the electronic properties of $La_{1-y}FeO_3$ where y = -0.003, 0.0 and 0.003. The conductivity was found to be independent of y, with secondary phases of $La_2O_3$ or $Fe_2O_3$ found in the non-stoichiometric samples, instead of the off-stoichiometry introducing defects and therefore effecting the conductivity. Using their results Wærnhus *et al.*[49, 167] proposed a defect model that identified Schottky defects are being responsible for the *p*-type conductivity at high partial pressures, instead of isolated lanthanum vacancies as suggested by Mizusaki.[48] In addition, whereas Mizusaki *et al.*[48] identified lanthanum as being the cation vacancy aiding conductivity under high oxygen partial pressures, Wærnhus *et al.*[49, 167] suggested that both lanthanum and iron vacancies could be present in $LaFeO_3$ and therefore both could be involved in controlling the conductivity.

The works of Jones,[27] Ritzmann,[54, 175] Mizusaki[48] and Wærnhus[49, 167] have provided valuable insight into the defect chemistry of $LaFeO_3$. However, the lack of consideration of a full range of point defects and disorder schemes means we do not have a complete picture of the defect chemistry of stoichiometric $LaFeO_3$. The aim of our work in this area is to consider a large range of point defect species and disorder schemes in order to establish those which will be present under different operating conditions, their concentrations and their effect on conductivity.

Doing so will provide a starting point for investigating the effects dopants have on the concentration of these defects, and thus their effect on the conductivity regimes which are vital for efficient SOFC cathode applications.

### 1.4.4 Doped-$LaFeO_3$ Based Materials

A common method of increasing the ionic and electronic conductivity properties of perovskite oxides, is to introduce dopants on either the A- or B-site. For $LaFeO_3$ the most common example, as with $LaCoO_3$, is substituting strontium on the A-site; $La_{1-x}Sr_xFeO_3$ (LSF).

Doping $LaFeO_3$ affects its structural, transport and electrical properties.[171, 178–190] The introduction of $Sr^{2+}$ increases both the ionic and electronic conductivity of $LaFeO_3$, by introducing oxygen vacancies and holes, the latter of which tend to localise on the $Fe^{3+}$, forming $Fe^{4+}$ ions.[55, 90, 175, 191] Unlike $La_{1-x}Sr_xCoO_3$, LSF has shown improved compatibility with YSZ, both through its unreactivity towards the electrolyte material, and by having a similar TEC,[55, 191, 192] suggesting promising performance as an IT-SOFC cathode material.

The key factor in the performance of LSF is the strontium content. Increasing the strontium content causes an increase in desirable properties such as ionic and electronic conductivity;[175] however, as the strontium content increases, LSF begins to react with YSZ forming $SrZrO_3$ and $SrFe_{12}O_{19}$, both of which are insulating phases that will have a negative impact on cathode performance.[193] Increasing the strontium content also increases the TEC, meaning increasing the strontium content makes LSF materials less compatible with common electrolytes.[166] Therefore, the choice of strontium content is a balance between suitable conductivity properties and long term fuel cell stability.

The prominent issue with LSF, is that using iron instead of cobalt as the B-site cation has a negative impact on the ionic and electronic conductivity of the material and lower ionic and electronic conductivities leads to lower activity as an IT-SOFC cathode material and therefore lower efficiencies.[46, 194]

To address this issue, further doping strategies need to be considered, for example doping on the B-site - in addition to, or instead of A-site doping - or by using

alternative A-site dopants. In Chapter 6 we present our results on investigating a range of A- and B-site dopants in $LaFeO_3$ with the aim of assessing the most appropriate for improving the properties of $LaFeO_3$ for SOFC cathode applications.

Strategies for doping the A-site have focused on incorporating divalent alkali earth metals, because their similar size to $La^{3+}$ ions allows them to be easily incorporated into the perovskite structure without causing strain on the system while the lower valence of these dopant ions encourages the formation of charge compensating species important for conductivity, namely oxygen vacancies and holes.[178–180] Although most previous work on doping the A-site of $LaFeO_3$ focuses on strontium, some groups have considered calcium a viable alternative.[179, 180, 184, 195–197] Hung *et al.*[197] demonstrated that calcium doped $LaFeO_3$ has a similar electronic conductivity to LSF, in agreement with Ortiz-Vitoriano *et al.*[184] who found no significant difference in the electrochemical performance of $La_{1-x}Sr_xFe_{0.8}Ni_{0.2}O_{3-\delta}$ when strontium was replaced with calcium. They concluded that calcium is the optimum A-site dopant, of the alkali earths, as it is significantly cheaper than strontium as well as having a similar electrochemical performance. However, Bidrawn *et al.*[180] reported that calcium doped $LaFeO_3$ has a lower ionic conductivity than LSF and a higher activation energy for ionic transport meaning it will be less active as a SOFC cathode material compared to $La_{1-x}Sr_xFeO_3$. Hung *et al.*[197] did not consider the ionic conductivity of $La_{1-x}Ca_xFeO_{3-\delta}$ in their work and it is therefore difficult to form a conclusion on the performance of calcium doped $LaFeO_3$ compared to strontium doped $LaFeO_3$ for SOFC cathode applications. There is a clear need for clarity on the subject of A-site dopants in $LaFeO_3$ and our work uses a consistent approach on a range of potential dopants to establish the most appropriate dopant for the A-site.

Studies on B-site doped $LaFeO_3$ have focused on divalent first row transition metals. Through the addition of divalent transition metals the magnetic properties and electrical conductivity of $LaFeO_3$ can be tuned along with the TEC and sintering temperature.[178, 181–183, 185, 188, 198, 199] In common with the limited nature of previous work on A-site dopants in $LaFeO_3$, work on B-site dopants has

predominantly focused on two dopants; cobalt and nickel. The addition of cobalt to $LaFeO_3$ increases both electronic and ionic conductivity.[182] The electronic conductivity of $LaFe_{1-x}Co_xO_3$ increases with increasing Co content as cobalt is more reactive than iron and will more readily increase its valence state, facilitating conductivity via electron 'hopping',[187] while ionic conductivity increases due to the more favourable formation energies of oxygen vacancies in cobalt-based perovskites compared to iron-based perovskites.[183] These increases in conductivity are expected, considering the high electronic and ionic conductivities of $LaCoO_3$-based materials. However, the instabilities associated with these materials are also likely to be incorporated when cobalt is used as a dopant, including high TECs and reactivity towards common electrolyte materials; therefore only small amounts of cobalt are usually incorporated, to limit these drawbacks.[112]

Introducing nickel as a B-site dopant in $LaFeO_3$ increases the mobility of charge carriers, in turn increasing the conductivity of the material.[188] However, Coffey *et al*.[185] found that when nickel was introduced as a B-site dopant in LSF, despite increasing the electronic and ionic conductivity of the material, higher power densities were found for the undoped material; to explain this observation, Coffey suggested that nickel increased the number of active sites for the oxygen reduction reaction, but decreased their activity.[185]

As demonstrated by the work by Coffey *et al*.,[185] the majority of previous work on B-site dopants in $LaFeO_3$ has been performed with the aim of improving or tuning the properties of LSF,[185, 190] so there is limited data on the effect that only doping on the B-site has on the properties of $LaFeO_3$. In our work we consider the effect of individual dopants on $LaFeO_3$, in order to establish the optimum dopant for each site independently, providing a foundation on which work on double doping $LaFeO_3$ can be built.

Computational studies on both A- and B-site doped $LaFeO_3$ are limited and tend to focus on dopant concentration without first considering the most appropriate dopant for this system.[175, 179] Work that has examined a range of dopants has generally been carried out using interatomic potential-based methods.[27] However, using

these approaches to model transition metal ions accurately can pose challenges especially when considering both electronic and point defect charge compensation of the dopant site. Therefore, in our work we employ both interatomic potential techniques and DFT to study A- and B-site dopants in $LaFeO_3$, considering their energies of incorporation and the charge compensating species that are favourably produced. These two parameters will help establish the most favourable dopant for each site and the effect of these dopants on the conductivity of $LaFeO_3$.

### 1.4.5 Surface Studies on $LaFeO_3$

Another important consideration when assessing the suitability of a material for solid oxide fuel cell cathode applications is its surface chemistry and an analysis of potential surface structures of $LaFeO_3$ and their defect chemistry will form the final section of this thesis.

At the surface of a MIEC cathode material, oxygen is adsorped and reduced before migrating through the cathode to the electrolyte. This process is highly dependent on the surface termination, structure, composition, and the defects (if any) that are present. Studying surfaces, particularly the defect chemistry of surfaces, experimentally can be challenging, and therefore computational techniques can provide an invaluable insight in this area of research. In the following section, previous work on $LaFeO_3$ surfaces, along with surface studies of related perovskite type materials, will be discussed.

Both interatomic potentials,[72] and DFT-based techniques have been used to study perovskite surfaces,[200–207] although based on the difficulties interatomic potentials can encounter dealing with transition metals, and their importance in catalytic processes at the surface, DFT is most widely used.

Read *et al.*[72] studied surface properties of cubic $LaCoO_3$ using interatomic potentials and found that, of the low index surfaces, the (110) and (100) will be most prominent in the surface morphology of $LaCoO_3$ and that oxygen defects and strontium dopants are likely to segregate to the surface, as the formation energy of these defects on the surface is lower than in the bulk. These conclusions are in agreement with DFT studies which suggest that the (001) surface is the most stable in

lanthanum based perovskite oxides,[200, 208, 209] as the work by Read et al.[72] considered the cubic form of $LaCoO_3$ the (100) and (001) surfaces would be equivalent. In addition, DFT was employed to study the surfaces of $LaBO_3$, where B = Mn, Fe, Co or Ni,[92, 200] and also found that defect formation energies are lower on the surface of perovskite materials compared to the bulk, in line with the conclusions of Read *et al*.[72]

However, the work by Read *et al*.[72] used the same interatomic potentials in both the bulk and surface calculations performed, which was done to be consistent and allow comparison, but which assumes the charge on the ions and their polarisability do not change when going from the bulk to the surface, which could lead to errors when considering defects.

As mentioned, the (001) surface is considered the most stable surface of perovskite oxides and therefore the majority of DFT surface studies focus on this surface, considering the defect chemistry of the (001) surface, and their impact on the oxygen reduction reaction.[200–202, 209] Lee *et al*.[200] studied the (001) surface of $LaBO_3$ perovskites, where B = Mn, Fe, Co or Ni, and found that oxygen vacancies are more stable on the (001) surfaces compared to the bulk. They calculated oxygen vacancy formation energies for both the $BO_2$ and LaO terminated (001) surfaces, and concluded that the LaO terminated surface is probably catalytically inactive, as it consistently exhibited higher formation energies compared to the $BO_2$ termination; the same conclusion was found in studies of LSM (001) surfaces.[92, 206, 207] Contrary to this conclusion, recent work by Kizaki *et al*.[203] on $LaFeO_3$ and Akbay *et al*.[210] on $La_2NiO_4$ found that the LaO terminated (001) surfaces could be catalytically active. Kizaki suggested that this activity was due to hybridisation between the adsorbed species and the transition metal in the sub surface layer,[203] while Akbay concluded that the enhanced electronic configuration of the La sites adjacent to the surface species were responsible for the observed catalytic activity.[210] In addition, work on LSM suggests that strontium doping can lead to a stabilisation of the LaO terminated (001) due to the segregation of strontium ions to this surface.[204, 205, 211, 212] We will, therefore, consider both the $FeO_2$ and LaO

terminated (001) surfaces of $LaFeO_3$ in our work, as both may be of catalytic importance.

Studying surfaces, using DFT, can be highly demanding computationally. The majority of investigations utilise the slab model,[200–203] in which a supercell of the bulk structure is cleaved along an appropriate plane - depending on the desired surface - and a vacuum inserted, creating two surfaces either side of the vacuum. When using the slab model, the accuracy depends on the number of layers in the slab as well as the surface area of the top layer. There must be enough layers in the slab to encompass both surface and bulk layers, while the surface area of the top layer is particularly important when considering defects as it must be large enough to avoid strong interactions between defects in periodically repeated supercells. A further consideration is surface polarity: if there is a net dipole in the slab, the Coulombic energy is divergent. To aid investigations of ionic surfaces, Tasker[1] outlined the cause of the energy divergence and defined three types of surface: type I, type II and type III. In type I surface slabs, each layer has a stoichiometric ratio of cations and anions so that each layer has no net dipole and the slab will have a zero net dipole. Type II slabs have layers that have a net charge themselves, but the layers are arranged so that the net charges will cancel in the repeating cell unit, leaving a zero net dipole in the final slab. Type III slabs again have layers that have a net charge, with the repeating unit having a non-zero dipole leading to a dipole perpendicular to the surface when the cell is cleaved between any of the layers, Figure 1.10 shows a visual representation of types I to III. The (001) surface of $LaFeO_3$, along with similar low index surfaces in related perovskites, is a type III surface and the dipole must be cancelled in order to model these surfaces, this is achieved through reconstruction.

There is limited previous work focusing on $LaFeO_3$ surfaces in the context of SOFC cathode applications and those that are present use small numbers of layers and do not account for the surface polarity, reporting results for non-reconstructed polar surfaces.[203] Our work on the (001) surface of $LaFeO_3$ considers the $FeO_2$ and LaO terminated surfaces, with both reconstructed to correct for the polarity present.

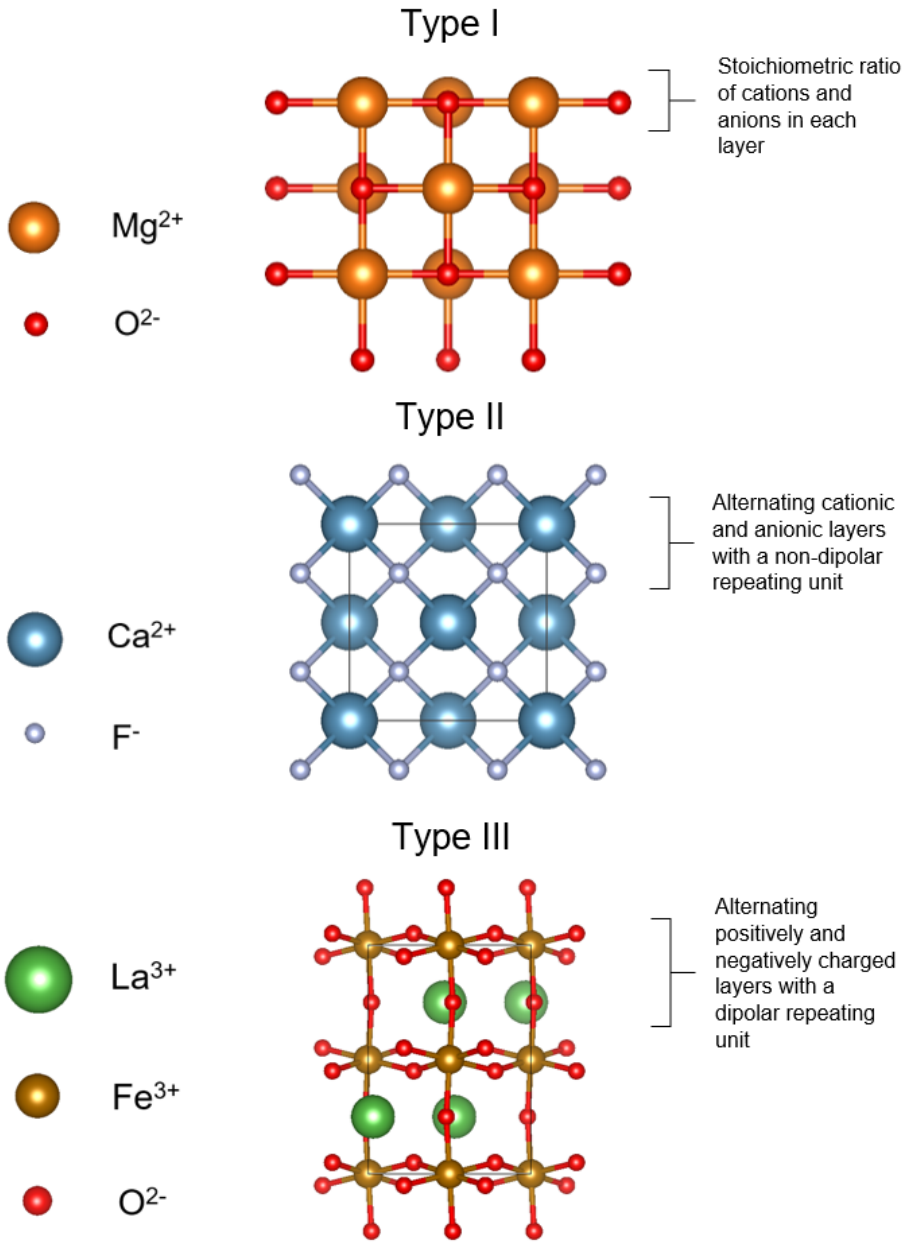


**Figure 1.10:** A visual representation of the types of surfaces defined by Tasker[1]; type I is demonstrated by the (001) surface of MgO, type II by the (001) surface of $CaF_2$ and type III by the (001) surface of $LaFeO_3$.

We will consider the defects important for cathode applications and compare their formation energies on both surface terminations and with the bulk material.

## 1.5 Concluding Remarks

In this introduction, the motivation behind our work has been outlined along with a detailed discussion regarding solid oxide fuel cells, their main component parts and the materials of interest for each. Focusing on the cathode, the predominant materials that are currently the subject of a large amount of research have been introduced, including $LaCoO_3$-based materials, BSCF, LSCF and $La_2NiO_4$ with the benefits and drawbacks of each material discussed. The final section introduced the material which is the focus of the rest of this thesis: $LaFeO_3$, with accounts of previous work on the areas of defect chemistry, doped $LaFeO_3$ materials and surface chemistry.

In the next chapter, the theory behind the computational techniques used in this work will be presented, followed by the specific details of the parameters used in these techniques. Chapters 4 to 7 cover our results on defect chemistry, oxide ion migrations, dopants and surface chemistry respectively before summarising the results of this thesis in Chapter 8.

# Chapter 2

# Theory: Modelling Solid State Systems

## 2.1 Introduction

Computational modelling is a powerful tool for studying materials and their properties. Modelling methods can be used to understand atomic level processes, controlling properties such as electrical conductivity, reactivity and degradation, many of which are dependent on defect structures. Modelling can also be applied to predicting such properties, making it invaluable in the search for new functional materials. For defects in solid state systems, on which a significant amount of the following work is focused, computational modelling is a particularly useful tool as studying defects experimentally is complex - both for performing the experiments themselves and analysing the results afterwards - and needs input from computational models. Analysis and interpretation of experimental data in particular can be aided by computational methods, further demonstrating why these techniques are so invaluable in this area of research.

In the following chapter, density functional theory (DFT) and interatomic potential-based modelling will be outlined in appropriate detail for the work that follows in the subsequent chapters. We also discuss how these theories are implemented in the modelling programs used in the appropriate sections. First we will introduce the basic mathematical functions employed in the theory on which computational mod-

elling is based, before covering how solid state materials are defined in the context of molecular modelling. Section 2.3 will cover the background and development of DFT, starting by outlining quantum mechanical principles and Hartree-Fock theory, leading on to the formulation of DFT. The theory behind interatomic potential (IP)-based calculations will then be covered and the final section will discuss methods for modelling defects under the two levels of theory.

### 2.1.1 Mathematical Concepts

Knowledge of a number of mathematical concepts is required when discussing the theoretical background of the modelling methods used to study solid state systems. Here I will briefly introduce these concepts for reference when they are discussed later in the chapter.

**Functions and Functionals**

A function acts on an input to give an output, and therefore can be defined as the relationship between two, or more, variables. Functions are commonly denoted with an $f$ and the input provided in brackets:

$$f(x) = ..... \tag{2.1}$$

A functional is often referred to as a function of a function, meaning that the input variable of a functional is another function (or functions):

$$f[f(x)] = ..... \tag{2.2}$$

**Taylor Series**

The Taylor Series is a series expansion that is particularly useful for approximating functions. A function, *f(x)*, can expanded about a point, e.g. $x_0$, such that:

$$f(x_0+x) = f(x_0) + \frac{x}{1!}f'(x_0) + \frac{x^2}{2!}f''(x_0) + \frac{x^3}{3!}f'''(x_0)... + \frac{x^n}{n!}f^n(x_0) \tag{2.3}$$

When $x_0$ = 0 the expansion is known as a Maclaurin series. A function can be expressed in this manner if it is continuous and single valued with continuous deriva-

tives.

**Lagrange Multipliers**

Lagrange Multiples are used to find stationary points of functions, subject to a set of constraints. If a function, *f(x, y)*, is subject to the constraint *g(x, y)* = 0 then the stationary point can be found. We start by finding the derivative of $f$:

$$df = \frac{\partial f}{\partial x}dx + \frac{\partial f}{\partial y}dy = 0 \tag{2.4}$$

We add to this term the derivative of the constraint *g(x,y)* multiplied by a parameter $\lambda$, known as the Lagrange multiplier, to give:

$$\left(\frac{\partial f}{\partial x} + \lambda\frac{\partial g}{\partial x}\right)dx + \left(\frac{\partial f}{\partial y} + \lambda\frac{\partial g}{\partial y}\right)dy = 0 \tag{2.5}$$

By setting each of the terms in the bracket to zero, a set of simultaneous equations is obtained that provide a value for $\lambda$ in terms of $x$ and $y$. When this is combined with the original constraint equation, *g(x, y)*, a stationary point can be identified.

**Fourier Series**

A periodic function, e.g. *x(t)*, with a period $\tau$ (i.e *x(t)* = *x(t+*$\tau$*)*) can be written as a sum of sine and cosine functions, known as a Fourier series, in order to make mathematical manipulation of that function easier:

$$x(t) = a_0 + \sum_{n=1}(a_n \cos n\omega_0 t + b_n \sin n\omega_0 t) \tag{2.6}$$

Where $\omega_0 = 2\pi/\tau$.

If we are considering coefficients that are complex numbers, the Fourier series can be written as

$$x(t) = \sum_{-\infty}^{+\infty} c_n e^{in\omega_0 t} \tag{2.7}$$

where $e^{in\omega_0 t}$ is

$$e^{in\omega_0 t} = cos\frac{n\pi t}{\tau} + isin\frac{n\pi t}{\tau} \tag{2.8}$$

and $c_n$ is expressed as

$$c_n = \frac{1}{\tau}\int_{-\tau/2}^{\tau/2} x(t)e^{in\omega_0 t}dt \tag{2.9}$$

This definition makes use of the following relationships

$$\sin\omega_0 t = [e^{i\omega_0 t} - e^{-i\omega_0 t}]/2i \tag{2.10}$$

$$\cos\omega_0 t = [e^{i\omega_0 t} + e^{-i\omega_0 t}]/2 \tag{2.11}$$

While the Fourier series represents a function that is periodic, the Fourier transform is used when a function is not periodic, or when a periodic function is infinite. The second Fourier series formalism outlined above (equations 2.7 to 2.9) is best used for functions which are non-periodic.

## 2.2 Defining Solid State Systems

When modelling solid state systems, two structures need to be defined: the unit cell in real space and the Wigner-Seitz cell[213, 214] in reciprocal space. The unit cell is defined by the lattice parameters **a**, **b** and **c**, and the angles between them: $\alpha$, $\beta$ and $\gamma$. Repeating the unit cell infinitely in the directions of each lattice parameter creates the crystal structure. Reciprocal space is similarly produced from a series of Wigner-Seitz cells,[213, 214] a single Wigner-Seitz cell is often referred to as the first Brillouin zone, and we shall use this term throughout the chapter.
A vector within the reciprocal lattice can be represented as:

$$\mathbf{G} = n\mathbf{a}^{\$} + m\mathbf{b}^{\$} + \mathbf{c}^{\$} = 2\pi n\mathbf{a}^{*} + 2\pi m\mathbf{b}^{*} + 2\pi\mathbf{c}^{*} \tag{2.12}$$

The function $e^{i\boldsymbol{G}\bullet\boldsymbol{r}}$ varies with the same periodicity as the real space lattice, therefore, if a function is written as a Fourier series of $e^{i\boldsymbol{G}\bullet\boldsymbol{r}}$, the resulting Fourier series will have the same periodicity as the real lattice. This property of the reciprocal lattice vectors is important when considering plane waves, which will be introduced in Section 2.3.5.

## 2.3 Quantum Mechanics

Quantum mechanics is employed to represent the electrons of a system explicitly, and to determine properties that depend on the electronic distribution.[215] In quantum mechanics, all particles, including electrons, behave like waves, and wave functions (denoted $\psi$ or $\Psi$) are used to describe the behaviour of these waves. From the wave function we are able to deduce various properties, so to deduce information about a system containing multiple ions or atoms, we need its many body wave function. There are two widely used approaches to quantum mechanics: one based on Hartree-Fock methods and the other based on density functional theory (DFT). In Hartree-Fock based methods, the many body wave function is constructed from single particle wave functions, whereas in density functional theory, single particle wave functions are used to build the charge density of the system, which is used instead of the many body wave function to describe the system.

In this section we will outline the theory behind both quantum mechanic approaches and how they are implemented in a practical sense. We will begin by covering the general features of quantum mechanics before moving on to Hartree-Fock theory followed by DFT. The quantum mechanics calculations performed in this work will use a DFT-based approach.

### 2.3.1 The Schrödinger Equation and its Solutions for Many-Particle Systems

A natural place to begin our discussion on quantum mechanics is with the time-independent Schrödinger equation, which links the energy of a particle in a stationary state, $E$, to its wave function, $\Psi(\boldsymbol{r})$:[216, 217]

$$\left\{-\frac{\hbar^2}{2m}\bigtriangledown^2+V\right\}\Psi(\mathbf{r})=E\Psi(\mathbf{r}) \tag{2.13}$$

This formulation of the Schrödinger equation represents a three dimensional system,[25] where $\bigtriangledown^2$ represents:

$$\bigtriangledown^2=\frac{\partial^2}{\partial x^2}+\frac{\partial^2}{\partial y^2}+\frac{\partial^2}{\partial z^2} \tag{2.14}$$

The Schrödinger equation is often shown in an abbreviated, more general, form where the left hand side of equation 2.13 is represented by the Hamiltonian operator, $\hat{H}$:

$$\hat{H}\Psi(\mathbf{r}) = E\Psi(\mathbf{r}) \tag{2.15}$$

To solve this equation, an eigenfunction must be found, i.e. a function that, when operated on by the Hamiltonian, gives the same value as the wave function multiplied by the energy. However, the Schrödinger equation can only be solved exactly for a small number of cases, an important example being the free electron. Therefore the majority of solutions calculated for systems with more than one electron, or particle, are only approximations to the exact solution, and the task becomes finding the most accurate solution possible, by finding an accurate representation of the many body wave function.

An important assumption to note here is the Born-Oppenheimer approximation[218] which forms the basis of any molecular modelling tool.[25] This approximation refers to the assumption that the motions of the electrons can be considered separately from the motions of the nuclei - the nuclei move so slowly compared to electrons that their motions can be considered as fixed. Under the Born-Oppenheimer approximation the nuclei of a system are treated as being in fixed positions with the electrons moving in the electric field caused by the presence of the nuclei

$$\Psi_{system}(\mathbf{r},\mathbf{R}) = \Psi_{electrons}(\mathbf{r},\mathbf{R})\Psi_{nuclei}(\mathbf{R}) \tag{2.16}$$

where $\mathbf{r}$ and $\mathbf{R}$ are the positions of the electrons and nuclei respectively. A constant term accounts for the energy of the nuclei and the Schrödinger equation is subsequently only solved for the wave functions of the electrons, $\Psi_{electrons}(\mathbf{r},\mathbf{R})$.

An additional consideration is electron spin: an electron can have one of two spin values - up or down, which means that a wave function that describes an electron needs to be a function of both its position, $\mathbf{r}$, and its spin state, $\sigma$; $\psi(\mathbf{r}, \sigma)$ abbreviated as $\psi(\mathbf{x_1})$. The Pauli exclusion principle[219] states that you can not have more

than one electron in a space-spin state. Consequently, the overall wave function should be anti-symmetric in terms of electron coordinates, i.e. the overall sign of the wave function should change on swapping the coordinates of two electrons. This leads to the following representation of the many-electron wave function

$$\psi(x_1,x_2,x_3,....x_N) = C\sum_P (-1)^P \hat{P}\psi_a(x_1)\psi_b(x_2)\psi_c(x_3).....\psi_n(x_N) \tag{2.17}$$

Here $C$ is a normalisation factor, and $\hat{P}$ is an operator that permutes the variables $x_1$ to $x_N$, and the sum is taken of all permutations.

### 2.3.2 Hartree-Fock Methods

The Hartree-Fock (HF) method is based on the assumption that the $N$ electrons in the system are independent particles, occupying single electron spin orbitals (molecular orbitals $\psi_x(\mathbf{r})$) with single electron wave functions. The molecular orbitals are constructed by combining together atomic orbitals; $\phi_x(\mathbf{r})$. Therefore, the initial guess at the many body wave function, $\Psi_T$, is a product of single electron wave functions from each molecular orbital:[25]

$$\Psi_T(x_1,x_2,x_3,....x_N) = C\sum_P (-1)^P \hat{P}\psi_a^\alpha(x_1)\psi_a^\beta(x_2)\psi_b^\alpha(x_3)\psi_b^\beta(x_4).....\psi_n^\beta(x_N) \tag{2.18}$$

where $\alpha$ and $\beta$ represent the spin of the electron. The expectation value of the total energy is:

$$< H >=< \Psi_T|\hat{H}|\Psi_T > \tag{2.19}$$

The Hartree-Fock method is variational and therefore obeys the variational principle, which states that the expectation value of the Hamiltonian, the energy of the system, calculated using an arbitrarily chosen wave function, will be higher than the true ground state energy. The energy of a system is minimised, to the best approximation of the ground state, by minimising the expectation value with respect to the parameters of the wave function. How close this process gets to the true ground

state is dependent on the approximation being used. In the case of Hartree-Fock, this means minimising the single electron orbitals.

Hartree-Fock theory works on the assumption that the $N$ electrons, in the system of interest, are uncorrelated, which has an effect on the Schrödinger equation. The modified set of equations, which the Hartree-Fock wave functions must satisfy are known as the Hartree-Fock equations.

The total energy of the system is calculated based on individual molecular orbitals; $\psi_m$:[25, 220–222]

$$f_1 \psi_m(x_1) = \varepsilon_m \psi_m(x_1) \tag{2.20}$$

where $f_1$ is the Fock operator:

$$f_1 = \frac{1}{2} \bigtriangledown_1^2 - \sum_{A=1}^{M} \frac{Z_A}{r_{1A}} + v^{HF}(x_1) \tag{2.21}$$

The first part of equation 2.21 is the expression for the core Hamiltonian, corresponding to the motion of a single electron in the field of M nuclei,[215] while $v^{HF}(x_1)$ is the Hartree-Fock potential which is made up of two electron interaction potentials; the Coulomb operator, $J$, and the exchange operator; $K$.

$$v^{HF}(x_1) = \sum_b 2J_b(x_1) - K_b(x_1) \tag{2.22}$$

$$J_b(x_1)\psi_a(x_1) = \left[ \int |\psi_b(x_2)|^2 \frac{1}{r_{12}} dx_2 \right] \psi_a(x_1) \tag{2.23}$$

$$K_b(x_1)\psi_a(x_1) = \left[ \int \psi_b^*(x_2)\psi_a(x_2) \frac{1}{r_{12}} dx_2 \right] \psi_b(x_1) \tag{2.24}$$

These equations can then be used to find the ground state energy and wave functions of a system. This is generally done by writing the Fock operator as a matrix, making the equations easier to solve. The molecular orbitals used above are expanded into atomic orbitals, making the eigenvalue equation:

$$F_{\mu\nu}C_{i\nu} = \varepsilon_i S_{\mu\nu}C_{i\nu} \tag{2.25}$$

where

$$F_{\mu\nu} = \int \phi_\mu(x_1) f(x_1) \phi_\nu(x_1) dx_1 \tag{2.26}$$

$$S_{\mu\nu} = \int \phi_\mu(x_1) \phi_\nu(x_1) dx_1 \tag{2.27}$$

where $C_{i\nu}$ are coefficients of the expansion of the molecular orbitals to atomic orbitals; $\phi$.

The ground state energy and wave function must then be found self-consistently as the equations for calculating the molecular orbitals, depend on the molecular orbitals themselves; the Hartree-Fock equations are solved for an initial set of molecular orbitals, which provides a new set of molecular orbitals which are then used in the Hartree-Fock equations. This process repeats until the ground state energy and wave function produced in consecutive cycles are consistent, to within a given set of criteria.

The Hartree-Fock approximation is a mean-field method; the potential for an electron comes from the mean (average) field of the other electrons. However, the Coulomb potential calculated for a molecular orbital, equation 2.23, contains the self interaction of the electron in the molecular orbital in question. This is corrected by exact cancellation from the exchange operator meaning the HF approximation is free of self-interaction error. This feature will be important when discussing density functional theory.

The Hartree-Fock approximation has been used widely, but the simplifications involved make it inaccurate. Subsequently, additional methods have been developed, based on Hartree-Fock, that model realistic systems with increased accuracy.

#### 2.3.2.1 Post Hartree-Fock

The most significant problem with using Hartree-Fock, is that it fails to describe electron correlation adequately. In Hartree-Fock theory, the electrons are assumed

to be moving in an average potential of other electrons, i.e. the position of each electron is not influenced by neighbouring electrons. In real systems, electrons tend to correlate so as to avoid each each other, meaning their motions are correlated. Neglecting the correlation effects of a system causes the Hartree-Fock energy to be inaccurate, which has a knock on effect on properties such as binding energies.

Methods that include the electron correlation energy (defined as the difference between the exact energy and the Hartree-Fock energy) or approximations to this energy, are known as Post Hartree-Fock methods.[220] Popular methods, including Many-Body Perturbation (MP) Theory and Configuration Interaction (CI), involve the addition of higher order wave functions onto the Hartree-Fock wave functions. Although these methods offer the ability to improve, systematically, the ground state energy calculated, making it closer to the exact energy of the system due to the variational principle, they come at a computational cost that scales rapidly with system size.[220] Perturbation methods, such as MP theory, also rely on the Hartree-Fock energy being an accurate initial approximation to the exact energy, thus they are ineffective in areas where Hartree-Fock fails.

Therefore, the accurate modelling of systems using Hartree-Fock based methods for periodic systems, containing hundreds of atoms, is largely impractical. An alternative approach has been developed, which is able to reduce the computational cost of electronic structure calculations by avoiding the use of a many body wave function and is now a commonplace method for studying large systems: Density Functional Theory.

### 2.3.3 Density Functional Theory

Whereas *ab initio* methods discussed thus far are concerned with finding an approximation to the full $N$ electron wave function in order to establish the total energy of a system, when implementing Density Functional Theory (DFT) only the electron density is used to establish the total electronic energy of a system of electrons in the external field of the systems nuclei.

The relationship between electron density and total electronic energy was first introduced by Thomas and Fermi in the Thomas-Fermi model.[223–225] They as-

sumed that the electrons form a gas, satisfying Fermi statistics, and used a classical Coulomb potential to determine the electron-electron interactions. The kinetic energy was described by a local density approximation; the contribution from point $\mathbf{r}$ is determined from the kinetic energy of the homogeneous electron gas with the same density as the system at point $\mathbf{r}$. However, there are some severe problems with the Thomas-Fermi model. Firstly, the charge density decays at a rate of $r^{-6}$ instead of exponentially as it should, causing the outer regions of atoms to be poorly described. Secondly, in the majority of cases, its application does not result in the binding of atoms or ions to form molecules[226] and therefore cannot be applied to any chemical problem.

The Thomas-Fermi model was built on by Dirac[227] who outlined the necessity of including exchange in the model, which involved modifying the equations outlined in Hartree-Fock theory to define the energy in terms of a density functional as opposed to single-determinant many-electron wave functions. The modification effectively added a correction term to the energy produced by the Thomas-Fermi model, by including the exchange energy for a homogeneous electron gas, previously derived by Bloch.[228]

However, it was not until 30 years later that DFT started to gain ground as a suitable approximation for ground state electronic structure calculations, catalysed by Hohenberg and Kohn.[229] They demonstrated that the ground state energy was uniquely defined by the electron density, through determining that the external potential, $\upsilon(\mathbf{r})$, had a 1:1 relationship with the ground state wave function and therefore, there was a 1:1 relationship between the ground state wave function and the ground state electron density; $\rho(\mathbf{r})$.

$$\rho(\mathbf{r}) = N \int \Psi^*(\mathbf{r}, \mathbf{r}_2, ....\mathbf{r}_n)\Psi(\mathbf{r}, \mathbf{r}_2, ....\mathbf{r}_n)d\mathbf{r}_2....d\mathbf{r}_N \tag{2.28}$$

Making the energy of the system a functional of $\rho(\mathbf{r})$, and the energy functional can be defined as:

$$E[\rho(\mathbf{r})] = \int V_{ext}(\mathbf{r})\rho(\mathbf{r})d\mathbf{r} + F[\rho(\mathbf{r})] \tag{2.29}$$

The first term represents the interaction between the electrons and an external potential, $V_{ext}(\boldsymbol{r})$, which usually represents the nuclei in the system. The second term, $F[\rho(\mathbf{r})]$, is the sum of the expectation values of both the kinetic energy of all the electrons in the system, $T$, and the interelectronic interactions, $V_{ee}$:

$$F[\rho(\mathbf{r})] = < \Psi_n | T + V_{ee} | \Psi_n > \tag{2.30}$$

Hohenberg and Kohn showed that the energy functional, $E[\rho(\mathbf{r})]$, satisfies a variational principle such that:

$$E_{GS} = minE[\rho(\mathbf{r})] \tag{2.31}$$

Therefore the ground state energy can be determined by minimising $E[\rho(\mathbf{r})]$ over all non-degenerate densities that can be derived from the ground state of an external potential. To minimise the energy, with respect to the electron density, $\rho(\mathbf{r})$, we introduce a constraint; that the number of electrons, $N$, in the system is fixed:

$$N = \int \rho(\mathbf{r}) d\mathbf{r} \tag{2.32}$$

This constraint is introduced as a Lagrange multiplier, -$\mu$

$$\frac{\delta}{\delta\rho(\mathbf{r})} \left[ E[\rho(\mathbf{r})] - \mu \int \rho(\mathbf{r}) d\mathbf{r} \right] = 0 \tag{2.33}$$

and therefore,

$$\mu = \left( \frac{\delta E[\rho(\mathbf{r})]}{\delta\rho(\mathbf{r})} \right)_{V_{ext}} \tag{2.34}$$

where the subscript $V_{ext}$ indicates that equation 2.34 is under constant external potential conditions, i.e. the nuclei in the system are fixed.

Equations 2.28 to 2.34 make up the Hohenberg-Kohn theorem, but these equations cannot be solved in practical terms as an exact value of F[$\rho(\mathbf{r})$] is unknown and therefore we cannot solve equation 2.29 to get the total electronic energy of the system.

The next step in the development of DFT came when Kohn and Sham,[230] proposed an approximation for $F[\rho(\mathbf{r})]$ by splitting it into three contributing terms;

$$F[\rho(\mathbf{r})] = E_{KE}[\rho(\mathbf{r})d\mathbf{r}] + E_H[\rho(\mathbf{r})d\mathbf{r}] + E_{XC}[\rho(\mathbf{r})d\mathbf{r}] \tag{2.35}$$

$E_{KE}$ is the kinetic energy, $E_H$ is the Hartree electrostatic energy and $E_{XC}$ is the exchange and correlation contributions to the energy.

Under Kohn and Sham's[230] approximation the kinetic energy is defined as the kinetic energy of a system of $N$ non-interacting electrons with the same electron density as the real, interacting system

$$E_{KE}[\rho(\mathbf{r})] = \sum_{i=1}^{N} \int \psi_i(\mathbf{r}) \left( -\frac{\nabla^2}{2} \right) \psi_i(\mathbf{r}) d\mathbf{r} \tag{2.36}$$

The Hartree electrostatic energy is the sum of the Coulomb interactions between all possible pairs of electrons, represented as a classical interaction between two charge densities

$$E_H[\rho(\mathbf{r})] = \frac{1}{2} \int \int \frac{\rho(\mathbf{r}_1)\rho(\mathbf{r}_2)}{|r_1 r_2|} d(\mathbf{r}_1) d(\mathbf{r}_2) \tag{2.37}$$

Finally, the exchange and correlation contributions are defined as the part of the energy not accounted for by the above two terms, or by the interaction of the electons with the external potential, $V_{ext}(\mathbf{r})\rho(\mathbf{r})d\mathbf{r}$.

These definitions give the following expression for the energy of a system of $N$ electrons:

$$\begin{aligned} E[\rho(\mathbf{r})] = \sum_{i=1}^{N} \int \psi_i(\mathbf{r}) \left( -\frac{\nabla^2}{2} \right) \psi_i(\mathbf{r}) d\mathbf{r} + \frac{1}{2} \int \int \frac{\rho(\mathbf{r}_1)\rho(\mathbf{r}_2)}{|r_1 r_2|} d(\mathbf{r}_1) d(\mathbf{r}_2) \\ + E_{XC}[\rho(\mathbf{r})] - \sum_{A=1}^{M} \int \frac{Z_A}{|\mathbf{r} - \mathbf{R}_A|} \rho(\mathbf{r}) d(\mathbf{r}) \end{aligned} \tag{2.38}$$

All terms in equation 2.38 can be evaluated exactly, except the exchange correlation energy. Therefore, this expression acts to define the exchange-correlation energy function, $E_{\mathrm{XC}}[\rho(\mathbf{r})]$, demonstrating that it contains, in addition to the exchange and

correlation contributions to the energy, a contribution from the difference between the true kinetic energy and the $E_{\mathrm{KE}}[\rho(\mathbf{r})]$, which under this approximation, is the kinetic energy of a system of non-interacting electrons.

In addition to defining the energy of the system in this manner, Kohn and Sham also introduced a definition of the electron density in terms of one electron, orthonormal orbitals, known as Kohn-Sham orbitals:

$$\rho(\mathbf{r}) = \sum_{i=1}^{N} |\psi_i(\mathbf{r})|^2 \tag{2.39}$$

which, after the application of the appropriate variational condition, result in the one electron Kohn-Sham equations

$$\left\{ -\frac{\bigtriangledown_1^2}{2} - \left( \sum_{A=1}^{M} \frac{Z_A}{r_{1A}} \right) + \int \frac{\rho(\mathbf{r}_2)}{r_{12}} d\mathbf{r}_2 + V_{XC}[\mathbf{r}_1] \right\} \psi_i(\mathbf{r}_1) = \varepsilon_i \psi_i(\mathbf{r}_1) \tag{2.40}$$

Here the external potential has been written in a form to show the interaction with $M$ nuclei, where $\varepsilon_{\mathrm{i}}$ are the orbital energies and $V_{XC}$ is known as the exchange correlation functional, with its relation to the exchange-correlation energy defined as:

$$V_{XC}[\mathbf{r}] = \left( \frac{\delta E_{XC}[\rho(\mathbf{r})]}{\delta \rho(\mathbf{r})} \right) \tag{2.41}$$

These expressions are then used to calculate the total electronic energy using equation 2.38. The energy is calculated using a self consistent approach, in which an initial guess of the electron density is used to establish a set of orbital energies, which are then used to calculate an improved electron density which is then used to establish a new set of improved orbital energies - this cycle will continue until convergence is reached.

#### 2.3.3.1 Spin-Polarised DFT

Spin-polarised DFT was developed to model systems containing unpaired electrons. Local spin density functional theory (LSDFT)[230] is an extension of DFT in which both the electron density and spin density are included in the energy calculation.[215] Spin density is defined as the difference between the densities

of spin up electrons and spin down electrons

$$\sigma(\mathbf{r}) = \rho_{\uparrow}(\mathbf{r}) - \rho_{\downarrow}(\mathbf{r}) \tag{2.42}$$

The total electron density is then the sum of the densities from both spin up and spin down electrons. The exchange correlation function is usually different for the spin up and spin down cases: we therefore get a set of spin-polarised Kohn-Sham equations, one for each spin. Equation 2.43 shows the general form of both equations, where $\sigma$ represents either $\alpha$ (spin up) or $\beta$ (spin down) electrons.

$$\left\{ -\frac{\nabla_1^2}{2} - \left( \sum_{A=1}^{M} \frac{Z_A}{r_{1A}} \right) + \int \frac{\rho(\mathbf{r}_2)}{r_{12}} d\mathbf{r}_2 + V_{XC}[\mathbf{r}_1, \sigma] \right\} \psi_i^{\sigma}(\mathbf{r}_1) = \varepsilon_i^{\sigma} \psi_i^{\sigma}(\mathbf{r}_1) \tag{2.43}$$

#### 2.3.3.2 The Exchange-Correlation Functional

The performance of DFT is reliant on the exchange-correlation functional, $V_{XC}$, as all other terms in the total energy expression are well defined. The choice of approximation used for this functional is dependent on the material in question and the properties of interest. Below we outline two different approximations; the local density approximation (LDA) and the generalised gradient approximation (GGA). Methods have also been developed to treat the exchange-correlation functional using the local parts of DFT (e.g. a LDA or GGA functional) combined with non-local quantum mechanical techniques (e.g. Hartree-Fock); this technique, known as Hybrid DFT, will also be outlined briefly in this section.

**Local Density Approximation**

The local density approximation (LDA) is the simplest approach to approximating the exchange-correlation functional, proposed by Kohn and Sham[230] when outlining their approximation for $E[\rho(\mathbf{r})]$. The approximation is based on the uniform electron gas model in which the electron density is constant throughout all space, which allows the exchange-correlation energy to be evaluated by integrating over all space.

$$E_{XC}^{LDA}[\rho(\mathbf{r})] = \int \rho(\mathbf{r})\varepsilon_{XC}(\rho(\mathbf{r}))d\mathbf{r} \tag{2.44}$$

where $\varepsilon_{\mathrm{XC}}$ is the exchange correlation energy per electron as a function of the electron density of the uniform electron gas, for which there are very accurate formulas determined by Monte Carlo simulations[231] and conveniently parametrised.[232] It is assumed that the exchange correlation energy of the uniform electron gas, in which the electron density does not depend on position, can be applied to a non-uniform system where the electron density does depend on position.

The exchange correlation functional is obtained by differentiating equation 2.44 with respect to the electron density:

$$V_{XC}^{LDA}[\mathbf{r}] = \rho(\mathbf{r})\frac{\delta\varepsilon_{XC}(\rho(\mathbf{r}))}{\delta\rho(\mathbf{r})} + \varepsilon_{XC}(\rho(\mathbf{r})) \tag{2.45}$$

At each point $\mathbf{r}$, in a system with electron density $\rho(\mathbf{r})$, the values of $\varepsilon_{\mathrm{XC}}(\rho(\mathbf{r}))$ and $\mathrm{V_{XC}}[\rho(\mathbf{r})]$ have the same value as if point $\mathbf{r}$ were in a uniform electron gas. As the value of $\varepsilon_{\mathrm{XC}}$ is known accurately for all densities of interest, it can be expressed in an analytical form and solved computationally. It is usual practice to split $\varepsilon_{\mathrm{XC}}(\rho(\mathbf{r}))$ into its exchange contribution and correlation contribution and consider these separately. There are a number of different ways to calculate these contributions, and the method implemented depends on the modelling package and the basis set. For solid state systems, plane waves are often used, as opposed to localised atomic basis sets which are common in molecular systems. Plane waves will be covered in more detail later in Section 2.3.5.

It is possible to generalise equation 2.44 for spin-polarised systems, leading to a local spin density approximation (LSDA):[233, 234]

$$E_{XC}^{LSDA}[\rho(\mathbf{r})] = \int \rho(\mathbf{r})\varepsilon_{XC}(\rho_{\uparrow}(\mathbf{r}),\rho_{\downarrow}(\mathbf{r}))d\mathbf{r} \tag{2.46}$$

where $\varepsilon_{XC}(\rho_{\uparrow}(\mathbf{r}),\rho_{\downarrow}(\mathbf{r}))$ is the exchange correlation energy per particle of a homogeneous, spin-polarised electron gas, where $\rho_{\uparrow}$ and $\rho_{\downarrow}$ refer to spin up and spin down densities, within the homogeneous electron gas, respectively.[233]

LDA has been found to perform well for a wide range of materials and problems. In the context of solid state modelling, it is able to reproduce lattice constants reasonably well, however it fails when studying energetic properties - due to electron densities generally being strongly inhomogeneous in real materials. Therefore, alternative methods for calculating the exchange correlation functional have been developed, including the generalised gradient approximation.

**Generalised Gradient Approximation**

Due to the inhomogeneity of electron density in a real system, it was proposed that the exchange correlation energy should depend on both electron density, $\rho$, and the gradient of the density, $\bigtriangledown\rho$, at each point in space.

$$E_{XC}^{GGA}[\rho(\mathbf{r})] = \int f(\rho, \bigtriangledown\rho) \tag{2.47}$$

where $f$ is a parameterised analytical function. The exchange-correlation functional is split and the exchange functional and correlation functional treated separately, as different variations with density are observed for each functional,

$$E_{XC} = E_X[\rho, \bigtriangledown\rho] + E_C[\rho, \bigtriangledown\rho] \tag{2.48}$$

The form each of these functionals will take depends on the type of GGA being used, which will differ by the approximations and assumptions used by the authors when developing it. One of the first GGAs was proposed by Langreth and Mehl [235, 236] which took the form:

$$E_{XC} = (E_{LDA}^{RPA})^{XC} + a\int \frac{[\bigtriangledown\rho(\mathbf{r})]^2}{[\rho(\mathbf{r})]^{4/3}}(2e^{-F} - \frac{7}{9})d^3\mathbf{r} \tag{2.49}$$

where

$$F = b\frac{|\bigtriangledown\rho(\mathbf{r})|}{[\rho(\mathbf{r})]^{7/6}} \tag{2.50}$$

and $a$ and $b$ are constants. As equation 2.49 shows, the gradient approximation is treated as a correction to the exchange-correlation functional of LDA. Langreth and Mehl used the exchange-correlation functional from the random phase approxima-

tion (RPA) of LDA, noting that it was not appropriate to use any other LDA $E^{XC}$ as the generalised gradient approximation correction was derived based on this form of LDA and therefore a large amount cancellation between the two terms would be lost if an alternative form was used.[236]

There were a number of issues with the GGA proposed by Langreth and Mehl, the most problematic being the behaviour of the exchange potential which fails to reproduce the asymptotic behaviour of the exchange energy density with $1/r$, making the approximation difficult to implement. Therefore, a number of adaptations were developed, including those by Becke [237] and Perdew and Wang[238–242]. The GGAs considered in the following work are PBE[243] and PBEsol.[244]

**PBE and PBEsol** The functional of Perdew-Burke-Ernzerhof (PBE)[243] was developed as a simple GGA with all parameters in the GGA correction (i.e. all parameters other than the LDA-based exchange-correlation functional) being fundamental constants. It is based on the Perdew-Wang 1991 GGA (PW91)[238, 245] which was developed with the aim of keeping all the best features of the LDA exchange-correlation functional while incorporating some inhomogeneity effects.

The PBE exchange correlation functional takes the form:

$$E_{XC}^{GGA}[\rho(\mathbf{r})] = \int \rho(\mathbf{r})\varepsilon_X^{unif}(\rho(\mathbf{r}))F_{XC}(r_s,\zeta,s)d^3\mathbf{r} \tag{2.51}$$

where $\varepsilon_X^{unif}$ is the exchange energy per particle of the uniform electron gas and $F_{XC}$ is an enhancement factor of the LDA uniform electron gas exchange, dependent on; $r_s$, the Seitz radius, $\zeta$, the relative spin polarisation and $s$, a density gradient.

PBEsol[244] was developed by Perdew *et al.* in order to improve the equilibrium properties of closely packed solids, compared to those produced using PBE. In order to outline the differences between the two functionals it is necessary to present the exchange and correlation functionals of PBE separately.

Firstly, the exchange energy of PBE is presented as:

$$E_X^{GGA}[\rho(\mathbf{r})] = \int e_X^{unif}(\rho(\mathbf{r}))F_X(s(\mathbf{r}))d^3\mathbf{r} \tag{2.52}$$

where $e_X^{unif}(\rho(\mathbf{r}))$ is the exchange energy density of a uniform electron gas, and $F_X(s(\mathbf{r}))$ is the enhancement factor.[243]

For a GGA that recovers the uniform gas limit, such as PBE;

$$F_x(s) = 1 + \mu s^2 + ... \qquad (s \to 0) \tag{2.53}$$

For PBE, $\mu$ = 0.2195 which is roughly equal to $2\mu_{GE}$, where $\mu_{GE}$ is the gradient expansion value, a parameter used when defining GGA-based functionals. PBEsol, however, uses $\mu = \mu_{GE}$; this value is accurate for slowly varying densities - such as densities in solids - whereas the value used in PBE is used to ensure accurate exchange energies for neutral atoms - which violates expansion for slowly varying densities.

Moving on to the correlation functional, within PBE it is expressed as:

$$E_C^{GGA}[\rho(\mathbf{r})] = \int \rho(\mathbf{r})\{\varepsilon_C^{unif}(\rho(\mathbf{r})) + \beta t^2(\mathbf{r}) + ....\} \quad d^3\mathbf{r} \tag{2.54}$$

where $\beta$ is a coefficient and $t$ is the reduced density gradient for correlation. The link between the exchange and correlation functions is that, in order to retain the LDA's response of a uniform gas to a weak potential - which is very accurate - then,

$$\mu = \frac{\pi^2\beta}{3} \tag{2.55}$$

since the value of $\mu$ has been altered in PBEsol, so must the value of $\beta$. In PBEsol, $\beta$ = 0.046 is used, which doesn't completely satisfy equation 2.55, which would require $\beta$ = 0.0375, but is closer to that value than the value used in PBE; $\beta$ = 0.0667.

These revisions to PBE make PBEsol closer to the LDA exchange-correlation functional compared to PBE. The slowly varying uniform electron gas, on which LDA is based, is a better approximation to the electronic properties of a solid than that of a free atom or molecule, leading to the improved performance of this functional for solid state systems.

**Hybrid DFT** The final approximation mentioned in the following work is a hybrid

version of the exchange-correlation functional, which, when used, is referred to as Hybrid DFT. This approximation aims to combine the exact treatment of exchange that the Hartree-Fock theory provides (referred to as "exact-exchange" in the context of Kohn-Sham DFT[229, 230]), with the LDA treatment of correlation, which can be evaluated easily and quickly, compared to post-HF methods which scale poorly with system size.[246]

The adiabatic connection formula[247–250] of DFT is used to combine the two approaches. The adiabatic connection formula connects the potential energy of the non-interacting reference system, $U_{XC}^0$, to the fully interacting system, $U_{XC}^1$,

$$E_{XC} = \int_0^1 U_{XC}^{\lambda} d\lambda \tag{2.56}$$

through increasing $\lambda$, the interelectronic coupling-strength parameter.

A first approximation to this, is a simple linear interpolation between the reference system and the fully interacting one:

$$E_{XC} = \frac{1}{2}U_{XC}^0 + \frac{1}{2}U_{XC}^1 \tag{2.57}$$

The first term of this expression, $U_{XC}^0$, is the Kohn-Sham exchange energy, $E_X$, and can be evaluated exactly. The second term, $U_{XC}^1$, can be approximated as the LDA exchange correlation energy, $U_{XC}^{LDA}$. Therefore, the exchange correlation functional with hybrid DFT becomes:

$$E_{XC} \simeq \frac{1}{2}E_X + \frac{1}{2}U_{XC}^{LDA} \tag{2.58}$$

The appropriateness of this exchange-correlation functional approximation for the system in question, $LaFeO_3$, along with the other functionals mentioned in this section, will be discussed in Chapter 3.

#### 2.3.3.3 The Hubbard $U$ Parameter

An additional benefit of using DFT over Hartree-Fock, besides the decrease in computational cost, is that dynamic electron correlation - the probability density of one electron reduces the probability of finding another electron in the same space - is

built into DFT explicitly, whereas this is not the case for Hartree-Fock, see section 2.3.2. However, Hartree-Fock includes the exact electron repulsion integrals whereas this is missing from DFT when using either LDA or GGA-based functionals.

There is, therefore, a need for a DFT-based method that includes a correct description for the strong Coulomb repulsions between localised electrons e.g. those occupying $d$ or $f$ orbitals. The Hubbard model was first designed after it was established that many electrons retain well localised character in some solid state materials, as opposed to to being a delocalised cloud in the weak electrostatic field of the nuclei - i.e. modelled via the homogeneous electron gas as in LDA - which has a tendency to over-delocalise the electrons.[251]

The key error this over-delocalisation introduces into the system,[252] particularly for the work presented here, is the band gap problem - with DFT predicting metallic ground states for a number of transition metal oxides instead of insulating ones.[253] Hybrid functionals, described earlier in the chapter, can be implemented to correct for this over-delocalisation, however they are computationally expensive and the amount of HF exchange to include can be difficult to assess, depending on the property of interest. An alternative method is to introduce the Hubbard $U$ parameter on specific ions that require a correct description of localised electrons. This method is referred to as DFT+$U$.

The Hubbard Model[121] is able to explain the transition between the limits of the band model in a conductor and the localised limit in an insulator, using only two interaction terms. Competing interactions - the kinetic energy operator and the weak electron-nuclear attraction, which favour delocalisation, and a Coulomb repulsion term resulting from the pairing of two electrons on an atomic site - are tuned, and the full Hamiltonian is represented as follows:

$$H = \sum_{ij}\sum_{\mu\nu} \hat{T}_{ij}^{\mu\nu} c_{i\mu}^{\dagger} c_{j\nu} + \sum_{ijkl}\sum_{\mu\nu\sigma\tau} \langle \mu_i \nu_j | \sigma_k \tau_l \rangle c_{i\mu}^{\dagger} c_{j\nu} c_{l\tau}^{\dagger} c_{k\sigma} \tag{2.59}$$

This expression can be split into two parts: the first is the transfer integral where the electrons are described as being able to move only between orbitals $\mu$ and $\nu$

on nearest neighbour sites: i and j. The second part corresponds to the electron-electron repulsion integrals of four orbitals; $\mu$, $\nu$, $\sigma$ and $\tau$ on four atomic sites: i, j, k and l. The original model can be greatly simplified by only considering electron-electron repulsions on the same atom, which are an order of magnitude greater than other electron-electron repulsions:[121]

$$H = -t \sum_{\langle i,j\rangle,\sigma} (c^{\dagger}_{i,\sigma} c_{j,\sigma} + c^{\dagger}_{j,\sigma} c_{i,\sigma}) + U \sum_{i=1}^{N} N^{I\uparrow} N^{I\downarrow} \tag{2.60}$$

Here the transfer integral is treated as a single parameter; $t$, and is the kinetic energy associated with delocalising the electrons, $U$ is the Coulomb energy required to pair two electrons on one atom, $N$ is the number of atoms, and $N^{I\uparrow}$ and $N^{I\downarrow}$ are the number of spin up or spin down electrons on each atom, respectively.[121] The original work only considered a single pair of electrons;[121] however it is usually employed across all $d$ or $f$ electrons in the system.[251]

**Anderson Model** The Anderson impurity model[122] includes all the elements of Hubbard's model described above, but additionally considers the hybridisation between the localised $d$ electrons with the delocalised $s$ electrons. His model is built on the basis that it is more important to describe the repulsion between opposite spin electrons, rather than the attraction between electrons with the same spins; known as the Coulomb (J) and Exchange (K) integrals respectively, in order to describe localised magnetic moments correctly. In implementing the Anderson Model the $U$ term is represented as $U_{eff}$:

$$U_{eff} = U - J \tag{2.61}$$

Where $U$ is the energy penalty of pairing two electrons on one atom, as is the case with Hubbard's model.

**Implementing DFT+*U*** An energy calculation in DFT+$U$ generally involves combining 3 terms; the DFT calculation ($E^{DFT}$), the Hubbard term ($E^{Hub}$) and a double counting term ($E^{DC}$):[251]

$$E^{DFT+U} = E^{DFT} + E^{Hub} - E^{DC} \tag{2.62}$$

The Hubbard term is the contribution to the energy from the Coulomb interaction between localised orbitals e.g. the $d$ orbitals, whereas the double counting term removes the mean field description of these orbitals obtained from the homogeneous electron gas model. A common form of the double counting terms is as follows:[254]

$$E^{DC}[N^I_{nl}] = \frac{1}{2}U^I_{nl}N^I_{nl}(N^I_{nl}-1) - \frac{1}{2}J[N^{I\uparrow}_{nl}(N^{I\uparrow}_{nl}-1) + N^{I\downarrow}_{nl}(N^{I\downarrow}_{nl}-1)] \tag{2.63}$$

where ${N_{nl}}^I$ is the total number of electrons in the localised subshell, with ${N_{nl}}^{I\uparrow}$ and ${N_{nl}}^{I\downarrow}$ being the number of spin up and spin down electrons in each subshell respectively.

There are a number of ways to implement DFT+$U$, which differ by a number of factors, for example the simplifications used, e.g. $U_{eff}$, or by the choice of local projection used.[255] In this work, DFT+$U$ is implemented as LDSA+$U$ introduced by Dudarev *et al.*[256] using a projector-augmented wave (PAW)-based approach,[257] as used in many electronic calculations in VASP.[258] This form of DFT+$U$ combines the rotationally invariant functional from Liechtenstein[259] and the orbital-dependent formulation by Anisimov *et al.*[260], while retaining the simplified $U_{eff}$ parameter employed in the Anisimov formulation. The LDSA+$U$ functional defined as:[256]

$$E^{LSDA+U} = E^{LSDA} + \frac{(\bar{U}-\bar{J})}{2}\sum_{\sigma}\left[\left(\sum_j \rho^{\sigma}_{jj}\right) - \left(\sum_{j,l}\rho^{\sigma}_{jl}\rho^{\sigma}_{lj}\right)\right] \tag{2.64}$$

Where $\bar{U}$ and $\bar{J}$ are spherically average matrix elements of the screened Coulomb electron-electron interaction and $\rho^{\sigma}_{jl}$ is the density matrix of $d$ electrons. At the limit of integer occupation numbers - where terms representing interger number of $d$ electrons and non-integer numbers of $d$ electrons cancel - the second term on the right hand side of equation 2.64 vanishes and the energy can be expressed in terms of Kohn-Sham eigenvalues: $\varepsilon_i$

$$E^{LSDA+U} = E^{LSDA}[\varepsilon_i] + \frac{(\bar{U}-\bar{J})}{2}\sum_{l,j,\sigma}\rho^{\sigma}_{lj}\rho^{\sigma}_{jl} \tag{2.65}$$

with the final term in equation 2.65 representing the double counting term as defined above.

### 2.3.4 Defining the Wave function: Plane waves and Pseudopotentials

Plane waves are a common basis set to use for periodic systems such as solids. Each orbital wave funtion is expressed as a linear combination of plane waves which differ by reciprocal lattice vectors:

$$\psi_i^{\mathbf{k}}(\mathbf{r}) = \sum_{\mathbf{G}} a_{i,\mathbf{k}+\mathbf{G}} exp(i(\mathbf{k}+\mathbf{G})\bullet\mathbf{r}) \tag{2.66}$$

where, **k** is the wave vector; which characterises the wave function in terms of both direction and magnitude. The Kohn-Sham equations then take on the following form:

$$\sum_{G'}\left\{\frac{\hbar^2}{2m}|\mathbf{k}+\mathbf{G}|\delta_{GG'} + V_{ion}(\mathbf{G}-\mathbf{G}') + V_{elec}(\mathbf{G}-\mathbf{G}') + V_{XC}(\mathbf{G}-\mathbf{G}')\right\} a_{i,\mathbf{k}+\mathbf{G}'} = \varepsilon_i a_{i,\mathbf{k}+\mathbf{G}'} \tag{2.67}$$

with $V_{ion}$, $V_{elec}$ and $V_{XC}$ defined as the electron-nuclei, the electron-electron and the exchange-correlation functionals respectively while $\delta_{GG'}$ is a function which is zero if G $\neq$ G'and 1 if G = G'.[215]

Plane waves are the physically correct solution for a free electron, and although they are a very efficient basis set, particularly when using periodic boundary conditions, difficulties arise when using them in real systems, due to the interaction of the electrons with the nuclear potential. These difficulties are addressed by using pseudopotentials.[220]

Ideally, when modelling a material, you would take all electrons in the system into consideration; however this is often not practical. Therefore, it is common to only consider the valence electrons as these are the electrons that are involved in bond-

ing and chemical reactions and therefore are the cause of the chemistry displayed by the material, while the main role of the core electrons is to screen the valence electrons from the potential of the nucleus. When using pseudopotentials, the core electrons are combined with the nuclear potential to form a new potential which matches the nuclear potential exactly outside the core radius, but curves smoothly within the core radius. Thus the large oscillations of the wave function near the nucleus that occur when using plane waves, is avoided. As these rapid oscillations lead to a large kinetic energy and therefore would require a large number of plane waves to be modelled accurately, the use of pseudopotentials makes calculations much more computationally efficient. Consequently, the wave function used to calculate the ground state energy only describes the properties of the valence electrons that are interacting with the potential of the nucleus and core electrons combined - a pseudowavefunction. It is often required that the pseudowavefunction is norm-conserving, meaning that the integral of the pseudowavefunction should match the integral of the all electron wave function, ensuring accuracy and reliability of the pseudopotential, but at increased computational cost.

The lack of the full electron wave function in the pseudopotential method can be limiting, leading to the wide spread use of a method similar to the pseudopotential method, but allows the calculation of the full electron wave function; the projector-augmented wave (PAW) approach.

The PAW-based approach obtains the all electron wave functions from pseudowavefunctions:[258]

$$|\psi_{n\mathbf{k}}^{\sigma}\rangle = |\tilde{\psi}_{n\mathbf{k}}^{\sigma}\rangle + \sum_i (|\phi_i\rangle - |\tilde{\phi}_i\rangle)\langle p_i|\tilde{\psi_{n\mathbf{k}}^{\sigma}}\rangle \tag{2.68}$$

where $|\phi_i\rangle$ and $|\tilde{\phi}_i\rangle$ are all electron and pseudo partial waves which are located on a particular atom, and $\langle p_i|$ are the PAW projector functions. In equation 2.68 $i$ represents the atomic index, $\alpha$, and the angular quantum numbers $l$ and $m$ and $\nu$, which refer to the reference energy at which the all electron partial waves are determined; $i = (\alpha \nu l m)$.

A further issue to be tackled when using a plane wave basis set is that, for a real

system, there can, effectively, be an infinite number of $k$-points in the Brillouin zone, each requiring a separate energy calculation. This problem is solved by sampling the Brillouin zone.

Sampling the Brillouin zone with a discreet number of points, as opposed to considering the infinite number of points that are present, is possible because the wave function at two different points that are close together in $k$-space is almost identical and therefore can be approximated using a single point. Doing this for the whole Brillouin zone leads to a discreet set of points, each with a weight factor which represents how much of the reciprocal space it represents.

There are a number of different methods that can be implemented to select a set of $k$-vectors which suitably represents the Brillouin zone such that properties, for example charge density, are approximated sufficiently accurately. A common scheme, and one used in this work, is the Monkhorst-Pack scheme,[261] which generates a set of special points in the Brillouin zone, with the appropriate symmetry for the material in question. The periodic wave vector function can then be efficiently determined by interpolating between these points.

## 2.4 Interatomic Potential (IP)-Based Methods

Whereas quantum mechanics focuses on the electrons of a system and uses them to calculate ground state energies and properties, IP calculates energies as a function of the nuclear positions within a system, with electronic terms subsumed into the potential. One advantage of this approach is the very significant reduction in the computational cost of modelling materials, making much larger or more complex systems more accessible.

These methods depend on several assumptions, the most important of which is the Born-Oppenheimer approximation.[218] Quantum mechanics uses this approximation to focus on the electronic motions in a system, whereas IP methods assume the potential energy of the system depends on the nuclear positions and therefore the energy of a system can be written purely as a function of nuclear coordinates.

The potential energy is then calculated from the contributions of interactions within

a system; two body interactions, three body interactions etc.

The potential or force field used in a calculation is defined by its functional form, and the parameters used for each interaction. The choice of interactions and parameters is usually dependent on the system being modelled, for example, whether it is an ionic solid or a protein, and the property of interest. Potentials are fitted, to a range of properties empirically, to experimentally determined parameters, or non-empirically, using results from DFT calculations.

### 2.4.1 Static Lattice Methods in Solids

A key difference between applying interatomic potentials to solids, as opposed to molecules for example, is the way the electrostatic terms are considered - in molecules a cutoff is usually used; however this approach is inadequate for solids, as crystalline systems contain long range order and often highly charged ions.

For ionic solids the starting point is writing the potential energy as a series including pairwise, and 3-body terms etc.:

$$V = V_0 + \sum_{i=1}^{N} \sum_{j=i+1}^{N} r_{ij}(r) + \sum_{i=1}^{N} \sum_{j=i+1}^{N} \sum_{k=j+1}^{N} r_{ijk}(r) + ... \tag{2.69}$$

The most commonly used form of this equation was proposed by Born,[262] who restricted the series to only pairwise terms, which were divided into long range Coulomb interactions and short-range repulsive terms.

The long range, Coulomb interactions tend to be the most time consuming part of these calculations and therefore need to be considered carefully. These interaction energies in solids are usually calculated using techniques such as the Ewald summation[263] which approximates summing a potentially infinite number of long range interactions by splitting the equation for the total Coulomb potential energy of a system of N particles;[264]

$$U = \frac{1}{2} \sum_{i=1}^{N} \sum_{j=1}^{N} \frac{q_i q_j}{r_{ij}} \tag{2.70}$$

a slowly converging sum, into three terms: a real space term that rapidly converges in real space, a reciprocal term that decays quickly in reciprocal space and a constant

term:

$$U_{Ewald} = U' + U''' + U^0 \tag{2.71}$$

The $U'$ and $U'''$ terms refer to the real and reciprocal space sum respectively, while $U^0$ is the constant or self-term:

$$U' = \frac{1}{2}\sum_{i=1}^{N}\sum_{j=1}^{N}\frac{q_i q_j}{r_{ij}} erfc\left(\eta^{\frac{1}{2}} r_{ij}\right) \tag{2.72}$$

$$U'' = \frac{1}{2}\sum_{i=1}^{N}\sum_{j=1}^{N}\sum_{G}\frac{4\pi}{V} q_i q_j \exp(iG.r_{ij})\frac{\exp\left(-\frac{G^2}{4\eta}\right)}{G^2} \tag{2.73}$$

$$U^0 = -\sum_{i=1}^{N} q_i^2 \left(\frac{\eta}{\pi}\right)^{\frac{1}{2}} \tag{2.74}$$

where $q$ is the charge, $G$ is a reciprocal lattice vector, $V$ is the unit cell volume and $\eta$ is a parameter that controls the division of work between real and reciprocal space. There are a number of modifications to the Ewald summation that have been proposed, particularly to make the summation more efficient for larger systems.

Now considering the short range repulsive term, if an inverse power law is used the potential energy expression becomes

$$V = \sum_{i=1}^{N}\sum_{j=i+1}^{N}\left(\frac{q_i q_j}{4\pi\varepsilon_0 r_{ij}} + \frac{A_i j}{r_{ij}^n}\right) \tag{2.75}$$

It is common to assume that the charges; $q_i$ and $q_j$, are equal to the oxidation state of the ion in question and only to consider repulsive interactions up to a specific cut off, leaving the parameters $A$ and $n$ to be established.

However, a widely used extension of this model is to use a Buckingham potential to model the short range interactions. The Buckingham potential models the overlap repulsion and van der Waals forces in the form:

$$V_{ij}(r) = A_{ij}\, e^{-\frac{r_{ij}}{\rho_{ij}}} - \frac{c_{ij}}{r_{ij}^6} \tag{2.76}$$

A significant inadequacy of the simple models, as outlined so far, is that polarisability is not taken into account, which will lead to errors in systems containing polarisable atoms or ions. There are a number of ways to incorporate polarisation effects into the Born model, one of the most popular and accurate is the Shell Model.

#### 2.4.1.1 Shell Model

A key reason for the wide application of the Shell model for including polarisation effects,[265] is its ability to account for the coupling between polarisation and short range repulsion. Polarisation distorts the valence electron distribution and short range repulsion occurs due to the overlap of electron density between ions. Coupling polarisation with the repulsive interactions tends to reduce polarisation effects.

In the Shell model the ions are represented as a mass containing a core and a massless shell which is linked to the core by a harmonic spring. Both the core and the shell have charges associated with them, which, when summed, reproduce the oxidation state of the ion. In an electric field the shell moves, with respect to the core, but maintains its charge. The polarisability, $\alpha$ of an isolated ion in the system is related to the charge on the shell, $Y$, and the spring constant of the harmonic spring, $k$, as follows:

$$\alpha \propto \frac{Y^2}{k} \tag{2.77}$$

In the Shell model, the short range repulsions are specified to act on the shells associated with each ion, therefore the short range repulsions effectively increase the spring constant, coupling the short range repulsions to the polarisation through equation 2.75.

The electrostatic interactions in this model are calculated by summing over all ions and shells, not counting the interactions of cores with their own shells.

## 2.5 Energy Minimisation

The potential energy of a system is a multi-dimensional function of its coordinates, usually referred to as the potential energy surface. The points of most interest on this

surface, are often the points where the energy is at a minimum as these correspond to a stable state of the system. There is usually a large number of minimum energy points on a given energy surface, known as local minima, with the global energy minimum being the lowest energy point on the whole surface; this point may be taken as the ground state of the system.

On obtaining an initial structure, it is often necessary to minimise this structure so it occupies a minimum site on the potential energy surface, which ensures any following calculations are being performed on a stable structure. Structure minimisations are performed using minimisation algorithms.

Minimisation algorithms locate minima by iteratively changing the coordinates of a system to produce configurations of lower energy, until the minimum is reached. The minimum amount of information required to find a minimum on the potential energy surface is therefore the energy of the system in question. However, the minimisation process is much more efficient when derivatives of the energy are included; the first derivatives being the forces on the atoms from which we can determine the local gradient of the energy, while the second derivatives can be built into a matrix known as the Hessian.[220] In this work we will focus on two minimising algorithms; conjugate gradient and Newton-Raphson; first and second derivative methods respectively.

### 2.5.1 Conjugate Gradient

Conjugate gradient is a first order derivatives method, it uses only first order derivatives of the energy, i.e. the gradient, to perform the minimisation. In each iteration, the energy moves in a direction $\boldsymbol{V}_k$ from point $\boldsymbol{x}_k$, which is calculated from the gradient, $\boldsymbol{g}_k$ at that point and direction from the previous iteration $\boldsymbol{V}_{k\text{-}1}$

$$\mathbf{V}_k = -\mathbf{g}_k + \gamma_k \mathbf{V}_{k-1} \tag{2.78}$$

where $\gamma_{\mathrm{k}}$ is a scalar constant:[220]

$$\gamma_k = \frac{\mathbf{g}_k \cdot \mathbf{g}_k}{\mathbf{g}_{k-1} \cdot \mathbf{g}_{k-1}} \tag{2.79}$$

The gradients at each step are orthogonal but the search directions are conjugate, this ensures that the minimisation process does not go back on itself, and each step moves closer to the minima.

Initially, the energy and forces of the starting structure are calculated and the atoms moved along the direction of the force until a minimum value, in that direction, is found. A new direction is then calculated and, to check that it is orthogonal to the previous direction, a line search is performed to locate the one-dimension minimum in each direction. A line search finds minimum points by bracketing the minimum between three points, and slowly decreasing the distance between those three points to narrow the minimum down to a small region. A line search is also used to check that the gradients are conjugate.

Conjugate gradient is generally a reliable method for minimising the energy of a system, and has the advantage of avoiding the large amount of storage space required to store the matrix of second derivatives needed in the second derivative methods discussed below. It can, however, be slowly converging.

### 2.5.2 Newton-Raphson

The Newton Raphson method is a second derivative method, meaning that in addition to the gradient, the second derivative of the energy is also used which gives information about the curvature of the energy surface.[215]

In this method the first derivative is defined as follows (based on a Taylor expansion):

$$V'(x) = xV'(x_k) + (x - x_k)V''(x_k) \tag{2.80}$$

For a function that is purely quadratic, an approximation for an energy well in the potential energy surface, the second derivative is the same everywhere so

$$V''(x) = V''(x_k) \tag{2.81}$$

At a minimum, when x = x*, the first derivative equals zero, and therefore

$$x^* = x_k - V'(x_k)/V''(x_k) \tag{2.82}$$

For multi-dimensional functions the point, $x_k$, and the first and second derivatives, are represented as vectors:

$$\mathbf{x}^* = \mathbf{x_k} - \mathbf{V}'(\mathbf{x_k})\mathbf{V}''^{-1}(\mathbf{x_k}) \tag{2.83}$$

$\boldsymbol{V''^{-1}(x_k)}$ is the inverse Hessian matrix of second derivatives which must be inverted in order to calculate the minimum. A number of steps are needed to find the minimum, in the majority of cases, and the Hessian matrix must be calculated and inverted for each step. This makes this algorithm expensive, unless more approximate methods are used to update the Hessian as discussed below. We note that second derivative methods are generally more rapidly converging than those based on first derivatives especially when close to the minimum.

#### 2.5.2.1 Quasi-Newton Methods

Quasi-Newton methods aim to avoid the time-consuming process of calculating and inverting the Hessian by gradually building up an approximate inverse Hessian in successive iterations, using the gradient of the current and previous iteration.

The method used to update the Hessian depends on the particular Quasi-Newton method being implemented. There are many different methods that could be used, for example DFP (Davidon-Fletcher-Powell)[266, 267] and BFGS (Broyden-Fletcher-Goldfarb-Shanno).[268–272] However, the method implemented in the following work, when using quasi-Newton optimisations, is DIIS (direct inversion in iterative subspace).[273]

This method works by first finding a quadratic region of the potential energy surface, via simple relaxation, then solving a linear system of equations involving the current and previous steps to find a new set of coordinates. A simple relaxation is performed for the new set of coordinates, to see if convergence is reached, and if not, a new set of linear equations is generated. This iterative procedure continues until convergence is reached.[273]

## 2.6 Modelling Solid State Defects

Defect species - vacancies or interstitials - will be present in any material above absolute zero, due to entropic effects, and are responsible for many properties of interest, including ionic and electronic conductivity and specific heat capacity.

Modelling defects pose particular challenges arising, predominantly, from the long range perturbation of the electronic and physical structure that result from the presence of a defect. Two methods have been implemented in this work to study defects: the Mott-Littleton approach and the Supercell method.

### 2.6.1 Mott-Littleton Methodology

In the Mott-Littleton methodology[274] the defect energy is calculated by splitting the system into two regions; in the first region the ions are fully and explicitly affected by the defect, which sits at the centre of the region, whereas for region 2, which extends to infinity, only the displacements of the ions, caused by the presence of the defect, are considered.

The total energy is then calculated using the following equation:

$$E = E_1(x) + E_{12}(x,y) + E_2(y) \tag{2.84}$$

where $E_1$ is the energy of region 1, dependent on the coordinates, $x$, of the ions in the region, $E_{12}$ is the interaction between regions 1 and 2, and $E_2$ is the energy of region 2, dependent on the displacements, y, of the ions in this region.

Therefore, in order to determine the defect energy, the energy of the system needs to be minimised with respect to the positions x and displacements y. However, the displacements in region 2 are themselves dependent on the positions of the ions in region 1, making the energy minimisation difficult. Therefore, in order to simplify the minimisation process, the forces on the ions in region 1 are required to be zero, instead of the energy of the region being at a minimum. Additionally, the ions in region 2 need to be at equilibrium to minimise the energy.

In practice, it turns out that atomistic interactions with region 1 need to be considered only for a small component of region 2. Consequently, region 2 is split into two

sections; region 2a and region 2b. In region 2a the interactions with ions in region 1 are calculated explicitly, and the positions of the ions displaced by the forces acting on them from the electrostatic field of the defect. Whereas for region 2b, which extends to infinity, it is assumed only polarisation of the ions changes as a result of the defect, and is treated as an electrostatic potential surrounding the lattice with all ions remaining in a fixed position. Therefore, the energy associated with region 2b is the polarisation of the ions in region 2b by the electrostatic field of the defect.

When calculating the defect energy, an iterative approach is used to find the configuration in which all the forces in region 1 are zero and the displacements in region 2a are at equilibrium. The final defect energy is then taken as the difference between the total energy of the defective lattice and the perfect lattice. Importantly, calculated energies of vacancies and interstitials are with respect to the added or removed ion at infinite distance.

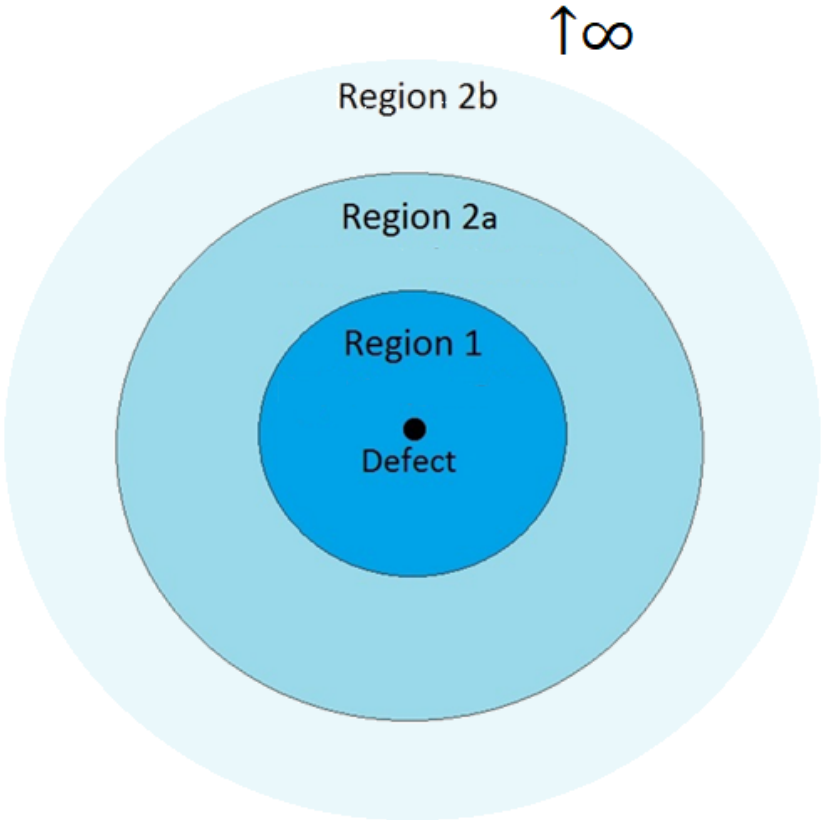


**Figure 2.1:** A visual representation of the Mott-Littleton methodology for calculating defect energies.

### 2.6.2 Supercell Method

Whereas in the Mott-Littleton method an isolated defect, or defect cluster, is placed at the centre of a lattice which is then modelled to infinity, the supercell method places a defect in a supercell, which is then subject to periodic boundary conditions.[275–277]

The main challenge associated with this method is that, instead of an isolated defect at the centre of a lattice, as in Mott-Littleton,[274] a periodic array of defects is generated. Therefore the potential interactions between defects in neighbouring supercells needs to be addressed. Interactions that need considering include: electrostatic, magnetic and elastic. All interactions will become small at large enough supercell sizes; however, the large computational requirements for such supercell sizes mean that it is impractical to employ such a method to remove these errors. Therefore alternative methods are employed to minimise their effect on the final result.

The effect of elastic and magnetic interactions between defects in neighbouring supercells tend to be neglected in solid state systems; elastic interactions, which arise when the defect distorts the surrounding lattice, are assumed to be negligible at the supercell size used in this work, discussed further in Chapter 3, while there is currently no scheme that systematically corrects for magnetic interactions in supercells.[278] The effect of electrostatic interactions on defect formation energies, on the other hand, has been addressed, and the methods used to correct for these interactions are outlined below.

Electrostatic interactions occur when the defect species present in the supercell cause the supercell to have an overall non-zero net charge. The presence of a net charge causes several issues including; the Ewald summation - used to determine the Coulombic contribution to the energies - diverging,[279, 280] defects interacting with images of themselves - due to the slow decay of the Coulomb potential of the charged defect - and the defect changing the electrostatic potential of the supercell compared to the defect-free (pure) supercell, which in turn effects the formation energy of the defect.

The first of these is tackled by compensating for the net charge by introducing a uniform background charge density which effectively sets the average electrostatic potential of the supercell to zero.[278] The interaction of defects with images of themselves and the potential alignment issue are corrected after calculations have been performed with correction schemes.

An image charge correction scheme was initially proposed by Makov and Payne[280] who suggested a correction scheme in a linear supercell dimension $L$, where $L$ is equal to the cube root of the supercell volume.[281]

$$\Delta E_{MP} = \frac{q^2 \alpha_M}{2\varepsilon L} + \frac{2\pi q Q_r}{3\varepsilon L^3} \tag{2.85}$$

where $\alpha$ is the lattice dependent Madelung constant, $\varepsilon$ is the static dielectric constant of the pure supercell and $Q_r$ is the second radial moment of the electron density difference between the defective supercell and pure supercell.

However, a number of issues were raised on whether this charge correction was appropriate and if it lead to improved results.[282–285] Leading to Lany and Zunger[281] suggesting a slightly altered correction:

$$\Delta E_{MP} = (1+f)\frac{q^2 \alpha_M}{2\varepsilon L} \tag{2.86}$$

based on the proportionality of the first and third order terms in equation 2.85

$$\Delta E^3_{MP} = f \Delta E^1_{MP} \tag{2.87}$$

where $\Delta E^1_{MP}$ and $\Delta E^3_{MP}$ refer to the first and second terms in equation 2.85 respectively, and f is a proportionality factor which Lany and Zunger found equals $-0.35$.[281]

A key aspect of this correction scheme being more well regarded than the original scheme proposed by Makov and Payne[280] was the inclusion of the potential alignment correction as these two corrections are not independent and therefore needed to be treated consistently.[278]

The potential alignment correction[286–288] addresses the final issue caused by

electrostatic interactions. To correct for the defect changing the electrostatic potential of the supercell, the average electrostatic potential of the defective supercell is shifted so it is in line with the electrostatic potential of the pure bulk material:

$$\Delta E_{PA}(D,q) = q(V^r_{D,q} - V^r_H) \tag{2.88}$$

where $D$ refers to the defect species in charge state $q$, and $V^r$ are the reference potentials of the charged defect and the host, $H$. The reference potentials are determined from atomic-sphere-averaged electrostatic potentials at atomic sites far away from the defect.[281]

## 2.7 Computer Codes

Two main computer codes have been used throughout the work presented in this thesis, the Vienna *ab initio* simulation package (VASP),[289, 290, 290] and the general utility lattice program (GULP).[291] Here we give a brief overview of each code.

### 2.7.1 VASP

VASP is an atomic scale materials modelling program that can use either DFT or the HF approximation to compute an approximate solution the many-body Schrödinger equation. In our work, VASP is used for DFT calculations. VASP uses plane wave basis sets to express quantities such as the one-electron orbitals, with the interactions between electrons and ions described using either pseudopotentials or the projector-augmented-wave method, as described in Section 2.3.4. The implementation of DFT and DFT+$U$ is well known to be accurate and reliable in VASP, and is therefore well suited to our work, which considers both DFT and DFT+$U$ when choosing modelling parameters, which will be discussed in Chapter 3.

### 2.7.2 GULP

For our interatomic potential-based calculations, the GULP code[291] was used. GULP is a force field-based code for modelling condensed phases and has a wide variety of capabilities, while being designed to be as easy to use as possible. The

variety of tasks GULP can perform, along with the ease of implementation, made this code well suited to the interatomic potential-based calculations performed for this thesis.

## 2.8 Computer Hardware

Calculations have been run on several clusters throughout this project, including three based at UCL and two national systems. In this section we will briefly cover how each was used and their architecture.

### 2.8.1 UCL-based

Three UCL hosted clusters have been used; Faraday, Legion and Grace. Faraday is a small, shared research cluster for the UCL Chemistry department, it has 240 cores and was therefore used for our interatomic potential-based calculations, which are computationally inexpensive compared to DFT. Legion and Grace are both larger clusters, Legion contains 8 different types of node and is a mixed use cluster whereas Grace is designed for parallel workloads, having 680 identical nodes available each with 16 cores (2×8 core Intel Xeon processors). Legion was used initially, and our work establishing a DFT-based modelling approach for $LaFeO_3$ (Chapter 3) was performed on Legion, along with defect calculations using DFT (Chapter 4). Grace was used for our work on dopants (Chapter 6) and the Nudged Elastic band calculations for oxide ion migration (Chapter 5). Grace was also used for establishing a number of parameters for our surface model of $LaFeO_3$ (Chapter 7).

### 2.8.2 National

Two national high performance computing (HPC) facilitates have been used to run calculations; Archer and the Hartree Centre. Archer is the UK National Supercomputing Service, provided by EPSRC, NERC, EPCC, Cray Inc. and The University of Edinburgh, it is designed for calculations that require large numbers of cores working in parallel. Archer consists of the Cray XC30 MPP supercomputer, and has 4920 compute nodes, each with 24 cores (2×12 core Ivy Bridge series processors). Time to run calculations on Archer was requested and granted through my

membership of the UK's HPC Materials Chemistry Consortium (MCC), funded by the EPSRC (Grant number EP/L000202). The Hartree Centre is part of the Science and Technology Facilities Council and provides a range of HPC facilities. Through the partnership of The Hartree Centre with the EPSRC project 'Energy Materials: Computational Solutions' (EP/K016288/1) I was provided access to Iden and Napier. Iden has 84 nodes each of which has 24 cores ($2\times12$ core Intel Xeon processors) while Napier has 360 nodes with 24 cores - of the same design as Iden. Both Archer and the computing facilities at the Hartree Centre were used to run surface relaxation calculations along with defect calculations on the (001) surface of $LaFeO_3$ (Chapter 7).

## 2.9 Concluding Remarks

In this chapter the theoretical background to the computational techniques used in the following work have been outlined, covering the general topic of modelling solid state materials, as well as the more specific subject of studying defective systems. In the next chapter, more details will be given regarding the software and parameters used in the calculations performed in this work, thus providing a complete picture of the methods implemented and our reasoning for using them.

# Chapter 3

# Computational Details

## 3.1 Introduction

In the previous chapter, we gave the theoretical background to density functional theory (DFT) and static lattice (interatomic potential-based) approaches, the two main techniques used in the following work. In the present chapter, further, specific detail is given, where required, regarding the implementation of these techniques in the modelling packages chosen for this work; VASP (Vienna *ab initio* simulation package)[289, 290, 292] for DFT and GULP (General Utility Lattice Program)[291] for static lattice calculations. This chapter will also provide details of the parameters used for each modelling approach; the exchange-correlation functional used in the DFT calculations, along with the value of the $U_{eff}$ parameter in DFT+$U$, and the forcefield potentials used in the static lattice calculations.

The chapter proceeds as follows: the interatomic potential-based methods will be outlined first, in section 3.2, including details of the potential parameters used for the forcefields and the extent to which they reproduce the structural parameters of $LaFeO_3$. Then parameters used in the DFT-based calculations will be presented, in section 3.3, including our consideration of a range of exchange-correlation functionals and $U_{eff}$ values and our approach to selecting the most appropriate of each for our applications.

## 3.2 Interatomic Potential-Based Methods

### 3.2.1 $LaFeO_3$ Structure Model

As introduced in Chapter 2 section 2.4.1, the interatomic potential calculations implemented in the GULP code,[291] are based on the Born model of a solid, which is split into two terms; a long range Coulombic interaction between each pair of ions, calculated using the Ewald summation, and a short range Buckingham term which models the overlap repulsion and van der Waals forces. We recall that the Buckingham term takes the form:

$$V_{ij}(r) = A_{ij}\, e^{-\frac{r_{ij}}{\rho_{ij}}} - \frac{c_{ij}}{r_{ij}^6} \tag{3.1}$$

where $V_{ij}$ is the short range potential energy between the ions i and j separated by distance $r$, $A_{ij}$, $\rho_{ij}$ and $C_{ij}$ are the potential parameters particular to each pair.

The short-range potential parameters used in the Buckingham term are shown in Table 3.1. These parameters, derived by Cherry *et al.*,[173] were originally designed for cubic perovskites and determined by empirical fitting to structural parameters of a range of cubic perovskites. However, as can be seen in Table 3.2, the potential parameters reproduce the orthorhombic structure of $LaFeO_3$ to within 0.55% of the experimental lattice parameter, demonstrating that they are suitable for modelling other, non-cubic, perovskite structures. A cut off of 12.0 Å was used for all Buckingham potentials.

**Table 3.1:** Buckingham potential parameters and the shell charge and spring constant used for each species.

| Short Range Potential Parameters | | | | Shell Model | |
|---|---|---|---|---|---|
| Interaction | A / eV | P / Å$^6$ | C / eV Å$^6$ | Y / e | k / eV Å$^{-2}$ |
| Perfect Lattice | | | | | |
| $La^{3+}$••••$O^{2-}$ | 1545.21 | 0.3590 | 0.0 | -0.250 | 145.00 |
| $Fe^{3+}$••••$O^{2-}$ | 1156.36 | 0.3299 | 0.0 | 2.040 | 304.70 |
| $O^{2-}$••••$O^{2-}$ | 22764.30 | 0.1490 | 43.0 | -2.240 | 42.00 |

The electronic polarisability of the ions in $LaFeO_3$ is modelled using the shell model,[265] as described in Chapter 2 section 2.4.1.1. The shell charge, Y, and

**Table 3.2:** Calculated and experimental[2] lattice parameters for orthorhombic $LaFeO_3$.

| Parameter | Calculated | Experimental | % Difference |
|---|---|---|---|
| a / Å | 5.558 | 5.553 | 0.090 |
| b / Å | 5.564 | 5.563 | 0.018 |
| c / Å | 7.905 | 7.862 | 0.544 |

the harmonic force constant, k, for each species are shown in Table 3.1.

## 3.3 DFT-based Methods

All electronic structure calculations were performed using spin-polarised Kohn-Sham DFT[229, 230] and DFT+$U$[256] using the plane wave pseudopotential technique with the projector augmented-wave[258] (PAW) approach to model the core-valence electron interaction, further details of which are given in Chapter 2 sections 2.3.4. The use of pseudopotentials and the PAW approach are standard in the Vienna *ab initio* simulation package (VASP),[289, 290, 290] which was used for all electronic structure calculations.

The valence electron configurations used for each ion are: La ($5s^2 5p^6 6s^2 5d^1$), Fe ($4s^2 3d^8$) and O ($2s^2 2p^4$), as defined by the pseudopotentials in VASP. The pseudopotentials also define the cut-off used; 219, 268 and 400 eV respectively for La, Fe and O, however, we determined a separate cut-off to use in our modelling of $LaFeO_3$ by calculating the energy of the system at increasing cut-off values, starting at 400 eV, until convergence was reached. The cut-off used in all calculations, unless otherwise stated, is 650 eV; the total energy converged to within 0.001 eV per atom.

A range of exchange-correlation functionals were initially considered, including LDA,[230] GGA with PBE parameters,[243] GGA with PBEsol parameters[244] and each of these with the $U_{eff}$[256] parameter. In order to determine the most appropriate to use for the system in question, a structural relaxation, using the Murnaghan equation of state, was performed using each functional and the resulting structural parameters compared with experimentally determined values.[2–4, 123] The results are shown in Table 3.3. Hybrid functionals, although successfully em-

ployed for a number of materials, have not been considered in this work. Previous research[293] suggested that no significant improvement in structural parameters was observed when using hybrid functionals compared to using purely DFT-based functionals on a family of perovskite materials. Given the increased computational cost of the technique, we chose to eliminate this form of functional from our study and investigate purely DFT-based functionals. The calculations performed with the $U_{eff}$ parameter used a value of 5.0 eV in all cases as an example value.

**Table 3.3:** Calculated lattice parameters; a, b and c, bond lengths, angles, relaxed cell volume, band gap and magnetic moment of $LaFeO_3$ for LDA, LDA+$U$ GGA (PBE), GGA+$U$ (PBE+$U$), PBEsol and PBEsol+$U$ functionals along with experimental values. For this initial evaluation of functionals, a $U_{eff}$ value of 5.0 eV was used in all cases.[a]Ref[2], [b]Ref[3], [c]Red[4].

| Parameters | Exp. | LDA | LDA+$U$ | PBE | PBE+$U$ | PBEsol | PBEsol+$U$ |
|---|---|---|---|---|---|---|---|
| a / Å | 5.553[a] | 5.354 | 5.459 | 5.572 | 5.571 | 5.505 | 5.511 |
| b / Å | 5.563[a] | 5.285 | 5.465 | 5.692 | 5.629 | 5.584 | 5.540 |
| c / Å | 7.862[a] | 7.524 | 7.705 | 7.915 | 7.902 | 7.798 | 7.793 |
| Fe-$O_{ax}$ / Å | 2.009[a] | 1.909 | 1.968 | 2.035 | 2.027 | 2.000 | 1.995 |
| Fe-$O_{eq}$ / Å | 2.007[a] | 1.904 | 1.972 | 2.062 | 2.035 | 2.019 | 2.001 |
| Fe-$O_{eq}$ / Å | 2.002[a] | 1.906 | 1.966 | 2.032 | 2.024 | 2.001 | 1.993 |
| La-O / Å | 2.416[a] | 2.371 | 2.379 | 2.412 | 2.411 | 2.390 | 2.390 |
| La-O / Å | 2.591[a] | 2.547 | 2.537 | 2.517 | 2.545 | 2.505 | 2.538 |
| La-O / Å | 2.455[a] | 2.404 | 2.415 | 2.449 | 2.443 | 2.422 | 2.426 |
| La-O / Å | 2.656[a] | 2.565 | 2.609 | 2.657 | 2.663 | 2.628 | 2.628 |
| La-O / Å | 2.805[a] | 2.695 | 2.742 | 2.790 | 2.798 | 2.752 | 2.771 |
| Fe-O-$Fe_{ax}$ / ° | 156.32[a] | 160.319 | 156.476 | 153.030 | 154.126 | 154.215 | 155.064 |
| Fe-O-$Fe_{eq}$ / ° | 157.22[a] | 161.723 | 157.474 | 153.256 | 154.620 | 154.463 | 155.988 |
| Volume of Cell / $Å^3$ | 60.717[a] | 53.223 | 57.470 | 62.755 | 61.950 | 59.928 | 59.485 |
| Band Gap / eV | 2.1[b] | - | 1.786 | 0.036 | 2.031 | 0.490 | 1.996 |
| Magnetic Moment / $\mu_B$ | 4.6 +/- 0.2[c] | ± 0.77 | ± 4.18 | ± 3.73 | ± 4.22 | ± 3.66 | 4.22 |

Interestingly, PBEsol, a functional designed to reproduce improved lattice parameters compared to PBE, does not perform as well as PBE in the case of $LaFeO_3$. The superior performance of PBE in reproducing lattice parameters and bond lengths compared to the other functionals considered meant that this was chosen as the functional for all further calculations. The second conclusion draw from Table 3.3 is that, in order to model the band gap of $LaFeO_3$ correctly, the $U_{eff}$ parameter is

needed, as expected.

The $U_{eff}$ parameter (also referred to as the $U$ parameter in the following work), which represents the difference between the Coulomb ($U$) and exchange ($J$) parameters ($U_{eff}$ = $U$ - $J$) is used to correct for the inadequate description of localized electrons, in this case the 3$d$ electrons on iron,[256] further details are discussed in Chapter 2 section 2.3.3.3. The value to use for $Fe^{3+}$ was determined in a similar way to the functional; comparing experimental structure parameters and properties[2–4, 123] to those calculated at increasing values of $U_{eff}$; the results of which are shown in Table 3.4.

**Table 3.4:** Lattice parameters, bond lengths, angles, relaxed cell volume, band gap and magnetic moment of $LaFeO_3$ with increasing $U$ using GGA+$U$, along with experimental values. [a]Ref[2], [b]Ref[3], [c]Ref[4].

| Parameters / $U$ eV | Exp. | 4 | 5 | 6 | 7 | 8 |
|---|---|---|---|---|---|---|
| a / Å | 5.553[a] | 5.572 | 5.571 | 5.567 | 5.563 | 5.558 |
| b / Å | 5.563[a] | 5.638 | 5.629 | 5.620 | 5.608 | 5.588 |
| c / Å | 7.862[a] | 7.903 | 7.902 | 7.898 | 7.887 | 7.875 |
| Fe-$O_{ax}$ / Å | 2.009[a] | 2.028 | 2.027 | 2.025 | 2.020 | 2.016 |
| Fe-$O_{eq}$ / Å | 2.007[a] | 2.039 | 2.035 | 2.031 | 2.026 | 2.018 |
| Fe-$O_{eq}$ / Å | 2.002[a] | 2.027 | 2.024 | 2.020 | 2.016 | 2.008 |
| La-O / Å | 2.416[a] | 2.409 | 2.411 | 2.410 | 2.413 | 2.410 |
| La-O / Å | 2.591[a] | 2.539 | 2.545 | 2.550 | 2.554 | 2.572 |
| La-O / Å | 2.455[a] | 2.443 | 2.443 | 2.444 | 2.446 | 2.449 |
| La-O / Å | 2.656[a] | 2.662 | 2.663 | 2.662 | 2.661 | 2.650 |
| La-O / Å | 2.805[a] | 2.796 | 2.798 | 2.799 | 2.796 | 2.809 |
| Fe-O-$Fe_{ax}$ / ° | 156.32[a] | 153.832 | 154.126 | 154.385 | 154.818 | 155.138 |
| Fe-O-$Fe_{eq}$ / ° | 157.22[a] | 154.296 | 154.620 | 154.967 | 155.398 | 156.306 |
| Volume of Cell / $Å^3$ | 60.717[a] | 62.065 | 61.950 | 61.775 | 61.520 | 61.148 |
| Band Gap / eV | 2.1[b] | 1.681 | 2.031 | 2.329 | 2.626 | 2.924 |
| Magnetic Moment / $\mu_B$ | 4.6 +/- 0.2[c] | ± 4.14 | ± 4.22 | ± 4.31 | ± 4.40 | ± 4.51 |

On increasing the $U$-value, the lattice structural properties improve, with $U$ = 8 eV reproducing the lattice parameters, bond lengths and bond angles most accurately. The magnetic moment of $Fe^{3+}$ is also closer to the experimental values at higher $U$-values, with both $U$ = 7 and 8 eV giving a magnetic moment within the experimental range. However, the band gap is closest to the experimental value when $U$ =

5 eV. Therefore a value of 7 eV was selected in order to get the correct balance between structural and electronic properties, while maintaining the correct magnetic moment for $Fe^{3+}$. The effect of the $U$-value on calculated defect energies was also considered, as defect calculations form a considerable part of the following work. We found that changing the $U$-value from 3 to 8 eV caused a decreased of 0.5 eV overall, see Appendix A. As the defect energy calculated for $U = 7$ eV is similar to defect energies reported previously[119, 175] this further verifies our choice of $U$ parameter.

The above analysis, to find the appropriate functional and $U$-value, was also carried out for $LaCoO_3$, the other parent compound of LSCF, results are shown in Tables 3.5 and 3.6 respectively.

**Table 3.5:** Calculated lattice parameters; a and $\alpha$, bond lengths, relaxed cell volume and band gap of $LaCoO_3$ for LDA, LDA+$U$ GGA (PBE), GGA+$U$ (PBE+$U$), PBEsol and PBEsol+$U$ functional along with experimental values. [a]Ref[6], [b]Ref[7].

| Parameters | Exp. | LDA | LDA+$U$ | PBE | PBE+$U$ | PBEsol | PBEsol+$U$ |
|---|---|---|---|---|---|---|---|
| a / Å | 5.342[a] | 5.245 | 5.248 | 5.361 | 5.374 | 5.291 | 5.296 |
| $\alpha$ / Å | 60.990[a] | 61.344 | 60.937 | 61.600 | 61.165 | 61.405 | 61.047 |
| Co-O / Å | 1.924[a] | 1.897 | 1.887 | 1.951 | 1.944 | 1.918 | 1.909 |
| La-O / Å | 2.685[a] | 2.639 | 2.637 | 2.704 | 2.706 | 2.665 | 2.663 |
| La-O / Å | 2.428[a] | 2.378 | 2.397 | 2.392 | 2.412 | 2.380 | 2.405 |
| La-O / Å | 2.993[a] | 2.972 | 2.925 | 3.098 | 3.056 | 3.023 | 2.974 |
| Volume of Cell / $Å^3$ | 55.085[a] | 52.545 | 52.180 | 56.440 | 56.305 | 54.010 | 53.750 |
| Band Gap / eV | 0.9[b] | - | 0.525 | - | 0.753 | - | 0.683 |

The results show that choosing the appropriate functional and $U$-value is not as straight forward for $LaCoO_3$ as for $LaFeO_3$. Starting with functionals, both PBE and PBEsol perform equally well for reproducing structural parameters, although PBE reproduces the experimental band gap more successfully. However, for the $U$-values, some structural parameters (a and a La-O bond length) are reproduced best with $U = 3$ eV, others are reproduced best with a higher $U$-value; $U = 7$ or 8 eV. The situation is further complicated when the spin state is considered, $LaCoO_3$ has three spin states; low spin, intermediate spin and high spin, and although the experimental ground state is low spin, the DFT ground state depends on the functional and the $U$-

value used. As calculations are not reported on this material, it will not be discussed further in this work. However, details of the accurate modelling of $LaCoO_3$ can be found in Ref[123].

**Table 3.6:** Lattice parameters; a and $\alpha$ bond lengths, relaxed cell volume and band gap of $LaCoO_3$ with increasing $U$ using PBE+$U$, along with experimental values. [a]Ref[6], [b]Ref[7].

| Parameters / $U$ eV | Exp. | 3 | 4 | 5 | 6 | 7 | 8 |
|---|---|---|---|---|---|---|---|
| a / Å | 5.342[a] | 5.367 | 5.372 | 5.374 | 5.379 | 5.281 | 5.380 |
| $\alpha$ / Å | 60.990[a] | 61.363 | 61.236 | 61.154 | 61.023 | 60.951 | 60.936 |
| Co-O / Å | 1.924[a] | 1.946 | 1.945 | 1.943 | 1.943 | 1.941 | 1.940 |
| La-O / Å | 2.685[a] | 2.705 | 2.706 | 2.706 | 2.708 | 2.708 | 2.707 |
| La-O / Å | 2.428[a] | 2.402 | 2.409 | 2.412 | 2.413 | 2.418 | 2.422 |
| La-O / Å | 2.993[a] | 3.075 | 3.062 | 3.055 | 3.049 | 3.040 | 3.034 |
| Volume of Cell / Å$^3$ | 55.085[a] | 56.335 | 56.320 | 56.305 | 56.280 | 56.250 | 56.215 |
| Band Gap / eV | 0.9[b] | 0.245 | 0.595 | 0.753 | 0.841 | 0.910 | 0.980 |

Further $U$-values were established for a range of divalent transition metals, for our study on dopants in $LaFeO_3$; see Chapter 6. Using the metal oxide, for example MnO for $Mn^{2+}$, the structural parameters and magnetic moment were calculated at increasing $U$-values, from 3 to 7 eV, and the $U$ chosen based on which value best reproduces the experimental structural parameters and magnetic moment, see Appendix B for the results. We found that, unlike $LaFeO_3$ and $LaCoO_3$, the structural properties of some metal oxides vary very little with $U$-value. When this was the case, we also took $U$-values used previously in the literature into account. More details are given in Chapter 6.

The divalent transition metals we investigate as dopants in Chapter 6 are manganese, cobalt, nickel and copper, using $U$-values of 4, 4, 7 and 7 eV respectively.

To summarise, all DFT+$U$ calculations of $LaFeO_3$ were performed using a PBE functional and a $U$-value of 7 eV on $Fe^{3+}$. Further parameters, chosen after convergence testing, include a $k$-mesh of $(4\times4\times3)$, generated by the Monkhorst-Pack[261] scheme, for Brillouin zone sampling of the $LaFeO_3$ unit cell, which was converged to within 0.05 eV. Integration over the first Brillouin-zone used Gaussain smearing ($\sigma = 0.05$) during structural relaxations.

The supercell approach was used to calculate defect formation energies under DFT.

A $2\times2\times1$ supercell of $LaFeO_3$ was used, convergence of which is given in Appendix C, with antiferromagnetic G ordering of the $Fe^{3+}$ ions; this is the experimental magnetic ground state for $LaFeO_3$, as discussed in Chapter 1, a ground state reproduced by PBE+*U*, see Appendix D. The energies of supercells containing defects, either intrinsic or extrinsic, were calculated at the lattice parameters of the relaxed perfect supercell in order to model the dilute limit of defect concentration.

# Chapter 4

# Defects

## 4.1 Introduction

Our study of $LaFeO_3$ will start by considering the defect structure of the pure, stoichiometric material. Knowledge of the defect chemistry will aid our understanding of the mixed ionic electronic conductivity $LaFeO_3$ displays, and allow us to identify species that need to be promoted or suppressed, either through modifying the growth conditions or by extrinsic doping, to promote this property. Defect formation energies allow one to establish which defects are likely to occur, the concentrations of these defects and the effects each will have on ionic and electronic conductivity properties. Two methods will be used to calculate defect energies; an interatomic potential-based method, which utilises the Mott-Littleton methodology[274] and a DFT-based method, which utilises the supercell approach. The advantages and disadvantages of each method have been discussed previously, and in this chapter we will compare the results from both methods and assess the most appropriate for studying defects in $LaFeO_3$. A range of intrinsic defects have been studied; we will briefly define each of these defects in the following section.

### 4.1.1 Intrinsic Defects

To start, we will first discuss the formation energies of isolated point defects, namely vacancies and interstitials. A vacancy occurs when an ion is missing from its lattice site, an interstitial occurs when an ion occupies a lattice site which is usually empty in the perfect crystal structure of the material. Defects can form through redox pro-

cesses and in response to dopants or other external influences, such as oxygen partial pressure. The redox processes through which defects can form are represented by the following defect equations; equations 4.1 to 4.3 showing the equations for vacancy formation, equations 4.4 to 4.6 showing these for interstitials.

$$\mathrm{La}_{\mathrm{La}}^{\times} \leftrightarrow \mathrm{V}_{\mathrm{La}}^{'''} + 3\mathrm{h}^{\bullet} + \mathrm{La} \tag{4.1}$$

$$\mathrm{Fe}_{\mathrm{Fe}}^{\times} \leftrightarrow \mathrm{V}_{\mathrm{Fe}}^{'''} + 3\mathrm{h}^{\bullet} + \mathrm{Fe} \tag{4.2}$$

$$\mathrm{O}_{\mathrm{O}}^{\times} \leftrightarrow \mathrm{V}_{\mathrm{O}}^{\bullet\bullet} + 2\mathrm{e}^{'} + \frac{1}{2}\mathrm{O}_2 \tag{4.3}$$

$$\mathrm{La}_{\mathrm{La}}^{\times} + \mathrm{La} \leftrightarrow \mathrm{La}_{\mathrm{i}}^{\bullet\bullet\bullet} + 3\mathrm{e}^{'} \tag{4.4}$$

$$\mathrm{Fe}_{\mathrm{Fe}}^{\times} + \mathrm{Fe} \leftrightarrow \mathrm{Fe}_{\mathrm{i}}^{\bullet\bullet\bullet} + 3\mathrm{e}^{'} \tag{4.5}$$

$$\mathrm{O}_{\mathrm{O}}^{\times} + \frac{1}{2}\mathrm{O}_2 \leftrightarrow \mathrm{O}_{\mathrm{i}}^{''} + 2\mathrm{h}^{\bullet} \tag{4.6}$$

It is also possible for neutral vacancies to form, and, for lanthanum and iron, whether the ion leaves as a metal or an oxide will depend on the partial pressure of oxygen, in equations 4.7 and 4.8 the ion leaves as a metal, representing the oxygen poor scenario.

$$\mathrm{La}_{\mathrm{La}}^{\times} \leftrightarrow \mathrm{V}_{\mathrm{La}}^{\times} + \mathrm{La} \tag{4.7}$$

$$\mathrm{Fe}_{\mathrm{Fe}}^{\times} \leftrightarrow \mathrm{V}_{\mathrm{Fe}}^{\times} + \mathrm{Fe} \tag{4.8}$$

$$\mathrm{O}_{\mathrm{O}}^{\times} \leftrightarrow \mathrm{V}_{\mathrm{O}}^{\times} + \frac{1}{2}\mathrm{O}_2 \tag{4.9}$$

In addition to these redox processes, thermal disorder such as Frenkel and Schottky type disorder, see below, will also be considered in this work. The process of an ion vacating a lattice site and occupying an empty site in the lattice (i.e. the compensating combination of a vacancy and an interstitial) is known as Frenkel disorder, while Schottky disorder occurs when multiple ions vacate their lattice sites and form a separate phase on the surface of the material, usually a metal oxide. For full Schottky type disorder, the ions which leave the site must balance in stoichiometry, so the material retains the same composition. An example of Schottky type disorder in $LaFeO_3$ is $La_2O_3$ partial Schottky disorder, in which two lanthanum vacancies and three oxygen vacancies form in $LaFeO_3$ and the ions precipitate out as lanthanum oxide.

The following defect equations outline the Frenkel and Schottky disorder we have investigated in this work.

Frenkel Disorder:

$$A_A^{\times} \leftrightarrow V_A^{\times} + A_i^{\times} \tag{4.10}$$

$La_2O_3$ partial Schottky disorder:

$$2La_{La}^{\times} + 3O_O^{\times} \leftrightarrow 2V_{La}^{\times} + 3V_O^{\times} + La_2O_3 \tag{4.11}$$

$Fe_2O_3$ partial Schottky disorder:

$$2Fe_{Fe}^{\times} + 3O_O^{\times} \leftrightarrow 2V_{Fe}^{\times} + 3V_O^{\times} + Fe_2O_3 \tag{4.12}$$

Full Schottky disorder:

$$La_{La}^{\times} + Fe_{Fe}^{\times} + 3O_O^{\times} \leftrightarrow V_{La}^{\times} + V_{Fe}^{\times} + 3V_O^{\times} + LaFeO_3 \tag{4.13}$$

Here, Kröger-Vink[294] notation has been used in which $V_A$ represents a vacancy of ion A, $A_i$ represents an interstitial of ion A. The superscript symbol, $\times$, refers to the charge state of the defect site, $\times$ refers to the defect site being neutral, however other options are $'$ for a single negative charge and $\bullet$ for a single positive charge in

the defective site. This notation will be used throughout this work.

Another common feature in perovskite-type materials is anti-site defects, in which one of the cations in $LaFeO_3$ occupies the site of the other cation. Three types of anti-defect are considered in this work, $Fe_{La}'$, $La_{Fe}'$ and $Fe_{La}'$ + $La_{Fe}'$, these are outlined respectively in the following defect equations:

$$La_2O_3 + Fe_{Fe}^{\times} \leftrightarrow La_{Fe}^{\times} + LaFeO_3 \tag{4.14}$$

$$Fe_2O_3 + La_{La}^{\times} \leftrightarrow Fe_{La}^{\times} + LaFeO_3 \tag{4.15}$$

$$La_{La}^{\times} + Fe_{Fe}^{\times} \leftrightarrow Fe_{La}^{\times} + La_{Fe}^{\times} \tag{4.16}$$

Additional Kröger-Vink[294] notation has been introduced here, with $A_B$ symbolising ion A occupying an ion B lattice site. The same notation is used to show the charge on the site; $\times$ for neutral, $'$ for negative, $\bullet$ for positive.

Section 4.2 of this chapter will discuss how formation energies of these defects and disorder schemes are calculated under each method used, then in section 4.3 the formation energies will be presented and discussed. The interatomic potential and DFT results will be presented separately, starting with interatomic potentials. The results from the two methods will be compared as the DFT results are presented.

## 4.2 Calculating Defect Formation Energies

Formation energies calculated in the following work are approximations to the Gibbs free energy; $G$. The Gibbs free energy is the sum of enthalpy, $H$, and entropy, $S$, terms;

$$G = H + TS \qquad with \quad H = U + pV \tag{4.17}$$

where $T$ is temperature and $U$ is the internal energy. Computationally modelling is done under 0 K, therefore entropy terms are not considered, and as there is no external pressure on the system, the Gibbs free energy is approximated to the internal

energy of the system.

### 4.2.1 Interatomic Potentials

When using interatomic potentials, the Mott-Littleton methodology[274] is employed to calculate defect energies. In the Mott-Littleton method, the defect is considered to be at the centre of a sphere separated into two regions; the region containing the defect, region 1, and a region surrounding this, region 2. Further details of this methodology can be found in Chapter 2 Section 2.6.1.

The defect energies from the Mott Littleton methodology are then calculated as the difference between the lattice, modelled as a sphere with the defect at the centre, and the ions at infinite distance.

The radius of region 1 was converged separately for each defect studied by increasing the radius of region 1 until the defect energy converged, to within 0.02 eV. Therefore, the radius of region 1 ranges from 10.0 to 12.0 Å, corresponding to between 670 and 1222 ions.

Calculating the formation energies of defects using interatomic potentials, according to equations 4.1 to 4.6, requires the energy of charge compensating species $e'$ and $h^{\bullet}$ to be calculated. This would require the implementation of crude models, such as $Fe^{2+}$ or the electron affinity of $LaFeO_3$ for $e'$ and $O^{-}$ or $Fe^{4+}$ for $h^{\bullet}$. The reliability of these models are difficult to assess for defect formation energies, as these values cannot be established experimentally. Alternatively, the defect equations could be written as such - using lanthanum and oxygen vacancies as examples:

$$La_{La}^{\times} \leftrightarrow V_{La}^{'''} + La^{\bullet\bullet\bullet} \tag{4.18}$$

$$O_{O}^{\times} \leftrightarrow V_{O}^{\bullet\bullet} + O^{2-} \tag{4.19}$$

which would involve using experimental values; e.g. the first, second and third ionisation potentials of La and the first and second electron affinities of oxygen. Again, with no way to check the reliability of the results from this method, care must be taken when combining calculated and experimental values. Additionally,

there is no way to reliably measure the second electron affinity of oxygen - although values are available, which have been referred from reaction energies - leading to a further source of error in the calculation.

As a result the point defect energies are presented as defect energies, not formation energies, with formation energies only calculated for the charge compensated disorder schemes, i.e. Frenkel and Schottky disorder.

### 4.2.2 Density Functional Theory

For our *ab initio* study of defects, defect energies are calculated using the supercell method, details of which are discussed in Chapter 2 Section 2.6.2. Formation energies for defects, in charge state $q$ ($\Delta H_f(q)$), were calculated using the following equation:

$$\Delta H_f(q) = E^{defect} - E^{perfect} \pm \sum n_x(E_x + \mu_x) + q(E_{VBM} + E_F + \Delta E_{pot}) + q^2 E_{ic} \tag{4.20}$$

with $E^{defect}$ being the total energy of the relaxed supercell containing the defect, $E^{perfect}$ the energy of the relaxed perfect supercell, $n_x$ the number of defect atoms or ions added or removed when forming the defect; $n_x < 0$ when atoms are removed, $E_x$ the elemental reference energy, i.e. the energy of an element in its standard state, and $\mu_x$ is the chemical potential of the defect; where $x$ is La, Fe or O. The elemental reference energies of lanthanum and iron were calculated using the respective metals and oxygen by using a triplet oxygen molecule in a large supercell.

For charged defects, where $q \neq 0$, the chemical potential of the electrons in the system needs to be taken into account, which is done with $E_{VBM}$, the energy of the valence band maximum (VBM), and $E_F$, the Fermi energy, defined with respect to the VBM. In addition, a correction term is required, comprising: $\Delta E_{pot}$, the correction that accounts for the difference between the potential of the perfect supercell and the supercell containing the charged defect and $E_{ic}$, the correction to the interaction of charged defects with their periodic image.[281]

Two methods of calculating $E_{ic}$ were investigated: one designed for cubic systems,

in which the dielectric tensor is constant along a, b and c lattice parameters,[281] and the other which takes into account the anisotropy between dielectric tensors along different lattice parameters.[295] Orthorhombic $LaFeO_3$ is only slightly distorted from the cubic perovskite structure and therefore only small differences, reaching a maximum of 0.026 eV for $q = \pm 3$, were found between the correction values calculated by each method, demonstrating that the choice of method has minimal impact on our results. However, in order to model defects in orthorhombic $LaFeO_3$ as accurately as possible, the method outlined by Murphy and Hine,[295] which takes into account the differences in dielectric tensors along the three lattice parameters, was selected.

#### 4.2.2.1 Varying Formation Conditions

The formation energy of defects under different conditions can be investigated by varying the chemical potential, $\mu_x$, in equation 4.20, which requires the range of chemical potentials under which $LaFeO_3$ forms preferentially, over competing phases, to be calculated. We use the chemical potential limits analysis program (CPLAP)[296], which employs calculated enthalpies of formation, at thermodynamic equilibrium, of $LaFeO_3$ and its competing phases, to determine the ranges of chemical potentials in which $LaFeO_3$ is stable with respect to these phases. The competing phases we considered were the oxides of both iron and lanthanum; iron has multiple oxides it can form due to the ability of iron to occupy various oxidation states, and we also considered $La_3FeO_6$ which can form if lanthanum is present in a higher concentration than iron. The chemical potential values at which $LaFeO_3$ is stable are contained in the grey shaded region of Figure 4.1. The chemical potential values for lanthanum and iron; $\mu_{La}$ and $\mu_{Fe}$, are shown in Figure 4.1, the chemical potential of oxygen; $\mu_O$, is then determined using the the following relationship:

$$\mu_{La} + \mu_{Fe} + \frac{3}{2}\mu_{O_2} \leq \Delta H(LaFeO_3) \tag{4.21}$$

Defect formation energies were calculated at the chemical potential values of two different points within this shaded region, marked A and B. These points were cho-

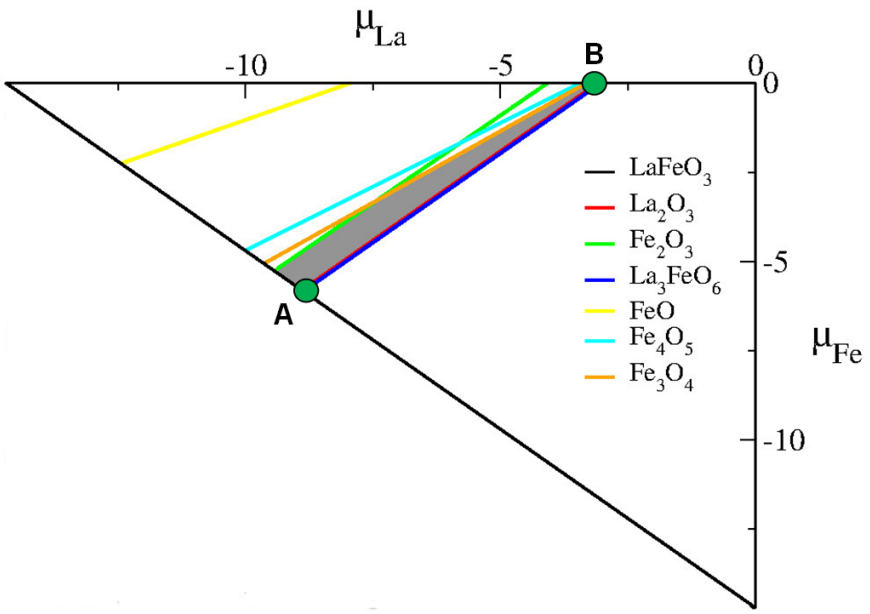


**Figure 4.1:** The accessible chemical potential ranges for $LaFeO_3$ with respect to competing phases. The shaded region indicates the chemical potential values where $LaFeO_3$ is stable.

sen as they represent the extremes of possible conditions in which $LaFeO_3$ forms preferentially. A, bound by $La_2O_3$ and $LaFeO_3$, represents lanthanum and iron poor and oxygen rich conditions, with chemical potential values $\mu_{La}$ = -8.89 eV, $\mu_{Fe}$ = -5.80 eV and $\mu_O$ = 0.00 eV and B, bound by $La_2O_3$ and Fe metal, represents lanthanum and iron rich and oxygen poor conditions, with chemical potential values $\mu_{La}$ = -3.09 eV, $\mu_{Fe}$ = 0.00 eV, $\mu_O$ = -3.87 eV. Oxygen rich conditions represent both operating and growth conditions of SOFC cathode materials whereas oxygen poor represent reducing conditions; the use of these two regimes allows us to investigate how varying oxygen partial pressure affects this material and its defect chemistry.

## 4.3 Results

The calculated formation energies of intrinsic defects will be presented separately for each computational modelling method used. First the results from interatomic potential methods will be discussed, followed by the results from *ab initio* methods.

### 4.3.1 Interatomic Potentials

#### 4.3.1.1 Vacancies and Interstitials

The defect energies of isolated vacancies and interstitials of all three ions in $LaFeO_3$ are presented in Tables 4.1 and 4.2 respectively.

**Table 4.1:** Defect energies of vacancies calculated using interatomic potentials in $LaFeO_3$.

| Defect | Energy / eV |
|---|---|
| $V_{La}'''$ | 42.87 |
| $V_{Fe}'''$ | 55.37 |
| $V_O^{\bullet\bullet}$ (O1) | 19.35 |
| $V_O^{\bullet\bullet}$ (O2) | 19.32 |

The defect energies for the two oxygen sites only differ by 0.03 eV, close to the 0.02 eV that the defect energies were converged to. Therefore there may not be a significant difference between oxygen vacancies at the two inequivalent sites when using interatomic potentials.

For studying interstitials in $LaFeO_3$ it is first necessary to identify possible interstitial sites, i.e. sites that are not occupied by an ion in the pure, defect free material. Orthorhombic $LaFeO_3$ belongs to the symmetry group *Pbnm* no. 62,[165] and therefore the possible interstitial positions, in the primitive cell, in fractional coordinates are: $(\frac{1}{2}, \frac{1}{2}, 0)$, (0, 0, 0), $(0, 0, \frac{1}{2})$ and $(\frac{1}{2}, \frac{1}{2}, \frac{1}{2})$ as determined from the Wyckoff positions. The defect energies of interstitials at all four positions were calculated to assess if any of the ions have a favoured interstitial position in this material.

**Table 4.2:** Defect energies of interstitials calculated using interatomic potentials in $LaFeO_3$.

| Defect | Interstitial Position | | | |
|---|---|---|---|---|
| | $(\frac{1}{2}, \frac{1}{2}, 0)$ | (0, 0, 0) | $(0, 0, \frac{1}{2})$ | $(\frac{1}{2}, \frac{1}{2}, \frac{1}{2})$ |
| $La_i^{\bullet\bullet\bullet}$ | -23.73 | -23.73 | -23.73 | -23.73 |
| $Fe_i^{\bullet\bullet\bullet}$ | -39.38 | -39.38 | -39.38 | -39.38 |
| $O_i$" | -10.99 | -10.99 | -10.99 | -10.99 |

In order to draw meaningful conclusions from the values presented here it is necessary to calculate the solution energies of Frenkel and Schottky disorder. However,

we can see that all interstitial positions are equivalent, with none of the ions favouring one over the other. Therefore, when interstitials are considered later in this work, we will only consider one site.

**Split-Interstitials**

Before calculating Frenkel and Schottky solution energies, we must first investigate split interstitial formation in $LaFeO_3$. A split interstitial forms when two ions share a lattice position, and can occur in tightly packed materials such as perovskites.[297, 298] The stability of split interstitials compared to single interstitials was evaluated by comparing defect energies of split interstitials with those calculated for single interstitials, shown in Table 4.2. A split interstitial was modelled by replacing one ion with two of the same ion equidistance from the now vacant lattice site.

For split interstitials, the direction of the split is likely to have an impact on its defect energy. Therefore a range of directions were considered; in the direction of the three lattice parameters, a, b and c, and also towards other lattice sites - the lanthanum, iron and oxygen sites, with both the O1 and O2 oxygen sites considered. Figure 4.2 shows the crystallographic directions and can be used to see the split-interstitial directions considered.

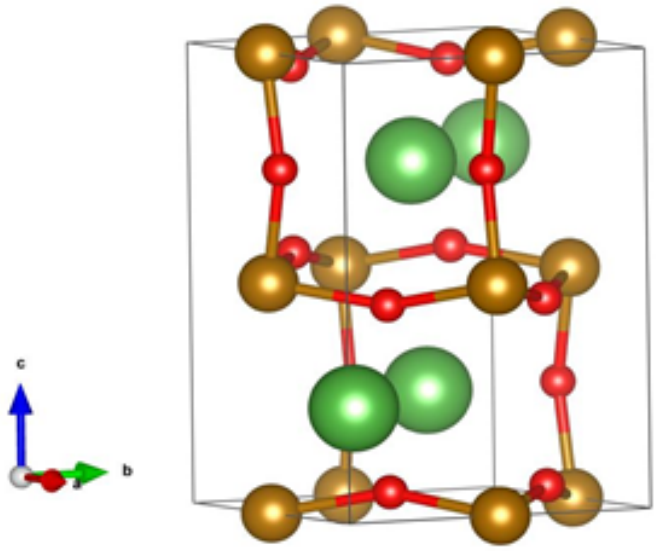


**Figure 4.2:** Orthorhombic $LaFeO_3$ showing the direction of the lattice vectors, all of which are tested as directions for split interstitials.

The defect energies calculated for split interstitials in $LaFeO_3$ are shown in Tables 4.3 and 4.4, with the former showing the defect energies of split-interstitials split along the three lattice parameters, while the latter shows the defect energies for the split-interstitials being split towards the 4 ion sites.

**Table 4.3:** Defect energies of split interstitials in $LaFeO_3$, split along the three lattice parameters.

| Interstitial Species | Direction of Split | | |
|---|---|---|---|
| | a | b | c |
| La | -25.73 | -25.73 | -24.60 |
| Fe | -38.23 | -38.58 | -36.82 |
| O | -10.64 | -11.04 | -11.78 |

**Table 4.4:** Defect energies of split interstitials in $LaFeO_3$, split towards the other lattice sites, denoted by the ion that occupies the site.

| Interstitial Species | Direction of Split | | | |
|---|---|---|---|---|
| | La | Fe | O1 | O2 |
| La | -24.60 | -25.59 | -25.59 | -25.73 |
| Fe | -36.82 | -38.73 | -38.12 | - |
| O1 | -10.37 | -11.47 | -11.50 | -11.50 |
| O2 | -9.20 | -11.55 | -11.58 | -11.04 |

Firstly looking at lanthanum, we see that the most favourable direction for the split-interstitial is along the a and b lattice parameters, in fact, observation of the relaxed structure shows the split-interstitial has relaxed along an ab direction in both cases, explaining the equivalence of these two values. However, an interstitial split towards both Fe and O1 ions is only 0.14 eV less favourable than a split in the ab direction, so this could also be a possible orientation for the lanthanum split-interstitial to take. Most importantly, we see that split-interstitials, in all orientations investigated, are more favourable than a single interstitial and therefore if lanthanum interstitials are present in $LaFeO_3$ they will be split-interstitials.

For $Fe^{3+}$ interstitials, splitting towards other Fe and La ion sites are the most favoured orientations of the split-interstitial. However, these values are less favourable than the defect energy of a single interstitial, suggesting iron intersti-

tials are likely to form single interstitials in $LaFeO_3$.

Finally, considering oxygen interstitials, interestingly, unlike lanthanum - in which all orientations of the split-interstitial were more favourable than a single interstitial - some orientations of the oxygen split-interstitial are less favourable than a single oxygen interstitial. However, the most favourable split-interstitial orientation, along the c lattice parameter, is 0.8 eV more favourable than a single interstitial, suggesting split-interstitials are likely to dominate if oxygen interstitial are present in $LaFeO_3$.

#### 4.3.1.2 Frenkel and Schottky disorder

The defect reactions governing the formation of Frenkel and Schottky defects are shown in equations 4.10 to 4.13 in section 4.1.1.

The calculated formation energies associated with each of these defect equations are listed in Table 4.5. As there are two inequivalent oxygen sites in $LaFeO_3$; O1 and O2, the defect energies of a vacancy in each site have been calculated separately. When calculating Frenkel and Schottky disorder formation energies, that include oxygen vacancies, they have been calculated twice; with the O1 vacancy energy and with the O2 vacancy energy. The oxygen vacancy energy that has been used is denoted by O1 and O2 in Table 4.5. For La and O Frenkel disorder, the defect energies of split-interstitials have been used, while the defect energies of single interstitials were used for Fe Frenkel, as these are the more favourable form of interstitial in each case.

**Table 4.5:** Calculated formation energies for Frenkel and Schottky type disorder in $LaFeO_3$.

| Frenkel Disorder | Energy defect$^{-1}$ | Schottky Disorder | Energy defect$^{-1}$ |
|---|---|---|---|
| La Frenkel | 8.58 | $La_2O_3$ Partial (O1) | 3.20 |
| Fe Frenkel | 8.02 | $La_2O_3$ Partial (O2) | 3.18 |
| O1 Frenkel | 3.80 | $Fe_2O_3$ Partial (O1) | 3.85 |
| O2 Frenkel | 3.78 | $Fe_2O_3$ Partial (O2) | 3.84 |
| | | Full Schottky (O1) | 3.52 |
| | | Full Schottky (O2) | 3.50 |

Firstly, we can see that Schottky disorder, in the majority of cases, is more

favourable than Frenkel disorder and therefore vacancies will be present in higher concentrations than interstitials. The lowest energy form is $La_2O_3$ partial Schottky disorder, but all values are high and therefore vacancy concentrations are likely to be low.

#### 4.3.1.3 Anti-Site Defeccts

The formation of anti-site defects, and the defect equations associated with these processes are discussed in section 4.1.1; equations 4.14 to 4.16. All three forms of anti-site defect were investigated for $LaFeO_3$ and the solution energies are shown in Table 4.6.

**Table 4.6:** Anti-site solution energies calculated using interatomic potentials.

| Anti-Site Defect | Energy defect$^{-1}$ / eV |
|---|---|
| $La_{Fe}^{\times}$ | 2.85 |
| $Fe_{La}^{\times}$ | 1.99 |
| $La_{Fe}^{\times}$ + $Fe_{La}^{\times}$ | 2.31 |

We see that, for $LaFeO_3$, all anti-site defects have a similar solution energy, with $Fe_{La}^{\times}$ having the lowest. This type of disorder, in all cases, is more favourable than Frenkel and Schottky disorder, and therefore are likely to have the highest concentration of the intrinsic defects present in $LaFeO_3$, according to our interatomic potential-based calculations.

### 4.3.2 Density Functional Theory

Having calculated defect energies of vacancies, interstitials, Frenkel and Schottky disorder and anti-site defects using interatomic potentials, we will now discuss the results from the *ab initio* study. Due to the nature of interatomic potential-based methods, the charge states of defects are limited to the charge state of the ion determined by the potentials, in the case of $LaFeO_3$ this is $La^{3+}$, $Fe^{3+}$ and $O^{2-}$. However, we are able to explore alternative charge states, including neutral defects - where the defective site remains neutral - using *ab initio* methods. We will present the results of neutral, isolated vacancies and interstitials first, then discuss Frenkel and Schottky disorder and anti-site defects. The final part of this section will address

non-zero charge states of defective sites and which are most favourable under the two chemical potential environments considered.

#### 4.3.2.1 Vacancies and Interstitials

The formation energies of intrinsic defects, both neutral and charged, have been calculated, within the two chemical potential environments outlined in section 4.2.2.1. Table 4.7 shows the defect formation energies of neutral vacancies of La, Fe and O, see equations 4.7 to 4.9, for neutral defects $q$ from equation 4.20 is 0 and therefore the formation energy calculation becomes

$$\Delta H_f(q) = E^{defect} - E^{perfect} \pm \sum n_x(E_x + \mu_x) \tag{4.22}$$

Due to the antiferromagnetic ordering of iron ions in $LaFeO_3$, iron in spin up and spin down orientations, with respect to the c lattice parameter, are present (as can be seen in Figure 4.3). Therefore defects involving iron in each orientation have been investigated. As with the interatomic potentials study, vacancies of the two oxygen sites are reported separately.

As our interatomic potentials study demonstrated that all interstitial sites in $LaFeO_3$ are equivalent for all three ions, only one interstitial site is considered in the *ab initio* study; position ($\frac{1}{2}$, $\frac{1}{2}$, $\frac{1}{2}$) in the primitive cell.

**Table 4.7:** The defect formation energies of neutral vacancies in $LaFeO_3$.

| Neutral Defect | Defect Formation Energy / eV | |
|---|---|---|
| | O Rich / La & Fe Poor | O Poor / La & Fe Rich |
| $V_{La}^{\times}$ | 3.333 | 9.136 |
| $V_{Fe}^{\times}$ (Spin Up) | 2.639 | 8.442 |
| $V_{Fe}^{\times}$ (Spin Down) | 2.940 | 8.743 |
| $V_{O}^{\times}$ (O1) | 3.960 | 0.092 |
| $V_{O}^{\times}$ (O2) | 3.829 | -0.040 |

The formation energies of oxygen vacancies have been calculated previously by Mastrikov *et al.*[119] and by Ritzmann *et al.*[175] who reported values of 4.41 and 4.01 eV respectively, comparing well with the values calculated here; 3.960 and 3.829 eV for oxygen rich conditions. The differences between the results are

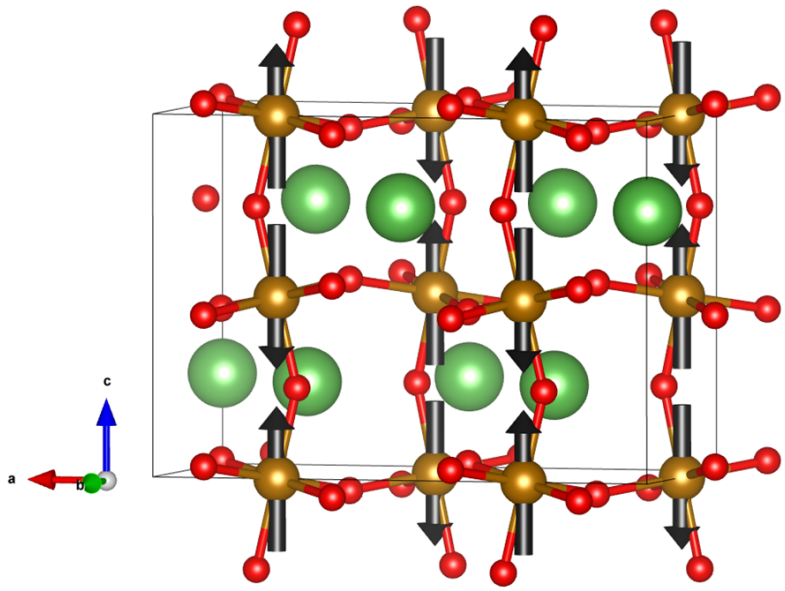


**Figure 4.3:** A 2×1×1 supercell of $LaFeO_3$ showing the spin orientations on iron, the black arrows represent the magnetic moment of the iron ion, either +4.4 or -4.4 $\mu_B$.

due to differences in the method used. Mastrikov *et al.*[119] employed the GGA functional, not GGA+*U*, whereas, although Ritzmann *et al.*[175] used GGA+*U*, they used a smaller *U*-value; 4.3 eV, and used a supercell with fixed cubic lattice parameters - allowing the internal coordinates to relax - whereas our work used orthorhombic lattice parameters. The negative formation energy for oxygen vacancies under oxygen poor conditions suggests that this material will be significantly oxygen deficient under reducing conditions.

On comparing the formation energies of neutral vacancies to those of neutral interstitials, shown in Table 4.8, we see that in general interstitials have higher formation energies, as is to be expected for a close packed material such as $LaFeO_3$, with the exception of $O_i$ in oxygen rich conditions which have relatively low formation energies.

Initially, interstitials were placed at the centre of the 2×2×1 supercell, occupying a square planar positions between four oxygens; position 0.5, 0.5, 0.5 in fractional coordinates. However, examination of the optimised position of lanthanum and oxygen interstitials reveal they form split-interstitials with a nearby ion on its lattice site, as can be seen in Figure 4.4a and 4.4b, with a single interstitial of these ions not sta-

**Table 4.8:** The defect formation energies of neutral interstitials in $LaFeO_3$.

| Neutral Defect | Defect Formation Energy / eV | |
|---|---|---|
| | O Rich / La & Fe Poor | O Poor / La & Fe Rich |
| $La_i^{\times}$ | 12.550 | 6.747 |
| $Fe_i^{\times}$ (Spin Up) | 8.708 | 2.904 |
| $Fe_i^{\times}$ (Spin Down) | 8.006 | 2.203 |
| $O_i^{\times}$ | 1.628 | 5.496 |

bilising in $LaFeO_3$. These results suggests that split-interstitials are more favourable than single interstitials for both lanthanum and oxygen, in agreement with interatomic potential results presented in the previous section. The preferential formation of split-interstitials for the A-site and oxygen ions has been found in similar materials including the (Ba,Sr)(Co,Fe)$O_{3-\delta}$ (BSCF) family of perovskites.[92, 299] As with the interatomic potentials study, a number of different orientations for split-interstitials within this structure were investigated to find the most favourable. For both lanthanum and oxygen, splitting the interstitial along the three lattice parameters, a, b and c, was investigated, with configurations along and perpendicular to the Fe-O-Fe bond also investigated for oxygen. Splitting the interstitials towards other lattice sites was not considered in this case, as the interatomic potentials study demonstrated that the most favourable splitting orientations were along one (or more) of the lattice parameters, for all ions.

It was found that the orientations shown in Figure 4.4a and 4.4b are the most stable for lanthanum and oxygen split interstitials; (-**a**, 0.84**b**) for lanthanum and (-**a**, -0.26**b**, 0.11**c**) for oxygen. The length of the bond between the two oxygen ions in Figure 4.4b is 1.46 Å just under the reported bond length of classical peroxides, $O_2^{2-}$, 1.49 $\pm$ 0.02 Å.[300] When compared to the bond lengths of alternative oxygen species; 1.21 for $O_2$[25] and 1.348 $\pm$ 0.008 Å for $O_2^{-}$,[301] 1.49 $\pm$ 0.02 Å is the closest and therefore $O_2^{2-}$ is the most likely charge state of the oxygen split interstitial.

Interestingly, worked on lanthanum substituted $SrTiO_3$ found that perovskite materials with an oxygen excess form ordered oxygen rich defect phases which decrease oxide ion conductivity due to defect-defect interactions preventing mobility

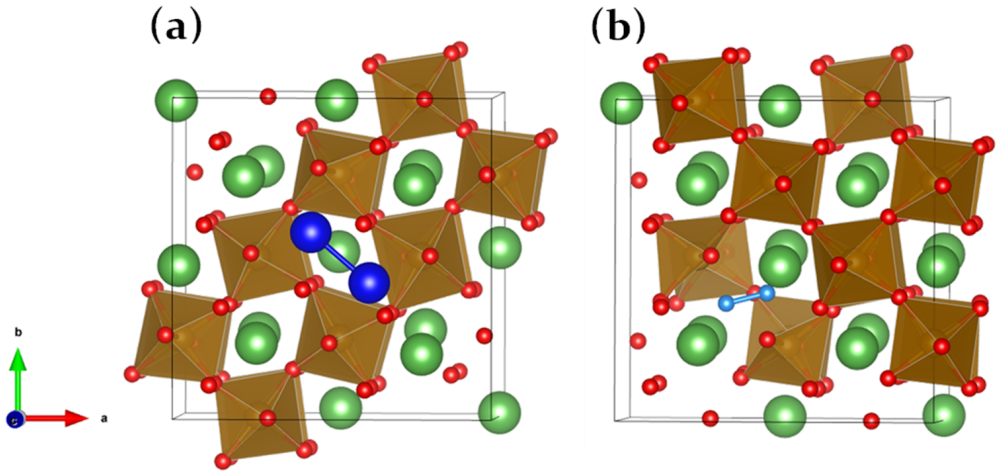


**Figure 4.4:** Split interstitials of (a) lanthanum, shown in dark blue and (b) oxygen shown in pale blue.

of oxide ions.[302] The ordered defect phases could take the form of oxygen split interstitials, as our results show these defects form favourably in perovskite oxides. In order to achieve the high ionic conductivity required for intermediate cathode applications these defects must be avoided, demonstrating the importance of understanding the defect chemistry of $LaFeO_3$; in order to identify both desired defects and those we do want to promote within the material.

Iron split-interstitials were also investigated. However, all orientations studied converged into single interstitials, suggesting that this is the most favourable form for iron, in agreement with the interatomic potential results.

The optimised position of iron interstitials, in both spin up and spin down orientations, is shown in Figure 4.5b. Figure 4.5a shows the initial position of the interstitial, which has a square planar configuration. In Figure 4.5b we see that the interstitial has shifted to a tetrahedral position. The magnetic moment of the interstitial in the tetrahedral position is 3.7 $\mu_B$, a decrease from the bulk magnetic moment of 4.4 $\mu_B$, suggesting that iron interstitials are incorporated as $Fe^{2+}$ ions, with the excess charge delocalised onto the oxygens surrounding the interstitial.

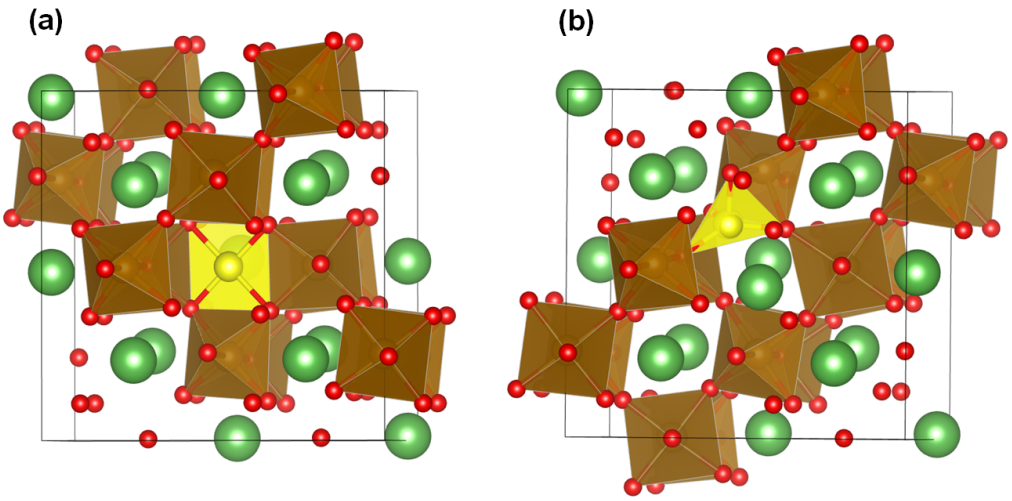


**Figure 4.5:** The change in position of an iron interstitial found in this material, the iron interstitial is shown in yellow: (a) between two lanthanum ions, the front lanthanum ion has been removed from the image for ease of viewing, this is the position initially used for all interstitials; it has a square planar configuration with the surrounding oxygen ions, (b) displaced from this site in an -**ab** direction; it has a tetrahedral configuration with the surrounding oxygen ions.

#### 4.3.2.2 Frenkel and Schottky Disorder

The formation energies calculated for vacancies and interstitials of lanthanum, iron and oxygen can be used to calculate the energies of Frenkel and Schottky type disorder, as shown in equations 4.10 to 4.13.

The formation energies of these processes have been calculated for both neutral and charged vacancies and interstitials, with the values calculated for Frenkel and Schottky disorder shown in Tables 4.9 and 4.10 respectively. The energies reported for Frenkel and Schottky disorder using charged defects, have used defect energies for the 3+ charge states for lanthanum and iron and 2- for oxygen. The formation energies of Frenkel and Schottky disorder are independent of iron rich and poor conditions and therefore only one set of values are presented.

Defect energies of iron vacancies and interstitials in both spin up and spin down orientations have been used in calculating the solution energies of Frenkel and Schottky disorder. The orientation that has been used is given by the su (spin up) or sd (spin down) label.

**Table 4.9:** Energies of Frenkel type disorder in $LaFeO_3$.

| Frenkel | Energy defect$^{-1}$ / eV | |
|---|---|---|
| | Neutral | Charged |
| La | 7.941 | 5.807 |
| Fe (sd) | 5.473 | 4.444 |
| Fe (su) | 5.673 | 4.435 |
| O1 | 2.794 | 3.291 |
| O2 | 2.728 | 3.287 |

**Table 4.10:** Energies of Schottky disorder in $LaFeO_3$.

| Schottky | Energy defect$^{-1}$ / eV | |
|---|---|---|
| | Neutral | Charged |
| $La_2O_3$ Partial O1 | 3.710 | 2.198 |
| $La_2O_3$ Partial O2 | 3.631 | 2.193 |
| $Fe_2O_3$ Partial O1 (sd) | 3.749 | 2.419 |
| $Fe_2O_3$ Partial O2 (sd) | 3.670 | 2.414 |
| $Fe_2O_3$ Partial O1 (su) | 3.629 | 2.414 |
| $Fe_2O_3$ Partial O2 (su) | 3.550 | 2.409 |
| Full O1 (sd) | 3.631 | 2.210 |
| Full O2 (sd) | 3.552 | 2.205 |
| Full O1 (su) | 3.571 | 2.207 |
| Full O2 (su) | 3.492 | 2.203 |

For lanthanum and iron, charged Frenkel pairs have lower formation energies than their neutral counterparts; for oxygen, however, neutral Frenkel disorder will form preferentially. For Schottky disorder, $La_2O_3$ partial Schottky and full Schottky will form preferentially over $Fe_2O_3$ partial Schottky disorder.

The favourable formation of Schottky disorder supports work done by Mizusaki *et al.*[48] and the more recent work by Wærnhus *et al.*,[49, 167] who measured electronic conductivity in $LaFeO_3$ under different $O_2$ partial pressure. Both observed *p*-type conductivity at high partial pressures, with fully ionised cation vacancies required in order to keep the material charge neutral under this conductivity scheme. Mizusaki *et al.* assumed that lanthanum vacancies would be the most favourable due to the fixed stoichiometry of the iron with its surrounding oxygens,[48] while Wærnhus *et al.* suggested that cation vacancies were incorporated into $LaFeO_3$ through Schottky disorder, although, as they were unable to identify the type of

cation vacancy involved, they assumed both would be present.[49, 167] The results in Table 4.10 suggest that $La_2O_3$ partial Schottky and full Schottky defects are likely to form meaning that vacancies of both cations will be present in the material, although $La^{3+}$ vacancies may dominate. This finding builds on the conclusions drawn in both pieces of work: *p*-type conductivity is compensated by both $La^{3+}$ and $Fe^{3+}$ vacancies formed through $La_2O_3$ partial and full Schottky disorder.

Table 4.11 presents the solution energies of Frenkel and Schottky disorder calculated by both the interatomic potentials-based method and DFT+*U* for ease of comparison. The DFT+*U* results presented are the formation energies calculated from charged defect energies as these are most comparable with the interatomic potential results.

**Table 4.11:** Energies of Frenkel and Schottky type disorder in $LaFeO_3$ calculated using interatomic potentials and DFT+*U*.

| Disorder | Energy defect$^{-1}$ / eV | |
|---|---|---|
| | Interatomic Potentials | DFT+*U* |
| La Frenkel | 9.57 | 5.807 |
| Fe Frenkel | 8.02 | 4.435 |
| O1 Frenkel | 4.18 | 3.291 |
| O2 Frenkel | 4.16 | 3.287 |
| Full Schottky O1 | 3.52 | 2.207 |
| Full Schottky O2 | 3.50 | 2.203 |
| $La_2O_3$ Partial Schottky O1 | 3.20 | 2.198 |
| $La_2O_3$ Partial Schottky O2 | 3.18 | 2.193 |
| $Fe_2O_3$ Partial Schottky O1 | 3.85 | 2.414 |
| $Fe_2O_3$ Partial Schottky O2 | 3.84 | 2.409 |

The formation energies of La and Fe Frenkel disorder differ most between the two methods, with the values calculated using interatomic potentials being significantly higher in both cases. The majority of the energies calculated for Frenkel and Schottky disorder differ by roughly 1.0 eV, a significant value that impacts the conclusions on whether this type of disorder will predominate, especially for Schottky type disorder. The source of this difference was investigated by using each technique to calculate the heat of formation of $LaFeO_3$ in order to compare to the experimental value of -18.21 eV.[22] The resulting values are shown in Table 4.12. DFT is

known to underestimate the heat of formation, whereas interatomic potentials may overestimate the heat of formation, due to the assumption of pure ionic bonding.

**Table 4.12:** The experimental heat of formation, and the values calculated using interatomic potentials and DFT+$U$. [a]Ref[22].

| Technique | $\Delta H_f$ / eV |
|---|---|
| Experimental | -18.21[a] |
| *ab initio* | -14.70 |
| Interatomic Potentials | -27.02 |

The heat of formation was calculated with *ab initio* methods by taking the difference between the cohesive energy of $LaFeO_3$ and the sum of the atoms in their standard state, equation 4.23, whereas for interatomic potentials a Born-Haber cycle was used; Figure 4.6. Table 4.13 contains the values used in equation 4.23 and Table 4.14 for the values used in the Born-Haber Cycle.

$$E_x(La(s)) + E_x(Fe(s)) + E_x\left(\frac{3}{2}O_2(g)\right) \rightarrow E_f(LaFeO_3) \tag{4.23}$$

**Table 4.13:** The cohesive energy of the atoms in $LaFeO_3$ in their standard states, along with the formation enthalpy of $LaFeO_3$. All values were calculated using DFT+$U$.

| Species | Energy / eV |
|---|---|
| La(s) | -4.920 |
| Fe(s) | -3.851 |
| $O_2$(g) | -9.513 |
| $LaFeO_3$ | -37.759 |

These results show that although DFT+$U$ does underestimate the heat of formation and may, as a consequence, underestimate to some degree the vacancy energies, interatomic potentials overestimate it considerably. This over estimation is likely to be the basis of the difference in the defect formation energies shown in Table 4.11 and may be related to the lack of covalency present in the interatomic potential model. A degree of covalency has been found in related materials in which it mediates charge transfer and is therefore vital for catalytic processes.[210]

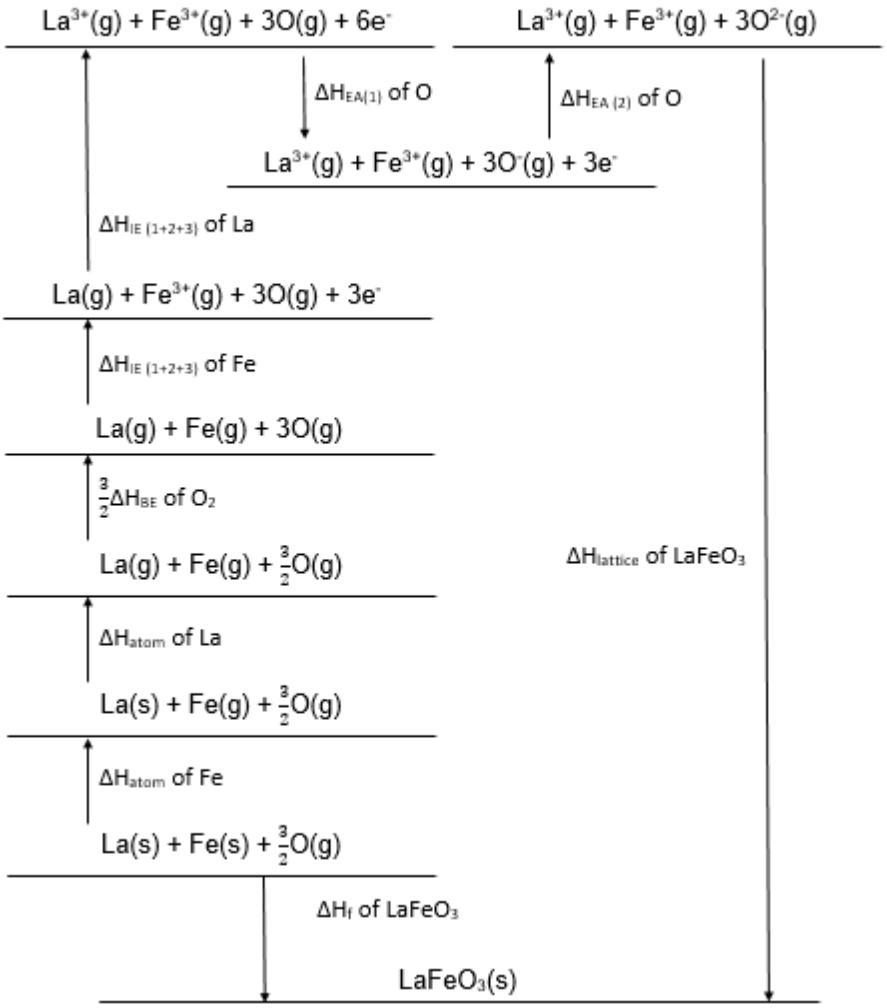


**Figure 4.6:** The Born-Haber Cycle used to calculate the formation energy of $LaFeO_3$; $\Delta H_f$ $LaFeO_3$. Experimental values were used for each of the parameters (see Table 4.14) except for $\Delta H_{lattice} LaFeO_3$ which was calculated using interatomic potentials.

Table 4.15 show solution energies of Frenkel disorder using vacancies and interstitials of non-zero charge states. An example defect equation for non-zero Frenkel disorder is as follows, using $La^+$ as an example:

$$La_{La}^{\times} \leftrightarrow V_{La}^{'} + La_i^{\bullet} \tag{4.24}$$

Comparing the solution energies of Frenkel disorder formed from ions with non-zero charge states, interestingly we find lower energies for higher charge states of lanthanum, suggesting that formation of interstitials from lattice ions does not re-

**Table 4.14:** Values used for each of the terms in the Born-Haber cycle (Figure 4.6). All values are experimentally determined values except $\Delta H_{lattice}$ of $LaFeO_3$ which was calculated using interatomic potentials. [a]Ref [23], [b]Ref [24], [c]Ref [25] and [d]Ref [26].

| Parameter | Value / kJ $mol^{-1}$ |
|---|---|
| $\Delta H_{atom}(La)$ | 431.0[a] |
| $\Delta H_{atom}(Fe)$ | 415.0[b] |
| $\Delta H_{BE}(O_2)$ | 497.0[c] |
| $\Delta H_{IE(1)}(Fe)$ | 759.2[d] |
| $\Delta H_{IE(2)}(Fe)$ | 1561.1[d] |
| $\Delta H_{IE(3)}(Fe)$ | 2957.3[d] |
| $\Delta H_{IE(1)}(La)$ | 538.1[d] |
| $\Delta H_{IE(2)}(La)$ | 1067.1[d] |
| $\Delta H_{IE(3)}(La)$ | 1849.6[d] |
| $\Delta H_{EA(1)}(O)$ | -141.0[c] |
| $\Delta H_{EA(2)}(O)$ | 844.0[c] |
| $\Delta H_{lattice}(LaFeO_3)$ | -13390.460 |

**Table 4.15:** Energies of Frenkel type disorder for defects of non-zero charge states.

| Frenkel | Energy $defect^{-1}$ / eV | Frenkel | Energy $defect^{-1}$ / eV |
|---|---|---|---|
| $La^{+}$ | 6.956 | $Fe^{2+}$ (su) | 4.197 |
| $La^{2+}$ | 6.621 | $Fe^{3+}$ (su) | 4.435 |
| $La^{3+}$ | 5.807 | $O1^{-}$ | 3.601 |
| $Fe^{+}$ (sd) | 4.778 | $O1^{2-}$ | 3.291 |
| $Fe^{2+}$ (sd) | 4.287 | $O2^{-}$ | 3.615 |
| $Fe^{3+}$ (sd) | 4.444 | $O2^{2-}$ | 3.287 |
| $Fe^{+}$ (su) | 4.527 | | |

sult in a change of charge state of the ion. However, this is not the case for iron or oxygen. For iron, the $Fe^{2+}$ Frenkel is more stable, because the formation of a displaced interstitial in a 2+ charge state is stabilised, compared to a $Fe^{3+}$ interstitial, due to the tetrahedral environment the displaced interstitial occupies favouring the 2+ charge state. For oxygen, the neutral interstitial is more stable than any of the charged interstitials, suggesting that when an oxygen Frenkel Pair is formed the electrons are left in the vacancy, where they are likely to be stabilised by surrounding iron ions.

#### 4.3.2.3 Anti-Site Defects

The final type of defect to study in our *ab initio* investigation is anti-site defects, the equations of which are shown in section 4.1.1; equations 4.14 to 4.16.

All three anti-site defects were investigated and the resulting formation energies are shown in Table 4.16. For comparison the solutions energies of anti-site defects calculated using interatomic potentials, presented in the previous section, have been included in Table 4.16. As with Frenkel and Schottky disorder, anti-site defects are independent of the chemical potential environment.

**Table 4.16:** Defect formation energies of anti-site defects in $LaFeO_3$ calculated using DFT+$U$ and interatomic potentials.

| Anti-Site Defect | Energy defect$^{-1}$ / eV | |
|---|---|---|
| | DFT+$U$ | Interatomic Potentials |
| $La_{Fe}^{\times}$ | 3.010 | 2.852 |
| $Fe_{La}^{\times}$ | 2.590 | 1.989 |
| $La_{Fe}^{\times}$ + $Fe_{La}^{\times}$ | 2.303 | 2.305 |

The energies calculated for each anti-site defect compare well between the two techniques, although, interestingly, the most favourable type changes between the two techniques. $La_{Fe}^{\times}$ has a high formation energy and is therefore not likely to contribute to the defect chemistry of $LaFeO_3$, however, $Fe_{La}^{\times}$ and $La_{Fe}^{\times}$ + $Fe_{La}^{\times}$ have formation energies comparable with $La_2O_3$ and full Schottky disorder and therefore may play a role in the chemistry of $LaFeO_3$, particularly at high temperatures.

Investigating the effect of changing the charge state of the ion in the anti-site revealed that all charge states, for both ions, have higher formation energies than their neutral counterparts when $E_F = 0$, as can be seen in Table 4.17. However, as the Fermi energy is increased, lower charge states become more favourable, as can be seen in the following section.

The preferential formation of Schottky-type disorder over anti-site disorder, which is seen when solution energies are calculated using DFT+$U$, is found in other perovskite-based materials, including BSCF in which Schottky-disorder causes the material to decompose.[92, 299] Schottky disorder in $LaFeO_3$ has a higher formation energy than in BSCF; therefore the material will not be as susceptible to

**Table 4.17:** Defect formation energies of anti-site defects in varying charge states.

| Anti-Site Defect | Energy defect$^{-1}$ / eV |
|---|---|
| $La_{Fe}'$ | 4.786 |
| $La_{Fe}''$ | 7.134 |
| $Fe_{La}'$ | 3.198 |
| $Fe_{La}'$ | 5.632 |

decomposition through this route.

#### 4.3.2.4 Formation Energies as a Function of Fermi Energy

The formation energies of charged defects depend on the Fermi energy, $E_F$, as seen in equation 4.20. Therefore the defect formation energies of charged intrinsic defects, vacancies, interstitials and anti-site defects, have been calculated at increasing values of $E_F$, from 0.0 eV - the valence band maximum - to 2.1 eV the conduction band minimum. Figure 4.7 shows how the formation energy of each defect changes with the Fermi energy within each set of conditions: oxygen rich/lanthanum and iron poor and oxygen poor/lanthanum and iron rich. In these plots, the different charge states of the defects have been grouped, with only the charge state with the lowest formation energy being shown. The gradient indicates the defect charge state, with neutral being horizontal and $\pm$ 3 being the steepest slope. Where the gradient of the lines change, i.e. where the formation energies of two charge states are equal, a thermodynamic transition occurs. For lanthanum and iron defects, +1, +2 and +3 charge states have been investigated, for oxygen defects -1 and -2 charge states have been investigated.

We see from Figure 4.7, that for oxygen rich conditions, $O^{2-}$ vacancies and neutral oxygen interstitials dominate the defect chemistry at low $E_F$ values. However, cation vacancies, both $La^{3+}$ and $Fe^{3+}$, become the most favourable defect just before $E_F$ = 1.0 eV. This result further supports the work done by Mizusaki *et al.*[48] and Wærnhus *et al.*,[49, 167] by showing that cation vacancies form favourably in oxygen rich conditions.

In oxygen poor conditions oxygen vacancies dominate across all values of Fermi energy, with the 2- charge state having the lowest formation energy until $E_F$ = 1.5

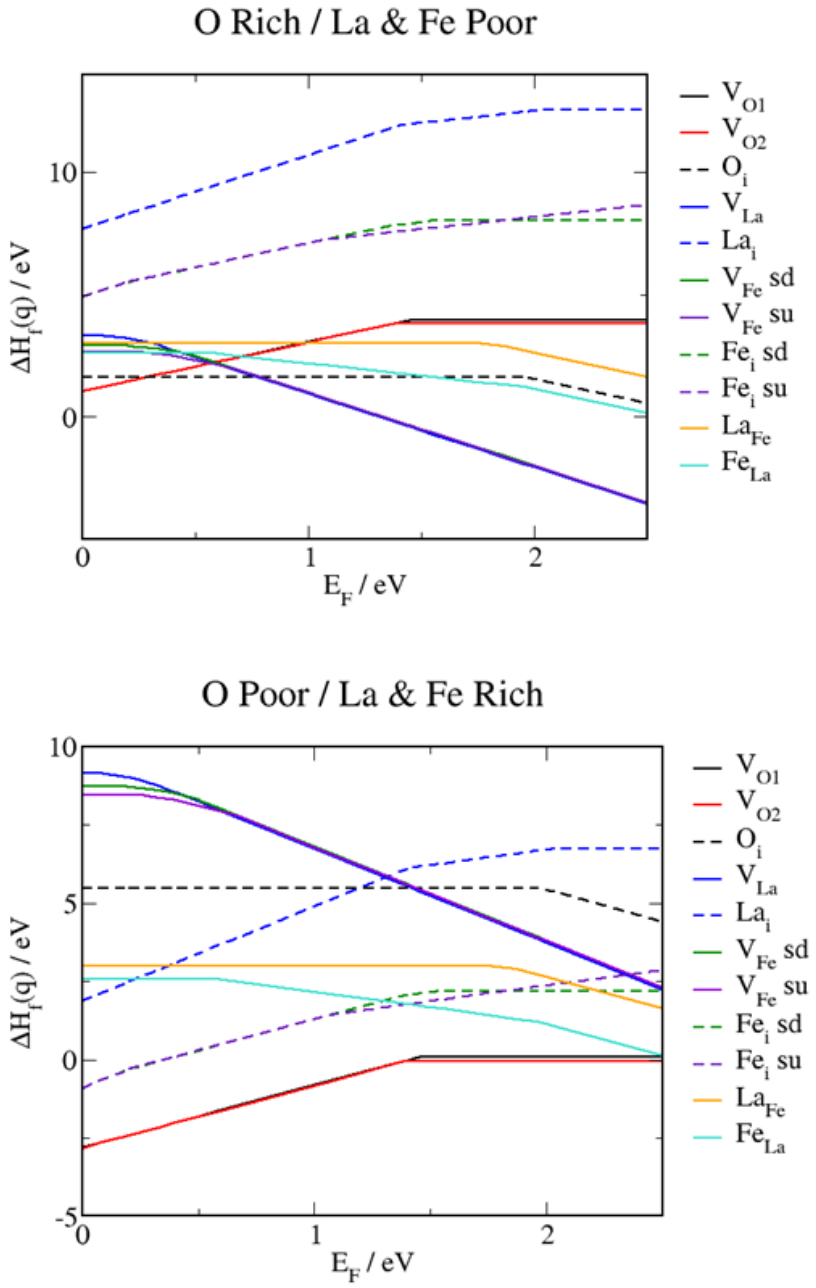


**Figure 4.7:** The change in defect energies of intrinsic defects in $LaFeO_3$ with increasing Fermi energy ($E_F$) from the VBM (0 eV) to the CBM (2.1 eV), under oxygen rich, lanthanum and iron poor and oxygen poor, lanthanum and iron rich conditions.

eV, where the neutral vacancy becomes more favourable. Experimental studies on the conductivity of $LaFeO_3$ under varying oxygen partial pressures show that *n*-type conductivity is observed under low oxygen partial pressures which originates from the formation of oxygen vacancies and a reduction of $Fe^{3+}$ to $Fe^{2+}$.[48, 49] The

negative defect formation energy of $O^{2-}$ vacancies, reported here across all values of Fermi energy, supports the observation of the dominance of $O^{2-}$ vacancies, and therefore an *n*-type conductivity scheme, under low partial pressures.

The position of the Fermi level in $LaFeO_3$, under oxygen rich and oxygen poor conditions, was calculated using SC-FERMI,[303, 304] an in-house developed code, which uses defect formation energies to calculate the concentration of defects and charge carriers and, therefore, the Fermi level that satisfies the constraint that the system be overall charge neutral. Under oxygen rich conditions, the Fermi level is at 0.87 eV, where cation vacancies become the most favourable defect in the system. For oxygen poor conditions, the Fermi level is at 1.55 eV, where the most favourable charge state of oxygen vacancies becomes neutral instead of 2-. Therefore one would expect the material to be *p*-type in O-rich and *n*-type in O-poor which corresponds well to the experimental results.

### 4.3.3 Relating Oxygen Chemical Potential to Oxygen Partial Pressure

In order to compare results of our defect studies to experimental data, it is necessary to relate our theoretical limits of oxygen chemical potential to values of oxygen chemical potential under varying temperature and partial pressure conditions, as these factors can be controlled experimentally. This was done following the method outlined by Reuter and Scheffler.[305] Firstly, the dependence of oxygen chemical potential on temperature is defined at a constant partial pressure, standard pressure $\rho^\circ$ = 1 atm with reference to a zero state; $\mu_O$(0K, $\rho^\circ$) = $\frac{1}{2}$ $E_{O_2}{}^{total}$ = 0, as follows:

$$\mu_O(T,\rho^\circ) = \frac{1}{2}[H(T,\rho^\circ,O_2) - H(0K,p^\circ,O_2)] - \frac{1}{2}T[S(T,\rho^\circ,O_2) - S(0K,\rho^\circ,O_2)] \tag{4.25}$$

$\mu_O$(T, $\rho^\circ$) was calculated from 600 to 1500 K, using data from thermochemical tables,[306] and the results are shown in Table 4.18.

Using these values, the chemical potential of oxygen at varying oxygen partial pressures at a given temperature can be calculated via:

**Table 4.18:** The variation of oxygen chemical potential with temperature at standard oxygen partial pressure.

| Temperature / K | $\mu_O$(T, $\rho^\circ$) / eV | Temperature / K | $\mu_O$(T, $\rho^\circ$) / eV |
|---|---|---|---|
| 600 | -0.6109 | 1100 | -1.2712 |
| 700 | -0.7295 | 1200 | -1.3998 |
| 800 | -0.8505 | 1300 | -1.5300 |
| 900 | -0.9738 | 1400 | -1.6617 |
| 1000 | -1.0990 | 1500 | -1.7948 |

$$\mu_O(T,\rho) = \mu_O(T,\rho^\circ) + \frac{1}{2}kTln(\frac{\rho}{\rho^\circ}) \tag{4.26}$$

From equation 4.26, we can calculate oxygen chemical potential values at varying temperatures and pressures, as demonstrated in Tables 4.19 and 4.20 respectively. When varying temperature, a partial pressure of 0.21 atm was chosen, which is a common operating partial pressure for solid oxide fuel cells,[52] and when varying pressure a temperature of 1000K was chosen as it falls into the current target operating temperature region for SOFCs: 500 to 800°C.

The oxygen chemical potential values used in the present study encompass the oxygen chemical potentials in Tables 4.19 and 4.20. Defect formation energies under operational conditions, which will lie between the two extreme oxygen partial pressure conditions we have considered, will, therefore, lie between the formation energies calculated in this work under oxygen poor and oxygen rich conditions. Interestingly, Ritzmann *et al.*[175] calculated the free energy of formation of oxygen vacancies, $\Delta G_{f,vac}$, at 700°C, without taking the chemical potential of oxygen into account. They found that the contribution from entropy is -0.95 eV ($\Delta H_{f,vac}$ at 700°C = 3.99 eV whereas $\Delta G_{f,vac}$ = 3.04 eV). Our $\mu_O$ at 1000K, at 1 atm oxygen partial pressure, is -1.00 eV, suggesting that just taking into account the change in oxygen chemical potential with temperature and pressure provides a good estimation of the entropy contribution to the free energy of vacancy formation.

**Table 4.19:** The variation in oxygen chemical potential with temperature at $\rho_{O_2}$ = 0.21 atm.

| Temperature / K | $\mu_O$(T, $\rho$) / eV | Temperature / K | $\mu_O$(T, $\rho$) / eV |
|---|---|---|---|
| 600 | -0.6512 | 1100 | -1.3450 |
| 700 | -0.7765 | 1200 | -1.4805 |
| 800 | -0.9043 | 1300 | -1.6175 |
| 900 | -1.0343 | 1400 | -1.7558 |
| 1000 | -1.1663 | 1500 | -1.8956 |

**Table 4.20:** The variation in oxygen chemical potential with oxygen partial pressure at 1000 K.

| $\rho_{O_2}$ / atm | $\mu_O$(T, $\rho$) / eV | $\rho_{O_2}$ / atm | $\mu_O$(T, $\rho$) / eV |
|---|---|---|---|
| 1 x $10^{-9}$ | -1.9919 | 1 x $10^{1}$ | -0.9998 |
| 1 x $10^{-7}$ | -1.7935 | 1 x $10^{3}$ | -0.8014 |
| 1 x $10^{-5}$ | -1.5951 | 1 x $10^{5}$ | -0.6030 |
| 1 x $10^{-3}$ | -1.3967 | 1 x $10^{7}$ | -0.4046 |
| 1 x $10^{-1}$ | -1.1983 | 1 x $10^{9}$ | -0.2062 |

#### 4.3.3.1 Stoichiometry of $LaFeO_3$ under varying oxygen partial pressures

As can be seen in Figure 4.7, oxygen vacancies will form spontaneously in $LaFeO_3$ under oxygen poor conditions, changing the stoichiometry of the material, resulting in $LaFeO_{3-\delta}$. Jacob and Ranjani[307] measured the change in stoichiometry of $LaFeO_{3-\delta}$ with oxygen partial pressure at 1473K, and if we calculate $\delta$ at varying oxygen chemical potentials, which are equivalent to the partial pressures Jacob and Ranjani[307] used, we can generate results that can be directly compared to their experimental work. They represented their results using the following equation,

$$\ln \delta = -0.1632 \ln(\frac{\rho_{O_2}}{\rho^\circ}) - 9.0532 \tag{4.27}$$

The non-stoichiometry factor, $\delta$, can be evaluated using the following expression,

$$\delta = N \exp^{-\frac{\Delta H_f(q)}{kT}} \tag{4.28}$$

where $N$ is the number of species in a formula unit; e.g. 3 for oxygen and $\Delta H_f(q)$ is

the defect formation energy in charge state $q$. A value for $\mu_O(T, \rho^\circ)$ at 1473K was interpolated from the values in Table 4.18 and used to calculated $\mu_O(T, \rho)$ at a range of partial pressures; Jacob and Ranjani used the range $\ln(\rho_{O_2}/\rho^\circ)$= -30 to 0.[307] These oxygen chemical potential values are then used in calculating $\Delta H_f(q)$, thus affecting the value of $\delta$.

Results from section 4.3.2.4 demonstrate that, as well as the oxygen chemical potential changing with oxygen partial pressure, the Fermi level, and therefore Fermi energy, in the material also changes. In Figure 4.8 we compare results from Jacob and Ranjani[307] to values of non-stoichiometry calculated using the defect formation energy of neutral oxygen vacancies - which form favourably in oxygen poor conditions - and values of non-stoichiometry calculated using the defect formation energy of oxygen vacancies taking into account the change in Fermi energy from 0.87 eV, in oxygen rich conditions, to 1.55 eV in oxygen poor.

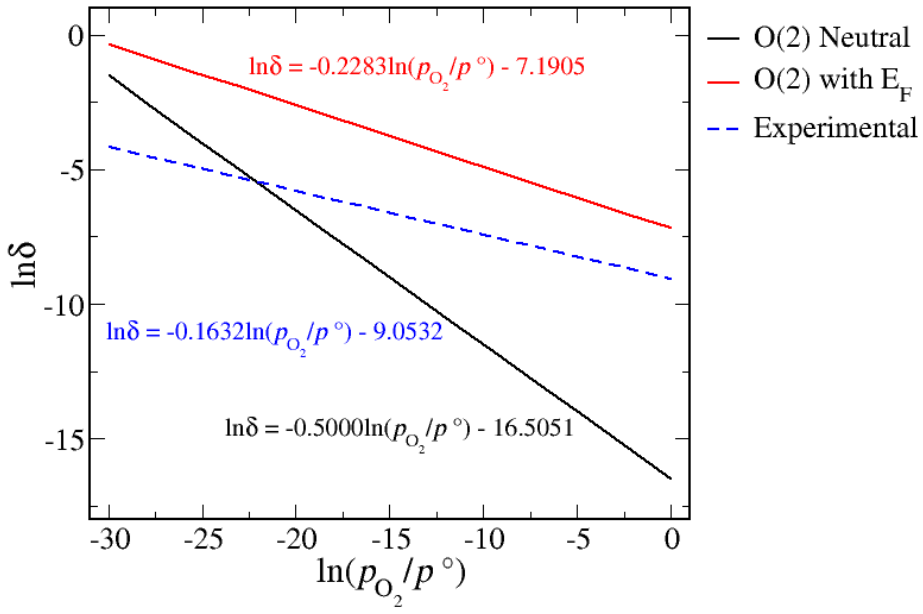


**Figure 4.8:** Dependence of the non-stoichiometry factor on oxygen partial pressure with reference to neutral oxygen vacancies and oxygen vacancies calculated at different Fermi energies, from 0.87 eV at $\ln(\rho_{O_2}/\rho^\circ)$ = 0 to 1.55 eV at $\ln(\rho_{O_2}/\rho^\circ)$ = -30. Experimental results from Jacob and Ranjani at 1473K.[307]

Comparing the fitted trend lines for each set of data to the one fitted to the experimental data of Jacob and Ranjani,[307] reveals that $\delta$ values calculated by taking

the changing Fermi level into account show a significantly better agreement with the experimental results, validating our estimated Fermi levels and the defect model presented. It is likely that the oxygen rich and oxygen poor conditions, used to calculate the Fermi levels in our work, correspond to oxygen partial pressures beyond the range used in the experimental non-stoichiometry study, which could be the cause of the difference between our calculated values and the experimental results, and a narrower range may be necessary to improve the agreement between them.

## 4.4 Summary and Conclusions

In this chapter we have calculated defect energies, formation energies and solution energies of isolated defects and disorder schemes in order to establish those which will predominate in $LaFeO_3$.

The results from interatomic potential-based calculations suggest that anti-site defects are likely to be the prevailing defect species in $LaFeO_3$, with Frenkel and Schottky type disorders having high solution energies in all cases. However, results from *ab initio*-based calculations suggest that Schottky type disorder does play an important role in the defect chemistry of $LaFeO_3$. These results are in line with experimental results, thus suggesting that the *ab initio* treatment of $LaFeO_3$ is needed in this case to gain accurate results. However, the source of this over-estimation of Schottky-type disorder has been successfully identified as resulting from the the over-estimation of the formation energy of $LaFeO_3$. If this is taken into account in future work, interatomic potential calculations can provide useful insight.

The results presented in this chapter suggest that under oxygen rich conditions, cation vacancies are the most favoured defect and will form in significant enough concentrations as to contribute to the conductivity in this material, particularly $La^{3+}$ vacancies. These cation vacancies are compensated by holes, which enable *p*-type conductivity. Under oxygen poor conditions oxygen vacancies dominate, a promising results as the migration of oxygen vacancies through $LaFeO_3$ is vital for increased activity as a SOFC cathode material. We found that this model - which establishes the value of the Fermi level in $LaFeO_3$ under each condition - is verified

by experimental studies conducted by Jacob and Ranjani[307].

Establishing this defect chemistry of $LaFeO_3$ is an essential start, with both ionic and electronic conductivity promoted by the species present. However, both defective species, but particularly oxygen vacancies, need to be promoted further for increased catalytic activity. Doping perovskites is an established way to do this, and this will be discussed in Chapter 6. The next chapter will cover oxygen ion migration in stoichiometric $LaFeO_3$.

# Chapter 5

# Oxide Ion Migration

## 5.1 Introduction

In Chapter 4, we established that oxygen vacancies will form in $LaFeO_3$, particularly under oxygen poor conditions. However, to enhance the ionic conductivity of the material, the $O^{2-}$ ions need to be able to migrate through $LaFeO_3$ at a relatively small energetic cost. Therefore, the next step is to investigate possible oxide ion migration pathways and the activation energies, associated with each, knowledge of which can help establish methods to optimise oxide ion migration further. In this respect, modelling plays a vital role as it allows us to explore these process at the atomic level.

Previous computational work on oxide ion migration in $LaFeO_3$ has shown that the energy barrier is low for oxide ion migration. Using DFT+$U$, Ritzmann *et al.*[175] calculated an activation energy of 0.79 eV, while Mastrikov *et al.*[119] calculated a value of 0.75 eV. Both studies used cubic $LaFeO_3$ and hence only reported one activation energy as all oxygen sites are equivalent in cubic $LaFeO_3$. Work on orthorhombic $LaFeO_3$ has been carried out by Jones and Islam[27] who calculated the barrier of three pathways using interatomic potential-based methods. We will compare their results to the work presented here throughout the chapter.

It is generally agreed that oxide ion diffusion in perovskite-type materials occurs via a vacancy mediated mechanism, partly due to the formation of interstitials being unfavourable in the tightly packed structure of these materials, and work by

Ishigaki *et al.*[16] and Mizusaki *et al.*[48] helped establish that this was the case. If the diffusion mechanism is related to oxygen defects, i.e. a oxygen vacancy mediated process, then the self-diffusion coefficient should be proportional to the concentration of point defects. Ishigaki established that the self diffusion coefficient, $D_O^*$, of $LaFeO_3$ was inversely proportional to the partial pressure of oxygen: $D_O^* \propto \rho_{O_2}^{-0.58}$, which when combined with the result reported by Mizusaki that the concentration of oxygen vacancies is also inversely proportional to oxygen partial pressure: $[V_O^{\bullet\bullet}] \propto \rho_{O_2}^{-0.5}$, suggests that oxide ion diffusion occurs via a vacancy mediated mechanism.

Due to the two inequivalent oxygen sites in orthorhombic $LaFeO_3$, shown in Figure 5.1, there are three possible pathways for oxide ion migration, assuming the conduction is mediated by the presence of oxygen vacancies; O1 to O1, O1 to O2 and O2 to O2, also shown in Figure 5.1 by the arrows labelled 1, 2 and 3 respectively. Activation energies of all three pathways have been calculated, using both interatomic potential-based methods and DFT+$U$, as done for intrinsic defects in Chapter 4. First, the methods used for each level of theory will be outlined and then the results discussed. The chapter will conclude by discussing which pathways are most favourable for oxide ion migration in $LaFeO_3$.

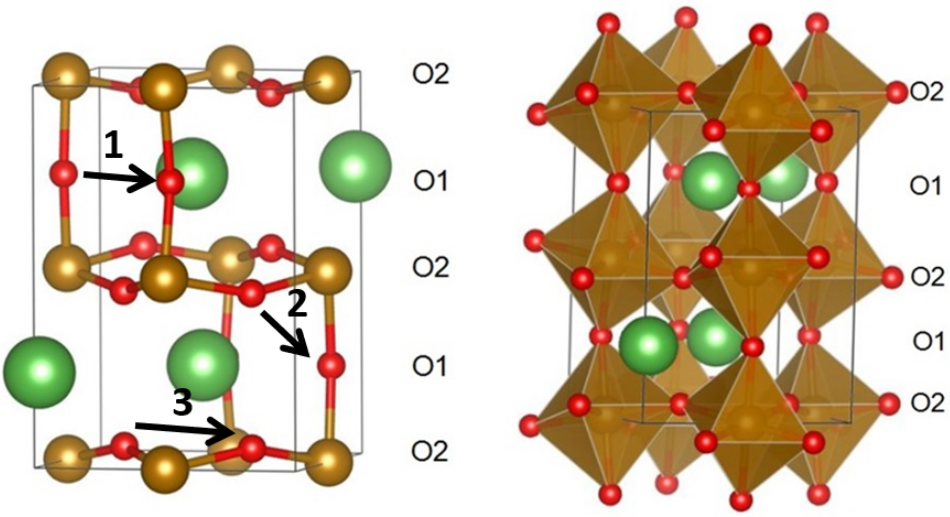


**Figure 5.1:** Orthorhombic $LaFeO_3$ showing the inequivalent oxygens sites (labelled O1 and O2) and the three potential pathways investigated in this chapter, denoted using black arrows: O1 to O1 (1), O1 to O2 (2) and O2 to O2 (3).

## 5.2 Methods

Both interatomic potentials and DFT-based methods were used to investigate oxide ion migration; here the methods used for each level of theory will be outlined. Interatomic potentials were used initially to establish a pathway, then the start, end and saddle point of each pathway were optimised using DFT+$U$ to find a DFT-based migration barrier. Finally, the Nudged Elastic Band (NEB) method was implemented in DFT+$U$ to get a DFT-based view of the migration pathway as well as the migration barrier. The interatomic potentials-based approach will be outlined first, followed by the DFT-based methods.

### 5.2.1 Interatomic Potentials

The interatomic potentials-based calculations were carried out using the potentials given in Table 3.1 (Chapter 3), the same as those used for the defect calculations in Chapter 4. For each of the three pathways, five points, at equal intervals, were chosen along a straight line connecting the two oxygen sites. Previous ion migration studies on perovskite-type oxides have shown that ions can travel via a curved path.[27, 60, 173, 174, 308] Therefore, at each chosen position along the straight line, the energy of the migrating oxygen species was calculated at a range of points on a $10\times10$ two-dimensional grid around the original position, in a perpendicular direction to the oxide ion path; further details are given in Appendix E. Performing multiple calculations at each position allowed us to find the lowest energy point for the oxide ion perpendicular to each site along the initial, linear pathway, thus allowing a curved pathway to form. Each energy calculation was carried out using the Mott-Littleton methodology,[274] using a region 1 size of 10 Å and a region 2 size of 22 Å.

It was assumed that the saddle point of the migration pathway would be situated between the two highest energy points along the path. Once these two sites had been identified for each pathway, the configuration with the oxide ion at the halfway point between the two sites was optimised and the saddle point found using the rational function optimisation (RFO) method of minimisation. This minimisation method uses Newton-Raphson techniques to locate a saddle point on the potential energy

surface by following an eigenvalue towards a local stationary point. The Hessian matrix is diagonalised to find the appropriate eigenvalue to follow, then small steps are used in the direction identified to ensure convergence on a saddle point.[309] Throughout the minimisation, the migrating ion is relaxed as well as the crystal structure in order to obtain the correct energy of the saddle point.

The centre of the Mott-Littleton[274] defect calculation was kept constant for each ion migration pathway, as the middle point between the two oxygen vacancy sites, thus keeping systematic errors to a minimum. The energy at the saddle point, along with the lowest oxygen vacancy formation energy, was then used to calculate the activation energy. All calculations were carried out using the GULP code.[291]

### 5.2.2 DFT+*U*

Using the pathways identified with interatomic potentials, the activation energies were calculated using DFT+*U*. The position of the oxide ion at the saddle point of each pathway was taken from the static lattice calculations and used to position the oxide ion in an 80 atom supercell - the same supercell used for modelling defects, see Chapter 3 for further details. All other ions in the supercell were relaxed and the migrating ion, at the saddle point, kept fixed. The energies of oxygen vacancies at the beginning and end of the migration pathway were calculated and the activation energy was evaluated as the difference between the supercell with the saddle point oxide ion and the supercell containing an oxygen vacancy. As with the previous method, where the energies of the oxygen vacancies at the beginning and end of the migrating pathway differed, the lowest energy oxygen vacancy was used for calculating the migration barrier.

The PBE functional was used with a *U*-value of 7 eV used on the $Fe^{3+}$ ions for all calculations, in line with the defect calculations carried out in Chapter 4.

#### 5.2.2.1 Nudged Elastic Band

The Nudged Elastic Band (NEB) approach constructs a pathway of images, connected by harmonic springs, which are then relaxed to find the minimum energy pathway (MEP).[310] The minimisation process involves zeroing the forces acting

on each image. These forces can be split into two categories; forces from the springs which attach each image to its adjacent images and the forces from the potential energy of the system, which act on the tangent of each image.[310] Each of these forces can again be split into two components, the force acting perpendicular to the pathway and the force acting parallel to the pathway. However, not all of these forces are included when minimising the images, as some are counter-productive to the process of finding the MEP. Firstly, the perpendicular component of the spring force, which ensures each image is collinear with its neighbouring images, can pull the string of images (i.e. the band) away from the MEP if the MEP is curved. This force is, therefore, zeroed to allow curved pathways to minimise properly. Secondly the parallel component of the force from the potential energy is also zeroed. This force pulls the images towards the reactants or products, depending on which side of the saddle point the image is, leading to a higher number of points closer to the start and end points of the pathway, and a smaller number, and thus lower resolution, at the saddle point, which results in a less accurate energy for the transition state. Zeroing this force leads to a more accurate approximation to the saddle point.[310] The zeroing of forces that compete with the convergence of the pathway is known as a force projection scheme, and its use in the NEB method makes this approach particularly efficient for finding MEPs.[311] Therefore, the total force acting on each image is the sum of the parallel component of the spring force and the perpendicular component of the force from the potential energy:[312]

$$\mathbf{F}_i^{NEB} = \mathbf{F}_i^{V_{per}} + \mathbf{F}_i^{S||} \tag{5.1}$$

where $\mathbf{F}_i^{NEB}$ is the total force acting on image $i$ and $\mathbf{F}^{V_{per}}$ and $\mathbf{F}^{S||}$ refer to the perpendicular component of the potential energy force and the parallel component of the spring energy force, respectively. The minimisation to the MEP then follows by adjusting the position of each image until the total force acting on each image is zero. A variety of energy minimisers can be utilised to minimise the pathway including steepest descent, conjugate gradient and BFGS-based methods.[312] In our work the DIIS method, discussed in Chapter 2, has been used.

Various adjustments to the NEB approach have been suggested and implemented. A popular example is the climbing image-NEB (CI-NEB).[312] In this method the highest energy image does not have any spring forces acting on it, and is therefore able to climb to the saddle point of the pathway via a reflection of the perpendicular potential energy force. Using this adjustment to the NEB approach means an accurate saddle point and the MEP of a reaction can be found with only one calculation, instead of finding the pathway and minimising the highest energy image to the saddle point in two separate steps.[312]

## 5.3 Results

The results from both the interatomic potentials and DFT+$U$ studies of oxide ion migration are presented in the following section. The results from the interatomic potentials-based study will be presented first, followed by the DFT+$U$ relaxation of the saddle point identified for each pathway during the interatomic potentials study, and their associated oxygen vacancies. Finally the Nudged Elastic Band results will be discussed, including a comparison with the pathway found using interatomic potentials and the activation energies calculated using the other two methods.

### 5.3.1 Interatomic potentials

#### 5.3.1.1 Pathway 1: O2 to O2

Figure 5.2 shows the pathway of the migrating oxide ion and the defect energy difference for seven of the eight points along the pathway (start, end and saddle points, as well as the five points along the pathway, the point closest to the saddle point has been removed for clarity), compared to the defect energy of an oxygen vacancy which is used as the zero point. The activation energy was calculated as the difference between the energy of the saddle point and the energy of the system with an oxygen vacancy, i.e. the start or end point.

The activation energy calculated for this pathway is 0.50 eV, which is identical to the activation energy calculated previously by Jones and Islam for the O2 to O2 pathway.[27] Although they also used interatomic potentials, as have been used here, there are differences in the methods used to establish the migration pathway.

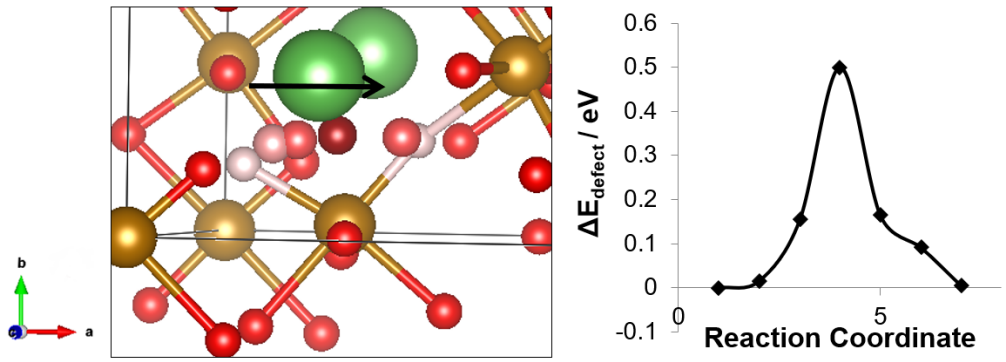


**Figure 5.2:** The migration pathway (left) and energy barrier (right) for an oxide ion moving between two O2 oxygen sites. In the image of the pathway, the oxygen sites at the start and end of the pathway are shown in pale pink, while the relaxed position of each of the five points are shown in shades of red, getting darker towards the saddle point - which is shown in dark red. Two of the points have been removed from this image for clarity; a table of coordinates for each point, including those excluded from the image, is provided in Appendix E. The black arrow indicates the direction of migration. For the energy barrier plot, the defect energy of an oxygen vacancy is taken as the zero point and the difference between this value and the energies of the other points is used on the y-axis, a line has been interpolated between each point to estimate how the energy changes along the pathway. Each point along the pathway represents a reaction coordinate from 1 to 7; 1 and 7 are the oxygen vacancies at the beginning and end of the pathway.

In our method we have explored a 2D space around each point to ensure the migrating ion was in the most favourable position at that point in the pathway. However, Jones and Islam[27] calculated the energy at specific points in the pathway - without exploring the area around the chosen point to ensure that it was in a favourable position. Figure 5.2 shows that an oxide ion migrating via the O2 to O2 pathway in $LaFeO_3$ follows a curved pathway, as was also found by Jones and Islam,[27] and has been observed in a number of other perovskite oxides.[173, 174, 313]

#### 5.3.1.2 Pathway 2: O1 to O2

Figure 5.3 shows the pathway and energy barrier calculated for an oxide ion travelling between an O1 and an O2 oxygen site. As with the previous pathway, seven points are shown: the initial and final position of the oxygen vacancy, four of the five optimised points along the pathway, the point closest to the saddle point has been removed, and the saddle point. For this pathway, the initial and final energies are different, as there is a difference in the defect energies of the O1 and O2 oxy-

gen vacancies; the lowest of these energies, the O2 oxygen vacancy, was used for calculating the activation energy.

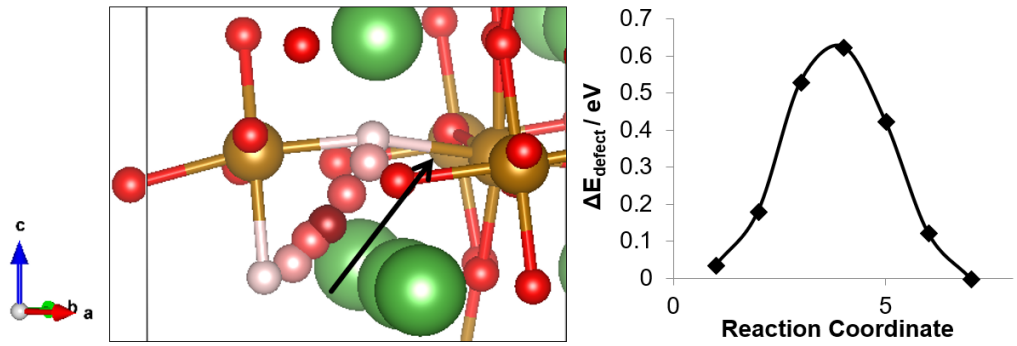


**Figure 5.3:** The migration pathway (left) and energy barrier (right) for an oxide ion moving from an O1 to an O2 oxygen site. In the image of the pathway, the oxygen sites at the start and end of the pathway are shown in pale pink, while the position at each of the five points are shown in shades of red, getting darker towards the saddle point - which is shown in dark red. The point closest to the saddle point has been removed from both the image of the pathway and the energy barrier plot; the list of coordinates for all points is provided in Appendix E. The black arrow indicates the direction of migration. For the energy barrier plot, the defect energy of the O2 oxygen vacancy is taken as the zero point and the energy of the other points displayed as an energy difference from the O2 vacancy energy. A line has been interpolated between each point to estimate how the energy changes along the pathway. Each point in the pathway represents a reaction coordinate from 1 to 7; 1 and 7 are the oxygen vacancies at the beginning and end of the pathway.

The activation energy calculated from this pathway is 0.63 eV. Jones and Islam reported a value 0.19 eV lower than ours.[27] As mentioned previously, the method used in this work differs from the method used by Jones and Islam. However, the similarity in the activation energy of the previous pathway suggests that the origin of the discrepancy could be due to a difference in defect energies of the oxygen vacancies - the initial and final points of the pathway. As with the O2 to O2 pathway, the oxide ion follows a curved pathway when migrating from an O1 site to an O2 site, agreeing with the results from Jones and Islam.[27] The similarity between the pathways found in both studies is further evidence that the disagreement between the activation energies is due to the oxygen vacancy energy and not differences between the pathways.

### 5.3.1.3 Pathway 3: O1 to O1

Figure 5.4 shows the pathway and energy barrier calculated for an oxide ion travelling between two O1 oxygen sites in $LaFeO_3$. Four of the five optimised points along the pathway, the point closest to the saddle point has been removed, and the relaxed saddle point are shown in relation to the start and end positions of the oxide ion.

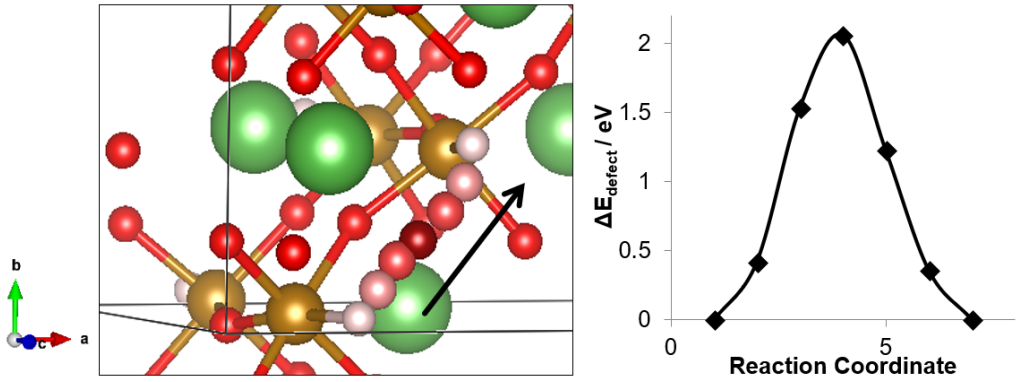


**Figure 5.4:** The migration pathway (left) and energy barrier (right) for an oxide ion moving between two O1 oxygen sites. In the image of the pathway, the oxygen sites at the start and end of the pathway are shown in pale pink, while the position at each of the five points are shown in shades of red, getting darker towards the saddle point - which is shown in dark red. The point closest to the saddle point has been removed from the migration pathway image and the energy barrier plot; the list of coordinates for all points is provided in Appendix E. The black arrow indicates the direction of migration. For the energy barrier plot, the defect energy of an oxygen vacancy is taken as the zero point and the energy of all other points presented as a difference to this energy. A line has been interpolated between each point to estimate how the energy changes along the pathway, between each calculated point. Each point in the pathway represents a reaction coordinate from 1 to 7; 1 and 7 are the oxygen vacancies at the beginning and end of the pathway.

The activation energy calculated from this plot is 2.06 eV, considerably higher than the other two pathways. This value is supported well by previously calculations performed by Jones and Islam who calculated an activation energy of 2.13 eV for this pathway in $LaFeO_3$.[27] From Figure 5.4 we see that unlike the O2 to O2 and O1 to O2 pathways, the O1 to O1 pathway is straight. A straight pathway was also found by Jones and Islam, and could contribute, along with the larger distance between two O1 oxygen sites compared to between the oxygen sites of the other two pathways, to the larger activation energy. This large activation energy, compared

with those of the other two potential pathways, suggests that migration between two O1 oxygen sites is unlike to occur in orthorhombic $LaFeO_3$.

The similarity between the activation energy for the O1 to O1 pathway in this work with that from Jones and Islam confirms that the mismatch in values for the O1 to O2 pathway are likely due to difference between calculated formation energies of the two inequivalent oxygen vacancies in $LaFeO_3$.

#### 5.3.1.4 DFT+*U* relaxation of the Energy Barriers

Having obtained the saddle points for each pathway using the method described in Section 5.2.1, the position of the oxide ion at the saddle point, and the associated start and end point oxygen vacancies, were converted into Cartesian coordinates and placed in the 80 atom, $2\times2\times1$ $LaFeO_3$ supercell used in previous defect calculations, see Chapter 4. The energy of the supercell with the saddle point and two oxygen vacancies was then calculated, along with the defect energy of each of the oxygen vacancies in this supercell.

All ions in the supercell were allowed to relax in all energy calculations, except the oxide ion at the saddle point whose position was fixed. Allowing the oxide ion at the saddle point to relax was tested, however the ion relaxed into one of the oxygen vacancy sites in all trial calculations, instead of relaxing into a position along the migration pathway, making it necessary to keep its position fixed while relaxing the supercell around it in all energy barrier calculations.

The activation energy was calculated as the difference between the energy of the supercell containing two relaxed oxygen vacancies and the fixed oxide ion at the saddle point, and the supercell containing a single oxygen vacancy. Where the defect energy of the start and end oxygen vacancy positions differed, the lowest energy vacancy was used. The result of this calculation for each pathway is shown in Table 5.1 along with the interatomic potential results for comparison.

Similar results are seen in the DFT+*U* study compared to the interatomic potentials study; the O2 to O2 and O1 to O2 pathways are low in energy, while the O1 to O1 pathway has a high activation energy. Further comparison between the different methods will be discussed along with the Nudged Elastic Band results in the

**Table 5.1:** The activation energies of oxide ion migration along the three possible pathways in $LaFeO_3$ calculated using interatomic potentials and DFT+*U*.

| Pathways | Activation Energy / eV | |
|---|---|---|
| | Interatomic Potentials | DFT+*U* |
| O1-O1 | 2.06 | 1.87 |
| O1-O2 | 0.63 | 0.66 |
| O2-O2 | 0.50 | 0.58 |

following section.

Due to the difficulties encountered in relaxing the saddle point configuration using this method, the Nudged Elastic Band method was used to implement a fully relaxed DFT+*U* study of the energy barriers. This method also provided us with a DFT-based pathway to compare with those found using interatomic potentials.

Compared to the methods used so far in the oxide ion migration study, the NEB approach has a high computational expense associated with it. The O1 to O1 pathway, which has a high activation energy compared to the other two pathways, is unlikely to play a role in oxide ion migration in $LaFeO_3$ and therefore, was not investigated using this method.

### 5.3.2 Nudged Elastic Band

In the following section the results from studying the two most favourable pathways using the Nudged Elastic Band (NEB) methodology are presented. The Climbing Image Nudged Elastic Band (CI-NEB) method has been implemented, in order to find the optimised position of the saddle point while also optimising all images along the pathway. In all calculations, 5 images have been used with a spring constant of -5 while the SCF convergence criteria have been tightened, compared to previous DFT+*U* calculations, to $1\times10^{-8}$ eV per step.

#### 5.3.2.1 Pathway 1: O2 to O2

Figure 5.5 shows the optimised pathway (left) and energy barrier (right) of an oxide ion migrating via the O2 to O2 pathway. The zero point on the energy barrier plot refers to the defect energy of an O2 oxygen vacancy in orthorhombic $LaFeO_3$.

Comparing the pathway and energy migration plot resulting from the NEB study of

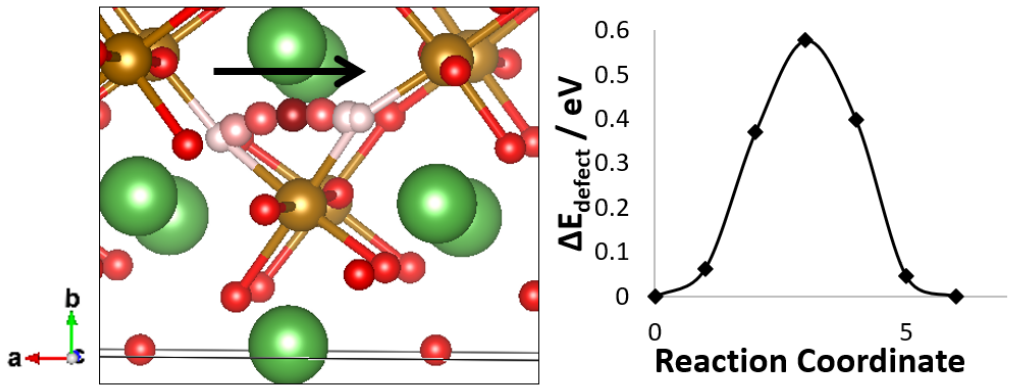


**Figure 5.5:** The migration pathway (left) and energy barrier (right) for an oxide ion moving from one O2 oxygen site to another. In the image of the pathway, the oxygen lattice sites, that the ion is moving between, are shown in pale pink, while the relaxed position of each of the five images are shown in shades of red, getting darker towards the saddle point, which is shown in dark red. The optimised coordinates of each image are given in Appendix F. The black arrow indicates the direction of migration. For the energy barrier plot, the defect energy of an oxygen vacancy is taken as the zero point with the energies of each image presented as an energy difference to this energy. A line has been interpolated between each point on the plot to estimate how the energy changes along the pathway. Each image, including the start and end points, in the pathway represents a reaction coordinate from 1 to 7; 1 and 7 are the oxygen vacancies at the beginning and end of the pathway.

the O2 to O2 pathway, to those from the interatomic potentials study of this pathway, we first see that the position of the images are spaced more evenly along the migration path, clarifying the trajectory of the pathway and resulting in a smoother energy barrier plot. The activation energy for this pathway is 0.58 eV, matching well with the previously calculated DFT+$U$ activation energy. Table 5.2 shows the activation energy calculated for each pathway using the three different methods utilised in this work, along with results from Jones and Islam.[27] We see that for the O2 to O2 pathway the activation energy calculated from the NEB study is identical to the value calculated from the previous DFT+$U$ study, suggesting that the original optimisation of the pathway with interatomic potentials produced an accurate MEP. Ishigaki *et al.*[16] determined the activation energy of oxide ion migration in $LaFeO_3$ using gas-solid isotopic exchange techniques and found a value of 0.77 eV; only one activation energy was reported as their work was based on cubic $LaFeO_3$ in which all oxygen sites are equivalent. The energy barrier found for the O2 to O2 pathway is higher and therefore, closer to the experimental value when calculated

using the DFT+$U$ and NEB approaches compared to the interatomic potentials-based method. However, the differences between the energy barrier calculated using the interatomic potentials-based approach and the DFT+$U$-based approaches are minor, therefore all three approaches are applicable to studying this pathway.

**Table 5.2:** The activation energies of oxide ion migration along the three possible pathways in $LaFeO_3$ calculated using interatomic potentials, DFT+$U$ and NEB, along with computational results reported previously by Jones and Islam[27].

| Pathways | Activation Energy / eV | | | |
|---|---|---|---|---|
| | Interatomic Potentials | DFT+$U$ | NEB | Jones *et al.* |
| O1-O1 | 2.06 | 1.87 | - | 2.13 |
| O1-O2 | 0.63 | 0.66 | 0.65 | 0.44 |
| O2-O2 | 0.50 | 0.58 | 0.58 | 0.50 |

#### 5.3.2.2 Pathway 2: O1 to O2

Figure 5.6 shows the optimised pathway (left) and energy barrier (right) of an oxide ion migrating via the O1 to O2 pathway. As with the interatomic potentials study, the lowest oxygen vacancy energy; the O2 oxygen vacancy, was chosen as the zero point in the energy barrier calculation.

The activation energy calculated for this pathway using the NEB approach is 0.65 eV. This value agrees well with those calculated via the other methods considered in this work especially the DFT+$U$ approach, which, as with the previous pathway, suggests that the interatomic potentials method provided an accurate saddle point. The activation energy for this pathway is the closest to the experimental value reported by Ishigaki *et al.*[16] (0.77 eV) with the DFT+$U$ methodology producing an activation energy in closest agreement - although the differences between all three values are negligible.

## 5.4 Summary and Conclusion

Multiple techniques have been employed to study oxide ion migration in orthorhombic $LaFeO_3$. Three pathways were initially considered: O1 to O1, O1 to O2 and O2 to O2, taking into account the two inequivalent oxygen sites in orthorhombic $LaFeO_3$.

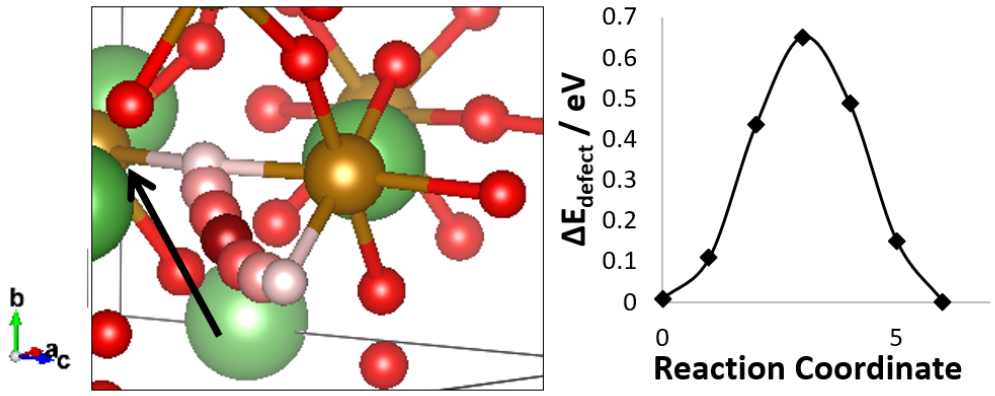


**Figure 5.6:** The migration pathway (left) and energy barrier (right) for an oxide ion moving from an O1 oxygen site to an O2 site. In the image of the pathway, the oxygen lattice sites, that the ion is moving between, are shown in pale pink, while the relaxed position of each of the five images are shown in shades of red, getting darker towards the saddle point, which is shown in dark red. The optimised coordinates of each image are given in Appendix F. The black arrow indicates the direction of migration. For the energy barrier plot, the defect energy of an O2 oxygen vacancy (point 7) is taken as the zero point and the energies of the other images are presented as an energy difference. A line has been interpolated between each point on the plot to estimate how the energy changes along the pathway. Each image, including the start and end points, in the pathway represents a reaction coordinate from 1 to 7; 1 and 7 are the oxygen vacancies at the beginning and end of the pathway.

The interatomic potential results show that both the O1 to O2 and O2 to O2 pathways are curved, as has been observed previously in $LaFeO_3$,[27] and other perovskite-type materials.[173, 174, 313] These two pathways both have low activation energies, 0.63 and 0.50 eV respectively; however, the energy barrier calculated for the O1 to O2 pathway calculated in this work is significantly higher than that reported by Jones and Islam.[27] We have found that the O2 to O2 pathway is the lowest in energy of those we have considered, in contrast to Jones and Islam, who found that the O1 to O2 pathway had the lowest energy. We attribute the disagreement to a difference in the defect energies of the oxygen vacancies at the beginning and end of the pathway. The agreement we have found for the O1 to O2 migration barrier among the different methods employed in this work suggests that the activation energy we have calculated is accurate and reliable.

Good agreement has been found for all three pathways across the different methods investigated in this work leading to the conclusion that oxide ions will migrate via the O1 to O2 and O2 to O2 pathways in orthorhombic $LaFeO_3$. DFT+$U$ and

NEB results for the energy barrier found a slightly increased value for these two pathways, bringing them in closer agreement with the experimental value of 0.77 eV reported by Ishigaki *et al.*[16] The similarity in results from the two methodologies suggests that steric factors govern the oxide ion migration process, rather than electronic factors which are not included explicitly in interatomic potential-based calculations.

The high energy associated with the O1 to O1 pathway is likely the result of the O1 oxide ions being opposite sides of the $FeO_6$ octahedra while the pathway between two O1 ions on different octahedra is long and involves passing between two large lanthanum ions. Both the O2 to O2 and O1 to O2 pathways involve migrating to a neighbouring position on the $FeO_6$ octahedra and therefore are much lower in energy.

This work has successfully shown that oxide ion migration is a favourable process in $LaFeO_3$, a vital property for solid oxide fuel cell cathode materials, in agreement with experimental results.

Oxide ion migration depends proportionally on both the vacancy diffusion coefficient and the concentration of oxygen vacancies present in the material. In Chapter 4 we established that oxygen vacancies will form favourably in $LaFeO_3$ and will, therefore, be present in a significant concentration. The vacancy diffusion coefficients of $LaFeO_3$ were determined by Ishigaki *et al.*[16] by depth profile measurements, for temperatures between 900 and 1100°C; these are shown in Table 5.3.

**Table 5.3:** The vacancy diffusion coefficients of $LaFeO_3$ determined by Ishigaki *et al.*[16] by depth profile measurements.

| Temperature / °C | $D_V$ / $cm^2$ $sec^{-1}$ |
|---|---|
| 900 | $4.02 \times 10^{-6}$ |
| 950 | $3.64 \times 10^{-6}$ |
| 1000 | $7.44 \times 10^{-6}$ |
| 1050 | $9.06 \times 10^{-6}$ |
| 1100 | $1.07 \times 10^{-5}$ |

The reported temperature range is above the temperature range of interested for IT-SOFC applications; however from the values listed is Table 5.3 we can estimate a

value for the vacancy diffusion coefficient in the desired intermediate temperature range, based on a fitted linear relationship, see Appendix G. For 700°C we estimate a $D_V$ value of $2.0 \times 10^{-6}$ $cm^2$ $sec^{-1}$, a value which is four times smaller than the vacancy diffusion coefficients at current SOFC operating temperatures (between 800 and 1000°C). It is, therefore, essential that we maximise the concentration of vacancies within $LaFeO_3$, without compromising its stability, in order to increase the oxide ion migration at intermediate temperatures. The following chapter explores doping $LaFeO_3$, which is widely used for enhancing the oxygen vacancy concentration and improving oxide ion conductivity in $LaFeO_3$ and related ion conductors. For example, doping $LaGaO_3$, an orthorhombic perovskite material like $LaFeO_3$, with strontium and magnesium improves the oxide ion conductivity both through introducing oxygen vacancies and by decreasing the tilt of the $GaO_6$ octahedra, allowing for a more open pathway between oxygen sites.[58, 59] Both strontium and magnesium, along with other alkali earth metals and a range of transition metals are considered as dopants for $LaFeO_3$ in the following chapter.

# Chapter 6

# Dopants

## 6.1 Introduction

As discussed in Chapter 1, doped $LaFeO_3$-based materials, such as (La,Sr)$FeO_3$ and La(Fe,Co)$O_3$, show enhanced ionic and electronic conductivity properties compared to the pure, stoichiometric material. The presence of dopants, which are often divalent or multi-valent species, within the lattice results in the formation of defect species in compensation for the charge difference between the dopant and the trivalent lanthanum or iron cation it replaces. Compensating species, including oxygen vacancies and holes, can contribute to the ionic and electronic conductivity respectively.

Previous research into doped $LaFeO_3$, and related materials, has focused on the concentration of dopants required to boost conductivities, before first establishing the most appropriate dopants for the site and material in question.[175, 179]

Work on A-site doped $LaFeO_3$ has predominantly focused on strontium while cobalt is the most common B-site dopant considered.[55, 90, 112, 166, 175, 183, 187, 191–193] There are few studies that have considered alternatives to these dopants,[179, 180, 184, 185, 188, 195–197] and even less have carried out a wide ranging comparative investigation. Computational work that has considered a range of dopants has been carried out using interatomic potential-based methods[27] which, although provides useful insights, can encounter problems when modelling transition metals, as is needed for both bulk $LaFeO_3$ and if we are to consider a wide range of dopants

for this material.

In the present chapter we will assess a range of dopants, in both the A- and B-site of $LaFeO_3$, in order to find the most appropriate for each site for promoting ionic and electronic conductivity. We use both interatomic potential-based methods and Density Functional theory (DFT) to calculate the solution energies for incorporating each divalent dopant into the lattice and binding energies of the dopants to charge compensating species. Using these two factors we determine the most appropriate dopants for each site. Two compensation schemes are considered: compensating via oxygen vacancies, in which two divalent dopants are compensated by one doubly charged oxygen vacancy, and hole compensation which give a one to one ratio.

Our aim is to perform a thorough study of a large range of possible dopants in $LaFeO_3$; therefore we consider alkali earth and transition metal dopants for the A-site. The alkali earth dopants magnesium, calcium, strontium and barium, are well studied A-site dopants in perovskite oxide materials, of the form $A^{III}B^{III}O_3$ such as $LaFeO_3$, whereas transition metals; manganese, iron, cobalt, nickel and copper, are considered as typical B-site dopants, in both cases due to the similarities in ionic radii between the dopants and the host cations. For the B-site we considered transition metals; manganese, cobalt, nickel and copper, as well as magnesium, the smallest alkali earth metal of those considered in this study.

In this chapter, the methods used to calculate solution and binding energies will be presented first, followed by the results from the interatmomic potential and DFT study, which are presented separately. The results from the two methods will be compared before summarising the main results and conclusions.

## 6.2 Modelling Doped Systems

Solution energies and binding energies of divalent dopants in the A- and B-site of $LaFeO_3$ have been calculated using both interatomic potentials-based and DFT methods, but there are a number of differences between the two studies. First, a smaller set of dopants have been considered for the interatomic potentials study: the alkali earth metals; Mg, Ca, Sr and Ba, for the A-site and the transition met-

als; Mn, Co, Ni and Cu, on the B-site. We did not consider A-site transition metal dopants owing to the difficulty of modelling transition metals accurately at this level of theory, which would be particularly prominent in an atypical environment, such as the 12-coordinate site of lanthanum. Secondly, as with the DFT study of intrinsic defects, two formation conditions have been considered when calculating the solution energies of dopants with DFT: anion rich and anion poor, whereas only anion rich conditions are considered in the interatomic potential study, which represents the most realistic solid oxide fuel cell operating conditions. Finally, as with the defect study, the Mott-Littleton methodology[274] has been used to calculate dopant energies in the interatomic potentials study, whereas the supercell method is used for the DFT calculations.

### 6.2.1 Interatomic Potentials

In addition to the potentials used to model bulk $LaFeO_3$, given in Chapter 3 Table 3.1, potentials that describe interactions involving each of the dopant species are required. As noted, the dopants modelled using interatomic potential-based methods are the alkali earth metals: magnesium, calcium, strontium and barium on the A-site and the transition metals: manganese, cobalt, nickel and copper on the B-site. Each dopant is assumed to be in its divalent charge state, we use the potentials shown in Table 6.1, taken from reference [28] and [29], which model interatomic interactions via a Buckingham potential (see Chapter 2 equation 2.76).

#### 6.2.1.1 Calculating Solution Energies

The solution energy ($E_{sol}$) to incorporate a dopant into $LaFeO_3$ was calculated using the following equations, taking into account compensation by oxygen vacancies and holes, respectively:

$$E_{sol} = 2E^{dopant} + E_{V_O^{\bullet\bullet}} + E_{bulk}(A_2O_3) - 2E_{bulk}(MO) \tag{6.1}$$

$$E_{sol} = 2E^{dopant} + 2E_{h^\bullet} + E_{bulk}(A_2O_3) - (\frac{1}{2}O_{dis} + E_O^1 + E_O^2) - 2E_{bulk}(MO) \tag{6.2}$$

**Table 6.1:** Buckingham potential parameters (A, P and C), shell charge (Y) and spring constant (k) used for each dopant species. [a] Ref[28] [b]Ref[29].

| Short Range Potential Parameters | | | | Shell Model | |
|---|---|---|---|---|---|
| Interaction | A / eV | P / Å$^6$ | C / eV Å$^6$ | Y / e | k / eV Å$^{-2}$ |
| $Mg^{2+}$••••$O^{2-a}$ | 1428.50 | 0.2945 | 0.0 | 1.585 | 361.60 |
| $Ca^{2+}$••••$O^{2-a}$ | 1090.40 | 0.3437 | 0.0 | 3.135 | 110.20 |
| $Sr^{2+}$••••$O^{2-a}$ | 959.10 | 0.3721 | 0.0 | 3.251 | 71.70 |
| $Ba^{2+}$••••$O^{2-a}$ | 905.70 | 0.3976 | 0.0 | 9.203 | 459.20 |
| $Mn^{2+}$••••$O^{2-a}$ | 1007.40 | 0.3262 | 0.0 | 3.420 | 95.00 |
| $Co^{2+}$••••$O^{2-a}$ | 1491.70 | 0.2951 | 0.0 | 3.503 | 110.50 |
| $Fe^{2+}$••••$O^{2-a}$ | 1207.60 | 0.3084 | 0.0 | 2.997 | 62.90 |
| $Ni^{2+}$••••$O^{2-a}$ | 1582.50 | 0.2882 | 0.0 | 3.344 | 93.70 |
| $Cu^{2+}$••••$O^{2-b}$ | 3860.60 | 0.2427 | 0.0 | 1.000 | 99999.00 |

where $E^{dopant}$ is the defect energy, the difference between the perfect lattice and the lattice containing a dopant; $E_{V_O}$•• is the defect energy of an isolated oxygen vacancy; $E_h$• is the energy for an isolated hole, modelled as an oxide ion binding a polaron, $O^-$. $O_{dis}$ is the oxygen dissociation energy, $E_O{}^X$ are the electron affinities of oxygen and $E_{bulk}$ is the lattice energy of the perfect lattice specified in brackets; A represents La for A-site dopants and Fe for B-site dopants. In these calculations the values of 5.11, -1.46 and 8.75 eV were used for the oxygen dissociation energy and the first and second electron affinities of oxygen respectively.[25, 314]

The defect energies of doped systems were calculated using the Mott-Littleton methodology;[274] with a region 1 radius of 10.0 Å and a region 2 radius of 15.0 Å used for both A- and B-site substitution.

#### 6.2.1.2 Calculating Binding Energies

Although it is important to know how easily a dopant can be incorporated into the bulk lattice of a material, and which compensation scheme is favoured as a result, it is equally important to establish if this charge compensating species will contribute to the overall conductivity of the material, which can be established by calculating the binding energy of each dopant to the charge compensating species. Significant binding energies can limit conductivity as the mobile charge carriers can be trapped by the dopant. The binding energy of a dopant to an oxygen vacancy is calculated

as follows

$$E_{Bind} = E_{cluster} - (E_{V_O^{\bullet\bullet}} + 2E_{M_{La}'}) \tag{6.3}$$

where $E_{cluster}$ is the defect energy of the dopant and vacancy cluster, $E_{V_O^{\bullet\bullet}}$ is the defect energy of the isolated oxygen vacancy and $E_{M_{La}'}$ is the defect energy of the isolated dopant. A negative value indicates the cluster is more stable than the isolated defects and therefore the dopant will bind to oxygen vacancies. The defect energy of the dopant-vacancy cluster was calculated using the Mott-Littleton methodology[274] with both the dopant and a vacant nearest neighbour oxygen site at the centre of the sphere. The same region 1 radius was used in the calculations of the clusters as used for the isolated dopants: 10.0 Å.

### 6.2.2 DFT+*U*

For studying A- and B-site transition metal dopants, the DFT+*U* method has been employed, as for bulk $LaFeO_3$, in which a $U_{eff}$ value is applied to the transition metals in the system. The *U*-values used for each transition metal dopant in this work were determined using the method employed for establishing the *U*-value for $Fe^{3+}$; see Chapter 3 Section 3.3.[315] Using the appropriate metal monoxide (for example MnO for $Mn^{2+}$), structural and magnetic properties were calculated using a range of *U*-values and compared to experimentally established values, the results of which are shown in Appendix B. Where changing the *U*-value had little effect on the structural or magnetic properties, common values from the literature were used as a guide: between 4.0 and 5.0 eV for CoO,[123, 316, 317] between 5.0 and 8.0 eV for NiO,[318–321] 7.0 eV for CuO[322, 322–324] and between 3.0 and 5.0 eV for MnO.[320, 325, 326] Leading to the use of the following *U*-values in our work: 4.0 eV for $Mn^{2+}$ and $Co^{2+}$ and 7.0 eV for $Ni^{2+}$ and $Cu^{2+}$.

#### 6.2.2.1 Calculating Solution Energies

Solution energies of dopants in charge state *q* ($\Delta H_f(q)$) were calculated using the following equation:

$$\Delta H_f(q) = E^{dopant} - E^{perfect} \pm \sum n_x(E_x + \mu_x) + q(E_{VBM} + E_F + \Delta E_{pot}) + q^2 E_{ic} \tag{6.4}$$

with $E^{dopant}$ being the total energy of the relaxed supercell, at constant volume, containing the dopant, one dopant is included in a 2×2×1 supercell, containing 80 atoms, leading to a doped stoichiometry of $La_{0.94}M_{0.06}FeO_3$ for A-site dopants and $LaFe_{0.94}M_{0.06}O_3$ for B-site dopants. All other parameters are as defined in Chapter 4 section 4.2.2, with the exception of chemical potential.

The chemical potential, $\mu_x$, was varied by changing the elemental reference state from a pure metal to a metal oxide, using the anion poor and anion rich (representing the limits of low and high oxygen partial pressures, $\rho_{O_2}$) equations; 6.5 and 6.6, respectively. Under anion poor (i.e. reducing) conditions the replaced ion, A, precipitates out as a metal, whereas under anion rich (i.e. oxidising) conditions the replaced ion forms an oxide with the excess oxygen. The following equations use nickel on the A-site as an example dopant:

$$2A_A^x + O_O^x + 2Ni(s) \leftrightarrow 2Ni_A' + 2A(s) + V_O^{\bullet\bullet} + \frac{1}{2}O_2 \tag{6.5}$$

$$2A_A^x + O_O^x + 2NiO \leftrightarrow 2Ni_A' + V_O^{\bullet\bullet} + A_2O_3 \tag{6.6}$$

For anion poor, nickel metal is used as the elemental reference state and for anion rich nickel(II) oxide is used. The above equations include oxygen vacancies, $V_O{}^{\bullet\bullet}$, to compensate for the charge imbalance. Compensation via holes, $h^{\bullet}$, was also investigated in both anion poor and anion rich conditions, which are represented respectively in equations 6.7 and 6.8 (again using nickel as a demonstrative example):

$$A_A^x + Ni(s) \leftrightarrow Ni_A' + A(s) + h^{\bullet} \tag{6.7}$$

$$A_A^x + NiO + \frac{1}{4}O_2 \leftrightarrow Ni_A' + h^\bullet + \frac{1}{2}A_2O_3 \tag{6.8}$$

At ambient temperatures and pressures, anion rich represents the more realistic operating conditions for SOFCs.

#### 6.2.2.2 Calculating Binding Energies

Binding energies were calculated using the same expression as for the interatomic potentials study i.e. equation 6.3. In addition, the binding energies of dopants to holes was calculated at this level of theory, using a similar expression:

$$E_{Bind} = E_{cluster} - (E_{h^\bullet} + E_{M_A'}) \tag{6.9}$$

where $E_{cluster}$ is the formation energy of the dopant and hole cluster and $E_{h^\bullet}$ is the defect energy of an isolated hole.

To calculate the binding energy to oxygen vacancies, the most stable configuration of two dopants and an oxygen vacancy in a $2\times2\times1$ $LaFeO_3$ supercell needs to be identified in order to determine an accurate energy for the dopant-vacancy cluster. This was achieved using the Site Occupancy Disorder (SOD) program[327] which identifies all the unique configurations of a given structure within a supercell. In this study, the most stable configuration of the dopant-vacancy clusters was established in two steps: initial screening of all unique configurations was performed using interatomic potentials, then the resulting ten most stable configurations were relaxed using DFT+$U$ and the most favourable configuration was found, which was done first with two dopant ions, without the compensating oxygen vacancy, with the process repeated, to find the most favourable site for the compensating oxygen vacancy, using the doped $LaFeO_3$ supercell. The interatomic potential calculations were performed using the potentials in Table 6.1 using the GULP code.[291]

## 6.3 Results

### 6.3.1 Interatomic Potentials

Results from the A- and B-site study will be presented separately, starting with the A-site.

#### 6.3.1.1 A-Site

The solution energies, calculated for A-site alkali earth metal dopants with both oxygen vacancy and hole compensation, are shown as a function of ionic radii in Figure 6.1.

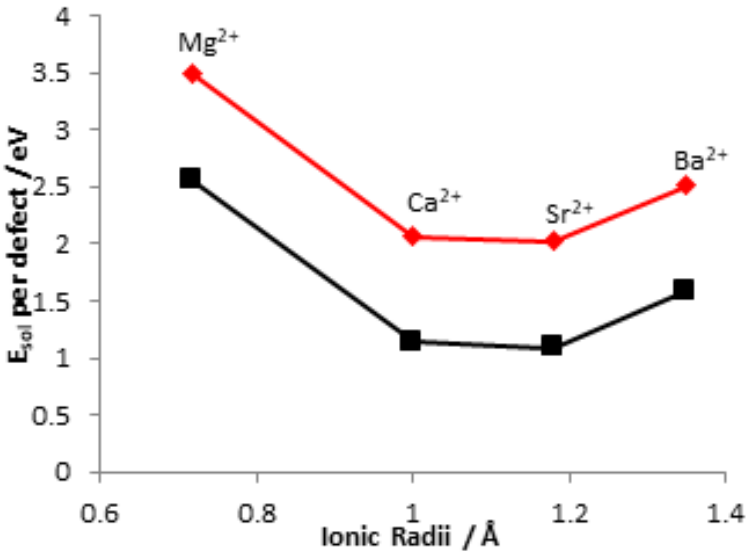


**Figure 6.1:** The solution energies as a function of ionic radii for alkaline earth metal dopants in $LaFeO_3$ with oxygen vacancy compensation (black) and hole (oxygen polaron) compensation (red).

From Figure 6.1, we see that oxygen vacancy compensation is more favourable than hole compensation, by a significant value, 1 eV. We conclude that oxygen vacancy compensation is likely to dominate in these doped materials, although compensation via holes will be present to some extent, and the equilibrium between the two compensation mechanisms will depend on the oxygen partial pressure, a point discussed further in Section 6.3.2, when the DFT+*U* results are discussed.

We note that the model used for hole compensation relies on the assumption that the hole will be localised on a single oxygen atom. The validity of this assumption will be discussed in Section 6.4 in reference to the DFT results, but due to this crude model, it is difficult to draw definite conclusions about hole compensation at this level of theory.

The solution energies of $Ca^{2+}$ and $Sr^{2+}$ are lower than those for the other alkaline-earth metals studied, probably because their ionic radii are closest to that of $La^{3+}$: 1.36 Å.[328] The low solution energy of strontium calculated in this work is consistent with experimental work where strontium has commonly been used as an A-site dopant in this material and is known to increase ionic and electronic conductivity,[113] with our results also suggesting that $Ca^{2+}$ should be equally soluble.

Further information on the most suitable A-site dopant for these systems can be obtained by analysing the binding energies of these dopants to the charge compensation species; specifically oxygen vacancies as these are the most favourable compensating species according to this study. A high binding energy will trap oxygen vacancies meaning they will no longer be able to contribute to the ionic conductivity of the material. Table 6.2 shows the binding energies of the four A-site dopants we have investigated to a nearest neighbour oxygen vacancy in $LaFeO_3$. As $LaFeO_3$ has two inequivalent oxygen sites, labelled O1 and O2, the binding energy of each dopant with an oxygen vacancy in both sites has been calculated, negative values indicate that the dopant favourably binds to the oxygen vacancy.

**Table 6.2:** Binding energies of oxygen vacancies to A-site dopants, calculated using interatomic potentials.

| Dopant | Bind Energy / eV | | | |
|---|---|---|---|---|
| | Mg | Ca | Sr | Ba |
| $LaFeO_3$ (O1) | -2.407 | -1.144 | -0.922 | 1.298 |
| $LaFeO_3$ (O2) | -2.431 | -0.840 | -0.718 | -0.801 |

We can see that all the alkali earth metal dopants bind to oxygen vacancies. However, strontium and calcium, which show the lowest solution energies, show the

lowest binding energies, in the majority of cases, which further suggests that these are the most appropriate A-site alkali earth dopants for $LaFeO_3$. The low binding energies and low solution energies observed for strontium and calcium are in line with previous work that has shown similar electrochemical performance between strontium doped $LaFeO_3$ and calcium doped $LaFeO_3$.[184, 197] However, strontium does have a lower binding energy than calcium, meaning strontium has the lowest binding energy of the alkali earth metals considered, which may be why other work has reported calcium doped $LaFeO_3$ as having a lower ionic conductivity than its strontium doped counterpart.[180]

The binding energy results suggest that the inclusion of these dopants could cause oxygen vacancies to be bound to the alkali earth dopants, but previous studies have observed an increase in ionic conductivity with strontium and calcium doping. These high binding energies could be the result of the Mott-Littleton methodology used in the calculation of dopant-vacancy clusters. The treatment of the defects as point charges in these systems could lead to errors in the energy of the dopant-vacancy cluster and therefore errors in the binding energies.

#### 6.3.1.2 B-site

The calculated solution energies for the substitution of Mn, Co, Ni and Cu onto the B-site of $LaFeO_3$, with oxygen vacancy compensation and hole compensation, are shown in Figure 6.2 as a function of ionic radii.

Comparing the solution energies between the two compensation schemes, we see that, similarly to the A-site results, oxygen vacancy compensation is the favoured scheme, by $\sim$1 eV. It is likely that both compensation schemes will be present, dependent on oxygen partial pressure, and the large difference between the solution energies may be caused by the crude modelling employed for hole compensation in this study, as discussed previously.

For $LaFeO_3$, $Co^{2+}$ and $Ni^{2+}$ have the lowest solution energy. The ratio of Fe to Co ions at the B-site has been investigated previously and it has been shown that small amounts of Co ions increase the oxygen diffusion coefficient in comparison to stoichiometric $LaFeO_3$.[329] However, there is no significant difference between

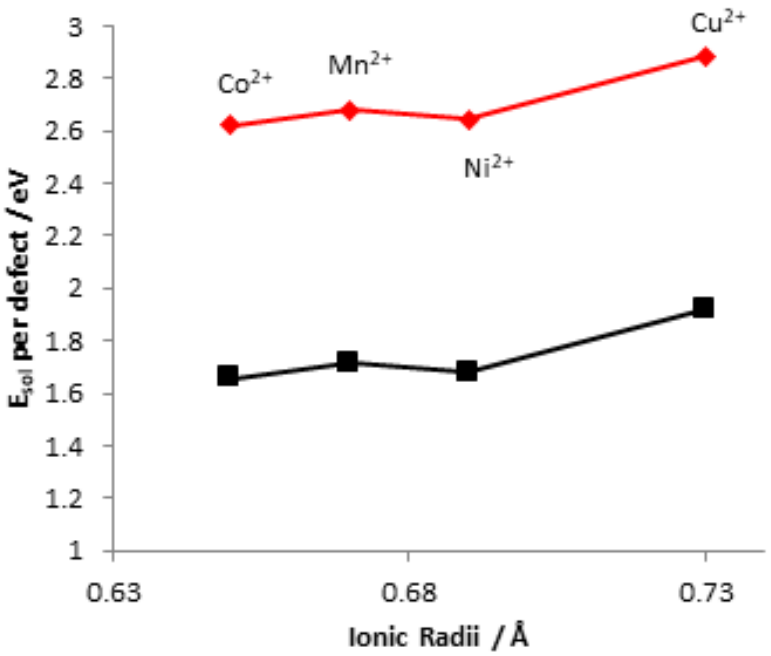


**Figure 6.2:** The solution energies as a function of ionic radii for transition metal dopants in $LaFeO_3$ with oxygen vacancy compensation (black) and hole (oxygen polaron) compensation (red).

the solution energies of all B-site dopants investigated, with the exception of copper which has a higher energy under both compensation mechanism compared to the other dopants, therefore it is difficult to identify the most appropriate dopant based on the solution energy alone.

As with the A-site dopants, the binding energies of the B-site dopants with an oxygen vacancy were evaluated. These are shown in Table 6.3.

**Table 6.3:** Binding energies of oxygen vacancies to B-site dopants, calculated using interatomic potentials.

| Dopant | Binding Energy / eV | | | |
|---|---|---|---|---|
| | Mn | Co | Ni | Cu |
| $LaFeO_3$ (O1) | -1.065 | -1.012 | -1.036 | -0.991 |
| $LaFeO_3$ (O2) | -1.161 | -1.076 | -1.094 | -1.018 |

Firstly, we see that the binding energies of B-site transtion metal dopants to oxygen vacancies are high, with the O2 vacancy bound more than the O1 vacancy; which is likely due to this oxygen site being closer to the B-site than the O1 oxygen site. The

dopants that exhibit the lowest binding energies are copper and cobalt. However, as with the solution energies, the binding energies to oxygen vacancies in each site are similar for all transition metal dopants studied, so it is difficult to assess the most appropriate dopant for this site, based on these results. Input from DFT-based methods will be particularly useful for this set of dopants.

### 6.3.2 DFT+*U*

As has been done for the results of the interatomic potentials study, we will discuss the results from the DFT+*U* study of A- and B-site dopants separately, starting with the A-site.

#### 6.3.2.1 A-Site

The solution energies of a range of divalent alkali earth metal dopants: Mg, Ca, Sr and Ba, and transition metal dopants; Mn, Fe, Co, Ni, Cu, on the A-site of $LaFeO_3$ have been calculated with both hole and oxygen vacancy compensation investigated, using equations 6.4 to 6.8, as described above. The results are shown in Table 6.4 in comparison with the experimental metal-oxygen bond distance in the associated binary oxide,[8, 11, 13, 30–33] a parameter chosen to take into account the effect of Jahn-Teller distortions on the octahedra for copper, which is not represented by ionic radii.

For the alkali earth dopants, the solution energies decrease with increasing metal to oxygen (M-O) bond length until barium, for which the solution energy increases. For the transition metals, the solution energies decrease as the M-O bond length increases. For both sets of dopants, the closer their M-O bond length is to the average La-O bond length (2.596 Å) in this material, the lower is its solution energy. This trend is followed by both compensation mechanisms, as is shown clearly in Figure 6.3.

When modelling transition metal dopants we should consider the spin orientation of the dopant. In stoichiometric $LaFeO_3$, the B-site $Fe^{3+}$ ions are antiferromagnetically ordered which may affect the spin direction of dopants in either the A- or B-site. Therefore, the solution energies of transition metal dopants in both spin

**Table 6.4:** The solution energies of divalent alkali earth metal and transition metal A-site dopants, in anion poor and anion rich conditions, using either hole ($h^{\bullet}$) or oxygen vacancy ($V_O^{\bullet\bullet}$) compensation, in relation to the metal-oxygen bond length in the dopant's associated binary oxide; M-O.[a]Ref[11] [b]Ref[30] [c]Ref[31] [d]Ref[32] [e]Ref[13] [f]Ref[8] [g]Ref[33].

| Dopant | M-O / Å | Solution Energy / eV | | | |
|---|---|---|---|---|---|
| | | $h^{\bullet}$ | | $V_O^{\bullet\bullet}$ | |
| | | Poor | Rich | Poor | Rich |
| Alkali Earth Metals | | | | | |
| $Mg_{La}'$ | 2.109[a] | 4.961 | 1.739 | 3.598 | 1.450 |
| $Ca_{La}'$ | 2.406[b] | 3.316 | 0.587 | 2.501 | 0.682 |
| $Sr_{La}'$ | 2.580[c] | 3.306 | 0.079 | 2.494 | 0.343 |
| $Ba_{La}'$ | 2.770[d] | 3.992 | 0.248 | 2.952 | 0.456 |
| Transition Metals | | | | | |
| $Cu_{La}'$ | 1.951[e] | 9.050 | 1.886 | 6.324 | 1.548 |
| $Ni_{La}'$ | 2.089[a] | 7.762 | 2.110 | 5.465 | 1.697 |
| $Co_{La}'$ | 2.130[f] | 7.162 | 1.343 | 5.065 | 1.186 |
| $Fe_{La}'$ | 2.163[g] | 5.896 | 1.551 | 4.221 | 1.325 |
| $Mn_{La}'$ | 2.223[a] | 6.159 | 1.330 | 4.397 | 1.177 |

up and down orientations, with respect to the c lattice parameter, were calculated and compared. On the A-site, there was no significant difference observed between these solution energies; the largest difference is observed for $Fe^{2+}$; 0.02 eV, suggesting spin does not play a strong role on this site.

Clearly incorporating dopants under anion rich conditions is more favourable for both sets of dopants and both compensation mechanisms, compared to anion poor conditions, driven by the formation of the stable $A_2O_3$ product. Interestingly, under anion rich conditions, (which are more likely to prevail in many experimental conditions), the difference between the solution energies of the two compensation mechanisms is small indicating that, in doped systems formed under these conditions, both holes and oxygen vacancies will be present, demonstrating the mixed ionic electronic properties of doped systems. Of the alkali earth dopants, strontium has the lowest solution energy, under both conditions. However, under anion poor conditions, the solution energies of strontium and calcium are almost identical, while, oxygen vacancy compensation is clearly more favourable; therefore, incorporating dopants under these conditions will serve to increase the ionic, but not the

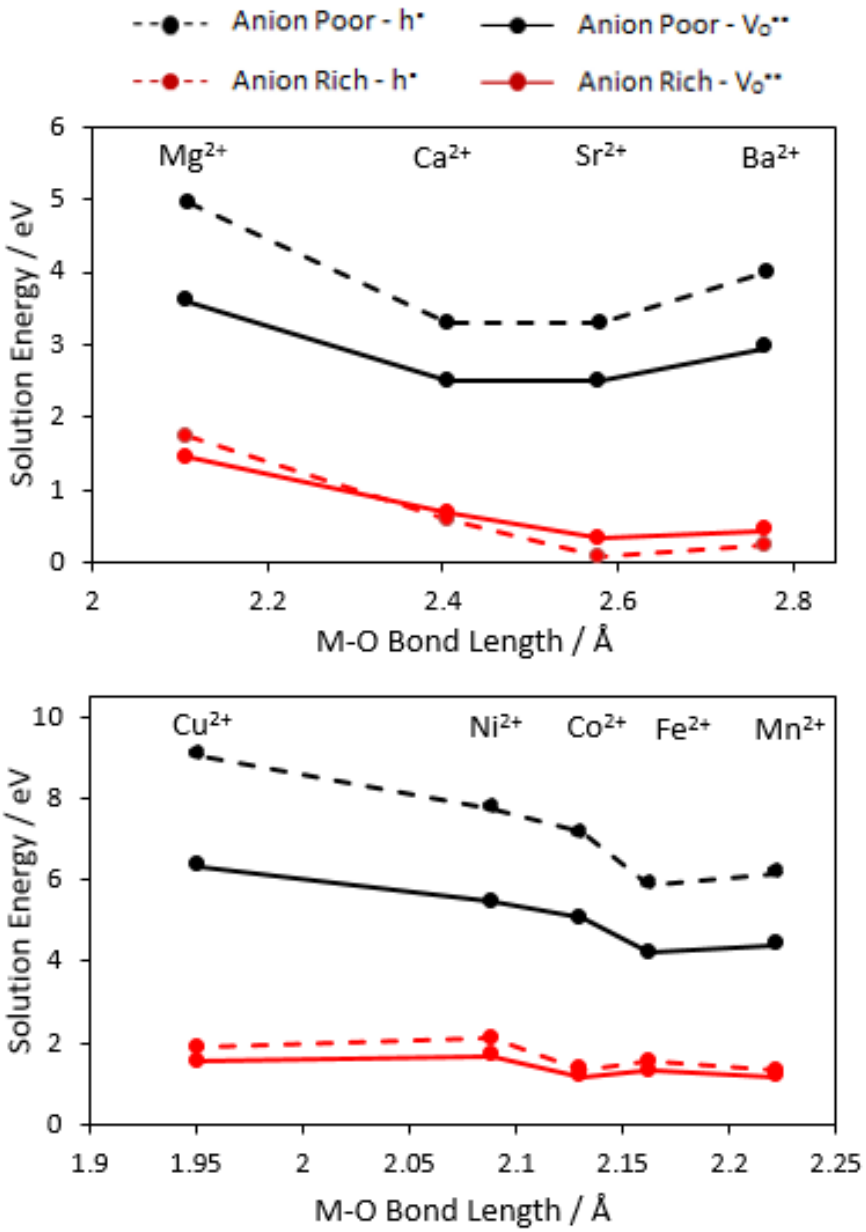


**Figure 6.3:** Solution energies of A-site dopants with increasing M-O bond length under anion poor (black) and anion rich (red) conditions; alkali earth metals are on top and transition metals on the bottom, with oxygen vacancy (solid line) and hole (dashed line) compensation.

electronic conductivity of the material.

For the transition metals, manganese has the lowest solution energy, under both anion rich and poor conditions. However, in anion rich conditions, there is only a small difference between the solution energies of all the transition metals studied. As with the alkali earth dopants, there is a significant difference between oxygen va-

cancy and hole compensation under anion poor conditions, with oxygen vacancies forming in preference, leading to an increase in oxygen vacancy concentration on doping under these conditions, but not holes. In contrast, anion rich conditions will promote the formation of both types of compensation, again enhancing the mixed ionic, electronic properties of $LaFeO_3$.

**Hole Localisation** The extent to which a hole localises was determined by comparing the charge densities of the doped and undoped systems. Due to the self-interaction error present in DFT, modelling hole localisation accurately is a challenge and often produces erroneous results. However, in our investigation we found that introducing a hole only affected the oxygen sub lattice in $LaFeO_3$ in a minor way; either by the hole localising on a set of specific oxygen ions, or by delocalising throughout the lattice. As only one sub lattice is involved, the most significant error using GGA+$U$ will be systematic, allowing us to study the trends in hole localisation for each set of dopants. Attempts to localise the hole further, by distorting the oxide ions surrounding the dopant, were unsuccessful, suggesting small polaron formation onto a specific ion is unfavourable.

For the alkali earth metal dopants, when a hole is generated in compensation, the hole tends to delocalise around the lattice, with only slight localisation on the oxygen ions surrounding the dopant. This delocalisation increases from magnesium to strontium, with magnesium showing some localisation on the nearest neighbour oxygens, before decreasing for barium, which again displays a degree of localisation on the oxygen ions surrounding the barium. For the transition metals, however, the hole is consistently localised on the nearest neighbour oxygen ions surrounding the dopant from manganese to copper. The delocalisation of the hole in the case of alkali earth doping, (except for magnesium) may account for the hole compensation being slightly more favourable than oxygen vacancy compensation under anion rich conditions for these dopants, whereas the opposite is seen for those dopants that show hole localisation, i.e. magnesium.

The effect of hole localisation on the oxygens surrounding the dopant, for Mg and Ba, is further demonstrated by the change in metal-oxygen bond lengths caused

by the dopant: the greater the difference from the lanthanum-oxygen bond length in the pure material, the higher the degree of hole localisation (or small polaron formation). For both sets of A-site dopants, where localisation is observed, the hole predominantly localises on the six oxygens that have the shortest La-O bonds in the pure material. The bond lengths in doped $LaFeO_3$ for these six bonds are shown in Tables 6.5 and 6.6 for the alkali earth and the transition metal dopants respectively.

**Table 6.5:** The bulk $LaFeO_3$ La-O bond lengths and the M-O bond lengths in alkali earth doped $LaFeO_3$ with hole compensation.

| La-O / Å | Bond Length / Å | | | |
|---|---|---|---|---|
| | Mg-O | Ca-O | Sr-O | Ba-O |
| 2.555 | 3.557 | 2.514 | 2.650 | 2.786 |
| 2.659 | 3.485 | 2.670 | 2.743 | 2.816 |
| 2.659 | 3.485 | 2.670 | 2.743 | 2.816 |
| 2.442 | 2.045 | 2.433 | 2.535 | 2.652 |
| 2.442 | 2.045 | 2.433 | 2.535 | 2.652 |
| 2.407 | 2.042 | 2.400 | 2.493 | 2.602 |

Only in the case of magnesium and barium do we see a notable change in bond length compared to the La-O bond. The localisation of the hole adjacent to $Mg^{2+}$ and $Ba^{2+}$ is due to the significant difference in ionic radii between these dopants and $La^{3+}$; the dopants with similar radii; $Sr^{2+}$ and $Ca^{2+}$, do not cause hole localisation. Figure 6.4 shows the charge difference between the pure supercell and the doped supercell with hole compensation. We can see that the hole localises on the oxygen ions surrounding magnesium and barium, but not on those surrounding strontium. For barium, the hole localisation is spread equally between the 6 closest oxygens, while for magnesium there is see an increased localisation on the oxygen ions that the magnesium ion has shifted away from. These trends are also mirrored in the changes in bond length, which are all roughly equivalent for barium, whereas there is a significant amount of variation for magnesium.

For all the transition metal dopants studied, hole localisation on the surrounding oxygens is observed for all dopants, but to varying degrees. The largest hole density on neighbouring oxygen ions is seen for cobalt and copper, whose bond lengths to neighbouring oxygens show the largest difference to La-O, as can be seen in

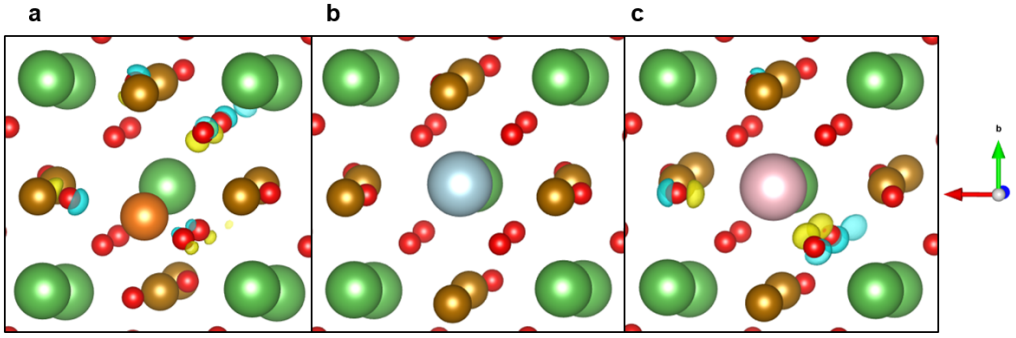


**Figure 6.4:** The charge density difference plots for the A-site alkali earth dopants magnesium (a), strontium (b), and barium(c). Lanthanum is shown in green, iron in gold, oxygen in red, magnesium in orange, strontium in silver and barium in pink. Accumulation of charge density is shown in yellow, while depletion of charge density is shown in blue using an isodensity of 0.27 $bohr^{-3}$ in all cases.

Table 6.6. Another factor that needs considering when discussing hole localisation for transition metal dopants, is the possibility of the hole localising on the dopant itself, due to their variable oxidation states. The extent of hole localisation on the dopant was established by comparing the relaxed magnetic moment of the dopant, in the 2×2×1 $LaFeO_3$ supercell, with its expected value as a divalent dopant. The expected values for the transition metal dopants are; 5, 4, 3, 2 and 1 $\mu_B$ for Mn, Fe, Co, Ni and Cu respectively. The relaxed magnetic moments have been scaled to account for $Fe^{3+}$, which has a $d^5$ configuration, having a relaxed magnetic moment of 4.4 $\mu_B$ in our supercell. Iron is in a high spin state in $LaFeO_3$ and therefore should have a magnetic moment of 5, leading to a scaling factor of 5/4.4 = 1.136.

After scaling, the relaxed magnetic moments of the transition metal dopants in an A-site are; 5.1, 4.3, 3.2, 2.1 and 0.85 $\mu_B$, in line with those expected for these dopants in their divalent charge state, demonstrating that there is no hole localisation on the transition metal dopants when they occupy the A-site.

The charge difference plots of the transition metal A-site dopants: manganese, cobalt and copper, with hole compensation are shown in Figure 6.5. All three dopants show charge localisation on the oxygen ions surrounding the dopant. The hole localisation increases from manganese to cobalt, before decreasing again, although only slightly, for copper, which is in line with the changes in bond lengths.

**Table 6.6:** The bulk $LaFeO_3$ La-O bond lengths and the M-O bond lengths in transition metal doped $LaFeO_3$ with hole compensation.

| La-O / Å | Bond Length / Å | | | | |
|---|---|---|---|---|---|
| | Mn-O | Fe-O | Co-O | Ni-O | Cu-O |
| 2.555 | 2.577 | 2.099 | 3.711 | 3.173 | 3.520 |
| 2.659 | 3.038 | 3.098 | 3.599 | 3.202 | 3.511 |
| 2.659 | 3.009 | 3.103 | 3.601 | 3.209 | 3.389 |
| 2.442 | 2.140 | 2.015 | 1.941 | 2.013 | 2.020 |
| 2.442 | 2.131 | 2.015 | 1.927 | 2.012 | 1.924 |
| 2.407 | 2.139 | 1.957 | 1.864 | 2.007 | 1.989 |

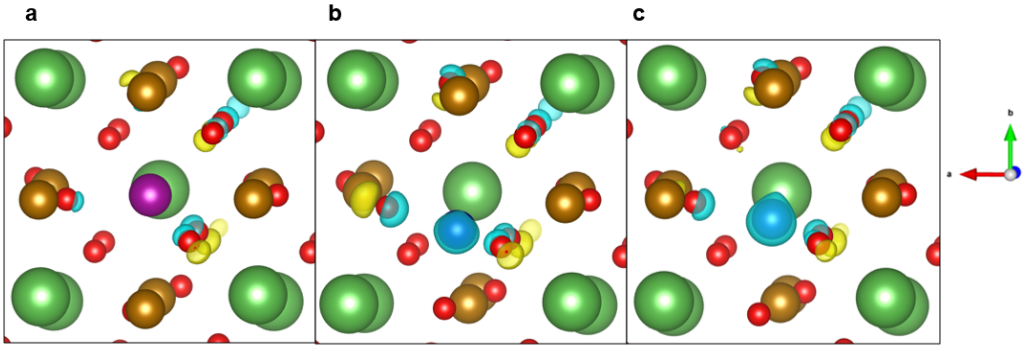


**Figure 6.5:** The charge density difference plots for A-site transition metal dopants manganese (a), cobalt (b) copper (c). Lanthanum are shown in green, iron in gold, oxygen in red, manganese in purple, cobalt in dark blue and copper in light blue. Accumulation of charge density is shown in yellow, while depletion of charge density is shown in blue using an iso-density of 0.3 $bohr^{-3}$ for all transition metal dopants.

**Binding Energies** The binding energies of the A-site alkali earth and transition metal divalent dopants with the two charge compensating species should be considered before choosing the most appropriate dopant. All dopants studied promote both oxygen vacancy and hole formation. However, to effect an increase in conductivity, the dopant must not bind strongly to these species. Tables 6.7 and 6.8 show the binding energies for the divalent A-site alkali earth and transition metal dopants respectively.

Oxygen vacancies do not bind significantly to either calcium or strontium: the weak binding of calcium, and strontium to O1 vacancies, will be overcome under SOFC operating conditions ($kT$ = 0.075 eV at 873 K, the lower limit of intermediate temperature SOFC operating temperatures). However, magnesium and particularly bar-

**Table 6.7:** Calculated binding energies of A-site alkali earth dopants with oxygen vacancies and holes in $LaFeO_3$, binding energies for oxygen vacancies in both the O1 and O2 sites have been calculated.

| Dopant | Binding Energy / eV | | | |
|---|---|---|---|---|
| | Mg | Ca | Sr | Ba |
| $V_{O1}^{\bullet\bullet}$ | -0.393 | -0.034 | -0.061 | -0.620 |
| $V_{O2}^{\bullet\bullet}$ | -0.102 | -0.033 | 0.092 | -0.507 |
| $h^{\bullet}$ | 0.243 | 0.202 | 0.188 | 0.129 |

ium have larger binding energies, probably due to the mismatch in ionic radii of these dopants compared to lanthanum (0.89, 1.61 and 1.36 Å respectively for $Mg^{2+}$, $Ba^{2+}$ and $La^{3+}$), as has been observed in related systems.[330] It is of interest that all dopants have a stronger binding to vacant O1 sites compared to O2 sites, a promising result as O2 vacancies form more favourably compared to O1 vacancies.

The optimum site for the oxygen vacancy in each doped system, which was determined separately for each dopant using SOD[327] is dependent on the dopant species as well as the type of oxygen vacancy: O1 or O2, causing the difference in the binding energies observed for the two sites. For the O1 site, with the exception of magnesium, in the most stable configuration of two dopants and an oxygen vacancy in a $2\times2\times1$ supercell, the vacancy occupies one of the nearest neighbour oxygen sites to one of the dopants, whereas for the O2 site, for strontium and barium, the vacancy is in an oxygen site between the two dopants, which distributes the charge from the vacant site between the two dopants, causing a smaller binding energy to either of the positively charged dopants. For magnesium, the aforementioned exception, the O2 vacancy is located next to only one dopant and the O1 site is not a nearest neighbour site, but a next nearest neighbour site. For calcium, both O1 and O2 sites are bonded only to one dopant, which results in very similar binding energies of calcium to the two oxygen vacancy sites.

None of the alkali earth metal dopants studied bind to holes, suggesting these dopants should cause an increase in electrical conductivity in the material, if incorporated under the appropriate conditions. Combining these results with the calculated solution energies suggests that strontium or calcium would be appropriate

A-site alkali earth metal dopants, in line with experimental results, which show increased ionic conductivity in Sr- and Ca-doped $LaFeO_3$ compared to the undoped material,[180, 184] as well as an increase in the electronic conductivity.[195, 196, 331, 332]

**Table 6.8:** Calculated binding energies of A-site transition metal dopants with oxygen vacancies and holes in $LaFeO_3$, binding energies to oxygen vacancies in both the O1 and O2 sites have been calculated.

| Dopant | Binding Energy / eV | | | | |
|---|---|---|---|---|---|
| | Cu | Ni | Co | Fe | Mn |
| $V_{O1}^{\bullet\bullet}$ | -0.380 | -0.567 | -0.054 | -0.464 | -0.143 |
| $V_{O2}^{\bullet\bullet}$ | -0.159 | -0.624 | -0.112 | -0.117 | -0.155 |
| $h^{\bullet}$ | 0.303 | 0.284 | 0.237 | 0.154 | 0.224 |

Interestingly, whereas the alkali earth metal dopants bind to O1 oxygen vacancies stronger than to O2, the transition metal dopants have a stronger binding to O2 oxygen vacancies, in the majority of cases, the key exceptions being Fe and Cu. The binding energy of transition metal dopants to oxygen vacancies generally increase as the M-O bond length of the associated binary oxide decreases, except for Cu, which shows a lower binding energy than expected and Fe with an O1 vacancy, which is significantly higher than expected. The difference for copper can be attributed to the greater stability of Cu in a square planar geometry compared to the 12-coordinate geometry of lanthanum in $LaFeO_3$. The A-site copper dopant shifts away from the La site into a square planar site between four of the oxygen ions (see Figure 6.6) stabilising the dopant and decreasing the magnitude of its binding energy. However, this distortion to the lattice makes it highly unlikely that copper will occupy an A-site in this material, and favours the B-site instead, a point discussed in the next section.

The significantly larger binding energy for Fe to an O1 oxygen can be attributed to the nucleation of a secondary $Fe_2O_3$ phase within the structure, as shown in Figure 6.7. As the O2 vacancy is a nearest neighbour to one of the Fe dopant ions it breaks up this secondary phase; therefore, this higher binding energy is only seen for the O1 vacancy. The tendency of the majority of transition metal dopants to bind to O2

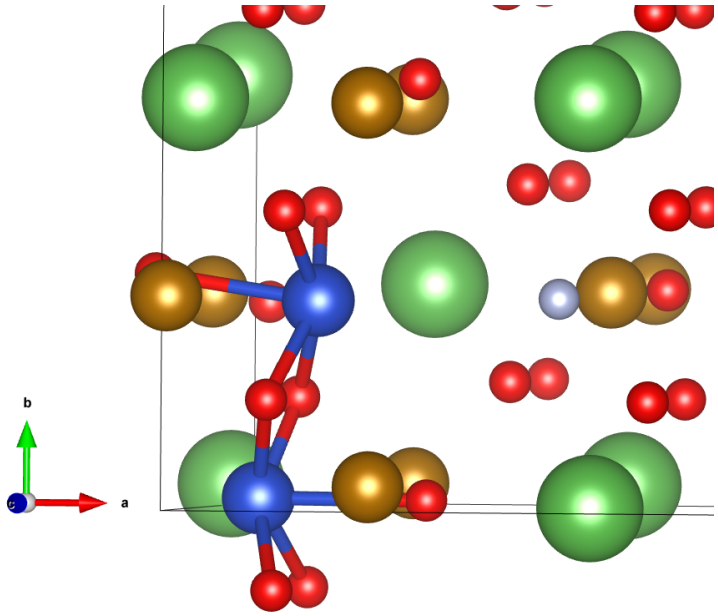


**Figure 6.6:** The most stable dopant-vacancy cluster for an A-site copper dopant, showing relaxed position of an A-site copper dopant (blue). The dopant has shifted significantly away from one oxygen ion to form a pseudo-square planar geometry with four of the other oxygen ions. This shift will be more favourable if the oxygen site it is shifting away from is vacant, as is shown here with the oxygen vacancy shown in grey.

site vacancies is probably due to the closer proximity of the O2 site to the lanthanum site compared with O1.

As with the alkali earth dopants, none of the transition metal dopants studied bind significantly to holes, suggesting they will all encourage electronic conductivity in $LaFeO_3$. Combining the solution energy and binding energy results suggests that $Mn^{2+}$ could be an appropriate A-site dopant, due to its low solution energy and small binding energy.

Although strontium is often used as an A-site dopant for perovskite materials such as $LaFeO_3$,[50, 333, 334] manganese has previously been assumed to occupy the B-site when used as a dopant, a point that is discussed further in the next section. It would be of interest to investigate the effect of doping the A-site with both strontium and manganese which, according to our results, would lead to a promotion in both bulk ionic and electronic conductivity in $LaFeO_3$.

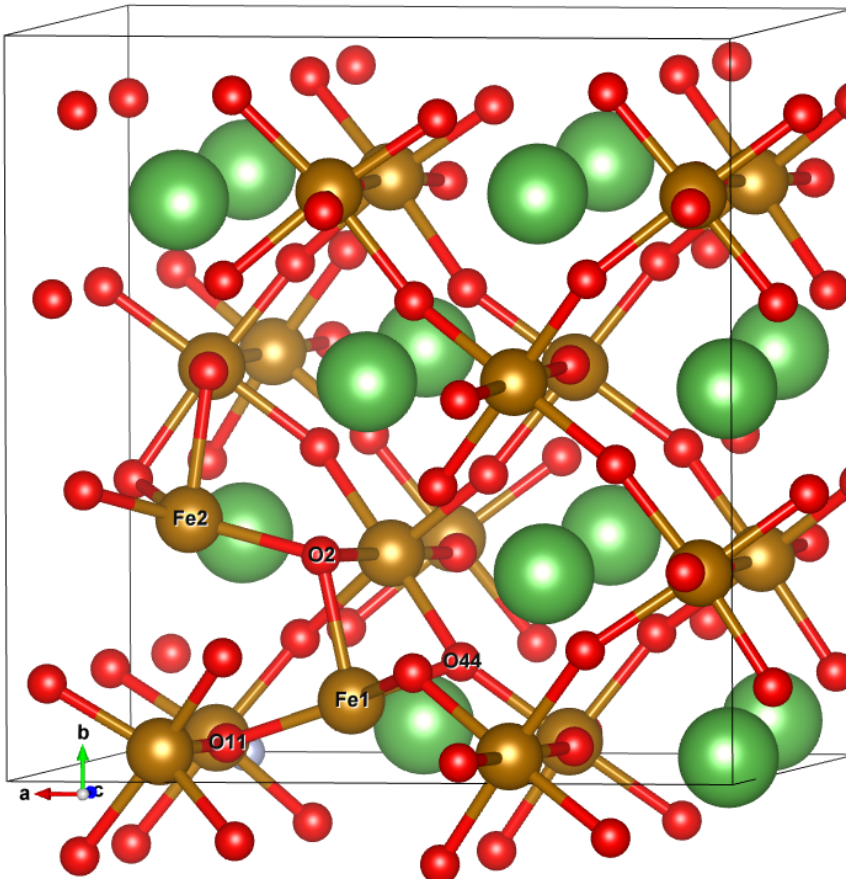


**Figure 6.7:** The high binding energy of Fe to O1 vacancies indicates incipient nucleation of an $Fe_2O_3$ phase. The A-site Fe dopants are labelled Fe and the oxygens labelled O are oxygens with a coordination number of 3, a feature of the $Fe_2O_3$ lattice. The O1 vacancy is shown in grey.

#### 6.3.2.2 Comparison of Site Stability

The results of the previous section suggest that manganese would be a promising A-site dopant, due to its low solution energy and low magnitude of binding energy. In order to establish the likelihood of manganese occupying an A-site as opposed to a B-site we compare the site stability of this dopant, and other transition metal dopants, on the A- and B-sites of $LaFeO_3$. The Goldschmidt tolerance factor, $t$,[335] is a hard sphere approximation that uses ionic radii to assess the distortion of the lattice caused by a dopant ion. The larger the distortion the less likely the dopant is to occupy that lattice site. It is calculated as follows

$$t = \frac{r_X + r_A}{\sqrt{2}(r_X + r_B)} \tag{6.10}$$

where $r$ is the ionic radii of the ion with subscripts $A$, $B$ and $X$ referring to the A-site cation, B-site cation and the anion, respectively.

An ideal cubic perovskite would have a Goldschmidt factor of 1 with the lattice becoming more distorted the more the Goldschmidt factor deviates from 1. The Goldschmidt tolerance factor for pure stoichiometric orthorhombic $LaFeO_3$ is 0.908 - using Shannon ionic radii.[328] To calculate the Goldschmidt factor of the doped system, the ionic radius of the divalent dopant was used instead of the ionic radii of $La^{3+}$ or $Fe^{3+}$ for A-site and B-site dopants respectively; these are shown in Table 6.9.

**Table 6.9:** The Goldschmit tolerance factor of divalent dopants on the A-site and B-site of $LaFeO_3$.

| Dopant | Goldschmidt Tolerance Factor | |
|---|---|---|
| | A-site | B-site |
| Alkali Earth Metals | | |
| $Mg_{Fe}'$ | 0.734 | 0.876 |
| Transition Metals | | |
| $Cu_{Fe}'$ | 0.737 | 0.872 |
| $Ni_{Fe}'$ | 0.722 | 0.889 |
| $Co_{Fe}'$ | 0.797 | 0.865 |
| $Fe_{Fe}'$ | 0.804 | 0.851 |
| $Mn_{Fe}'$ | 0.818 | 0.832 |

The radius of an ion is highly dependent on the ion's coordination number in the material, with the ionic radius increasing with the coordination. For the transition metals only ionic radii up to a coordination number of 8 are available, so that although the tolerance factor values calculated for the B-site dopants will be accurate - using a coordination number of 6 - those calculated for the A-site will be less so, as the ionic radii associated with a coordination of 8, or 6 for nickel and copper, rather than the actual value of 12, were used. However, for the A-site the tolerance factor increases with larger ionic radii. As the ionic radius is expected to increase with a higher coordination number, we expect a higher tolerance factor, and therefore the predicted stability of the perovskite structure, with A-site transition metal dopants, will be greater.

It is clear that the majority of the transition metal dopants favour the B-site; the higher tolerance factors of this site compared to the A-site suggests less distortion, even with the underestimation of the A-site tolerance factors. However, manganese only causes slightly less distortion on the B-site compared to the A-site, especially considering that the A-site value could be underestimated. This similarity suggests that it may be possible to form $LaFeO_3$ with manganese as an A-site dopant, an interesting avenue for further investigation.

#### 6.3.2.3 B-site

The solution energies of a range of divalent transition metal dopants; manganese, cobalt, nickel and copper, on the B-site of $LaFeO_3$ have been calculated with both hole and oxygen vacancy compensation and are presented in Table 6.10. Magnesium, as the smallest alkali earth metal, was also considered as a dopant on the B-site for comparison.

**Table 6.10:** The solution energies of divalent B-site transition metal dopants in anion poor and anion rich conditions, using either hole ($h^{\bullet}$) or oxygen vacancy ($V_O^{\bullet\bullet}$) compensation in relation to the metal-oxygen bond length in the dopant's associated binary oxide; M-O.[a]Ref[11] [b]Ref[13] [c]Ref[8].

| Dopant | M-O / Å | Solution Energy / eV | | | |
|---|---|---|---|---|---|
| | | $h^{\bullet}$ | | $V_O^{\bullet\bullet}$ | |
| | | Poor | Rich | Poor | Rich |
| Alkali Earth Metals | | | | | |
| $Mg_{Fe}'$ | 2.109[a] | 0.737 | 1.038 | 0.784 | 0.985 |
| Transition Metals | | | | | |
| $Cu_{Fe}'$ | 1.951[b] | 4.872 | 1.283 | 3.538 | 1.146 |
| $Ni_{Fe}'$ | 2.089[a] | 2.938 | 0.861 | 2.249 | 0.865 |
| $Co_{Fe}'$ | 2.130[c] | 2.891 | 0.648 | 2.218 | 0.722 |
| $Mn_{Fe}'$ | 2.223[a] | 2.307 | 1.053 | 1.828 | 0.993 |

Considering the transition metal dopants initially, we see that, as with the A-site dopants, anion rich provides the most favourable formation conditions for both compensation mechanisms. However, unlike the A-site dopants, the orientation of the spin on the transition metal dopant ion was found to have an impact on the solution energy of the dopants, with lower solution energies if the spin orientation of the dopant is in line with the antiferromagnetic ordering of the $Fe^{3+}$ ions - a dopant

replacing a spin down $Fe^{3+}$ would favourably be in a spin down orientation.

Interestingly, different trends are observed for the two conditions investigated, as can be seen in Figure 6.8. Under anion poor conditions the solution energies decrease with increasing M-O bond length. Whereas, under anion rich conditions the solution energies reach a minimum at cobalt and then increase again. As with transition metal dopants on the A-site, there is only a small variation in the solution energies of the dopants studied under anion rich conditions, with the solution energies of dopants with the different compensation mechanisms being comparable so that both holes and oxygen vacancies are likely to be present in B-site doped $LaFeO_3$ formed under this condition. Under anion poor conditions, however, oxygen vacancies are more favourable.

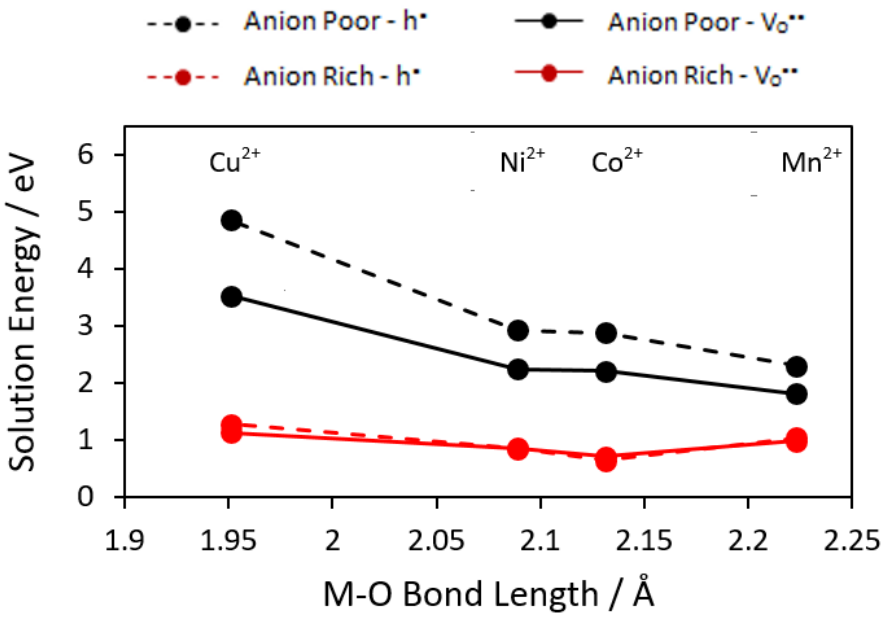


**Figure 6.8:** Solution energies of B-site transition metal dopants with increasing M-O bond length under anion poor (black) and anion rich (red) conditions. Solution energies are calculated with oxygen vacancy (solid line) and hole compensation (dashed line).

**Hole Localisation** As with the A-site dopants, only the oxygen sub lattice is affected when a hole is introduced in compensation, and the self-interaction error in DFT largely cancels. As a consequence, we can analyse the trends in hole localisation observed for these dopants.

Hole localisation with the B-site transition metal dopants follows a similar trend

to the A-site alkali earths. Initially, for manganese, the hole is localised on the six surrounding oxygen ions; this localisation decreases from manganese to cobalt, before increasing again for nickel and copper. The oxidation state of each of the dopants, used to establish if the hole has localised on the dopant, was calculated via their magnetic moment, following the same method used for the A-site transition metal dopants. It was found that all dopants are in their 2+ charge state, having magnetic moments of; 4.7, 3.0, 1.95 and 0.83 $\mu_B$ respectively for Mn, Co, Ni and Cu. Therefore, no localisation is expected on the dopant.

As with the A-site dopants, the hole localisation can be identified by the effect the dopant has on the bond length between the B-site ion and the oxygen ions. The greater the change in bond length caused by the dopant, shown in Table 6.11, the more localised the hole is on the surrounding oxygens, as the change in bond length is caused by the localised distortion due to the formation of a small polaron. The largest difference in bond length is seen when manganese is the dopant, and oxygen ions surrounding manganese show the highest degree of localisation. The change in bond length then decreases practically to zero for cobalt, consistent with no localisation seen on the oxygen ions surrounding cobalt. Finally, the change in bond length increases again for Ni and Cu.

**Table 6.11:** The bulk $LaFeO_3$ Fe-O bond lengths and the M-O bond lengths in transition metal doped $LaFeO_3$ with hole compensation. Those shown in bold are the bond lengths with oxygen ions that show hole localisation.

| Fe-O / Å | Bond Length / Å | | | |
|---|---|---|---|---|
| | Mn-O | Co-O | Ni-O | Cu-O |
| 2.023 | 2.032 | 2.020 | 2.053 | **2.081** |
| 2.028 | **2.117** | 2.024 | **2.068** | **2.061** |
| 2.018 | **2.070** | 2.030 | **2.058** | 1.997 |

We can visualise the hole localisation via the charge density difference between the doped and pure supercells, which, for the B-site transition metal dopants, is shown in Figure 6.9.

Here the trend of hole localisation can be seen clearly; the largest degree of hole localisation is seen for manganese, then no hole localisation is seen for cobalt, before

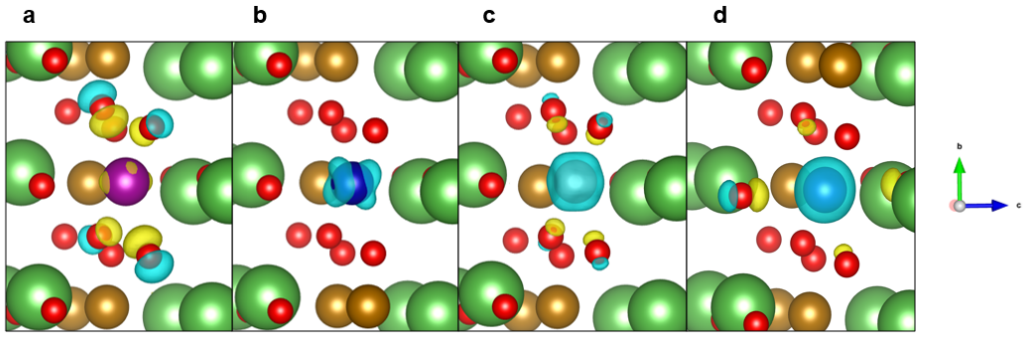


**Figure 6.9:** The charge density difference plots for B-site transition metal dopants manganese (a), cobalt (b), nickel (c) and copper (d). Lanthanum are shown in green, iron in gold, oxygen in red, manganese in purple, cobalt in dark blue, nickel in silver and copper in light blue. Accumulation of charge density is shown in yellow, while depletion of charge difference is shown in blue using an iso-density of 0.08 $bohr^{-3}$ for all transition metal dopants.

increasing again for nickel and copper.

**Binding Energies** The binding energies for the divalent B-site dopants to oxygen vacancies and holes are shown in Table 6.12.

**Table 6.12:** Calculated binding energies of B-site transition metal and magnesium dopants with oxygen vacancies and holes in $LaFeO_3$.

| Dopant | Binding Energy / eV | | | | |
|---|---|---|---|---|---|
| | Mg | Cu | Ni | Co | Mn |
| $V_{O1}^{\bullet\bullet}$ | -0.155 | -0.774 | -0.188 | -0.349 | -0.416 |
| $V_{O2}^{\bullet\bullet}$ | -0.172 | -1.397 | -0.197 | -0.417 | -0.403 |
| $h^{\bullet}$ | -0.030 | -0.249 | -0.005 | -0.358 | -0.676 |

The results show that all B-site dopants studied bind to both oxygen vacancies and holes. These dopants may therefore decrease the ionic and electronic conductivity of $LaFeO_3$; however the incorporation of B-site dopants could be necessary for the stability of the material and therefore a dopant should be chosen that limits this detrimental effect. Of the transition metals studied, nickel has the lowest binding energy for both oxygen vacancies and holes, although magnesium has lower binding energies to both compensating species. This observation would lead to the conclusion that cobalt, nickel and magnesium would be the optimum B-site dopants, as they have low solution energies and the minimal binding energies to both oxygen

vacancies and holes.

Experimentally, promising results have been observed when using cobalt and nickel as B-site dopants. LSCF-based materials, as mentioned previously, have high ionic and electronic conductivities, as well as being more resistant to chromium poisoning than other cathode materials.[50, 113, 115, 336] $La_xSr_{1-x}Fe_yNi_{1-y}O_{3-\delta}$ (LSNF) on the other hand, has attracted attention as a cathode material for solid oxide electrolysis cells, the reverse of a solid oxide fuel cells, due to its high electronic conductivity, thermal expansion coefficient similar to that of YSZ, and its high coking tolerance to CO.[337, 338] These first two properties have resulted in Ni-based perovskites also being considered as cathode materials for SOFCs,[339] and our results indicate that they should have ionic and electronic conductivities comparable to LSCF.

These observed properties suggest that the binding energies calculated in this work are not large enough to inhibit conductivity under operating conditions, particularly when A-site dopants are present. There is also evidence that transition metal dopants increase the ionic conductivity without A-site codopants. For example, Kharton *et al.*[340] found doping $LaFeO_3$ with nickel increased the electrical conductivity and bulk ionic conductivity of the material, demonstrating that the binding energies can be overcome.

The results for magnesium as a B-site dopant show promise: it has a lower solution energy than the transition metal dopants and binds less to both oxygen vacancies and holes. In addition, the tolerance factors for magnesium, shown in Table 6.9, show that it will cause less strain on the structure of $LaFeO_3$ if situated on the B-site as opposed to the A-site. Therefore magnesium, with its low solution energy and low binding energy to both oxygen vacancies and holes, could be a promising B-site dopant. This compatibility has recently been demonstrated experimentally; when comparing $LaFeO_3$ to $LaFe_{1-x}Mg_xO_3$ (x = 0.05) Díez-García and Gómez[341] found that the doped system had a higher efficiency as a photocathode for the oxygen reduction reaction, a key reaction in SOFCs.

The current work has only focused on the solution energies and binding energies to

charge carriers of these dopants. Other factors will play a role in their suitability for SOFC cathode applications, including the effect they have on the thermal expansion coefficient (TEC). The effect of nickel and cobalt on the TEC of $LaFeO_3$ is well reported; the presence of cobalt as a dopant causes an increase in the TEC, usually linearly with cobalt content,[342] so low concentrations of cobalt are often used in order to keep the TEC similar to those of common electrolyte materials, whereas Ni-doped $LaFeO_3$ materials have favourable TECs, in line with those of common electrolyte materials, even at large concentrations.[343, 344] The effect of Mg on the TEC of $LaFeO_3$ is less well reported, and would need to be investigated before proposing Mg as a B-site dopant. However, results from Mg B-site doping of a related compound, $La_{0.7}Sr_{0.3}MnO_{3-\delta}$ are promising, with low TECs and improved electrochemical performance compared to (La,Sr)$MnO_3$ reported.[345]

On comparing the solution energies of manganese on both the A-site and the B-site, we find that under anion poor conditions its solution energy as a B-site dopant is significantly smaller than its solution energy as an A site dopant. However, under anion rich conditions, the solution energies are very similar, particularly for oxygen vacancy compensation where the solution energy of manganese on the B-site is only 0.045 eV lower than that of Mn on the A-site.

#### 6.3.2.4 Variable Oxidation States

Transition metals are able to occupy a variety of oxidation states within a material, a factor which can help or hinder the conductivity properties. With this in mind, we calculated the energy of oxidation of the appropriate divalent transition metal B-site dopants in $LaFeO_3$. Manganese, cobalt, nickel and copper could form 3+ (or 4+ for manganese) oxidation states within $LaFeO_3$, therefore oxidation to these states was considered. The energy of oxidation was calculated based on the following equation, using manganese as an example dopant:

$$Fe_{Fe}^{X} + Mn_{Fe}^{'} \leftrightarrow Mn_{Fe}^{X} + Fe_{Fe}^{'} \tag{6.11}$$

With an additional oxidation step considered for generating manganese 4+

$$Fe_{Fe}^{X} + Mn_{Fe}^{X} \leftrightarrow Mn_{Fe}^{\bullet} + Fe_{Fe}^{'} \tag{6.12}$$

The reaction energies are shown in Table 6.13.

**Table 6.13:** The solution energies of transition metal B-site dopants undergoing oxidation to form 3+ oxidation states and 4+ in the case of manganese. In all cases the dopants in 2+, 3+ and 4+ states are in high spin states, the value for nickel in parentheses represents the low spin oxidation state.

| Dopant | Solution Energy / eV |
|---|---|
| $Mn_{Fe}^{X}$ | 0.300 |
| $Mn_{Fe}^{\bullet}$ | 0.735 |
| $Co_{Fe}^{X}$ | 0.860 |
| $Ni_{Fe}^{X}$ | 2.190 (1.782) |
| $Cu_{Fe}^{X}$ | 1.145 |

The calculated energies show that, particularly for manganese, the energy of oxidising these divalent dopants is low. Manganese is therefore likely to be present in 2+, 3+ and 4+ oxidations states, while the other transition metal dopants will be present in 2+ and 3+ oxidation states, both observations are in agreement with experimental findings.[199] However, nickel, not surprisingly, has a high barrier to oxidation. Interestingly, whereas the other dopants favour high spin configurations, nickel favourably oxidises into the low spin state.

## 6.4 Comparison of Methods

The results from the interatomic potentials study are most appropriately compared with the DFT+$U$ results under anion rich conditions.

The interatomic potentials study suggests that the most appropriate A-site dopants are strontium and calcium, with hole compensation being less favourable than oxygen vacancy compensation. However, the binding energies calculated at this level of theory suggest that both strontium and calcium could inhibit oxygen migration in a minor capacity, as both have negative binding energies to oxygen vacancies.

The DFT+$U$ study also found strontium and calcium to be the most appropriate A-site dopants, as they have the lowest solution energies of the alkali earth metals

investigated. However, the binding energies calculated were significantly smaller and the difference between the solution energies for oxygen vacancy and hole compensation were much smaller under anion rich conditions. The smaller, low values for the binding energies of strontium and calcium as A-site dopants is more in line with the experimental studies that have shown an increase in the ionic and electronic conductivity of $LaFeO_3$ on Ca- and Sr-doping, and the small difference between oxygen vacancy and hole compensation is in agreement with the mixed ionic, electronic properties observed for these materials.

From the interatomic potentials B-site dopant study, limited conclusions could be drawn on the most appropriate dopant, due to the similarity in solution energies and binding energies to oxygen vacancies across all dopants studied. However, as with the A-site alkali earth metal dopants, hole compensation was considerably less favourable compared to oxygen vacancy compensation.

In anion-rich conditions we see only minor differences between the solution energies of all the B-site dopants investigated within the DFT+$U$ study, similar to the interatomic potentials study. However, the difference in energy between hole compensation and oxygen vacancy compensation is very minor, and the binding energies of each dopant to charge compensating species do show variation, leading to the conclusion that nickel and cobalt are the most appropriate B-site dopants.

This difference between the two methods raises a number of interesting points regarding the interatomic potentials study. Firstly, it is clear that our model of the hole as being localised on a single oxygen ion is too simplistic. In fact, looking at the results of hole localisation from our DFT+$U$ calculations suggests that if a hole localises, it will be on several oxygen ions, and the extent to which this localisation occurs is dopant dependent. Secondly, the large negative binding energies of the alkali earth metal dopants to oxygen vacancies suggest the interatomic potential methods either overly stabilises the dopant-vacancy cluster, or destablises the isolated defects. The increase in ionic and electronic conductivity that has been observed in $LaFeO_3$ on doping the A-site with alkali earth metals,[55, 90, 175, 184, 191, 197] suggests that these dopants do not bind to oxygen vacancies significantly enough to

prevent ionic mobility. Finally, it has outlined the need for DFT+$U$ to treat transition metals accurately; the similarity across all transition dopants for the two energies (solution and binding energies), calculated using interatomic potentials, suggest the $d$-electrons have not been properly treated at this level of theory.

## 6.5 Summary and Conclusions

Two methods have been employed to study solution energies and binding energies of divalent dopants on both the A- and B-site of $LaFeO_3$, to find the most appropriate dopant for each site. Although the trends in solution energies were well matched between the two methods, the values for the binding energies calculated using interatomic potentials are considerably higher than those calculated with DFT. As the DFT results are more in line with what is expected based on observed ionic and electronic conductivities in doped $LaFeO_3$, we have based our conclusions on those results.

We find for A-site alkali earth metal doping that there is only minimal binding to oxygen vacancies and holes, with the exception of barium which binds strongly to oxygen vacancies in both oxygen sites. Low solution energies were calculated for $Ca^{2+}$, $Sr^{2+}$ and $Ba^{2+}$ under anion rich conditions, with $Sr^{2+}$ and $Ca^{2+}$ emerging as the most appropriate due to a combination of low solution energy and minimal binding energies.

For A-site transition metal dopants, the solution energies are all comparable. However, manganese has low binding energies compared to other transition metal A-site dopants, which, combined with the minimum distortion of the surrounding $LaFeO_3$ lattice suggests that it would be the most appropriate transition metal A-site dopant in $LaFeO_3$. Comparison with manganese as a B-site dopant showed similar solution energies under oxygen rich conditions and similar Goldschmidt tolerance factors, suggesting manganese could be a viable A-site dopant, in contrast to its widely assumed B-site position. Cobalt nickel and magnesium were found to be the most favourable B-site dopants, due to low solution energies and low binding energies to oxygen vacancies, along with minimal distortion - particularly for nickel to the

$LaFeO_3$ lattice.

Under anion rich conditions, all dopants, in both sites, demonstrate similar solution energies between the two charge compensation mechanisms investigated: oxygen vacancies and holes, which explains the origins of the mixed ionic electronic conductivity observed in doped perovskites, such as LSCF, a property that is vital to the application of these materials as cathode materials in intermediate temperature SOFCs.

# Chapter 7

# $LaFeO_3$ (001) Surfaces

## 7.1 Introduction

Our investigation of $LaFeO_3$ as an intermediate temperature solid oxide fuel cell (IT-SOFC) cathode material has so far focused on bulk $LaFeO_3$; the likely defects that will be present under SOFC conditions, and the dopants that can aid electronic and ionic conductivity in this material. In this chapter we will consider the surface chemistry of $LaFeO_3$.

During operation, oxygen, provided by an oxidant, enters the cathode chamber and is reduced to $O^{2-}$ before migrating through the cathode to the electrolyte. Although it is important to understand the bulk properties of the cathode material, as these will govern the migration of the oxide ion to the electrolyte, of equal importance are the surface properties. Understanding the surface properties of $LaFeO_3$, such as its composition and the predominant defects, will help elucidate the mechanism of the oxygen reduction reaction and the role of cathode surface chemistry.

In this chapter we will investigate the stability and defect chemistry of two possible surface terminations of the (001) surface of $LaFeO_3$. The (001) surface is considered to be the most stable for lanthanum-based perovskite oxides[200, 208, 209] and is therefore the focus of the present study. The $FeO_2$ and LaO terminated surfaces will be considered, and the defects energies of lanthanum, iron and oxygen vacancies calculated for each. We will compare the defect chemistry of the surface of $LaFeO_3$ to bulk $LaFeO_3$ and thus aim to understand how defects contribute to

the ORR process, from oxygen interacting with the surface of $LaFeO_3$ to oxide ions migrating through bulk $LaFeO_3$ to the electrolyte.

## 7.2 Methodology

The methodology outlined in Chapter 3 focuses on the methods used for modelling bulk $LaFeO_3$, and while a number of parameters are the same, some different techniques need to be applied when studying surfaces. Unlike the work done in previous chapters, only DFT+$U$ will be used in our surface studies, as previous results[92, 200, 203, 206, 207] suggest the transition metal will play an important role in the surface chemistry, both as a surface ion and a sub surface-ion, and, as previously mentioned, modelling transition metals accurately with interatomic potential-based methods can be challenging.

The parameters that have remained the same between our bulk and surface studies of $LaFeO_3$ to allow for comparisons include the $U$-value on the iron ions and the pseudopotentials used for $La^{3+}$, $Fe^{3+}$ and $O^{2-}$. Where parameters have been changed, they will be outlined in the following sections.

Our surface studies using DFT+$U$ have implemented the slab model, introduced in Chapter 1 Section 1.4.5. In the following section we will describe how we modelled $LaFeO_3$ surfaces, using the slab model, and how we calculated surface stability and defect energies.

### 7.2.1 $LaFeO_3$ Surface Model

For our work on $LaFeO_3$ surfaces, the (001) surface, with both $FeO_2$ and LaO terminations, will be considered. For both surface models a 16 Å vacuum was used to split a $2\times2\times7$ supercell along the c-axis, providing a 28 layer slab with two surfaces, each with a $2\times2$ surface area; equating to 124.80 $Å^2$ for $LaFeO_3$, these parameters were tested and are fully converged as discussed later. The structure of both terminations can be seen in Figure 7.1

#### 7.2.1.1 Modelling Polar Surfaces

Perovskite materials are built up of layers. In the simplest example of a cubic $ABO_3$ perovskite, these layers would be alternate AO and $BO_2$ layers. In a number of

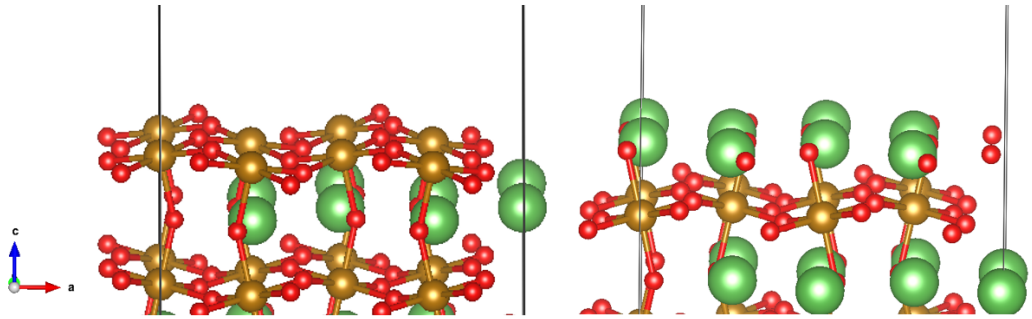


**Figure 7.1:** The $FeO_2$ (left) and LaO (right) terminations of the (001) surface of $LaFeO_3$.

perovskites, including $A^{III}B^{III}O_3$ perovskites, such as $LaFeO_3$, each layer has a net charge. In $LaFeO_3$, the LaO layers have a net charge of +1 while the $FeO_2$ layers have a net charge of -1. In the bulk material the charges of each layer will cancel out; however, when constructing a surface slab a net dipole forms at the surface, making the surface unstable as shown by Tasker.[1]

The (001) termination of $LaFeO_3$ is a type III surface, as defined by Tasker[1] and therefore the slab must be reconstructed before modelling. For $LaFeO_3$ (001) the top surface layer is split, with half of one side of the slab and half on the other, which is done for both LaO and $FeO_2$ terminations, this quenches the surface dipole by making the charge of each surface equal; $+\frac{1}{2}$ and $-\frac{1}{2}$ for the LaO and $FeO_2$ terminated surfaces of $LaFeO_3$ respectively. The final slabs used for modelling are shown in Figure 7.2.

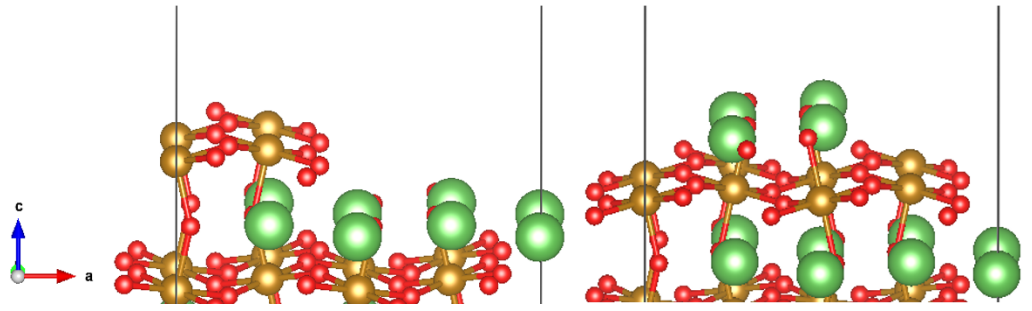


**Figure 7.2:** The $FeO_2$ (left) and LaO (right) terminations of the (001) surface of $LaFeO_3$ reconstructed to account for the net dipole present in both terminations.

A dipole correction can be included in VASP to correct for a net dipole moment that may be present in the calculation and is often implemented in slab models. How-

ever, this correction was not included in our calculations. The effect of including the dipole correction was investigated, and no difference in relaxed energies was observed with calculations which didn't include the dipole correction compared to those that did include the correction, suggesting that reconstructing the surface is sufficient to cancel out surface dipole moments.

### 7.2.2 Calculating Surface Energies

The surface energy, $\gamma$, of each termination was calculated using the following equation:

$$\gamma = \frac{1}{2}\frac{E_{surface} - nE_{bulk}}{A} \tag{7.1}$$

where $E_{surface}$ is the supercell containing the surface slab, $E_{bulk}$ is the energy per unit cell, $n$ is the number of unit cells in the slab supercell and $A$ is the surface area of the slab. Using relaxed and unrelaxed surface slab supercells, the relaxed, $\gamma_R$ and unrelaxed, $\gamma_U$ surface energies can be calculated respectively. The difference between the relaxed and unrelaxed surface energies gives the relaxation energy for the surface:

$$E_{rel} = \gamma_R - \gamma_U \tag{7.2}$$

Surface defect energies, $E_{defect}$, were calculated as the difference between the slab supercell containing the defects and the pure slab supercell:

$$E_{defect} = \frac{1}{2}\left(E_{defective} - E_{perfect}\right) \tag{7.3}$$

where $E_{defective}$ is the energy of the slab supercell containing the defects and $E_{perfect}$ is the relaxed slab supercell containing no defects. The energy is halved to get the defect energy per defect; the defective slab supercell contains two defects, one on each surface, to maintain equivalence between the surfaces. Only neutral defects can be modelled using the slab model, as introducing a net charge across the vacuum would cause the energy to diverge. Therefore only neutral oxygen, iron and

lanthanum vacancies were investigated. Interstitials were not considered as our previous study of bulk $LaFeO_3$ demonstrated that these defects do not occur in significant concentrations in this material. For all defect relaxations, eight layers in each slab were fixed at their bulk positions, to reduce the computational cost; only a $4.42\times10^{-4}$ eV difference was found between the defect energies of two oxygen vacancies (one on each surface) on a completely relaxed LaO terminated $2\times2\times7$ slab and two oxygen vacancies on a LaO terminated $2\times2\times7$ slab with the eight centred layers fixed. As with defects energies calculated for bulk $LaFeO_3$ we will report defect energies calculated under both anion rich and anion poor environments.

For all calculations, GGA+$U$ with PBE was used with a $U$ of 7 eV on $Fe^{3+}$, as with bulk $LaFeO_3$. The 16 Å vacuum was converged for each termination to within $9.5\times10^{-4}$ eV/formula unit; the number of layers in the slab was converged to within $2.0\times10^{-3}$ eV/formula unit and a $k$-point mesh of $6\times6\times1$ was used, converged to within $8.8\times10^{-5}$ eV/formula unit. Full details of model convergence can be found in Appendix H.

## 7.3 $FeO_2$ Terminated Surface

The $BO_2$ terminated surfaces of perovskite oxides are generally assumed to be the most catalytically active due to the presence of the transition metal, and previous work has found that these terminations have lower oxygen vacancy formation energies, compared to the LaO termination.[92, 200, 206, 207] In this section we shall investigate the relaxed structure of the $FeO_2$ surface before considering cationic and anionic surface defects and how the energies of these defects compare to bulk defect energies.

### 7.3.1 Surface Stability and Relaxation

Figure 7.3 shows the relaxed structure of the $FeO_2$ terminated $LaFeO_3$ (001) surface of a $2\times2\times7$ supercell and the unrelaxed structure for comparison. The surface energy of this termination is 0.50 $Jm^{-2}$.

The surface relaxation is mainly limited to the top surface layer and sub surface layer. The top layer restructures most significantly, with two iron ions relaxing

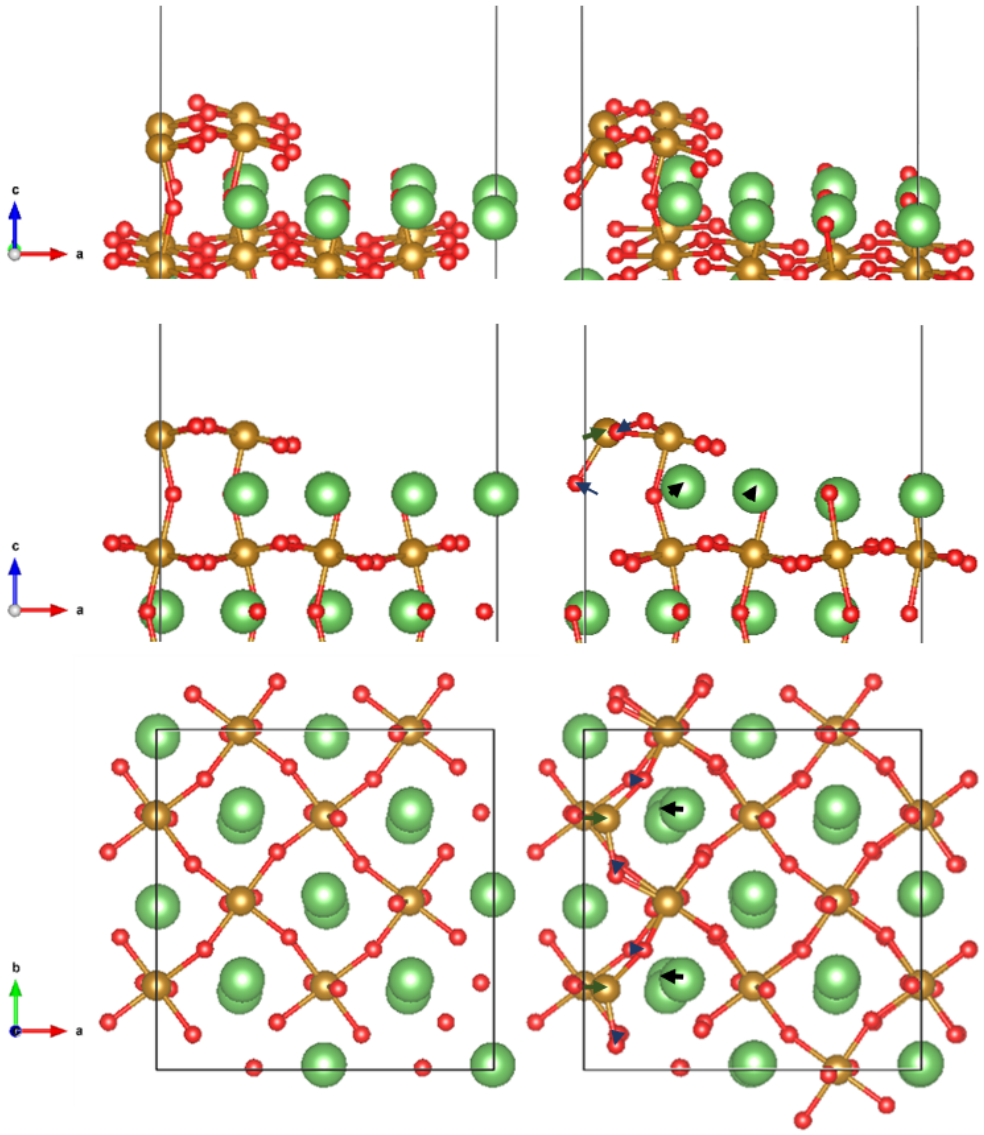


**Figure 7.3:** The unrelaxed (left) and relaxed (right) surface structure of the $FeO_2$ terminated (001) surface of $LaFeO_3$. Arrows have been used to indicate the direction and magnitude of relaxation; black arrows show the relaxation of lanthanum ions, dark green the relaxation of iron ions and dark blue the relaxation of oxygen ions.

towards the other iron sites on the surface, causing a shortening of both the axial and equatorial Fe-O bonds by 0.06 Å and between 0.13 and 0.16 Å respectively. In the sub surface, the lanthanum ions relax (by no more than 0.5 Å) off their ideal, bulk positions; the lanthanum ions below the surface iron ions shift closer to adjacent lanthanum ions in the sub-surface layer, while those that have no surface layer above

them, due to the reconstruction, shift closer to the bulk-like $FeO_2$ layer below the sub surface LaO layer.

### 7.3.2 Defects

The calculated defect formation energies for neutral lanthanum, iron and oxygen vacancies under both oxygen rich/cation poor and oxygen poor/cation rich conditions are shown in Table 7.1. The formation energies under each condition were calculated using the same chemical potentials used in the bulk defect study.

**Table 7.1:** The defect formation energies of neutral lanthanum, iron and oxygen vacancies on the $FeO_2$ terminated (001) surface of $LaFeO_3$. The defect energies have been calculated under oxygen rich/cation poor and oxygen poor/cation rich conditions.

| Defect | Defect Formation Energy / eV | |
|---|---|---|
| | O Rich & Cation Poor | O Poor & Cation Rich |
| $V_{La}^{X}$ | 1.898 | 7.701 |
| $V_{Fe}^{X}$ | -1.559 | 4.244 |
| $V_{O}^{X}$ | 1.219 | -2.650 |

As observed for bulk defects, the defect formation energies of cation vacancies are, as expected, lower in cation poor conditions, whereas, for oxygen vacancies the defect formation energy is lower in oxygen poor conditions. Interestingly, both iron and oxygen vacancies have negative formation energies under cation poor and oxygen poor conditions respectively. The chemical potentials used to calculate the formation energies under each condition represent the extremes of their respective condition, as mentioned in Chapter 4 Section 4.3.3. Therefore under operating conditions it is unlikely that either defect will have a negative defect formation energy. However they are likely to have low formation energies and, therefore, be present in significant concentrations. The defect formation energy for lanthanum is also low under oxygen rich conditions, suggesting the $FeO_2$ terminated surface will be highly defective under these conditions, which, as we have argued, are likely to dominate during fuel cell operation.

Figures 7.4, 7.5 and 7.6 show the relaxed surface structure of the $FeO_2$ terminated surface with a lanthanum, iron and oxygen vacancy respectively.

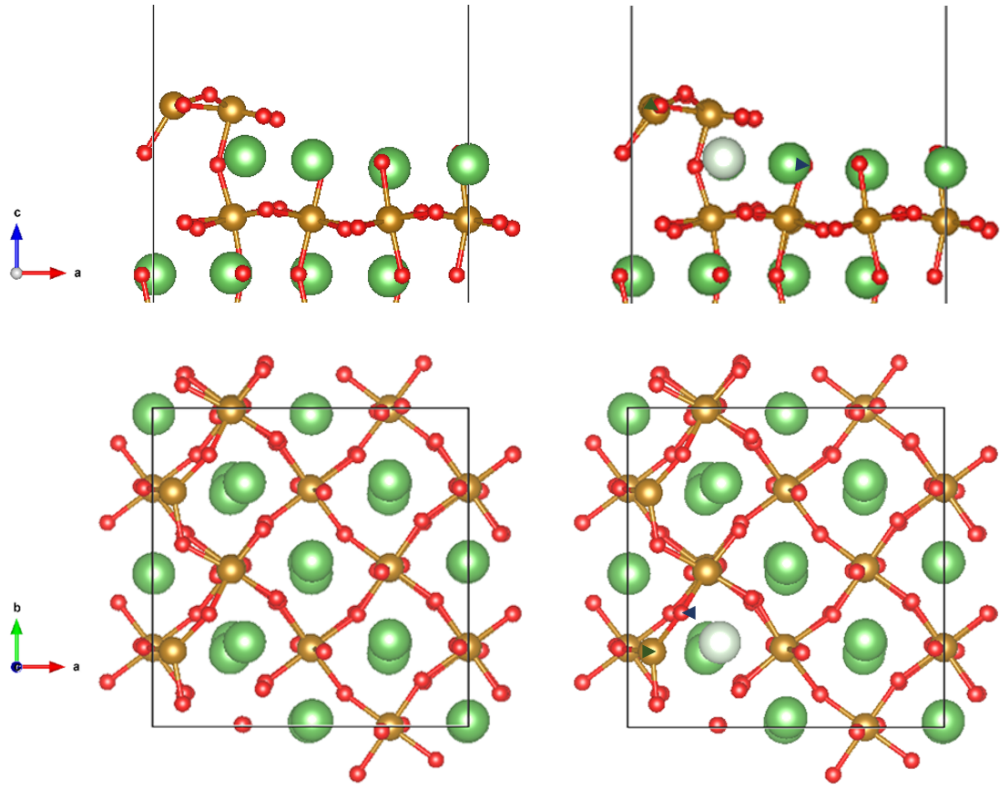


**Figure 7.4:** The pure surface (left) and the defective surface, containing a lanthanum vacancy, (right) of the $FeO_2$ terminated (001) surface of $LaFeO_3$. The position of the lanthanum vacancy is shown in pale green. Arrows have been used to indicate the direction and magnitude of relaxation; dark green arrows shows the relaxation of iron ions and dark blue the relaxation of oxygen ions.

The lanthanum vacancy does not cause a large amount of restructuring of the surface; neighbouring iron ions relax slightly towards the vacant site, while neighbouring oxygen ions in the same ab plane relax away from the vacant site. In contrast, an iron vacancy causes a large amount of restructuring, with two adjacent surface iron ions relaxing away from the vacant site by between 0.3 and 0.5 Å, while sub surface lanthanum ions relaxed marginally closer towards the surface. The presence of an iron vacancy has a large effect on the oxygen ions, especially the two oxygen ions previously bonded to the iron site that is now vacant which form an oxygen species on the surface. Based on its bond length (1.35 Å) the oxygen species is likely to be $O_2^-$; Ervin *et al.* reported bond lengths of $1.348 \pm 0.008$ Å for $O_2^-$, established by ultraviolet photoelectron spectroscopy.[301] Compared to the bond lengths of

alternative oxygen species; 1.49 ± 0.02 Å for classical peroxides, $O_2^{2-}$,[300] and 1.21 Å for $O_2$,[25] the reported bond length for $O_2^-$ is the closest and therefore this is the most likely form of the oxygen species on the surface.

The presence of the oxygen species could explain why the defect energy for the iron vacancy is so low, as the binding energy of the oxygen species, will contribute to the stability of the surface containing an iron vacancy. The other two surface oxygen ions that had been bonded to the now vacant iron site have also moved significantly, relaxing away from the now vacant site. Interestingly, the two sub surface oxygen ions, one axial to the vacant site the other axial to the adjacent surface iron ion, have moved towards the vacant site, closer to the surface of the material.

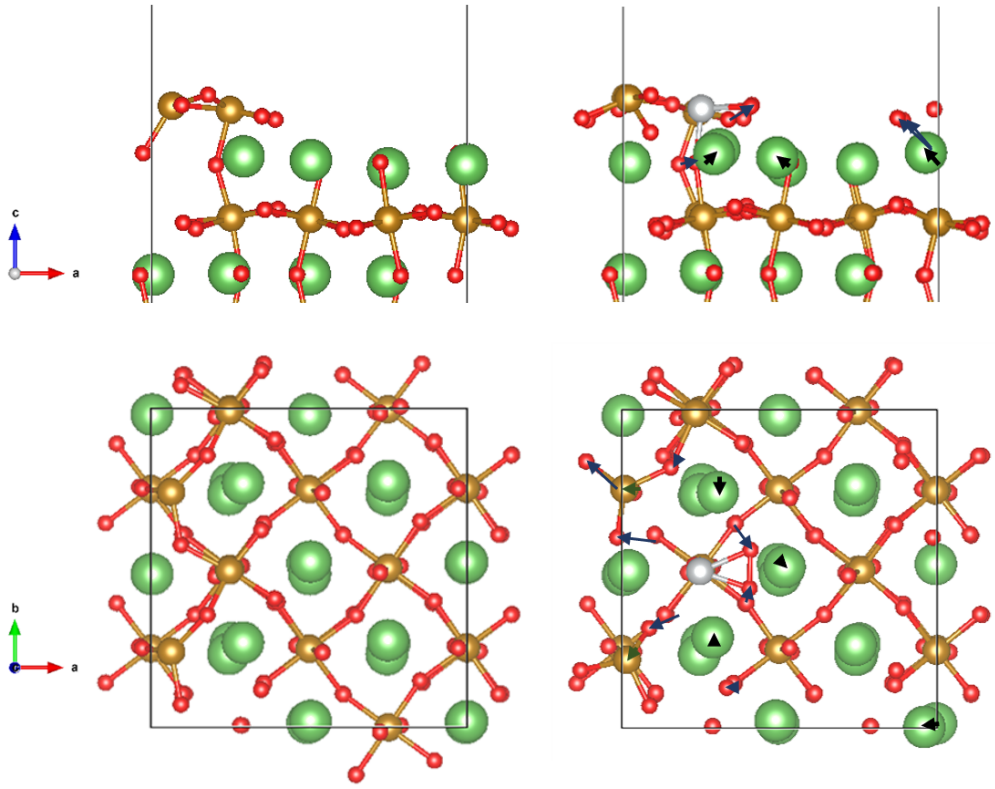


**Figure 7.5:** The pure surface (left) and the defective surface, containing an iron vacancy, (right) of the $FeO_2$ terminated (001) surface of $LaFeO_3$. The position of the iron vacancy is shown in grey. Arrows have been used to indicate the direction and magnitude of relaxation; black arrows show the relaxation of lanthanum ions, dark green the relaxation of iron ions and dark blue the relaxation of oxygen ions.

The presence of an oxygen vacancy on the $FeO_2$ terminated surface causes mainly

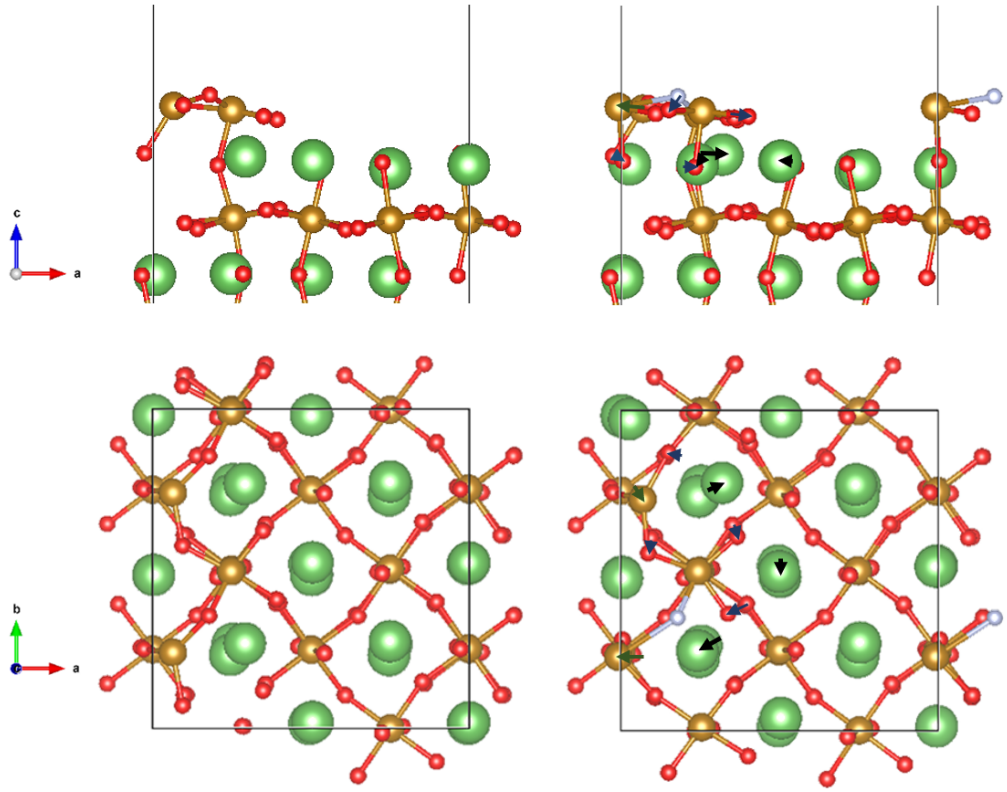


**Figure 7.6:** The pure surface (left) and the defective surface, containing an oxygen vacancy, (right) of the $FeO_2$ terminated (001) surface of $LaFeO_3$. The position of the oxygen vacancy is shown in grey. Arrows have been used to indicate the direction and magnitude of relaxation; black arrows show the relaxation of lanthanum ions, dark green the relaxation of iron ions and dark blue the relaxation of oxygen ions.

local changes to the closest ions, with one surface iron relaxing away from the vacancy significantly, while the closest sub surface lanthanum ion moves closer to the vacant site, along with the nearest neighbour surface oxygen ions.

Tables 7.2 and 7.3 show the surface defect formation energies compared to the neutral bulk defect formation energies presented in Chapter 4. The oxygen vacancy on the $FeO_2$ terminated surface is an O2 oxygen and therefore the energy of a bulk O2 oxygen vacancy has been used for comparison. For iron, bulk defect energies were calculated for both spin up and spin down iron ions. For the calculation of the surface iron vacancy energy, both a spin up and spin down iron vacancy were included in the supercell, to prevent a net magnetic moment across the vacuum of the supercell; therefore the defect energy for the surface iron vacancy has been compared to

the average of spin up and spin down bulk iron vacancies.

**Table 7.2:** The defect energies of neutral lanthanum, iron and oxygen vacancies on the $FeO_2$ terminated (001) surface of $LaFeO_3$ compared to the defect energies calculated for bulk $LaFeO_3$. The defect energies are for oxygen rich/ lanthanum and iron poor conditions.

| Defect | Formation Energy / eV | |
|---|---|---|
| | Surface | Bulk |
| $V_{La}^{X}$ | 1.898 | 3.333 |
| $V_{Fe}^{X}$ | -1.559 | 2.789 |
| $V_{O}^{X}$ | 1.219 | 3.829 |

**Table 7.3:** The defect energies of neutral lanthanum, iron and oxygen vacancies on the $FeO_2$ terminated (001) surface of $LaFeO_3$ compared to the defect energies calculated for bulk $LaFeO_3$. The defect energies are for oxygen poor/ lanthanum and iron rich conditions.

| Defect | Formation Energy / eV | |
|---|---|---|
| | Surface | Bulk |
| $V_{La}^{X}$ | 7.701 | 9.136 |
| $V_{Fe}^{X}$ | 4.244 | 8.592 |
| $V_{O}^{X}$ | -2.650 | -0.040 |

For all surface vacancies the surface defect formation energy is lower than the bulk formation energy. The minimum difference is 1.435 eV, which is observed between the bulk and surface lanthanum vacancies, while the maximum difference is seen for the iron vacancies, which have a 4.348 eV difference, the same differences are observed under both oxygen rich and oxygen poor conditions. The small difference between the lanthanum vacancies is probably due to the lanthanum ion being a sub-surface ion in this termination, compared to iron and oxygen which are surface ions. The large difference between the energies of the bulk iron vacancy and surface iron vacancy could be due to the previously discussed formation of the $O_2^-$ species on the $FeO_2$ terminated surface of $LaFeO_3$ when the surface has an iron vacancy, which, as noted above, is likely to stabilise this vacancy considerably, resulting in a substantially lower energy on the surface compared to within the bulk.

## 7.4 LaO Terminated Surface

Despite not containing the active transition metal, recently there has been an increased interest in the AO termination of perovskite oxides and related materials, as the subsurface transition metals could play a role in making this surface more active than previously thought.[203, 210] Therefore, as well as the commonly studied $FeO_2$ (001) termination of $LaFeO_3$, we have also investigated the surface stability of the LaO terminated surface. We shall discuss the stability of this termination in relation to the $FeO_2$ surface described above, as well as considering cationic and anionic defects and their formation energies in reference to the $FeO_2$ surface.

### 7.4.1 Surface Stability and Relaxation

Figure 7.7 shows the relaxed structure of the LaO terminated $LaFeO_3$ (001) surface (right) compared to the unrelaxed surface (left). The surface energy of this termination is 0.34 $Jm^{-2}$, lower than that for the $FeO_2$ termination.

The relaxation of the LaO terminated surface is minimal and only affects the top surface layer, with the lanthanum ions relaxing closer to the bulk material.

### 7.4.2 Defects

The calculated defect formation energies for neutral lanthanum, iron and oxygen vacancies under both oxygen rich/cation poor and oxygen poor/cation rich conditions are shown in Table 7.4. The formation energies were calculated using the same chemical potentials used in the bulk defect study.

**Table 7.4:** The defect formation energies of neutral lanthanum, iron and oxygen vacancies on the LaO terminated (001) surface of $LaFeO_3$. The defect energies have been calculated under oxygen rich/cation poor and oxygen poor/cation rich conditions.

| Defect | Defect Formation Energy / eV | |
|---|---|---|
| | O Rich & Cation Poor | O Poor & Cation Rich |
| $V_{La}^{X}$ | 1.610 | 7.413 |
| $V_{Fe}^{X}$ | 1.870 | 7.673 |
| $V_{O}^{X}$ | 3.109 | -0.760 |

We see that, as with defects on the $FeO_2$ terminated surface and bulk defects, cation vacancies are more favourable under cation poor conditions whereas oxygen va-

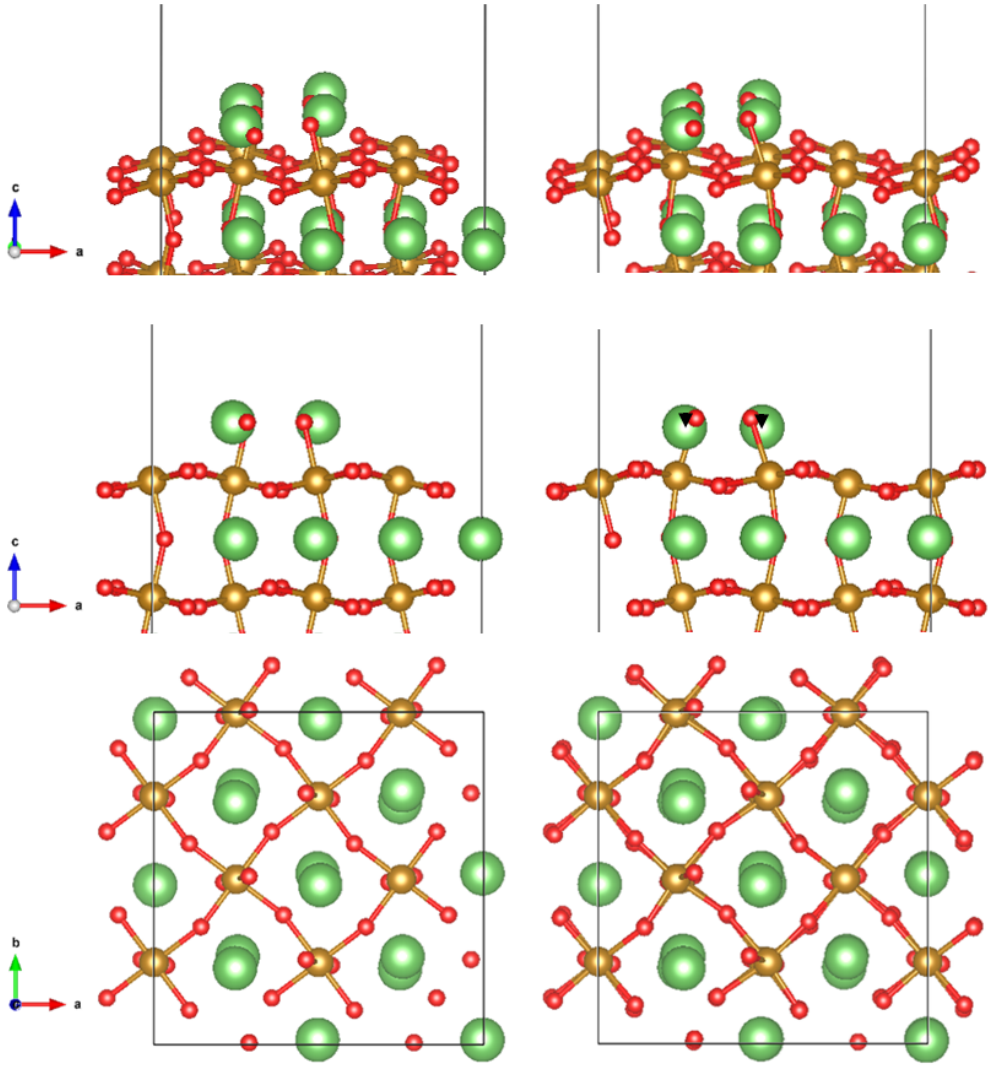


**Figure 7.7:** The unrelaxed (left) and relaxed (right) surface structure of the LaO terminated (001) surface of $LaFeO_3$. Arrows have been used to indicate the direction and magnitude of relaxation; black arrows show the relaxation of lanthanum ions.

cancies are more favourable under oxygen poor conditions. Under oxygen poor conditions, the oxygen vacancy has a negative formation energy, suggesting that they will form spontaneously, although as mentioned previously, the chemical potentials used in these calculations are extreme values and operating conditions are likely to be closer to O-rich, so oxygen vacancy formation energies are unlikely to be negative but will be low. Cation vacancies are less likely to form compared to oxygen vacancies, but the defect energy of both cation vacancies under cation poor

conditions suggest that they will be a significant concentration of these defects under these conditions. Lanthanum vacancies have slightly lower formation energies than iron under both conditions, which is probably due to lanthanum being the surface cation and therefore having a lower energy to remove. Figure 7.8, 7.9 and 7.10 show how the presence of each defect, a lanthanum, an iron and an oxygen vacancy, affects the structure of the LaO terminated surface.

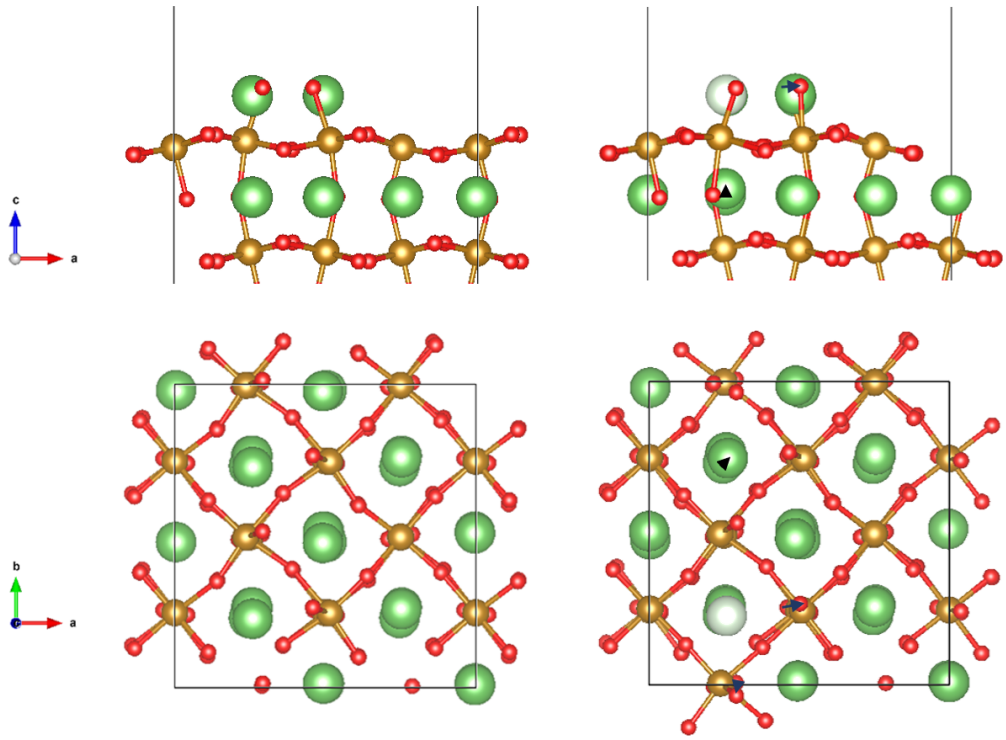


**Figure 7.8:** The pure surface (left) and the defective surface, containing a lanthanum vacancy, (right) of the LaO terminated (001) surface of $LaFeO_3$. The position of the lanthanum vacancy is shown in pale green. Arrows have been used to indicate the direction and magnitude of relaxation; black arrows show the relaxation of lanthanum ions, and dark blue the relaxation of oxygen ions.

When a lanthanum vacancy is introduced, only minor restructuring can be seen, with the two adjacent surface lanthanum ions moving closer (by 0.1 Å) to the site of the vacancy, whilst the nearest neighbour oxygen ions relax away from the site. A much larger restructuring is observed when an iron vacancy is introduced; again we see surface lanthanum ions moving closer to the site of the vacancy, with the relaxation of 0.4 and 0.7 Å, for the two closest lanthanum ions, being significantly

larger compared to when a lanthanum vacancy is introduced. We also observe the oxygen ions shifting away (by between 0.15 and 0.62 Å) from the vacancy site, as for lanthanum, but, again, the relaxation is more significant in the case of the iron vacancy compared to the lanthanum vacancy, both in terms of the distance the oxygen ions have relaxed and the number of oxygen ions that have been displaced. The larger effect of the iron vacancies on the structure of the surface compared to lanthanum vacancies, could also contribute to the iron vacancy having a higher formation energy compared to the lanthanum vacancy.

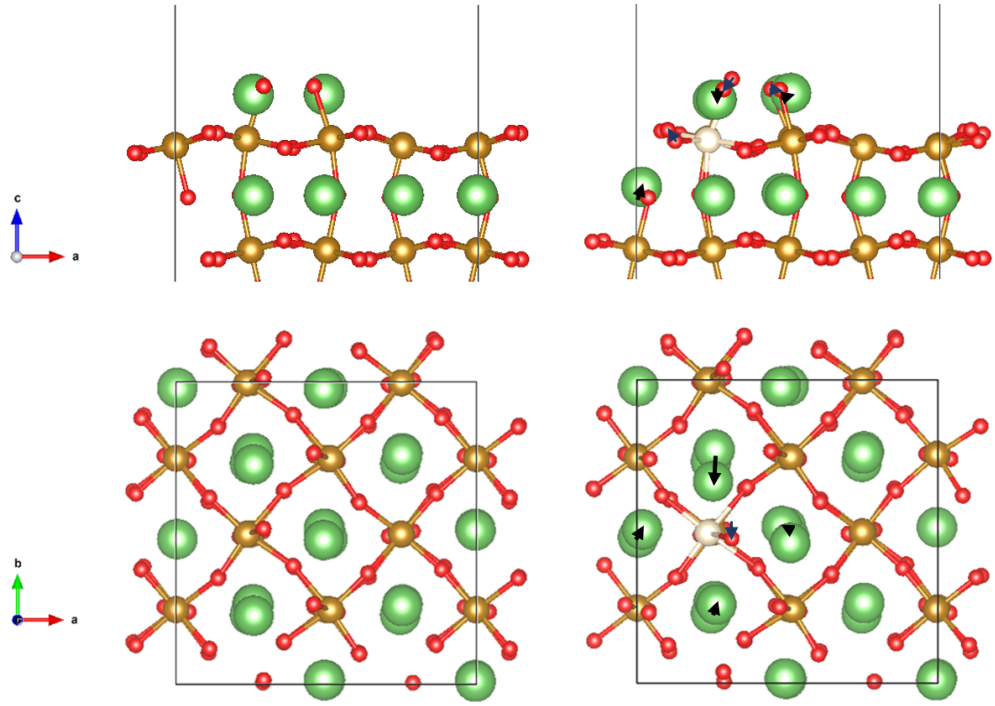


**Figure 7.9:** The pure surface (left) and the defective surface, containing an iron vacancy, (right) of the LaO terminated (001) surface of $LaFeO_3$. The position of the iron vacancy is shown in pale yellow. Arrows have been used to indicate the direction and magnitude of relaxation; black arrows show the relaxation of lanthanum ions and dark blue the relaxation of oxygen ions.

Examining how the oxygen vacancy affects the structure of the LaO terminated surface, we find that it does not cause a large amount of restructuring. Interestingly, a number of sub-surface oxygen ions move closer to the surface, to compensate for the vacant oxygen, while only a small relaxation is observed for both the iron and

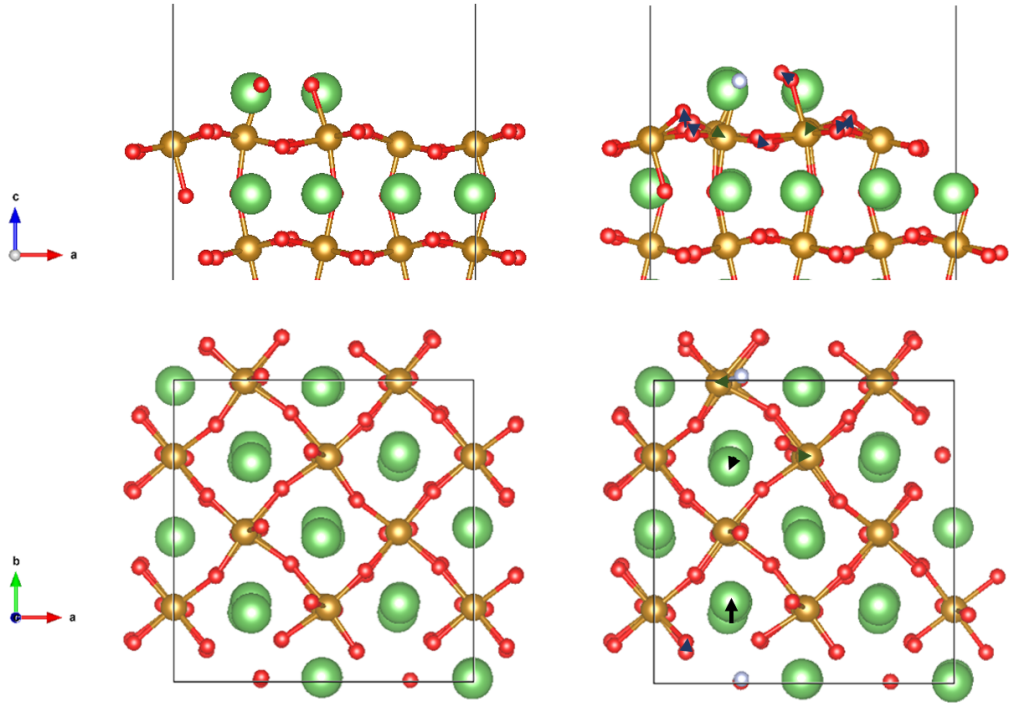


**Figure 7.10:** The pure surface (left) and the defective surface, containing an oxygen vacancy, (right) of the LaO terminated (001) surface of $LaFeO_3$. The position of the oxygen vacancy is shown in grey. Arrows have been used to indicate the direction and magnitude of relaxation; black arrows show the relaxation of lanthanum ions, dark green the relaxation of iron ions and dark blue the relaxation of oxygen ions.

lanthanum ions that are closest to the vacancy site.

Tables 7.5 and 7.6 show the surface defect formation energies compared to the neutral bulk defect formation energies presented in Chapter 4. The oxygen vacancy on the LaO terminated surface is an O1 oxygen and therefore the energy of a bulk O1 oxygen vacancy has been used for comparison. For iron, bulk defect energies were calculated for both spin up and spin down iron ions. As with the case of the $FeO_2$ terminated surface, for the calculation of the surface iron vacancy energy, both a spin up and spin down iron vacancy were included in the supercell, to prevent a net magnetic moment across the vacuum of the supercell; therefore, the defect energy for the surface iron vacancy is compared to the average of spin up and spin down bulk iron vacancies.

We see that for all vacancies, the surface formation energy is lower than the bulk formation energy; the differences being the same under both oxygen rich and poor

**Table 7.5:** The defect energies of neutral lanthanum, iron and oxygen vacancies on the LaO terminated (001) surface of $LaFeO_3$ compared to the defect energies calculated for bulk $LaFeO_3$. The defect energies are for oxygen rich/ lanthanum and iron poor conditions.

| Defect | Formation Energy / eV | |
|---|---|---|
| | Surface | Bulk |
| $V_{La}^X$ | 1.610 | 3.333 |
| $V_{Fe}^X$ | 1.870 | 2.789 |
| $V_O^X$ | 3.109 | 3.960 |

**Table 7.6:** The defect energies of neutral lanthanum, iron and oxygen vacancies on the LaO terminated (001) surface of $LaFeO_3$ compared to the defect energies calculated for bulk $LaFeO_3$. The defect energies are for oxygen poor/ lanthanum and iron rich conditions.

| Defect | Formation Energy / eV | |
|---|---|---|
| | Surface | Bulk |
| $V_{La}^X$ | 7.413 | 9.136 |
| $V_{Fe}^X$ | 7.673 | 8.592 |
| $V_O^X$ | -0.760 | 0.091 |

conditions. The biggest change is seen for lanthanum vacancies, with the difference between bulk and surface formation energies being 1.723 eV. The changes for iron and oxygen are similar; 0.919 and 0.851 eV respectively, the smaller difference for iron compared to lanthanum could be a consequence of lanthanum being the surface ion and therefore requiring less energy to remove than the sub surface iron ion.

## 7.5 Comparison of Surface Terminations

For the relaxed pure surface, we find that the LaO termination has a lower surface energy; 0.34 $Jm^{-2}$ compared to 0.50 $Jm^{-2}$ of the $FeO_2$ termination. The higher energy of the $FeO_2$ termination is probably caused by the breaking of the $FeO_6$ octahedra by the surface, requiring the surface to undergo significant relaxation to stabilise. The large relaxation required by the $FeO_2$ terminated surface compared to the LaO termination is reflected in the relaxation energies; -2.48 eV per surface unit cell ($1\times1\times7$) for $FeO_2$ compared to -0.96 eV per surface unit cell for the LaO termination.

Table 7.7 shows the defect formation energies for each defect on each termination,

under oxygen rich/cation poor conditions as these conditions are closest to operating conditions.

**Table 7.7:** The defect energies of neutral lanthanum, iron and oxygen vacancies on the $FeO_2$ and LaO terminated (001) surfaces of $LaFeO_3$. The defect energies are for oxygen rich/lanthanum and iron poor conditions.

| Defect | Formation Energy / eV | |
|---|---|---|
| | $FeO_2$ Terminated | LaO Terminated |
| $V_{La}^{X}$ | 1.90 | 1.61 |
| $V_{Fe}^{X}$ | -1.56 | 1.87 |
| $V_{O}^{X}$ | 1.22 | 3.11 |

The defect formation energies are generally lower on the $FeO_2$ terminated surface, the exception being the lanthanum vacancy, which has similar formation energies on both terminations but has a slightly lower formation energy on the LaO terminated surface, as it is the surface cation. These results suggest that the $FeO_2$ terminated surface will have a higher concentration of vacancies compared to the LaO terminated, which could be linked to the higher surface energy of the $FeO_2$ terminated surface.

The considerably lower formation energy of oxygen vacancies on the $FeO_2$ terminated surface compared to the LaO terminated surface agrees with the work of Lee *et al.*[200] However, the low formation of cation vacancies on the LaO terminated surface suggests there are likely to be cation vacancies present on the surface and sub-surface of the LaO terminated surface, which may cause the LaO terminated surface to be catalytically active, in disagreement with the conclusion of Lee *et al.*[200] but in agreement with the work of Kizaki *et al.*[203] on $LaFeO_3$ and Akbay *et al.*[210] on $La_2NiO_4$, as discussed in Chapter 1 Section 1.4.5. Recent experimental work by Stoerzinger *et al.*[346] found the LaO terminated (001) surface of $LaFeO_3$ to be more reactive towards water compared to the $FeO_2$ terminated (001) surface, with the LaO termination forming surface hydroxyls species and adsorbing water at lower relative humidity compared to the $FeO_2$ termination.

## 7.6 Summary and Conclusion

In this chapter, two terminations of the $LaFeO_3$ (001) surface, the $FeO_2$ and LaO terminations, have been studied. The surface energies and the defect formation energies of vacancies of all three ions have been calculated for both terminations. We found that the LaO terminated surface is more stable, having a lower surface energy than the $FeO_2$ termination. The $FeO_2$ termination is likely to be more defective, having low formation energies for lanthanum, iron and oxygen vacancies, suggesting it will be the most catalytically active of the two terminations. However, the low formation energies for cation vacancies, both lanthanum and iron, on the LaO terminated surface may suggest that this termination could also be catalytically active.

# Chapter 8

# Summary, Conclusions and Future Work

## 8.1 Introduction

In this thesis we have studied defects and dopants in bulk $LaFeO_3$, along with defects on the (001) terminated surface. $LaFeO_3$ is a promising base material for intermediate temperature solid oxide fuel cell cathode applications as a mixed ionic electronic conductor. By establishing the defect chemistry of the material we have gained greater understanding of the mixed ionic electronic conductivity of $LaFeO_3$ and can, therefore, suggest methods and approaches to maximising the conductivity schemes within this material, which are central to its promising performance as a SOFC cathode.

For our intrinsic defect study, we considered a range of isolated point defects along with various disorder schemes, followed by calculating the activation energy of oxide ion migration for which we considered three pathways, due to the two inequivalent oxygen sites in $LaFeO_3$. We then investigated a range of divalent dopants, for both the lanthanum and iron sites, calculating their solution energy and their binding energy to charge compensating species, in order to establish those easiest to incorporate and those that will promote conductivity within $LaFeO_3$. In these investigations, both interatomic potential-based techniques and DFT+$U$ were utilised and the results compared. Our final consideration was the surface chemistry of

$LaFeO_3$ in which we calculated defect energies for neutral vacancies of each of the three ions in $LaFeO_3$ on two terminations of the (001) surface; $FeO_2$ and LaO. As opposed to the defect and dopant studies, that used both interatomic potentials and DFT+$U$, only DFT+$U$ was employed for our surface calculations. Below we summarise our main results and our conclusions.

## 8.2 Main Conclusions

In our investigation of isolated point defects and disorder schemes in $LaFeO_3$ we considered vacancies, interstitials, anti-site defects, Frenkel disorder and Schottky disorder. In our DFT+$U$ calculations, defect energies were calculated under two conditions, oxygen rich / cation poor and oxygen poor / cation rich.

Our initial interatomic potential-based calculations suggested that anti-site defects would dominate in $LaFeO_3$ with this type of disorder having a lower energy than both Frenkel and Schottky disorder. However, results from our DFT+$U$-based calculations suggest that Schottky type disorder, instead of anti-site defects, plays an important role in the defect chemistry of $LaFeO_3$, in line with experimental results. The source of the high formation energies of Frenkel and Schottky disorder calculated by interatomic potentials was identified as an over-estimation of the formation energy of $LaFeO_3$; when comparing the formation energy calculated by interatomic potentials and DFT+$U$, DFT+$U$ is closer to the experimental value.

From our DFT+$U$ calculations, under oxygen rich conditions, we found cation vacancies to be the most favoured defect, with our results suggesting that they will form in significant enough concentrations as to contribute to the $p$-type conductivity in this material, as holes compensate for these cation vacancies. $La^{3+}$ vacancies displayed the lowest formation energy and are therefore likely to dominate, although the formation energy of $Fe^{3+}$ vacancies was also low under these conditions. Under oxygen poor conditions oxygen vacancies dominate - a promising results as the ionic conductivity of $LaFeO_3$ is dependent on oxygen vacancies. From our calculated defect formation energies we generated a model that established a value for the Fermi level in $LaFeO_3$ under each condition which were in agreement with the

experimental work of Jacob and Ranjani[307].

The migration of oxygen vacancies through $LaFeO_3$ is vital for increased activity as a SOFC cathode material. In our study of oxide ion migration, three pathways were considered: O1 to O1, O1 to O2 and O2 to O2.

As with our defect study, interatomic potentials were initially used to calculate the activation energy of oxide ion migration for our three pathways. Two pathways displayed low activation energies; 0.63 and 0.50 eV for the O1 to O2 and O2 to O2 respectively while the O1 to O1 pathway has a significantly higher activation energy of 1.87 eV. Therefore, our calculations suggest that the O2 to O2 pathway has the lowest activation energy, of those we have considered, in contrast to Jones and Islam,[27] who found that the O1 to O2 pathway had the lowest energy, a disagreement attributed to a difference in the defect energies of the oxygen vacancies at the beginning and end of the pathway. Our results from all three methods utilised in this work; interatomic potentials, DFT+$U$ and NEB, all found a similar migration barrier for the O1 to O2 pathway suggesting that the activation energy we have calculated is accurate and reliable.

Good agreement has been found for all three pathways across the different methods investigated in this work leading us to conclude that oxide ions will migrate via the O1 to O2 and O2 to O2 pathways in orthorhombic $LaFeO_3$ as both pathways have low migration barriers and are similar to the experimental migration barrier of 0.77 reported by Ishigaki *et al.*[16] The high energy associated with the O1 to O1 pathway is probably the result of the O1 oxide ions being opposite sides of the $FeO_6$ octahedra therefore the pathway between two O1 ions involves moving between two octahedra and includes passing between two large lanthanum ions. Both the O2 to O2 and O1 to O2 pathways involve migrating to a neighbouring position on the $FeO_6$ octahedra and therefore are much lower in energy.

Our work has successfully shown that oxide ion migration is a low energy process in $LaFeO_3$, in agreement with experimental results. In establishing the defect chemistry we found oxygen vacancies, as well as cation vacancies, need to be promoted further for increased catalytic activity. Thus, a range of dopants were considered on

both the A- and B-site of $LaFeO_3$ to establish which would be incorporated with low solution energies into $LaFeO_3$ and which are likely to promote desired conductivity species.

A range of divalent dopants were considered for both the A- and B-site in $LaFeO_3$. For the A-site, alkali earth ions magnesium, strontium, calcium and barium were considered, along with transition metal ions, manganese, iron, cobalt, nickel and copper. The same transition metals considered for the A-site were also investigated as B-site dopants, along with magnesium, as the smallest of the alkali earth ions included in this study. All dopants were considered in their divalent state and compensation via both oxygen vacancies and holes was investigated. Both results based on interatomic potentials and DFT+$U$ were reported. Although similar trends are observed between the two methods, for solution energies and binding energies, the binding energies calculated using interatomic potentials were significantly higher than those calculated using DFT+$U$. Our conclusions from this work are therefore based on the DFT+$U$ calculations, as the results are more in line with the observed ionic and electronic conductivities in doped $LaFeO_3$. Solution energies were calculated under both anion rich and anion poor conditions.

We found that, for the A-site, $Ca^{2+}$, $Sr^{2+}$ and $Ba^{2+}$ have low solution energies under anion rich conditions, with $Sr^{2+}$ and $Ca^{2+}$ emerging as the most appropriate due to a combination of low solution energy and minimal binding energies. For the A-site transition metal dopants, the solution energies are all comparable. However, manganese has low binding energies compared to other transition metal dopants, which, combined with Mn causing only minimum distortion to the surrounding $LaFeO_3$ lattice suggests that it would be the most appropriate transition metal A-site dopant in $LaFeO_3$. Although unexpected, further investigation, which included calculating the Goldschmidt tolerance factors for manganese as both an A- and B-site dopant, suggests manganese could be a viable A-site dopant, in contrast to its widely assumed B-site position.

For the B-site we found cobalt, nickel and magnesium to be the most favourable B-site dopants, due to low solution energies and low binding energies to oxygen

vacancies, along with minimal distortion - particularly for nickel - to the $LaFeO_3$ lattice.

Interestingly, we found that all dopants, in all sites, under anion rich conditions have similar solution energies when using either of the two charge compensation mechanisms investigated: oxygen vacancies and holes, which explains the origins of the mixed ionic electronic conductivity observed in doped $LaFeO_3$-based materials, such as LSCF.

In our surfaces study, the surface energy and defect chemistry of two terminations of the $LaFeO_3$ (001) surface, the $FeO_2$ and LaO terminations, were considered. Interatomic potential-based methods were not utilised here due to a known importance of the transition metal to the surface chemistry of $LaFeO_3$ and the challenges of accurately modelling transition metals using interatomic potentials.

From our DFT+$U$ calculations, we found that the LaO terminated surface is more stable, having a lower surface energy than the $FeO_2$ termination. However, the $FeO_2$ termination is likely to be more defective, having low formation energies for lanthanum, iron and oxygen vacancies. The presence of defects is vital for the catalytic process of a fuel cell cathode material and therefore it is likely that the $FeO_2$ termination will be more catalytically active than the LaO termination. The LaO termination, however, does exhibit low formation energies for cation vacancies, both lanthanum and iron, which may suggest that this termination could contribute to the catalytic activity of $LaFeO_3$.

## 8.3 Future Work

Through the work presented in this thesis we have made substantial progress towards understanding the defect chemistry, appropriate dopants and surface chemistry of $LaFeO_3$. However, there are two aspects which would benefit from further work.

Firstly, the findings in our dopants study, that manganese could occupy either the A- or B-site in $LaFeO_3$ would benefit from further probing, especially with experimental techniques. If our computational prediction is also observed experimentally, then

this could be a promising route to increasing the conductivity of $LaFeO_3$ as manganese can stably occupy a range of oxidation states, meaning it could significantly increases the electronic conductivity of $LaFeO_3$.

The second aspect that would benefit from further work is the study of $LaFeO_3$ surfaces. Having established the surface energy and formation energy of isolated defects on the $FeO_2$ and LaO terminated surface, further work is needed to understand fully the surface chemistry of $LaFeO_3$. Initially this work could include analysis of different surface sites for defects, particularly oxygen vacancies, to see if their formation energy depends on their position on the surface, along with an investigation of how the formation energy of an oxygen vacancy changes moving from the bulk material to the surface of the material, to understand how oxygen vacancies move through $LaFeO_3$. A similar investigation could also be performed on potential divalent dopants (strontium, calcium, manganese, cobalt and nickel). Calculating the solution energy of the dopant in the bulk and then in layers towards the surface, could help understand the surface segregation which has been observed, particular in strontium doped perovskites, and evaluate if other potential dopants we have identified also show a tendency to segregate towards the surface of $LaFeO_3$. Once a complete picture of the defect chemistry and dopant behaviour at the surface of $LaFeO_3$ has been established, the interaction of oxygen with the various defects and dopants on the surface could be investigated, providing further insight into how $LaFeO_3$ catalyses the oxygen reduction reaction and its promising behaviour as a base material for intermediate temperature SOFC applications.

# Appendix A

# How the *U*-Value Effects Defect Formation Energy

Table A.1 shows how the defect energy of a neutral oxygen vacancy, with reference to an oxygen molecule in its triplet state, changes as a function of the $U$ parameter applied to the $Fe^{3+}$ ion in $LaFeO_3$. A $U$-value of 7.0 eV has been used in all calculations in this work. This value produces a defect formation energy similar to those reported previously[119, 175] without compromising structural, magnetic and electronic properties of $LaFeO_3$.

**Table A.1:** The defect formation energies of neutral oxygen vacancies and how they change with increasing $U$-value.

| $U$ | Defect Formation Energy / eV |
|---|---|
| 3 | 4.313 |
| 4 | 4.258 |
| 5 | 4.160 |
| 6 | 4.068 |
| 7 | 3.960 |
| 8 | 3.871 |

# Appendix B

# Analysis of $U$-Values for Transition Metal Dopants

The most appropriate value for $U$ to use for each transition metal dopant was assessed by comparing structural, electronic and magnetic properties of its associated metal oxide, at increasing values of $U$, with experimental values. As each dopant was divalent, we used the monoxide in our calculations. Below are the results for this study for $Co^{2+}$, $Ni^{2+}$, $Cu^{2+}$ and $Mn^{2+}$, in Tables B.1, B.2, B.3 and B.4 respectively.

**Table B.1:** Calculated lattice parameters; a, b and c, bond lengths, angles, relaxed cell volume, bulk modulus and magnetic moment of CoO for increasing values of $U$, from 3 to 7 eV, along with experimental values. [a]Ref[8], [b]Ref[9], [c]Ref[10].

| Parameters / $U$ | Exp. | 3 | 4 | 5 | 6 | 7 |
|---|---|---|---|---|---|---|
| a / Å | 4.2603[a] | 4.308 | 4.308 | 4.306 | 4.305 | 4.302 |
| b / Å | 4.2603[a] | 4.308 | 4.308 | 4.306 | 4.305 | 4.302 |
| c / Å | 4.2603[a] | 4.308 | 4.308 | 4.306 | 4.305 | 4.302 |
| Co - O / Å | 2.130[a] | 2.154 | 2.154 | 2.153 | 2.152 | 2.151 |
| Co - Co / Å | 3.012[a] | 3.046 | 3.046 | 3.045 | 3.044 | 3.042 |
| Co - O - Co / ° | 90.0[a] | 90.0 | 90.0 | 90.0 | 90.0 | 90.0 |
| Volume of Cell / Å$^3$ | 77.33[a] | 79.920 | 79.920 | 79.860 | 79.770 | 79.620 |
| Bulk Modulus / GPa | 190.5[b] | 172.350 | 173.490 | 171.330 | 169.820 | 168.260 |
| Magnetic Moment / $\mu_B$ | 3.8[c] | $\pm$ 2.731 | $\pm$ 2.767 | $\pm$ 2.799 | $\pm$ 2.829 | $\pm$ 2.858 |

**Table B.2:** Calculated lattice parameters; a, b and c, bond lengths, angles, relaxed cell volume, bulk modulus and magnetic moment of NiO for increasing values of *U*, from 3 to 7 eV, along with experimental values.[a]Ref[11], [b]Ref[12], [c]Ref[10].

| Parameters / *U* | Exp. | 3 | 4 | 5 | 6 | 7 |
|---|---|---|---|---|---|---|
| a / Å | 4.1781[a] | 4.228 | 4.224 | 4.219 | 4.214 | 4.208 |
| b / Å | 4.1781[a] | 4.228 | 4.224 | 4.219 | 4.214 | 4.208 |
| c / Å | 4.1781[a] | 4.228 | 4.224 | 4.219 | 4.214 | 4.208 |
| Ni - O / Å | 2.089[a] | 2.114 | 2.112 | 2.110 | 2.107 | 2.104 |
| Ni - Ni / Å | 2.954[a] | 2.990 | 2.987 | 2.983 | 2.980 | 2.975 |
| Ni - O - Ni / ° | 90.0[a] | 90.0 | 90.0 | 90.0 | 90.0 | 90.0 |
| Volume of Cell / Å$^3$ | 72.93[a] | 75.570 | 75.350 | 75.110 | 74.830 | 74.510 |
| Bulk Modulus / GPa | 191[b] | 186.310 | 184.860 | 183.470 | 181.980 | 180.230 |
| Magnetic Moment / $\mu_B$ | 1.9[c] | 1.715 | 1.748 | 1.780 | 1.811 | 1.842 |

**Table B.3:** Calculated lattice parameters; a, b and c, bond lengths, angles, relaxed cell volume, bulk modulus and magnetic moment of CuO for increasing values of *U*, from 3 to 7 eV, along with experimental values.[a]Ref[13], [b]Ref[14], [c]Ref[15].

| Parameters / *U* | Exp. | 3 | 4 | 5 | 6 | 7 |
|---|---|---|---|---|---|---|
| a / Å | 4.6833[a] | 4.394 | 4.349 | 4.435 | 4.479 | 4.558 |
| b / Å | 3.4208[a] | 3.886 | 3.907 | 3.768 | 3.688 | 3.594 |
| c / Å | 5.1294[a] | 5.183 | 5.162 | 5.160 | 5.143 | 5.108 |
| Cu - O / Å | 1.951[a] | 1.961 | 1.955 | 1.950 | 1.946 | 1.948 |
| Cu - O / Å | 1.961[a] | 1.960 | 1.955 | 1.951 | 1.946 | 1.948 |
| Cu - Cu / Å | 2.9[a] | 2.938 | 2.925 | 2.912 | 2.902 | 2.902 |
| Cu - O - Cu / ° | 145.932[a] | 120.867 | 123.702 | 126.139 | 129.833 | 136.328 |
| Cu - O - Cu / ° | 108.781[a] | 120.311 | 116.317 | 118.212 | 116.846 | 113.188 |
| Cu - O - Cu / ° | 104.001[a] | 111.668 | 112.224 | 110.480 | 109.354 | 107.404 |
| O - Cu - O / ° | 95.684[a] | 97.002 | 96.867 | 96.615 | 96.464 | 96.342 |
| Volume of Cell / Å$^3$ | 81.03[a] | 88.970 | 88.120 | 86.630 | 85.310 | 83.870 |
| Bulk Modulus / GPa | 98[b] | 53.460 | 51.230 | 55.990 | 56.920 | 57.290 |
| Magnetic Moment / $\mu_B$ | 0.653[c] | ±0.552 | ±0.584 | ±0.611 | ±0.639 | ±0.669 |

**Table B.4:** Calculated lattice parameters; a, b and c, bond lengths, angles, relaxed cell volume, bulk modulus and magnetic moment of MnO for increasing values of *U*, from 3 to 7 eV, along with experimental values.[a]Ref[11], [b]Ref[9], [c]Ref[10].

| Parameters / *U* | Exp. | 3 | 4 | 5 | 6 | 7 |
|---|---|---|---|---|---|---|
| a / Å | 4.4461[a] | 4.491 | 4.498 | 4.504 | 4.509 | 4.512 |
| b / Å | 4.4461[a] | 4.491 | 4.498 | 4.504 | 4.509 | 4.512 |
| c / Å | 4.4461[a] | 4.491 | 4.498 | 4.504 | 4.509 | 4.512 |
| Mn - O / Å | 2.223[a] | 2.256 | 2.249 | 2.252 | 2.254 | 2.256 |
| Mn - Mn / Å | 3.14[a] | 3.191 | 3.181 | 3.185 | 3.188 | 3.191 |
| Mn - O - Mn / ° | 90.0[a] | 90.0 | 90.0 | 90.0 | 90.0 | 90.0 |
| Volume of Cell / Å$^3$ | 87.88[a] | 90.570 | 91.000 | 91.370 | 91.660 | 91.880 |
| Bulk Modulus / GPa | 144[b] | 146.220 | 145.010 | 143.860 | 142.800 | 141.810 |
| Magnetic Moment / $\mu_B$ | 5.0[c] | ±4.596 | ±4.640 | ±4.681 | ±4.719 | ±4.755 |

# Appendix C

# Convergence of Supercell Size

Table C.1 shows the defect energy, the difference between a perfect supercell and a defective supercell, of oxygen vacancies in $LaFeO_3$ with increasing supercell size. The results show how this energy has converged at $2\times2\times1$, with an increase to $2\times2\times2$ making a minimal difference, considering its increased computational cost.

**Table C.1:** The defect energies of oxygen vacancies for the two inequivalent oxygen sites at increasing supercell size.

| Supercell Size | $E_D$ | |
|---|---|---|
| | O1 | O2 |
| $1\times1\times1$ | 10.179 | 10.102 |
| $2\times1\times1$ | 8.752 | 8.669 |
| $2\times2\times1$ | 8.717 | 8.585 |
| $2\times2\times2$ | 8.609 | 8.567 |

# Appendix D

# Spin State of $Fe^{3+}$ Ions in $LaFeO_3$

Here, several different magnetic configurations of $Fe^{3+}$ ions were investigated to find the most favourable and therefore the magnetic ground state, according to our model, using PBE+*U*. Ferromagnetic, antiferromagnetic C, antiferromagnetic A and antiferromagnetic G ordering of the $Fe^{3+}$ ions were investigated, the configurations of each are shown in Figure D.1 a to d respectively. Antiferromagnetic G has the lowest formation energy and is therefore most favourable. This is in agreement with experimental findings.[4]

**Table D.1:** The cohesive energy calculated for the different magnetic configurations of $Fe^{3+}$ ion in $LaFeO_3$, calculations performed using PBE+*U*.

| Configurations | Cohesive Energy / eV |
|---|---|
| Ferromagnetism | -152.346 |
| Antiferromagnetism G | -153.152 |
| Antiferromagnetism C | -151.602 |
| Antiferromagnetism A | -151.294 |

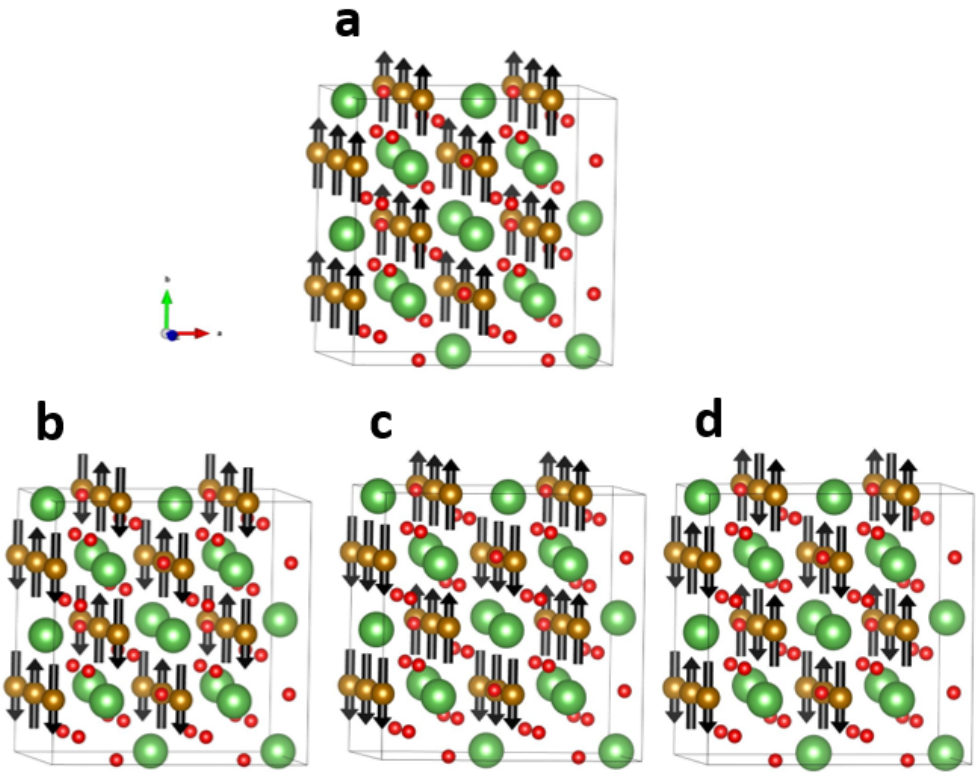


**Figure D.1:** Four different possible magnetic orientations for the spins on $Fe^{3+}$ relative to neighbouring iron ions; (a) Ferromagnetism, (b) Antiferromagnetism C, (c) Antiferromagnetism A and (d) Antiferromagnetism G.

## Appendix E

# Interatomic Potentials Study of Oxide Ion Migration

In our interatomic potentials study of oxide ion migration in $LaFeO_3$, five points were chosen in a straight line between the two oxygen vacancy sites, a grid was then constructed at each point to find the lowest energy position for the migrating oxide ion in the local area of each point. In this appendix we provide further details of this process. Figure E.1 shows how the grid was constructed at each point while the initial coordinates (i.e. when i = 0 and j = 0) are given for each point of each pathway below, along with how the coordinates of the migrating oxide ion are shifted when increasing i or j.

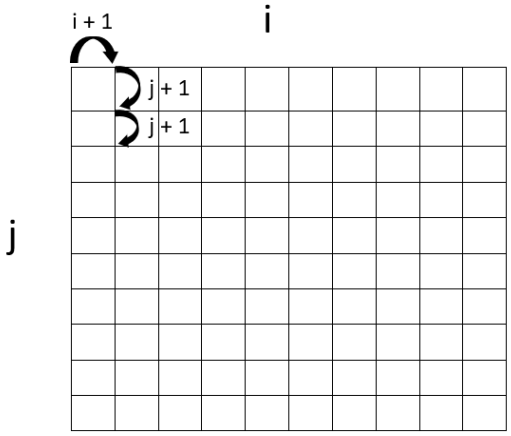


**Figure E.1:** Graphical representation of how a grid is constructed for each point in each pathway. Each pathway has a different directional shifts along the **x**, **y** and **z** directions within the $LaFeO_3$ lattice when moved in i and j.

## E.1 Path O2-O2

Table E.1 shows the initial Cartesian coordinates for each point in the O2 to O2 pathway, while Table E.2 shows how the lattice parameters are changed with increasing i and j.

**Table E.1:** The initial Cartesian coordinates for each point in the O2 to O2 pathway.

| Point | Lattice Parameter | | |
|---|---|---|---|
| | **x** | **y** | **z** |
| Point 1 | 1.240 | -1.421 | 2.165 |
| Point 2 | 1.503 | -2.677 | 1.093 |
| Point 3 | 1.966 | -2.607 | 0.998 |
| Point 4 | 2.529 | -1.875 | 1.392 |
| Point 5 | 2.892 | -2.468 | 0.809 |

**Table E.2:** The shift in lattice parameters for each grid direction; i and j.

| Grid Direction | Lattice Parameter Shift | | |
|---|---|---|---|
| | **x** | **y** | **z** |
| i | +0.050 | 0 | 0 |
| j | 0 | +0.331 | +0.244 |

Table E.3 shows the optimised position, in Cartesian coordinates, of the migrating oxide ion at each point in the O2 to O2 pathway. The optimised position was chosen as the position on the grid that has the lowest energy.

**Table E.3:** The Cartesian coordinates of the oxide ion in its optimised position at each point in the O2 to O2 pathway.

| Point | Lattice Parameter | | |
|---|---|---|---|
| | **x** | **y** | **z** |
| Point 1 | 1.390 | 1.230 | 4.120 |
| Point 2 | 1.643 | 1.499 | 4.172 |
| Point 3 | 2.036 | 1.568 | 4.078 |
| Point 4 | 3.759 | 1.638 | 3.983 |
| Point 5 | 3.732 | 1.708 | 3.888 |

## E.2 Path O1-O2

Table E.4 shows the initial Cartesian coordinates for each point in the O1 to O2 pathway, while Table E.5 shows how the lattice parameters are changed with increases in i and j.

**Table E.4:** The initial Cartesian coordinates for each point in the O1 to O2 pathway.

| Point | Lattice Parameter | | |
|---|---|---|---|
| | **x** | **y** | **z** |
| Point 1 | -0.912 | 1.475 | 3.153 |
| Point 2 | -0.708 | 1.696 | 3.528 |
| Point 3 | -0.505 | 1.917 | 3.903 |
| Point 4 | -0.302 | 2.137 | 4.278 |
| Point 5 | -0.099 | 2.358 | 4.653 |

**Table E.5:** The shift in lattice parameters for each grid direction; i and j.

| Grid Direction | Lattice Parameter Shift | | |
|---|---|---|---|
| | **x** | **y** | **z** |
| i | +0.300 | 0 | 0 |
| j | 0 | +0.276 | -0.163 |

Table E.6 shows the optimised position, in Cartesian coordinates, of the migrating oxide ion at each point in the O1 to O2 pathway. The optimised position was chosen as the position on the grid that has the lowest energy.

**Table E.6:** The Cartesian coordinates of the oxide ion in its optimised position at each point in the O1 to O2 pathway.

| Point | Lattice Parameter | | |
|---|---|---|---|
| | **x** | **y** | **z** |
| Point 1 | 0.588 | 3.132 | 2.178 |
| Point 2 | 0.792 | 3.353 | 2.553 |
| Point 3 | 0.995 | 3.574 | 2.928 |
| Point 4 | 1.198 | 3.794 | 3.302 |
| Point 5 | 1.701 | 3.739 | 3.840 |

## E.3 Path O1-O1

Table E.7 shows the initial Cartesian coordinates for each point in the O1 to O1 pathway, while Table E.8 shows how the lattice parameters are changed with increases in i and j.

**Table E.7:** The initial Cartesian coordinates for each point in the O1 to O1 pathway.

| Point | Lattice Parameter | | |
|---|---|---|---|
| | **x** | **y** | **z** |
| Point 1 | 2.499 | 1.288 | 5.396 |
| Point 2 | 2.834 | 1.755 | 5.396 |
| Point 3 | 3.169 | 2.221 | 5.396 |
| Point 4 | 3.504 | 2.688 | 5.396 |
| Point 5 | 3.839 | 3.155 | 5.396 |

**Table E.8:** The shift in lattice parameters for each grid direction; i and j.

| Grid Direction | Lattice Parameter Shift | | |
|---|---|---|---|
| | **x** | **y** | **z** |
| i | +0.200 | -0.144 | 0 |
| j | 0 | 0 | +0.100 |

Table E.9 shows the optimised position, in Cartesian coordinates, of the migrating oxide ion at each point in the O1 to O1 pathway. The optimised position was chosen as the position on the grid that has the lowest energy.

**Table E.9:** The Cartesian coordinates of the oxide ion in its optimised position at each point in the O1 to O1 pathway.

| Point | Lattice Parameter | | |
|---|---|---|---|
| | **x** | **y** | **z** |
| Point 1 | 3.499 | 0.570 | 5.896 |
| Point 2 | 3.834 | 1.037 | 5.896 |
| Point 3 | 4.369 | 1.360 | 5.896 |
| Point 4 | 4.704 | 1.827 | 5.896 |
| Point 5 | 5.039 | 2.293 | 5.896 |

## Appendix F

# The NEB Study of Oxide Ion Migration

For the nudged elastic band (NEB) study of oxide ion migration in $LaFeO_3$ only two pathways were considered; O2 to O2 and O1 to O2, due to the high activation energy calculated for the O1 to O1 pathway during the interatomic potentials study. For each pathway, five images were generated and optimised. The optimised position, in fractional coordinates, of the migrating oxide ion in each image are given in Tables F.1 and F.2 for pathways O2 to O2 and O1 to O2 respectively.

**Table F.1:** The optimised fractional coordinates for each image in the O2 to O2 pathway.

| Point | Lattice Parameter | | |
|---|---|---|---|
| | **x** | **y** | **z** |
| Image 1 | 0.612 | 0.373 | 0.528 |
| Image 2 | 0.566 | 0.394 | 0.503 |
| Image 3 | 0.512 | 0.400 | 0.492 |
| Image 4 | 0.462 | 0.401 | 0.485 |
| Image 5 | 0.416 | 0.397 | 0.474 |

**Table F.2:** The optimised fractional coordinates for each image in the O1 to O2 pathway.

| Point | Lattice Parameter | | |
|---|---|---|---|
| | **x** | **y** | **z** |
| Image 1 | 0.368 | 0.147 | 0.976 |
| Image 2 | 0.387 | 0.156 | 0.915 |
| Image 3 | 0.410 | 0.178 | 0.858 |
| Image 4 | 0.430 | 0.201 | 0.813 |
| Image 5 | 0.447 | 0.227 | 0.776 |

## Appendix G

# Oxide Ion Migration: Vacancy Diffusion Coefficients

In our work, we have calculated the activation energy of oxide ion migration in $LaFeO_3$ using interatomic potentials and DFT+*U*. Experimentally, the diffusion coefficient is measured at a range of temperatures and the activation energy is calculated from the gradient of a plot of the natural log of the diffusion coefficient against 1/T, where T is temperature.

We are interested in the vacancy diffusion coefficient of $LaFeO_3$ as the migration of oxide ions depends on the vacancy diffusion coefficient along with the concentration of oxygen vacancies. Ishigaki *et al.*[16] calculated the vacancy diffusion coefficients of $LaFeO_3$ in the temperature range of 900 to 1100°C, see Table G.1.

**Table G.1:** The vacancy diffusion coefficients of $LaFeO_3$ reported by Ishigaki *et al.*[16] at varying temperatures.

| Temperature / °C | $D_V$ |
|---|---|
| 900 | $4.02\times10^{-6}$ |
| 950 | $3.64\times10^{-6}$ |
| 1000 | $7.44\times10^{-6}$ |
| 1050 | $9.06\times10^{-6}$ |
| 1100 | $1.07\times10^{-5}$ |

We want to estimate a value within the intermediate temperature region for SOFCs (between 500 and 800 °C) to evaluate the effect decreasing the temperature from current operating temperatures; 1000°C, to intermediate temperatures has on oxide

ion migration. The estimate was calculated by plotting the values reported by Ishigaki *et al.*[16], shown in Figure G.1 and using the gradient to calculate a value at 800°C.

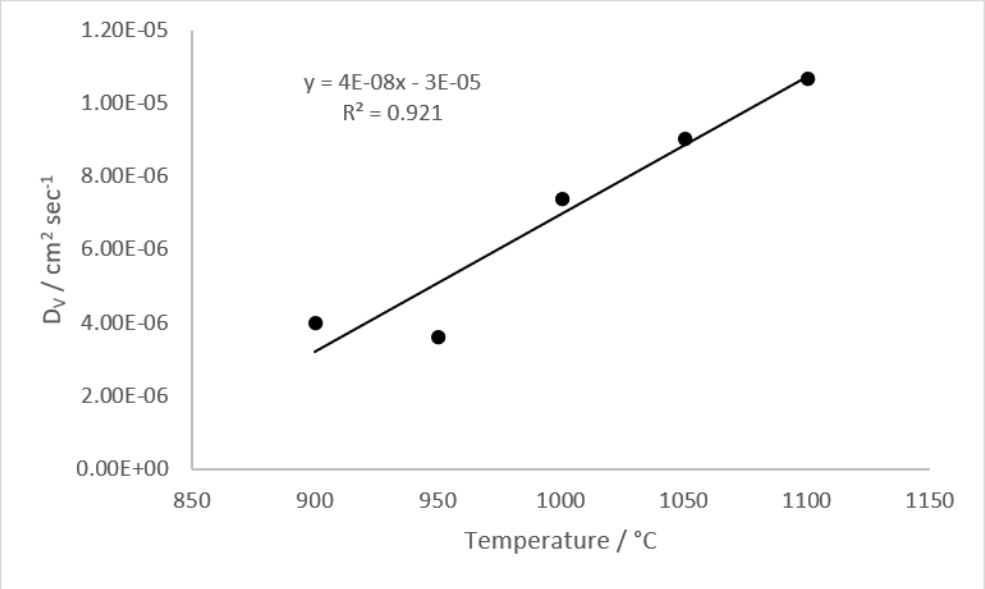


**Figure G.1:** A plot of the vacancy diffusion coefficients ($D_v$) reported by Ishigaki *et al.*[16] with the line of best fit used to estimate a vacancy diffusion coefficient for $LaFeO_3$ at 800°C.

## Appendix H

# Convergence of Parameters used in Surface Calculations

For our $LaFeO_3$ surface calculations, a number of parameters were optimised to ensure the accuracy of our surface model. The parameters that needed establishing were; the size of the vacuum between the two surfaces of our slab, which needed to be large enough to stop the two surfaces interacting, the number of layers in our slab, which needed to be large enough to include both surface-like layers and bulk-like layers, and the number of *k*-points. The results from the optimisation process for both terminations are presented in this appendix.

## H.1 $FeO_2$ Termination

**Table H.1:** The calculated energy of the $FeO_2$ terminated (001) surface slab of $LaFeO_3$ at increasing vacuum size.

| Vacuum / Å | Energy / eV | Energy atom$^{-1}$ / eV |
|---|---|---|
| 2 | -141.236 | -7.062 |
| 4 | -139.321 | -6.966 |
| 6 | -139.147 | -6.957 |
| 8 | -139.130 | -6.956 |
| 10 | -139.129 | -6.956 |
| 12 | -139.129 | -6.956 |
| 14 | -139.129 | -6.956 |
| 16 | -139.129 | -6.956 |
| 18 | -139.130 | -6.956 |
| 20 | -139.130 | -6.957 |

When establishing the number of layers to use in the slab model, the number of layers in increased until the surface energy is converged, the surface energy, for this purpose, is calculated using the following equation

$$\gamma = \frac{1}{2}E_{surface} - nE_{bulk} \tag{H.1}$$

To aid in the convergence of the surface energy, an adjusted bulk energy is calculated from the gradient of $E_{slab}$ plotted against n, referred to as Fitted $E_{bulk}$. Fitted $E_{bulk}$ is then used in the place of $E_{bulk}$ in equation H.1 to calcuate the surface energy. The energy of the slab, the original bulk energy, fitted bulk energy and surface energy are reported in Table H.2.

**Table H.2:** The surface energy, Fitted $E_{surf}$, of the $FeO_2$ terminated (001) surface of $LaFeO_3$ with increasing number of slab layers. The energy of the slab, $E_{slab}$ and the $LaFeO_3$ bulk energy, Fitted $E_{bulk}$ are used to calculated the surface energy.

| No. of Layers | $E_{slab}$ | $E_{bulk}$ | Fitted $E_{bulk}$ | Fitted $E_{surf}$ |
|---|---|---|---|---|
| 8 | -291.357 | -151.855 | -151.165 | 5.487 |
| 12 | -442.396 | -151.855 | -151.165 | 5.550 |
| 16 | -593.433 | -151.855 | -151.165 | 5.614 |
| 20 | -744.469 | -151.855 | -151.165 | 5.678 |
| 24 | -895.507 | -151.855 | -151.165 | 5.742 |
| 28 | -1046.546 | -151.855 | -151.165 | 5.805 |
| 32 | -1197.583 | -151.855 | -151.165 | 5.869 |
| 36 | -1348.623 | -151.855 | -151.165 | 5.931 |

For optimising *k*-points for the slab model of $LaFeO_3$, only *k*-points in the a and b directions need to be optimised, as this will give us information regarding the slab, whereas *k*-points in the c-direction will include information about the vacuum which we do not need.

## H.2 LaO Termination

The vacuum size, number of layers and *k*-points were optimised for the LaO terminated (001) surface in the same way as the $FeO_2$ terminated surface, the results are presented below, see section H.1 for calculation details.

**Table H.3:** The energy of the $FeO_2$ terminated (001) surface slab of $LaFeO_3$ at increasing *k*-points.

| *k*-points | Energy / eV | Energy atom$^{-1}$ / eV |
|---|---|---|
| 1×1×1 | -1020.462 | -7.289 |
| 2×2×1 | -1045.910 | -7.471 |
| 3×3×1 | -1046.522 | -7.475 |
| 4×4×1 | -1046.546 | -7.475 |
| 5×5×1 | -1046.546 | -7.475 |
| 6×6×1 | -1046.547 | -7.475 |
| 7×7×1 | -1046.547 | -7.475 |
| 8×8×1 | -1046.547 | -7.475 |

**Table H.4:** The calculated energy of the LaO terminated (001) surface slab of $LaFeO_3$ at increasing vacuum size.

| Vacuum / Å | Energy / eV | Energy/atom / eV |
|---|---|---|
| 2 | -294.755 | -7.369 |
| 4 | -291.854 | -7.296 |
| 6 | -291.393 | -7.285 |
| 8 | -291.341 | -7.284 |
| 10 | -291.336 | -7.283 |
| 12 | -291.337 | -7.283 |
| 14 | -139.129 | -6.956 |
| 16 | -139.129 | -6.956 |
| 18 | -139.130 | -6.956 |
| 20 | -139.130 | -6.957 |

**Table H.5:** The surface energy, Fitted $E_{surf}$, of the LaO terminated (001) surface of $LaFeO_3$ with increasing number of slab layers. The energy of the slab, $E_{slab}$ and the $LaFeO_3$ bulk energy, Fitted $E_{bulk}$ are used to calculated the surface energy.

| No. of Layers | $E_{slab}$ | $E_{bulk}$ | Fitted $E_{bulk}$ | Fitted $E_{surf}$ |
|---|---|---|---|---|
| 8 | -291.338 | -151.855 | -150.808 | 5.139 |
| 12 | -442.377 | -151.855 | -150.808 | 5.023 |
| 16 | -593.414 | -151.855 | -150.808 | 4.908 |
| 20 | -744.450 | -151.855 | -150.808 | 4.794 |
| 24 | -888.957 | -151.855 | -150.808 | 7.945 |
| 28 | -1046.527 | -151.855 | -150.808 | 4.564 |
| 32 | -1197.565 | -151.855 | -150.808 | 4.449 |
| 36 | -1348.604 | -151.855 | -150.808 | 4.333 |

**Table H.6:** The energy of the LaO terminated (001) surface slab of $LaFeO_3$ at increasing *k*-points.

| *k*-points | Energy / eV | Energy atom$^{-1}$ / eV |
|---|---|---|
| 1×1×1 | -1020.461 | -7.289 |
| 2×2×1 | -1045.906 | -7.471 |
| 3×3×1 | -1046.547 | -7.475 |
| 4×4×1 | -1046.528 | -7.475 |
| 5×5×1 | -1046.528 | -7.475 |
| 6×6×1 | -1046.528 | -7.475 |
| 7×7×1 | -1046.529 | -7.475 |
| 8×8×1 | -1046.528 | -7.475 |

# Bibliography


[1] P. W. Tasker. The Stability of Ionic Crystal Surfaces. *Journal of Physics C: Solid State Physics*, 12(22):4977–4984, 1979.

[2] M. Marezio and P. D. Dernier. The Bond Lengths in $LaFeO_3$. *Materials Research Bulletin*, 6(1):23–29, 1971.

[3] T. Arima, Y. Tokura, and J. B. Torrance. Variation of Optical Gaps in Perovskite-Type 3*d* Transition-Metal Oxides. *Physical Review B*, 48(23):17006–17009, 1993.

[4] W. C. C. Koehler and E. O. O. Wollan. Neutron-Diffraction Study of the Magnetic Properties of Perovskite-Like Compounds $LaBO_3$. *Journal of Physics and Chemistry of Solids*, 2(2):100–106, 1957.

[5] K. K. Bhargav, S. Ram, and S. B. Majumder. Small Polaron Conduction in Lead Modified Lanthanum Ferrite Ceramics. *Journal of Alloys and Compounds*, 638:334–343, 2015.

[6] G. Thornton, B. C. Tofield, and A. W. Hewat. A Neutron Diffraction Study of $LaCoO_3$ in the Temperature Range $4.2 < T < 1248$ K. *Journal of Solid State Chemistry*, 61(3):301–307, 1986.

[7] P. G. Radaelli and S.-W. Cheong. Structural Phenomena Associated with the Spin-State Transition in $LaCoO_3$. *Physical Review B*, 66(9):094408, 2002.

[8] R. E. Carter, F. D. Richardson, and C. Wagner. Oxidation of Cobalt Metal. *Journal of The Minerals, Metals and Materials Society*, 7(2):336–343, 1955.

[9] R. L. Clendenen and H. G. Drickamer. Lattice Parameters of Nine Oxides and Sulfides as a Function of Pressure. *The Journal of Chemical Physics*, 44(11):4223–4228, 1966.

[10] W. L. Roth. Magnetic Structures of MnO, FeO, CoO, and NiO. *Physical Review*, 110(6):1333–1341, 1958.

[11] S. Sasaki, K. Fujino, and Y. Takeuchi. X-ray Determination of Electron-Density Distributions in Oxides, MgO, MnO, CoO, and NiO, and Atomic Scattering Factors of their Constituent Atoms. *Proceedings of the Japan Academy*, 55:43–48, 1979.

[12] Y. Noguchi, M. Uchino, H. Hikosaka, T. Atou, K. Kusaba, K. Fukuoka, T. Mashimo, and Y. Syono. Equation of State of NiO Studied by Shock Compression. *Journal of Physics and Chemistry of Solids*, 60(4):509–514, 1999.

[13] N. E. Brese, M. O'Keeffe, B. L. Ramakrishna, and R. B. Von Dreele. Low-Temperature Structures of CuO and AgO and their Relationships to those of MgO and PdO. *Journal of Solid State Chemistry*, 89(1):184–190, 1990.

[14] S. Årsbrink, L. Gerward, J. Staun Olsen, and S. Steenstrup. High Pressure Studies up to 50GPa of CuO. *High Pressure Research*, 10(3):515–521, 1992.

[15] J. B. Forsyth, P. J. Brown, and B. M. Wanklyn. Magnetism in Cupric Oxide. *Journal of Physics C: Solid State Physics*, 21:2917–2929, 1988.

[16] T. Ishigaki, S. Yamauchi, J. Mizusaki, K. Fueki, H. Naito, and T. Adachi. Diffusion of Oxide Ions in $LaFeO_3$ Single Crystal. *Journal of Solid State Chemistry*, 55(1):50–53, 1984.

[17] K. T. Lee and A. Manthiram. Comparison of $Ln_{0.6}Sr_{0.4}CoO_{3-\delta}$ (Ln=La, Pr, Nd, Sm, and Gd) as Cathode Materials for Intermediate Temperature Solid Oxide Fuel Cells. *Journal of The Electrochemical Society*, 153(4):A794–A798, 2006.

[18] B. Wei, Z. Lü, X. Huang, J. Miao, X. Sha, X. Xin, and W. Su. Crystal Structure, Thermal Expansion and Electrical Conductivity of Perovskite Oxides $Ba_xSr_{1-x}Co_{0.8}Fe_{0.2}O_{3-\delta}(0.3 \leq x \leq 0.7)$. *Journal of the European Ceramic Society*, 26(13):2827–2832, 2006.

[19] L.-W. Tai, M. M. Nasrallah, H. U. Anderson, D. M. Sparlin, and S. R. Sehlin. Structure and Electrical Properties of $La_{1-x}Sr_xCo_{1-y}Fe_yO_3$. Part 2. The System $La_{1-x}Sr_xCo_{0.2}Fe_{0.8}O_3$. *Solid State Ionics*, 76(3-4):273–283, 1995.

[20] F. Tietz, F. J. Dias, B. Dubiel, and H. J. Penkalla. Manufacturing of $NiO/NiTiO_3$ Porous Substrates and the Role of Zirconia Impurities during Sintering. *Materials Science and Engineering B: Solid-State Materials for Advanced Technology*, 68(1):35–41, 1999.

[21] F. Tietz. Thermal Expansion of SOFC Materials. *Ionics*, 5(1-2):129–139, 1999.

[22] S. C. Parida, Z. Singh, S. Dash, R. Prasad, and V. Venugopal. Thermodynamic Studies on $LaFeO_3$(s). *Journal of Alloys and Compounds*, 280:94–98, 1998.

[23] R. H. Schumm, D. D. Wagman, S. M. Bailey, W. H. Evans, and V. B. Parker. *Selected Values of Chemical Thermodynamic Properties: Tables for the Lanthanide (Rare Earth) Elements*. National Bureau of Standards, Washington DC, 1973.

[24] D. D. Wagman, W. H. Evans, V. B. Parker, I. Halow, S. M. Bailey, and R. H Schumm. *Selected Values of Chemical Thermodynamic Properties Tables for Elements 35 Through 53 in the Standard Order of Arrangement*. National Bureau of Standards, Washington DC, 1969.

[25] P. Atkins and J. De Paula. *Atkins' Physical Chemistry*. $9^{th}$ ed. Oxford University Press, Oxford UK, 2014.

[26] P . Atkins, T. Overton, J. Rourke, M. Weller, and F. Armstrong. *Shriver and Atkins' Inorganic Chemistry*. $5^{th}$ ed. Oxford University Press, Oxford UK, 2010.

[27] A. Jones and M. S. Islam. Atomic-Scale Insight into $LaFeO_3$ Perovskite: Defect Nanoclusters and Ion Migration. *Journal of Physical Chemistry C*, 112(12):4455–4462, 2008.

[28] G. V. Lewis and C. R. A. Catlow. Potential Models for Ionic Oxides. *Journal of Physics C: Solid State Physics*, 18(6):1149–1161, 1985.

[29] M. S. Islam and L. J. Winch. Defect Chemistry and Oxygen Diffusion in the $HgBa_2Ca_2Cu_3O_{8+\delta}$ Superconductor: A Computer Simulation Study. *Physical Review B*, 52(14):10510–10515, 1995.

[30] D. K. Smith and H. R. Leider. Low-Temperature Thermal Expansion of LiH, MgO and CaO. *Journal of Applied Crystallography*, 1(4):246–249, 1968.

[31] D. Taylor. Thermal Expansion Data. I: Binary Oxides with the Sodium Chloride and Wurtzite Structures, MO. *T ransactions and Journal of the British Ceramic Society*, 83:5–9, 1974.

[32] L. Liu and W. Bassett. Effect of Pressure on the Crystal Structure and the Lattice Parameters of BaO. *Journal of Geophysical Research*, 77(26):4934–4937, 1972.

[33] H. Fjellvåg, F. Grønvold, S. Stølen, and B. Hauback. On the Crystallographic and Magnetic Structures of Nearly Stoichiometric Iron Monoxide. *Journal of Solid State Chemistry*, 124(1):52–57, 1996.

[34] S. P. Jiang. Development of Lanthanum Strontium Manganite Perovskite Cathode Materials of Solid Oxide Fuel Cells: A Review. *Journal of Materials Science*, 43(21):6799–6833, 2008.

[35] S. J. Skinner. Recent Advances in Perovskite-Type Materials for Solid Oxide Fuel Cell Cathodes. *International Journal of Inorganic Materials*, 3(2):113–121, 2001.

[36] A. Casanova. A Consortium Approach to Commercialized Westinghouse Solid Oxide Fuel Cell Technology. *Journal of Power Sources*, 71(1-2):65–70, 1998.

[37] M. Liu, M. E. Lynch, K. Blinn, F. M. Alamgir, and Y. Choi. Rational SOFC Material Design: New Advances and Tools. *Materials Today*, 14(11):534–546, 2011.

[38] C. Xia, W. Rauch, F. Chen, and M. Liu. $Sm_{0.5}Sr_{0.5}CoO_3$ Cathodes for Low-Temperature SOFCs. *Solid State Ionics*, 149(1-2):11–19, 2002.

[39] Z. Shao and S. M. Haile. A High-Performance Cathode for the Next Generation of Solid-Oxide Fuel Cells. *Nature*, 431(7005):170–173, 2004.

[40] S. M. Haile. Fuel Cell Materials and Components. *Acta Materialia*, 51(19):5981–6000, 2003.

[41] A. Tarancón, M. Burriel, J. Santiso, S. J. Skinner, and J. A. Kilner. Advances in Layered Oxide Cathodes for Intermediate Temperature Solid Oxide Fuel Cells. *Journal of Materials Chemistry*, 20(19):3799–3813, 2010.

[42] S. C. Singhal. Advances in Solid Oxide Fuel Cell Technology. *Solid State Ionics*, 135(1):305–313, 2000.

[43] N. Q. Minh and T. Takahashi. *Science and Technology of Ceramic Fuel Cells*. Elsevier, Amsterdam, 1995.

[44] R. M. Ormerod. Solid Oxide Fuel Cells. *Chemical Society Reviews*, 32(1):17–28, 2003.

[45] B. C. H. Steele and A. Heinzel. Materials for Fuel-Cell Technologies. *Nature*, 414(6861):345–352, 2001.

[46] J. A. Kilner and M. Burriel. Materials for Intermediate-Temperature Solid-Oxide Fuel Cells. *Annual Review of Materials Research*, 44(1):365–393, jul 2014.

[47] N. P. Brandon, S. Skinner, and B. C. H. Steele. Recent Advances in Materials for Fuel Cells. *Annual Review of Materials Research*, 33(1):183–213, 2003.

[48] J. Mizusaki, T. Sasamoto, W. R. Cannon, and H. K. Bowen. Electronic Conductivity, Seebeck Coefficient, and Defect Structure of $LaFeO_3$. *Journal of the American Ceramic Society*, 65(8):363–368, 1982.

[49] I. Wærnhus, P. E. Vullum, R. Holmestad, T. Grande, and K. Wiik. Electronic Properties of Polycrystalline $LaFeO_3$. Part I: Experimental Results and the Qualitative Role of Schottky Defects. *Solid State Ionics*, 176(37-38):2783–2790, 2005.

[50] S. P. Jiang. A Comparison of $O_2$ Reduction Reactions on Porous (La,Sr)$MnO_3$ and (La,Sr)(Co,Fe)$O_3$ Electrodes. *Solid State Ionics*, 146(1-2):1–22, 2002.

[51] F. Shen and K. Lu. Comparative Study of $La_{0.6}Sr_{0.4}Co_{0.2}Fe_{0.8}O_3$, $Ba_{0.5}Sr_{0.5}Co_{0.2}Fe_{0.8}O_3$ and $Sm_{0.5}Sr_{0.5}Co_{0.2}Fe_{0.8}O_3$ Cathodes and the Effect of $Sm_{0.2}Ce_{0.8}O_2$ Block Layer in Solid Oxide Fuel Cells. *International Journal of Hydrogen Energy*, 40(46):16457–16465, 2015.

[52] C. Endler-Schuck, J. Joos, C. Niedrig, A. Weber, and E. Ivers-Tiffée. The Chemical Oxygen Surface Exchange and Bulk Diffusion Coefficient Determined by Impedance Spectroscopy of Porous $La_{0.58}Sr_{0.4}Co_{0.2}Fe_{0.8}O_{3-\delta}$ (LSCF) Cathodes. *Solid State Ionics*, 269:67–79, 2015.

[53] K. Develos-Bagarinao, H. Kishimoto, J. De Vero, K. Yamaji, and T. Horita. Effect of $La_{0.6}Sr_{0.4}Co_{0.2}Fe_{0.8}O_{3-\delta}$ Microstructure on Oxygen Surface Exchange Kinetics. *Solid State Ionics*, 288:6–9, 2016.

[54] A. M. Ritzmann, A. B. Muñoz-García, M. Pavone, J. A. Keith, and E. A. Carter. Ab initio Evaluation of Oxygen Diffusivity in $LaFeO_3$: The Role of Lanthanum Vacancies. *MRS Communications*, 3(03):161–166, 2013.

[55] A. Aguadero, L. Fawcett, S. Taub, R. Woolley, K. T. Wu, N. Xu, J. A. Kilner, and S. J. Skinner. Materials Development for Intermediate-Temperature Solid Oxide Electrochemical Devices, *Journal of Materials Science*, 47(9):3925–3948, 2012.

[56] A. Chroneos, B. Yildiz, A. Tarancón, D. Parfitt, and J. A. Kilner. Oxygen Diffusion in Solid Oxide Fuel Cell Cathode and Electrolyte Materials: Mechanistic Insights from Atomistic Simulations. *Energy & Environmental Science*, 4(8):2774-2789, 2011.

[57] A. J. Jacobson. Materials for Solid Oxide Fuel Cells. *Chemistry of Materials*, 22(3):660–674, 2010.

[58] P. R. Slater, J. T. S. Irvine, T. Ishihara, and Y. Takita. The structure of the oxide ion conductor $La_{0.9}Sr_{0.1}Ga_{0.8}Mg_{0.2}O_{2.85}$ by powder neutron diffraction. *Solid State Ionics*, 107(3-4):319–323, 1998.

[59] P. R. Slater, J. T. S. Irvine, T. Ishihara, and Y. Takita. High-Temperature Powder Neutron Diffraction Study of the Oxide Ion Conductor $La_{0.9}Sr_{0.1}Ga_{0.8}Mg_{0.2}O_{2.85}$. *Journal of Solid State Chemistry*, 139(1):135–143, 1998.

[60] M. Yashima, K. Nomura, H. Kageyama, Y. Miyazaki, N. Chitose, and K. Adachi. Conduction Path and Disorder in the Fast Oxide-Ion Conductor $(La_{0.8}Sr_{0.2})(Ga_{0.8}Mg_{0.15}Co_{0.05})O_{2.8}$. *Chemical Physics Letters*, 380(3-4):391–396, 2003.

[61] L. Malavasi, C. A. J. Fisher, and M. S. Islam. Oxide-Ion and Proton Conducting Electrolyte Materials for Clean Energy Applications: Structural and Mechanistic Features. *Chemical Society Reviews*, 39(11):4370-4387, 2010.

[62] X.-D. Zhou, J. W. Templeton, Z. Nie, H. Chen, J. W. Stevenson, and L. R. Pederson. Electrochemical Performance and Stability of the Cathode for Solid Oxide Fuel Cells: V. High Performance and Stable $Pr_2NiO_4$ as the Cathode for Solid Oxide Fuel Cells. *Electrochimica Acta*, 71:44–49, 2012.

[63] E. Kendrick, M. S. Islam, and P. R. Slater. Developing Apatites for Solid Oxide Fuel Cells: Insight into Structural, Transport and Doping Properties. *Journal of Materials Chemistry*, 17(30):3104-3111, 2007.

[64] K. Kleveland, M.-A. Einarsrud, C. R. Schmidt, S. Shamisili, S. Faaland, K. Wiik, and T. Grande. Relation between Strontium-Substituted Lanthanum Manganite and Yttria-Stabilized Zirconia: II , Diffusion Couples. *Journal of the American Ceramic Society*, 82(3):729–734, 1999.

[65] G. Stochniol, E. Syskakis, and A. Naoumidis. Chemical Compatibility between Strontium-Doped Lanthanum Manganite and Yttria-Stabilized Zirconia. *Journal of the American Ceramic Society*, 78(4):929–932, 1995.

[66] T. Horita, K. Yamaji, M. Ishikawa, N. Sakai, H. Yokokawa, T. Kawada, and T. Kato. Active Sites Imaging for Oxygen Reduction at the $La_{0.9}Sr_{0.1}MnO_{3-x}$/Yttria-Stabilized Zirconia Interface by Secondary-Ion Mass Spectrometry. *Journal of the Electrochemical Society*, 145(9):3196–3202, 1998.

[67] S. P. Jiang and W. Wang. Fabrication and Performance of GDC-Impregnated (La,Sr)$MnO_3$ Cathodes for Intermediate Temperature Solid Oxide Fuel Cells. *Journal of The Electrochemical Society*, 152(7):A1398-A1408, 2005.

[68] S. Taniguchi, M. Kadowaki, H. Kawamura, T. Yasuo, Y. Akiyama, Y. Miyake, and T. Saitoh. Degradation Phenomena in the Cathode of a Solid Oxide Fuel Cell with an Alloy Separator. *Journal of Power Sources*, 55(1):73–79, 1995.

[69] S. P. S. Badwal, R. Deller, K. Foger, Y. Ramprakash, and J. P. Zhang. Inter-

action between Chromia Forming Alloy Interconnects and Air Electrode of Solid Oxide Fuel Cells. *Solid State Ionics*, 99(3-4):297–310, 1997.

[70] S. C. Paulson and V. I. Birss. Chromium Poisoning of LSM-YSZ SOFC Cathodes. *Journal of The Electrochemical Society*, 151(11):A1961–A1968, 2004.

[71] Y. Matsuzaki and I. Yasuda. Dependence of SOFC Cathode Degradation by Chromium-Containing Alloy on Compositions of Electrodes and Electrolytes. *Journal of The Electrochemical Society*, 148(2):A126–A131, 2001.

[72] M. S. D. Read, M. S. Islam, G. W. Watson, F. King, and F. E. Hancock. Defect Chemistry and Surface Properties of $LaCoO_3$. *Journal of Materials Chemistry*, 10(10):2298–2305, 2000.

[73] R. H. E. Van Doorn and A. J. Burggraaf. Structural Aspects of the Ionic Conductivity of $La_{1-x}Sr_xCoO_{3-\delta}$. *Solid State Ionics*, 128(1-4):65–78, 2000.

[74] Y. Teraoka, T. Nobunaga, K. Okamoto, N. Miura, and N. Yamazoe. Influence of Constituent Metal Cations in Substituted $LaCoO_3$ on Mixed Conductivity and Oxygen Permeability. *Solid State Ionics*, 48(3-4):207–212, 1991.

[75] F. M. Figueiredo, F. M. B. Marques, and J. R. Frade. Electrochemical Permeability of $La_{1-x}Sr_xCoO_{3-\delta}$ Materials. *Solid State Ionics*, 111(3-4):273–281, 1998.

[76] A. Y. Zuev, A. N. Petrov, A. I. Vylkov, and D. S. Tsvetkov. Oxygen Nonstoichiometry and Defect Structure of Undoped and Doped Lanthanum Cobaltites. *Journal of Materials Science*, 42(6):1901–1908, 2007.

[77] Y. Teraoka, M. Yoshimatsu, N. Yamazoe, and T. Seiyama. Oxygen-Sorptive Properties and Defect Structure of Perovskite-Type Oxides. *Chemistry Letters*, 13(6):893–896, 1984.

[78] M. Søgaard, P. V. Hendriksen, M. Mogensen, F. W. Poulsen, and E. Skou. Oxygen Nonstoichiometry and Transport Properties of Strontium Substituted Lanthanum Cobaltite. *Solid State Ionics*, 177(37-38):3285–3296, 2006.

[79] J. M. Vohs and R. J. Gorte. High-Performance SOFC Cathodes Prepared by Infiltration. *Advanced Materials*, 21(9):943–956, 2009.

[80] T. Horita, K. Yamaji, N. Sakai, H. Yokokawa, A. Weber, and E. Ivers-Tiffée. Oxygen Reduction Mechanism at Porous $La_{1-x}Sr_xCoO_{3-d}$ Cathodes/$La_{0.8}Sr_{0.2}Ga_{0.8}Mg_{0.2}O_{2.8}$ Electrolyte Interface for Solid Oxide Fuel Cells. *Electrochimica Acta*, 46(12):1837–1845, 2001.

[81] H. Y. Tu, Y. Takeda, N. Imanishi, and O. Yamamoto. $Ln_{1-x}Sr_xCoO_3$ (Ln=Sm, Dy) for the Electrode of Solid Oxide Fuel Cells. *Solid State Ionics*, 100(3-4):283–288, 1997.

[82] T. Setoguchi, M. Sawano, K. Eguchi, and H. Arai. Application of the Stabilized Zirconia Thin Film Prepared by Spray Pyrolysis Method to SOFC. *Solid State Ionics*, 40-41:502–505, 1990.

[83] H. Uchida, S. Arisaka, and M. Watanabe. High Performance Electrodes for Medium-Temperature Solid Oxide Fuel Cells: Activation of $La(Sr)CoO_3$ Cathode with Highly Dispersed Pt Metal Electrocatalysts. *Solid State Ionics*, 135(1-4):347–351, 2000.

[84] M. Shiono, K. Kobayashi, T. L. Nguyen, K. Hosoda, T. Kato, K. Ota, and M. Dokiya. Effect of $CeO_2$ Interlayer on $ZrO_2$ Electrolyte/$La(Sr)CoO_3$ Cathode for Low-Temperature SOFCs. *Solid State Ionics*, 170(1-2):1–7, 2004.

[85] C. Rossignol, J. M. Ralph, J. M. Bae, and J. T. Vaughey. $Ln_{1-x}Sr_xCoO_3$ (Ln=Gd, Pr) as a Cathode for Intermediate-Temperature Solid Oxide Fuel Cells. *Solid State Ionics*, 175:59–61, 2004.

[86] N. Sakai, H. Kishimoto, K. Yamaji, T. Horita, M. E. Brito, and H. Yokokawa. Interface Stability of Perovskite Cathodes and Rare-Earth Doped Ceria Inter-

layer in SOFCs. *Journal of The Electrochemical Society*, 154(12):B1331, 2007.

[87] M. Gödickemeier, K. Sasaki, and L. J. Gauckler. Perovskite Cathodes for Solid Oxide Fuel Cells Based on Ceria Electrolytes. *Solid State Ionics*, 86-88:691–701, 1996.

[88] V. V. Kharton, A. V. Kovalevsky, V. N. Tikhonovich, E. N. Naumovich, and A. P. Viskup. Mixed Electronic and Ionic Conductivity of $LaCo(M)O_3$ (M=Ga, Cr, Fe or Ni): II. Oxygen Permeation through Cr- and Ni-Substituted $LaCoO_3$. *Solid State Ionics*, 110(12):53–60, 1998.

[89] N. Sukpirom, S. Iamsaard, S. Charojrochkul, and J. Yeyongchaiwat. Synthesis and Properties of $LaNi_{1-x}Fe_xO_{3-\delta}$ as Cathode Materials in SOFC. *Journal of Materials Science*, 46(20):6500–6507, 2011.

[90] Z. Gao, L. V. Mogni, E. C. Miller, J. G. Railsback, and S. A. Barnett. A Perspective on Low-Temperature Solid Oxide Fuel Cells. *Energy Environmental Science*, 9(5):1602–1644, 2016.

[91] W. Zhou, R. Ran, and Z. Shao. Progress in Understanding and Development of $Ba_{0.5}Sr_{0.5}Co_{0.8}Fe_{0.2}O_{3-\delta}$-Based Cathodes for Intermediate-Temperature Solid-Oxide Fuel Cells: A Review. *Journal of Power Sources*, 192(2):231–246, 2009.

[92] M. M. Kuklja, E. A. Kotomin, R. Merkle, Y. A. Mastrikov, and J. Maier. Combined Theoretical and Experimental Analysis of Processes Determining Cathode Performance in Solid Oxide Fuel Cells. *Physical Chemistry Chemical Physics*, 15:5443–5471, 2013.

[93] R. Merkle, Y. A. Mastrikov, E. A. Kotomin, M. M. Kuklja, and J. Maier. First Principles Calculations of Oxygen Vacancy Formation and Migration in $Ba_{1-x}Sr_xCo_{1-y}Fe_yO_{3-\delta}$ Perovskites. *Journal of The Electrochemical Society*, 159(2):B219, 2012.

[94] S. Švarcová, K. Wiik, J. Tolchard, H. J. M. Bouwmeester, and T. Grande. Structural Instability of Cubic Perovskite $Ba_xSr_{1-x}Co_{1-y}Fe_yO_{3-\delta}$. *Solid State Ionics*, 178(35-36):1787–1791, 2008.

[95] M. Arnold, T. M. Gesing, J. Martynczuk, and A. Feldhoff. Correlation of the Formation and the Decomposition Process of the BSCF Perovskite at Intermediate Temperatures. *Chemistry of Materials*, 20(18):5851–5858, 2008.

[96] C. Niedrig, S. Taufall, M. Burriel, W. Menesklou, S. F. Wagner, S. Baumann, and E. Ivers-Tiffée. Thermal Stability of the Cubic Phase in $Ba_{0.5}Sr_{0.5}Co_{0.8}Fe_{0.2}O_{3-\delta}$ (BSCF)1. *Solid State Ionics*, 197(1):25–31, 2011.

[97] K. Efimov, Q. Xu, and A. Feldhoff. Transmission Electron Microscopy Study of $Ba_{0.5}Sr_{0.5}Co_{0.8}Fe_{0.2}O_{3-\delta}$ Perovskite Decomposition at Intermediate Temperatures. *Chemistry of Materials*, 22(21):5866–5875, 2010.

[98] D. N. Mueller, R. A. De Souza, T. E. Weirich, D. Roehrens, J. Mayer, and M. Martin. A Kinetic Study of the Decomposition of the Cubic Perovskite-Type Oxide $Ba_xSr_{1-x}Co_{0.8}Fe_{0.2}O_{3-\delta}$ (BSCF) ($x$ = 0.1 and 0.5). *Physical Chemistry Chemical Physics*, 12(35):10320, 2010.

[99] C. Setevich, L. Mogni, A. Caneiro, and F. Prado. Characterization of the $La_{1x}Ba_xCoO_{3-\delta}$ ($0 \leq x \leq 1$) System as Cathode Material for IT-SOFC. *Journal of The Electrochemical Society*, 159(1):B73, 2012.

[100] M. Lumeij, M. Gilleßen, H. Bouwmeester, T. Markus, J. Barthel, S. Roitsch, J. Mayer, and R. Dronskowski. Influence of the $Ba^{2+}/Sr^{2+}$ Content and Oxygen Vacancies on the Stability of Cubic $Ba_xSr_{1-x}Co_{0.75}Fe_{0.25}O_{3-\delta}$. *Physical Chemistry Chemical Physics*, 16(4):1333–1338, 2014.

[101] Y.-C. Chen, M. Yashima, T. Ohta, K. Ohoyama, and S. Yamamoto. Crystal Structure, Oxygen Deficiency, and Oxygen Diffusion Path of Perovskite-Type Lanthanum Cobaltites $La_{0.4}Ba_{0.6}CoO_{3-\delta}$ and $La_{0.6}Sr_{0.4}CoO_{3-\delta}$. *The Journal of Physical Chemistry C*, 116(8):5246–5254, 2012.

[102] S. Yakovlev, C. Y. Yoo, S. Fang, and H. J. M. Bouwmeester. Phase Transformation and Oxygen Equilibration Kinetics of Pure and Zr-Doped $Ba_{0.5}Sr_{0.5}Co_{0.8}Fe_{0.2}O_{3-\delta}$ Perovskite Oxide Probed by Electrical Conductivity Relaxation. *Applied Physics Letters*, 96(25):254101, 2010.

[103] M. M. Kuklja, Y. A. Mastrikov, B. Jansang, and E. A. Kotomin. First Principles Calculations Of (Ba,Sr)(Co,Fe)$O_{3-\delta}$ Structural Stability. *Solid State Ionics*, 230(C):21–26, 2013.

[104] M. Arnold, H. Wang, and A. Feldhoff. Influence of $CO_2$ on the Oxygen Permeation Performance and the Microstructure of Perovskite-Type $(Ba_{0.5}Sr_{0.5})(Co_{0.8}Fe_{0.2})O_{3-\delta}$ membranes. *Journal of Membrane Science*, 293(1-2):44–52, 2007.

[105] A. Yan, V. Maragou, A. Arico, M. Cheng, and P. Tsiakaras. Investigation of a $Ba_{0.5}Sr_{0.5}Co_{0.8}Fe_{0.2}O_{3-\delta}$ Based Cathode SOFC. II. The effect of $CO_2$ on the Chemical Stability. *Applied Catalysis B: Environmental*, 76(3-4):320–327, 2007.

[106] A. Yan, M. Cheng, Y. Dong, W. Yang, V. Maragou, S. Song, and P. Tsiakaras. Investigation of a $Ba_{0.5}Sr_{0.5}Co_{0.8}Fe_{0.2}O_{3-\delta}$ Based Cathode IT-SOFC. I. The effect of $CO_2$ on the Cell Performance. *Applied Catalysis B: Environmental*, 66(1-2):64–71, 2006.

[107] E. Bucher, A. Egger, G. B. Caraman, and W. Sitte. Stability of the SOFC Cathode Material (Ba,Sr)(Co,Fe)$O_{3-\delta}$ in $CO_2$-Containing Atmospheres. *Journal of The Electrochemical Society*, 155(11):B1218, 2008.

[108] K. Wang, R. Ran, W. Zhou, H. Gu, Z. Shao, and J. Ahn. Properties and Performance of $Ba_{0.5}Sr_{0.5}Co_{0.8}Fe_{0.2}O_{3-\delta}$ + $Sm_{0.2}Ce_{0.8}O_{1.9}$ Composite Cathode. *Journal of Power Sources*, 179(1):60–68, 2008.

[109] W. Zhou, R. Ran, Z. Shao, W. Jin, and N. Xu. Evaluation of A-site Cation-Deficient $(Ba_{0.5}Sr_{0.5})_{1-x}Co_{0.8}Fe_{0.2}O_{3-\delta}$ ($x > 0$) Perovskite as a Solid-Oxide Fuel Cell Cathode. *Journal of Power Sources*, 182(1):24–31, 2008.

[110] B. Liu, Y. Zhang, and L. Zhang. Characteristics of $Ba_{0.5}Sr_{0.5}Co_{0.8}Fe_{0.2}O_{3-\delta}$-$La_{0.9}Sr_{0.1}Ga_{0.8}Mg_{0.2}O_{3-\delta}$ Composite Cathode for Solid Oxide Fuel Cell. *Journal of Power Sources*, 175(1):189–195, 2008.

[111] B. Lin, H. Ding, Y. Dong, S. Wang, X. Zhang, D. Fang, and G. Meng. Intermediate-to-Low Temperature Protonic Ceramic Membrane Fuel Cells with $Ba_{0.5}Sr_{0.5}Co_{0.8}Fe_{0.2}O_{3-\delta}$-$BaZr_{0.1}Ce_{0.7}Y_{0.2}O_{3-\delta}$ Composite Cathode. *Journal of Power Sources*, 186(1):58–61, 2009.

[112] Y.-P. Fu, A. Subardi, M.-Y. Hsieh, and W.-K. Chang. Electrochemical Properties of $La_{0.5}Sr_{0.5}Co_{0.8}M_{0.2}O_{3-\delta}$ (M=Mn, Fe, Ni, Cu) Perovskite Cathodes for IT-SOFCs. *Journal of the American Ceramic Society*, 99(4):1345–1352, 2016.

[113] F. Tietz, V. A. C. Haanappel, A. Mai, J. Mertens, and D. Stöver. Performance of LSCF Cathodes in Cell Tests, *Journal of Power Sources*, 156:20–22, 2006.

[114] L. W. Tai, M. M. Nasrallah, H. U. Anderson, D. M. Sparlin, and S. R. Sehlin. Structure and Electrical Properties of $La_{1-x}Sr_xCo_{1-y}Fe_yO_3$. Part 1. The System $La_{0.8}Sr_{0.2}Co_{1-y}Fe_yO_3$. *Solid State Ionics*, 76(3-4):259–271, 1995.

[115] S. P. Simner, M. D. Anderson, M. H. Engelhard, and J. W. Stevenson. Degradation Mechanisms of La-Sr-Co-Fe-$O_3$ SOFC Cathodes. *Electrochemical and Solid-State Letters*, 9(10):A478–A481, 2006.

[116] A. Leonide, B. Rüger, A. Weber, W. A. Meulenberg, and E. Ivers-Tiffée. Impedance Study of Alternative (La,Sr)$FeO_{3-\delta}$ and (La,Sr)(Co,Fe)$O_{3-\delta}$ MIEC Cathode Compositions. *Journal of The Electrochemical Society*, 157(2):B234–B239, 2010.

[117] W. G. Wang and M. Mogensen. High-Performance Lanthanum-Ferrite-Based Cathode for SOFC. *Solid State Ionics*, 176(5-6):457–462, 2005.

[118] A. Mai, M. Becker, W. Assenmacher, F. Tietz, D. Hathiramani, E. Ivers-Tiffée, D. Stöver, and W. Mader. Time-Dependent Performance of Mixed-Conducting SOFC Cathodes. *Solid State Ionics*, 177(19-25 SPEC. ISS.):1965–1968, 2006.

[119] Y. A. Mastrikov, R. Merkle, E. A. Kotomin, M. M. Kuklja, and J. Maier. Formation and Migration of Oxygen Vacancies in $La_{1-x}Sr_xCo_{1-y}Fe_yO_{3-\delta}$ Perovskites: Insight from *ab initio* Calculations and comparison with $Ba_{1-x}Sr_xCo_{1-y}Fe_yO_{3-\delta}$. *Physical Chemistry Chemical Physics*, 15(3):911–918, 2013.

[120] A. M. Ritzmann, J. M. Dieterich, and E. A. Carter. Density Functional Theory + U Analysis of the Electronic Structure and Defect Chemistry of LSCF ($La_{0.5}Sr_{0.5}Co_{0.25}Fe_{0.75}O_{3-\delta}$). *Physical Chemistry Chemical Physics*, 18(17):12260–12269, 2016.

[121] J. Hubbard. Electron Correlations in Narrow Energy Bands. *Proceedings of the Royal Society A*, 276:238–257, 1963.

[122] P. W. Anderson. Localized Magnetic States in Metals. *Physical Review*, 124(1):41–53, 1961.

[123] J. Buckeridge, F. H. Taylor, and C. R. A. Catlow. Efficient and Accurate Approach to Modeling the Microstructure and Defect Properties of $LaCoO_3$. *Physical Review B - Condensed Matter and Materials Physics*, 93:155123, 2016.

[124] G. Amow and S. J. Skinner. Recent Developments in Ruddlesden-Popper Nickelate Systems for Solid Oxide Fuel Cell Cathodes. *Journal of Solid State Electrochemistry*, 10(8):538–546, 2006.

[125] G. Amow, I. J. Davidson, and S. J. Skinner. A Comparative Study of the Ruddlesden-Popper Series, $La_{n+1}Ni_nO_{3n+1}$ ($n = 1$, 2 and 3), for Solid-Oxide Fuel-Cell Cathode Applications. *Solid State Ionics*, 177(13-14):1205–1210, 2006.

[126] M. Greenblatt, Z. Zhang, and M. H. Whangbo. Electronic Properties of $La_3Ni_2O_7$ and $Ln_4Ni_3O_10$, Ln = La, Pr and Nd. *Synthetic Metals*, 85(1-3):1451–1452, 1997.

[127] M. Greenblatt. Ruddlesden-Popper Properties $Ln_{n+1}Ni_nO_{3n+1}$ Nickelates: Structure and Properties. *Current Opinion in Solid State & Materials Science*, 2(2):174–183, 1997.

[128] Y. Kobayashi, S. Taniguchi, M. Kasai, M. Sato, T. Nishioka, and M. Kontani. Transport and Magnetic Properties of $La_3Ni_2O_{7-\delta}$ and $La_4Ni_3O_{10-\delta}$. *Journal of the Physical Society of Japan*, 65(12):3978–3982, 1996.

[129] Z. Zhang and M. Greenblatt. Synthesis, Structure, and Properties of $Ln_4Ni_3O_{10-\delta}$ (Ln = La, Pr, and Nd). *Journal of Solid State Chemistry*, 117:236–246, 1995.

[130] Z. Zhang, M. Greenblatt, and J. B. Goodenough. Synthesis, Structure, and Properties of the Layered Perovskite $La_3Ni_2O_{7-\delta}$, *Journal of Solid State Chemistry*, 108:402–409, 1994.

[131] D. Pérez-Coll, A. Aguadero, M. J. Escudero, and L. Daza. Effect of DC Current Polarization on the Electrochemical Behaviour of $La_2NiO_{4+\delta}$ and $La_3Ni_2O_{7+\delta}$-Based systems. *Journal of Power Sources*, 192(1):2–13, 2009.

[132] S. A. Nedilko, V. A. Kulichenko, A. G. Dziazko, and E. G. Zenkovich. Oxygen Nonstoichiometry and Properties of Lanthanum Nickelates $La_{3-x}Ca_xNi_2O_{7-\delta}$ ($0 \leq x \leq 2.0$). *Journal of Alloys and Compounds*, 367:251–254, 2004.

[133] M. D. Carvalho, M. M. Cruz, A. Wattiaux, J. M. Bassat, F. M. A. Costa, and M. Godinho. Influence of Oxygen Stoichiometry on the Electronic Properties of $La_4Ni_3O_{10\pm\delta}$. *Journal of Applied Physics*, 88(1):544–549, 2000.

[134] M. D. Carvalho, A. Wattiaux, J. M. Bassat, J. C. Grenier, M. Pouchard, M. I. da Silva Pereira, and F. M. A. Costa. Electrochemical Oxidation and Reduc-

tion of $La_4Ni_3O_10$ in Alkaline Media. *Journal of Solid State Electrochemistry*, 7(10):700–705, 2003.

[135] J. M. Bassat, P. Odier, A. Villesuzanne, C. Marin, and M. Pouchard. Anisotropic Ionic Transport Properties in $La_2NiO_{4+\delta}$ Single Crystals. *Solid State Ionics*, 167(3-4):341–347, 2004.

[136] E. J. Opila, H. L. Tuller, B. J. Wuensch, and J. Maier. Oxygen Tracer Diffusion in $La_{2-x}Sr_xCuO_{4-y}$ Single Crystals. *Journal of the American Ceramic Society*, 76(9):2363–2369, 1993.

[137] J. Claus, G. Borchardt, S. Weber, J. M. Hiver, and S. Scherrer. Combination of EBSP Measurements and SIMS to Study Crystallographic Orientation Dependence of Diffusivities in a Polycrystalline Material: Oxygen Tracer Diffusion in $La_{2-x}Sr_xCuO_{4\pm\delta}$. *Materials Science and Engineering B*, 38(3):251–257, 1996.

[138] S. J. Skinner. Characterisation of $La_2NiO_{4+\delta}$ using in-situ High Temperature Neutron Powder Diffraction. *Solid State Sciences*, 5(3):419–426, 2003.

[139] R. Sayers, R. A. De Souza, J. A. Kilner, and S. J. Skinner. Low Temperature Diffusion and Oxygen Stoichiometry in Lanthanum Nickelate. *Solid State Ionics*, 181(8-10):386–391, 2010.

[140] A. Chroneos, D. Parfitt, J. A. Kilner, and R. W. Grimes. Anisotropic Oxygen Diffusion in Tetragonal $La_2NiO_{4+\delta}$: Molecular Dynamics Calculations. *Journal of Materials Chemistry*, 20(2):266–270, 2010.

[141] D. Parfitt, A. Chroneos, J. A. Kilner, and R. W. Grimes. Molecular Dynamics Study of Oxygen Diffusion in $Pr_2NiO_{4+\delta}$. *Physical Chemistry Chemical Physics*, 12(25):6834, 2010.

[142] A. Kushima, D. Parfitt, A. Chroneos, B. Yildiz, J. A. Kilner, and R. W. Grimes. Interstitialcy Diffusion of Oxygen in Tetragonal $La_2CoO_{4+\delta}$. *Physical Chemistry Chemical Physics*, 13(6):2242–2249, 2011.

[143] N. L. Allan and W. C. Mackrodt. Oxygen Ion Migration in $La_2CuO_4$. *Philosophical Magazine A*, 64(5):1129–1132, 1991.

[144] N. L. Allan, J. M. Lawton, and W. C. Mackrodt. A Comparison of the Calculated Lattice and Defect Structures of $La_2CuO_4$, $La_2NiO_4$, $Nd_2CuO_4$, $Pr_2CuO_4$, $Y_2CuO_4$, $Al_2CuO_4$: Relationship to High-Tc Superconductivity. *Philosophical Magazine Part B*, 59(2):191–206, 1989.

[145] S. N. Savvin, G. N. Mazo, and A. K. Ivanov-Schitz. Simulation of Ion Transport in Layered Cuprates $La_{2-x}Sr_xCuO_{4-\delta}$. *Crystallography Reports*, 53(2):291–301, 2008.

[146] G. N. Mazo and S. N. Savvin. The Molecular Dynamics Study of Oxygen Mobility in $La_{2-x}Sr_xCuO_{4-\delta}$. *Solid State Ionics*, 175(1):371–374, 2004.

[147] A. K. Ivanov-Shits, G. N. Mazo, S. N. Savvin, S. N. Putilin, and A. S. Samokhin. Prediction of Transport Properties of New Functional Materials Based on Lanthanum-Strontium Cuprates: Molecular Mechanics Calculations. *Russian Journal of Electrochemistry*, 44(12):1359–1365, 2008.

[148] M. Yashima, M. Enoki, T. Wakita, R. Ali, Y. Matsushita, F. Izumi, and T. Ishihara. Structural Disorder and Diffusional Pathway of Oxide Ions in a Doped $Pr_2NiO_4$-Based Mixed Conductor. *Journal of the American Chemical Society*, 130(9):2762–2763, 2008.

[149] J. M. Bassat, F. Gervais, P. Odier, and J. P. Loup. Anisotropic Transport Properties of $La_2NiO_4$ Single Crystals. *Materials Science and Engineering B*, 3(4):507–514, 1989.

[150] P. Odier, C. Allançon, and J. M. Bassat. Oxygen Exchange in $Pr_2NiO_{4+\delta}$ at High Temperature and Direct Formation of $Pr_4Ni_3O_{10-x}$. *Journal of Solid State Chemistry*, 153(2):381–385, 2000.

[151] J. G. Railsback, Z. Gao, and S. A. Barnett. Oxygen Electrode Characteristics

of $Pr_2NiO_{4+\delta}$-Infiltrated Porous $(La_{0.9}Sr_{0.1})(Ga_{0.8}Mg_{0.2})O_{3-\delta}$. *Solid State Ionics*, 274:134–139, 2015.

[152] B. Philippeau, F. Mauvy, C. Mazataud, S. Fourcade, and J.-C. Grenier. Comparative Study of Electrochemical Properties of Mixed Conducting $Ln_2NiO_{4+\delta}$ (Ln = La, Pr and Nd) and $La_{0.6}Sr_{0.4}Fe_{0.8}Co_{0.2}O_{3-\delta}$ as SOFC Cathodes Associated to $Ce_{0.9}Gd_{0.1}O_{2-\delta}$, $La_{0.8}Sr_{0.2}Ga_{0.8}Mg_{0.2}O_{3-\delta}$ and $La_9Sr_1Si_6O_{26.5}$ Electrolytes. *Solid State Ionics*, 249-250:17–25, 2013.

[153] A. V. Kovalevsky, V. V. Kharton, A. A. Yaremchenko, Y. V. Pivak, E. V. Tsipis, S. O. Yakovlev, A. A. Markov, E. N. Naumovich, and J. R. Frade. Oxygen Permeability, Stability and Electrochemical Behavior of $Pr_2NiO_{4+\delta}$-Based Materials. *Journal of Electroceramics*, 18(3-4):205–218, 2007.

[154] R. Sayers, J. Liu, B. Rustumji, and S. J. Skinner. Novel $K_2NiF_4$-type Materials for Solid Oxide Fuel Cells: Compatibility with Electrolytes in the Intermediate Temperature Range. *Fuel Cells*, 8(5):338–343, 2008.

[155] F. Mauvy, C. Lalanne, J.-M. Bassat, J.-C. Grenier, H. Zhao, L. Huo, and P. Stevens. Electrode Properties of $Ln_2NiO_{4+\delta}$(Ln = La,Nd,Pr). *Journal of The Electrochemical Society*, 153(8):A1547–A1553, 2006.

[156] C. Ferchaud, J. C. Grenier, Y. Zhang-Steenwinkel, M. M. A. Van Tuel, F. P. F. Van Berkel, and J. M. Bassat. High Performance Praseodymium Nickelate Oxide Cathode for Low Temperature Solid Oxide Fuel Cell. *Journal of Power Sources*, 196(4):1872–1879, 2011.

[157] C. Lalanne, G. Prosperi, J. M. Bassat, F. Mauvy, S. Fourcade, P. Stevens, M. Zahid, S. Diethelm, J. Van herle, and J. C. Grenier. Neodymium-Deficient Nickelate Oxide $Nd_{1.95}NiO_{4+\delta}$ as Cathode Material for Anode-Supported Intermediate Temperature Solid Oxide Fuel Cells. *Journal of Power Sources*, 185(2):1218–1224, 2008.

[158] J. C. Grenier, A. Wattiaux, J. P. Doumerc, P. Dordor, L. Fournes, J. P. Cham-

inade, and M. Pouchard. Electrochemical Oxygen Intercalation into Oxide Networks. *Journal of Solid State Chemistry*, 96(1):20–30, 1992.

[159] R. J. Woolley and S. J. Skinner. Functionally Graded Composite $La_2NiO_{4+\delta}$ and $La_4Ni_3O_{10-\delta}$ Solid Oxide Fuel Cell Cathodes. *Solid State Ionics*, 255:1–5, 2014.

[160] S. Choi, S. Yoo, J.-Y. Shin, and G. Kim. High Performance SOFC Cathode Prepared by Infiltration of $La_{n+1}Ni_nO_{3n+1}$ ($n$ = 1, 2, and 3) in Porous YSZ. *Journal of The Electrochemical Society*, 158(8):B995, 2011.

[161] S. Takahashi, S. Nishimoto, M. Matsuda, and M. Miyake. Electrode Properties of the Ruddlesden-Popper series, $La_{n+1}Ni_nO_{3n+1}$ ($n$ = 1, 2, and 3), as Intermediate-Temperature Solid Oxide Fuel Cells. *Journal of the American Ceramic Society*, 93(8):2329–2333, 2010.

[162] Z. Lou, N. Dai, Z. Wang, Y. Dai, Y. Yan, J. Qiao, J. Peng, J. Wang, and K. Sun. Preparation and Electrochemical Characterization of Ruddlesden-Popper Oxide $La_4Ni_3O_{10}$ Cathode for IT-SOFCs by Sol-Gel Method. *Journal of Solid State Electrochemistry*, 17(10):2703–2709, 2013.

[163] Z. Derakhshi, M. Tamizifar, K. Arzani, and S. Baghshahi. Synthesis and Characterization of $LaCo_xFe_{1-x}O_3$ ($0 \leq x \leq 1$) Nano-Crystal Powders by Pechini Type Sol-Gel Method. *Synthesis and Reactivity in Inorganic, Metal-Organic and Nano-Metal Chemistry*, 46(1):25–30, 2016.

[164] M. Mokhtar, A. Medkhali, K. Narasimharao, and S. Basahel. Divalent Transition Metals Substituted $LaFeO_3$ Perovskite Catalyst for Nitrous Oxide Decomposition. *Journal of Membrane and Separation Technology*, 3(4):206–212, 2014.

[165] S. M. Selbach, J. R. Tolchard, A. Fossdal, and T. Grande. Non-Linear Thermal Evolution of the Crystal Structure and Phase Transitions of $LaFeO_3$ Investigated by High Temperature X-ray Diffraction. *Journal of Solid State Chemistry*, 196:249–254, 2012.

[166] A. Fossdal, M. Menon, I. Waernhus, K. Wiik, M.-A. Einarsrud, and T. Grande. Crystal Structure and Thermal Expansion of $La_{1-x}Sr_xFeO_{3-\delta}$. *Journal of the American Ceramic Society*, 87(10):1952–1958, 2004.

[167] I. Wærnhus, T. Grande, and K. Wiik. Electronic Properties of Polycrystalline $LaFeO_3$. Part II: Defect Modelling including Schottky Defects. *Solid State Ionics*, 176(35-36):2609–2616, 2005.

[168] M. Idrees, M. Nadeem, M. Shah, T. J. Shin. Anomalous Octahedral Distortions in $LaFe_{1-x}Ni_xO_3$. *Journal of Physics D: Applied Physics*, 44(45):455303, 2011.

[169] C. A. L. Dixon, C. M. Kavanagh, K. S. Knight, W. Kockelmann, F. D. Morrison, P. Lightfoot. Thermal Evolution of the Crystal Structure of the Orthorhombic Perovskite $LaFeO_3$. *Journal of Solid State Chemistry*, 230:337–342, 2015.

[170] A. M. Glazer. The Classification of Tilted Octahedra in Perovskites. *Acta Crystallographica Section B Structural Crystallography and Crystal Chemistry*, 28(11):3384–3392, 1972.

[171] K. Huang, H. Y. Lee, and J. B. Goodenough. Sr- and Ni-Doped $LaCoO_3$ and $LaFeO_3$ Perovskites, *Journal of Electrochemistry Society*, 145(9):3220–3227, 1998.

[172] R. Choithrani. Transport Properties of Ferrite Perovskite Material. *Journal of Physical Science and Application*, 2(7):245–248, 2012.

[173] M. Cherry, M. S. Islam, and C. R. A. Catlow. Oxygen Ion Migration in Perovskite-Type Oxides. *Journal of Solid State Chemistry*, 118(1):125–132, 1995.

[174] M. S. Islam. Ionic transport in $ABO_3$ Perovskite Oxides: A Computer Modelling Tour. *Journal of Materials Chemistry*, 10(4):1027–1038, 2000.

[175] A. M. Ritzmann, A. B. Muñoz-García, M. Pavone, J. A. Keith, and E. A. Carter. Ab Initio DFT+U Analysis of Oxygen Vacancy Formation and Migration in $La_{1-x}Sr_xFeO_{3-\delta}$ ($x$ = 0, 0.25, 0.50). *Chemistry of Materials*, 25(15):3011–3019, 2013.

[176] Y. A. Mastrikov, S. Guo, F. Puleo, L. F. Liotta, and E. A. Kotomin. First Principles Modeling of Pd-doped (La,Sr)(Co,Fe)$O_3$ Complex Perovskites. *Fuel Cells*, 16(2):267–271, 2016.

[177] D. Gryaznov, M. W. Finnis, R. A. Evarestov, and J. Maier. Oxygen Vacancy Formation Energies in Sr-Doped Complex Perovskites: *ab initio* Thermodynamic Study. *Solid State Ionics*, 254:11–16, 2014.

[178] J. Mizusaki, M. Yoshihiro, S. Yamauchi, and K. Fueki. Nonstoichiometry and Defect Structure of the Perovskite-Type Oxides $La_{1-x}Sr_xFeO_{3-\delta}$. *Journal of Solid State Chemistry*, 58(2):257–266, 1985.

[179] R. Pushpa, D. Daniel, and D. P. Butt. Electronic Properties of Ca Doped $LaFeO_3$: A First-Principles Study. *Solid State Ionics*, 249-250:184–190, 2013.

[180] F. Bidrawn, S. Lee, J. M. Vohs, and R. J. Gorte. The Effect of Ca, Sr, and Ba Doping on the Ionic Conductivity and Cathode Performance of $LaFeO_3$. *Journal of The Electrochemical Society*, 155(7):B660–B665, 2008.

[181] J. Dho and N. H. Hur. Magnetic and Transport Properties of Lanthanum Perovskites with B-Site Half Doping. *Solid State Communications*, 138(3):152–156, 2006.

[182] W. Haron, T. Thaweechai, W. Wattanathana, A. Laobuthee, H. Manaspiya, C. Veranitisagul, and N. Koonsaeng. Structural Characteristics and Dielectric Properties of $La_{1-x}Co_xFeO_3$ and $LaFe_{1-x}Co_xO_3$ Synthesized via Metal Organic Complexes. *Energy Procedia*, 34:791–800, 2013.

[183] N. Lakshminarayanan, J. N. Kuhn, S. A. Rykov, J. M. M. Millet, and U. S. Ozkan. Doped $LaFeO_3$ as SOFC Catalysts: Control of Oxygen Mobility and Oxidation Activity. *Catalysis Today*, 157:446–450, 2010.

[184] N. Ortiz-Vitoriano, I. Ruiz de Larramendi, I. Gil de Muro, J. I. Ruiz de Larramendi, and T. Rojo. Nanoparticles of $La_{0.8}Ca_{0.2}Fe_{0.8}Ni_{0.2}O_{3-\delta}$ Perovskite for Solid Oxide Fuel Cell Application. *Materials Research Bulletin*, 45(10):1513–1519, 2010.

[185] G. W. Coffey, J. S. Hardy, L. R. Pederson, P. C. Rieke, and E. C. Thomsen. Oxygen Reduction Activity of Lanthanum Strontium Nickel Ferrite. *Electrochemical and Solid State Letters*, 6(6):A121–A124, 2003.

[186] Z. Zhong, K. Chen, Y. Ji, and Q. Yan. Methane Combustion over B-Site Partially Substituted Perovskite-Type $LaFeO_3$ Prepared by Sol-Gel Method. *Applied Catalysis A: General*, 156(1):29–41, 1997.

[187] K. Zhao, F. He, Z. Huang, G. Wei, A. Zheng, H. Li, and Z. Zhao. Perovskite-Type Oxides $LaFe_{1-x}Co_xO_3$ for Chemical Looping Steam Methane Reforming to Syngas and Hydrogen Co-Production. *Applied Energy*, 168:193–203, 2016.

[188] M. Idrees, M. Nadeem, M. Mehmood, M. Atif, K. H. Chae, and M. M. Hassan. Impedance Spectroscopic Investigation of Delocalization Effects of Disorder Induced by Ni Doping in $LaFeO_3$. *Journal of Physics D: Applied Physics*, 44(10):105401, 2011.

[189] G. L. Beausoleil II, P. Price, D. Thomsen, A. Punnoose, R. Ubic, S. Misture, and D. P. Butt. Thermal Expansion of Alkaline-Doped Lanthanum Ferrite near the Néel Temperature. *Journal of the American Ceramic Society*, 97(1):228–234, 2014.

[190] I. N. Sora, T. Caronna, F. Fontana, C. D. J. Fernández, A. Caneschi, and M. Green. Crystal Structures and Magnetic Properties of Strontium and Copper

Doped Lanthanum Ferrites. *Journal of Solid State Chemistry*, 191:33–39, 2012.

[191] S. P. Simner, J. F. Bonnett, N. L. Canfield, K. D. Meinhardt, V. L. Sprenkle, and J. W. Stevenson. Optimized Lanthanum Ferrite-Based Cathodes for Anode-Supported SOFCs. *Electrochemical and Solid-State Letters*, 5(7):A173–A175, 2002.

[192] J. M. Ralph, C. Rossignol, and R. Kumar. Cathode Materials for Reduced-Temperature SOFCs. *Journal of The Electrochemical Society*, 150(11):A1518–A1522, 2003.

[193] A. Martínez-Amesti, A. Larrañaga, L. M. Rodríguez-Martínez, A. T. Aguayo, J. L. Pizarro, M. L. Nó, A. Laresgoiti, and M. I. Arriortua. Reactivity between La(Sr)$FeO_3$ Cathode, Doped $CeO_2$ Interlayer and Yttria-Stabilized Zirconia Electrolyte for Solid Oxide Fuel Cell Applications. *Journal of Power Sources*, 185(1):401–410, 2008.

[194] A. Manthiram, J. H. Kim, Y. N. Kim, and K. T. Lee. Crystal Chemistry and Properties of Mixed Ionic-Electronic Conductors, *Journal of Electroceramics*, 27(2):93–107, 2011.

[195] R. Andoulsi, K. Horchani-Naifer, and M. Férid. Structural and Electrical Properties of Calcium Substituted Lanthanum Ferrite Powders. *Powder Technology*, 230:183–187, 2012.

[196] M. S. Hassan, K.-B. Shim, and O-B. Yang. Electrocatalytic Behavior of Calcium Doped $LaFeO_3$ as Cathode Material for Solid Oxide Fuel Cell. *Journal of Nanoscience and Nanotechnology*, 11(2):1429–1433, 2011.

[197] M.-H. Hung, M. V. M. Rao, and D.-S. Tsai. Microstructures and Electrical Properties of Calcium Substituted $LaFeO_3$ as SOFC Cathode. *Materials Chemistry and Physics*, 101(2-3):297–302, 2007.

[198] H.-C. Wang, C.-L. Wang, J.-L. Zhang, M.-L. Zhao, J. Liu, W.-B. Su, N. Yin, and L.-M. Mei. Cu Doping Effect on Electrical Resistivity and Seebeck Coefficient of Perovskite-Type $LaFeO_3$ Ceramics. *Chinese Physics Letters*, 26(10):107301, 2009.

[199] Z. X. Wei, Y. Wang, J. P. Liu, C. M. Xiao, W. W. Zeng, and S. B. Ye. Synthesis, Magnetization, and Photocatalytic Activity of $LaFeO_3$ and $LaFe_{0.9}Mn_{0.1}O_{3-\delta}$. *Journal of Materials Science*, 48(3):1117–1126, 2013.

[200] Y.-L. Lee, J. Kleis, J. Rossmeisl, and D. Morgan. *Ab initio* Energetics of La*B*O3(001) (*B* = Mn, Fe, Co, and Ni) for Solid Oxide Fuel Cell Cathodes. *Physical Review B Condensed Matter Materials Physics*, 80(22):224101, 2009.

[201] Y. Wang and H. P. Cheng. Oxygen Reduction Activity on Perovskite Oxide Surfaces: A Comparative First-Principles Study of $LaMnO_3$, $LaFeO_3$, and $LaCrO_3$. *Journal of Physical Chemistry C*, 117(5):2106–2112, 2013.

[202] Y.-L. Lee, M. J. Gadre, Y. Shao-Horn, and D. Morgan. *Ab initio* GGA+U Study of Oxygen Evolution and Oxygen Reduction Electrocatalysis on the (001) Surfaces of Lanthanum Transition Metal Perovskites $LaBO_3$ (B = Cr, Mn, Fe, Co and Ni). *Physical Chemistry Chemical Physics*, 17(33):21643–21663, 2015.

[203] H. Kizaki and K. Kusakabe. DFT-GGA study of NO Adsorption on the LaO (001) Surface of $LaFeO_3$. *Surface Science*, 606(3-4):337–343, 2012.

[204] S. Piskunov, E. Spohr, T. Jacob, E. A. Kotomin, and D. E. Ellis. Electronic and Magnetic Structure of $La_{0.875}Sr_{0.125}MnO_3$ Calculated by means of Hybrid Density-Functional Theory. *Physical Review B - Condensed Matter and Materials Physics*, 76(1):012410, 2007.

[205] S. Piskunov, E. Heifets, T. Jacob, E. A. Kotomin, D. E. Ellis, and E. Spohr. Electronic Structure and Thermodynamic Stability of $LaMnO_3$ and

$La_{1-x}Sr_xMnO_3$ (001) Surfaces: *Ab initio* Calculations. *Physical Review B - Condensed Matter and Materials Physics*, 78(12):121406, 2008.

[206] E. A. Kotomin, Y. A. Mastrikov, E. Heifets, and J. Maier. Adsorption of Atomic and Molecular Oxygen on the $LaMnO_3$ (001) Surface: *ab initio* Supercell Calculations and Thermodynamics. *Physical Chemistry Chemical Physics*, 10(31):4644, 2008.

[207] Y. A. Mastrikov, R. Merkle, E. Heifets, E. A. Kotomin, and J. Maier. Pathways for Oxygen Incorporation in Mixed Conducting Perovskites: A DFT-Based Mechanistic Analysis for (La, Sr)$MnO_{3-\delta}$. *Journal of Physical Chemistry C*, 114(7):3017–3027, 2010.

[208] R. A. Evarestov, E. A. Kotomin, Y. A. Mastrikov, D. Gryaznov, E. Heifets, and J. Maier. Comparative Density-Functional LCAO and Plane-Wave Calculations of $LaMnO_3$ Surfaces. *Physical Review B - Condensed Matter and Materials Physics*, 72(21), 2005.

[209] Y. Choi, D. S. Mebane, M. C. Lin, and M. Liu. Oxygen Reduction on $LaMnO_3$-Based Cathode Materials in Solid Oxide Fuel Cells. *Chemistry of Materials*, 19(7):1690–1699, 2007.

[210] T. Akbay, A. Staykov, J. Druce, H. Téllez, T. Ishihara, and J. A. Kilner. The Interaction of Molecular Oxygen on LaO Terminated Surfaces of $La_2NiO_4$. *Journal of Materials Chemistry A*, 4(34):13113–13124, 2016.

[211] T. T. Fister, D. D. Fong, J. A. Eastman, P. M. Baldo, M. J. Highland, P. H. Fuoss, K. R. Balasubramaniam, J. C. Meador, and P. A. Salvador. *In situ* Characterization of Strontium Surface Segregation in Epitaxial $La_{0.7}Sr_{0.3}MnO_3$ Thin Films as a Function of Oxygen Partial Pressure. *Applied Physics Letters*, 93(15):151904, 2008.

[212] R. Herger, P. R. Willmott, C. M. Schlepütz, M. Björck, S. A. Pauli, D. Martoccia, B. D. Patterson, D. Kumah, R. Clarke, Y. Yacoby, and M. Döbeli.

Structure Determination of Monolayer-by-Monolayer grown $La_{1-x}Sr_xMnO_3$ Thin Films and the onset of Magnetoresistance. *Physical Review B - Condensed Matter and Materials Physics*, 77(8):085401, 2008.

[213] E. Wigner and F. Seitz. On the Constitution of Metallic Sodium. *Physical Review*, 43(10):804–810, 1933.

[214] E. Wigner and F. Seitz. On the Constitution of Metallic Sodium II. *Physical Review*, 46(6):509–524, 1934.

[215] A. R. Leach. *Molecular Modelling: Principles and Application*. $2^{nd}$ ed. Prentice Hall, Harlow UK, 2001.

[216] E. Schrödinger. Quantisierung als Eigenwertproblem. *Annalen der Physik*, 80(13):437–490, 1926.

[217] E. Schrödinger. An Undulatory Theory of the Mechanics of Atoms and Molecules. *Physical Review*, 28(6):1049–1070, 1926.

[218] M. Born and R. Oppenheimer. Zur Quantentheorie der Molekeln. *Annalen der Physik*, 389(20):457–484, 1927.

[219] W Pauli. On the Connexion between the Completion of Electron Groups in an Atom with the Complex Structure of Spectra. *Zeitschrift Physik*, 31:1–13, 1925.

[220] V. Brázdová and D. R. Bowler. *Atomistic Computer Simulations*. Wiley-VCH Verlag GmbH & Co. KGaA, Weinheim Germany, 2013.

[221] C. C. J. Roothaan. New Developments in Molecular Orbital Theory. *Reviews of Modern Physics*, 23(2):69–89, 1951.

[222] C. C. J. Roothaan. Self-Consistent Field Theory for Open Shells of Electronic Systems. *Reviews of Modern Physics*, 32(2):179–185, 1960.

[223] L. H. Thomas. The Calculation of Atomic Fields. *Mathematical Proceedings of the Cambridge Philosophical Society*, 23(05):542–548, 1927.

[224] E. Fermi. Statistical Method to Determine some Properties of Atoms. *Rendiconti. Accademia Nazionale dei Lincei*, 6:602–607, 1927.

[225] E. Fermi. Eine Statistische Methode zur Bestimmung einiger Eigenschaften des Atoms und ihre Anwendung auf die Theorie des Periodischen Systems der Elemente. *Zeitschrift fur Physik*, 48(1-2):73–79, 1928.

[226] E. Teller. On the Stability of Molecules in the Thomas-Fermi Theory. *Reviews of Modern Physics*, 34(4):627–631, 1962.

[227] P. A. M. Dirac. Note on Exchange Phenomena in the Thomas Atom. *Mathematical Proceedings of the Cambridge Philosophical Society*, 26(03):376–385, 1930.

[228] F. Bloch. Bemerkung zur Elektronentheorie des Ferromagnetismus und der Elektrischen Leitfahigkeit. *Zeitschrift fur Physik*, 57(7-8):545–555, 1929.

[229] P. Hohenberg and W. Kohn. Inhomogeneous Electron Gas. *Physical Review*, 136(3B):B864–B871, 1964.

[230] W. Kohn and L. J. Sham. Self-Consistent Equations including Exchange and Correlation Effects. *Physical Review*, 140(4A):A1133–A1138, 1965.

[231] D. M. Ceperley and B. J. Alder. Ground State of the Electron Gas by a Stochastic Method. *Physical Review Letters*, 45(7):566–569, 1980.

[232] J. P. Perdew and Y. Wang. Accurate and Simple Analytic Representation of the Electron-Gas correlation energy. *Physical Review B*, 45(23):13244–13249, 1992.

[233] U. von Barth and L. Hedin. A Local Exchange-Correlation Potential for the Spin Polarized Case. I. *Journal of Physics C: Solid State Physics*, 5(13):1629–1642, 1972.

[234] A. K. Rajagopal and J. Callaway. Inhomogeneous Electron Gas. *Physical Review B*, 7(5):1912–1919, 1973.

[235] D. C. Langreth and M. J. Mehl. Easily Implementable Nonlocal Exchange-Correlation Energy Functional. *Physical Review Letters*, 47(6):446–450, 1981.

[236] D. C. Langreth and M. J. Mehl. Beyond the Local-Density Approximation in Calculations of Ground-State Electronic Properties. *Physical Review B*, 28(4):1809–1834, 1983.

[237] A. D. Becke. Density-Functional Exchange-Energy Approximation with Correct Asymptotic Behavior. *Physical Review A*, 38(6):3098–3100, 1988.

[238] J. Perdew, J. Chevary, S. Vosko, K. Jackson, M. Pederson, D. Singh, and C. Fiolhais. Atoms, Molecules, Solids, and Surfaces: Applications of the Generalized Gradient Approximation for Exchange and Correlation. *Physical Review B*, 46(11):6671–6687, 1992.

[239] J. P. Perdew. Accurate Density Functional for the Energy: Real-Space Cutoff of the Gradient Expansion for the Exchange Hole. *Physical Review Letters*, 55(16):1665–1668, 1985.

[240] J. P. Perdew and W. Yue. Accurate and Simple Density Functional for the Electronic Exchange Energy: Generalized Gradient Approximation. *Physical Review B*, 33(12):8800–8802, 1986.

[241] J. P. Perdew. Density-Functional Approximation for the Correlation Energy of the Imhomogeneous Electron Gas. *Physical Review B*, 33(12):8822, 1986.

[242] A. Selloni, P. Carnevali, E. Tosatti, and C. D. Chen. Voltage-Dependent Scanning-Tunneling Microscopy of a Crystal Surface: Graphite. *Physical Review B*, 31(4):2602–2605, 1985.

[243] J. P. Perdew, K. Burke, and M. Ernzerhof. Generalized Gradient Approximation made Simple. *Physical Review Letters*, 77(18):3865–3868, 1996.

[244] J. P. Perdew, A. Ruzsinszky, G. I. Csonka, O. A. Vydrov, G. E. Scuseria, L. A. Constantin, X. Zhou, and K. Burke. Restoring the Density-Gradient

Expansion for Exchange in Solids and Surfaces. *Physical Review Letters*, 100(13):136406, 2008.

[245] J. P. Perdew, J. A. Chevary, S. H. Vosko, K. A. Jackson, M. R. Pederson, D. J. Singh, and C. Fiolhais. Erratum: Atoms, Molecules, Solids, and Surfaces: Applications of the Generalized Gradient Approximation for Exchange and Correlation. *Physical Review B*, 48(7):4978–4978, 1993.

[246] A. D. Becke. A New Mixing of Hartree-Fock and Local Density-Functional Theories. *The Journal of Chemical Physics*, 98(2):1372–1377, 1993.

[247] J. Harris and R. O. Jones. The Surface Energy of a bounded Electron Gas. *Journal of Physics F: Metal Physics*, 4:1170–1186, 1974.

[248] O. Gunnarsson and B. I. Lundqvist. Exchange and Correlation in Atoms, Molecules, and Solids by Spin-Density Functional Formalism. *Physical Review B*, 13(10):4274–4298, 1976.

[249] D. C. Langreth and J. P. Perdew. Exchange-Correlation Energy of a Metallic Surface: Wave-Vector Analysis. *Physical Review B*, 15(6):2884–2901, 1977.

[250] J. Harris. Adiabatic-Connection Approach to Kohn-Sham Theory. *Physical Review A*, 29(4):1648–1659, 1984.

[251] H. J. Kulik. Perspective: Treating Electron Over-Delocalization with the DFT+U Method. *Journal of Chemical Physics*, 142(24):240901–114103, 2015.

[252] S. Hüfner. Electronic Structure of NiO and Related 3d-Transition-Metal Compounds. *Advances in Physics*, 43(2):183–356, 1994.

[253] K. Terakura, T. Oguchi, A. R. Williams, and J. Kübler. Band Theory of Insulating Transition-Metal Monoxides: Band-Structure Calculations. *Physical Review B*, 30(8):4734–4747, 1984.

[254] B. Himmetoglu, A. Floris, S. De Gironcoli, and M. Cococcioni. Hubbard-Corrected DFT Energy Functionals: The LDA+U Description of Correlated Systems. *International Journal of Quantum Chemistry*, 114(1):14–49, 2014.

[255] Y.-C. Wang, Z.-H. Chen, and H. Jiang. The Local Projection in the Density Functional Theory Plus *U* Approach: A Critical Assessment. *The Journal of Chemical Physics*, 144:144106, 2016.

[256] S. L. Dudarev, G. A. Botton, S. Y. Savrasov, C. J. Humphreys, and A. P. Sutton. Electron-Energy-Loss Spectra and the Structural Stability of Nickel Oxide: An LSDA+U Study. *Physical Review B*, 57(3):1505–1509, 1998.

[257] A. B. Shick, A. I. Liechtenstein, and W. E. Pickett. Implementation of the LDA+U Method using the Full-Potential Linearized Augmented Plane-Wave Basis. *Physical Review B*, 60(15):10763, 1999.

[258] P. E. Blöchl. Projector Augmented-Wave Method. *Physical Review B*, 50(24):17954–17979, 1994.

[259] A. I. Liechtenstein, V. I. Anisimov, and J. Zaanen. Density-Functional Theory and Strong Interactions: Orbital Ordering in Mott-Hubbard Insulators. *Physical Review B*, 52(8):R5467, 1995.

[260] V. I. Anisimov, I. V. Solovyev, M. A. Korotin, M. T. Czyyk, and G. A. Sawatzky. Density-Functional Theory and NiO Photoemission Spectra. *Physical Review B*, 48(23):16929–16934, 1993.

[261] H. J. Monkhorst and J. D. Pack. Special Points for Brillouin-Zone Integrations, *Physical Review B*, 13(12):5188–5191, 1976.

[262] M. Born. Volumes and Heats of Hydration of Ions. *Zeitschrift fuer Physik*, 1:45–8, 1920.

[263] P. P. Ewald. Die Berechnung Optischer und Elektrostatischer Gitterpotentiale. *Annalen der Physik*, 369(3):253–287, 1921.

[264] A. Y. Toukmaji and J. A. Board. Ewald Summation Techniques in Perspective: A Survey. *Computer Physics Communications*, 95(2-3):73–92, 1996.

[265] B. G. Jr Dick and A. W. Overhauser. Theory of the Dielectric Constants of Alkali Halide Crystals. *Physical Review*, 112(1):90–103, 1958.

[266] W. C. Davidon. Variable Metric Method for Minimization. *A.E.C Research and Development Report*, 1(1):1–17, 1959.

[267] R. Fletcher and M. J. D. Powell. A Rapidly Convergent Descent Method for Minimization. *The Computer Journal*, 6(2):163–168, 1963.

[268] C. G. Broyden. The Convergence of a Class of Double-Rank Minimization Algorithms 1. General Considerations. *IMA Journal of Applied Mathematics (Institute of Mathematics and Its Applications)*, 6(1):76–90, 1970.

[269] C . G . Broyden. The Convergence of a Class of Double Rank Minimization Algorithms: 2. The New Algorithm. *Journal of the Institute of Mathematics and Its Applications*, 6(3):222–231, 1970.

[270] R. Fletcher. A New Approach to Variable Metric Algorithms. *The Computer Journal*, 13(3):317–322, 1970.

[271] D. Goldfarb. A Family of Variable-Metric Methods Derived by Variational Means. *Mathematics of Computation*, 24(109):23–23, 1970.

[272] D. F. Shanno. Conditioning of Quasi-Newton Methods for Function Minimization. *Mathematics of Computation*, 24(111):647–647, 1970.

[273] P. Pulay. Convergence Acceleration of Iterative Sequences. The Case of SCF Iteration. *Chemical Physics Letters*, 73(2):393–398, 1980.

[274] N. F. Mott and M. J. Littleton. Conduction in Polar Crystals. I. Electrolytic Conduction in Solid Salts. *Transactions of the Faraday Society*, 34:485–499, 1938.

[275] R. P. Messmer and G. D. Watkins. Linear Combination of Atomic Orbital-Molecular Orbital Treatment of the Deep Defect Level in a Semiconductor: Nitrogen in Diamond. *Physical Review Letters*, 25(10):656–659, 1970.

[276] R. P. Messmer and G. D. Watkins. Molecular-Orbital Treatment for Deep Levels in Semiconductors: Substitutional Nitrogen and the Lattice Vacancy in Diamond. *Physical Review B*, 7(6):2568–2590, 1973.

[277] S. G. Louie, M. Schlüter, J. R. Chelikowsky, and M. L. Cohen. Self-Consistent Electronic States for Reconstructed Si Vacancy Models. *Physical Review B*, 13(4):1654–1663, 1976.

[278] C. Freysoldt, B. Grabowski, T. Hickel, J. Neugebauer, G. Kresse, A. Janotti, and C. G. Van De Walle. First-Principles Calculations for Point Defects in Solids. *Reviews of Modern Physics*, 86(1):253–305, 2014.

[279] M. Leslie and N. J. Gillan. The Energy and Elastic Dipole Tensor of Defects in Ionic Crystals Calculated by the Supercell Method. *Journal of Physics C: Solid State Physics*, 18(5):973–982, 1985.

[280] G. Makov and M. C. Payne. Periodic Boundary Conditions in *ab initio* Calculations. *Physical Review B*, 51(7):4014–4022, 1995.

[281] S. Lany and A. Zunger. Assessment of Correction Methods for the Band-Gap Problem and for Finite-Size Effects in Supercell Defect Calculations: Case Studies for ZnO and GaAs. *Physical Review B - Condensed Matter and Materials Physics*, 78:235104, 2008.

[282] J. Lento, J.-L. Mozos, and R. M. Nieminen. Charged Point Defects in Semiconductors and the Supercell Approximation. *Journal of Physics: Condensed Matter*, 14(14):2637–2645, 2002.

[283] J. Shim, E. K. Lee, Y. J. Lee, and R. M. Nieminen. Density-Functional Calculations of Defect Formation Energies using Supercell Methods: Defects

in Diamond. *Physical Review B - Condensed Matter and Materials Physics*, 71(3):035206, 2005.

[284] C. W. M. Castleton, A. Höglund, and S. Mirbt. Managing the Supercell Approximation for Charged Defects in Semiconductors: Finite-Size Scaling, Charge Correction Factors, the Band-Gap Problem, and the *ab initio* Dielectric Constant. *Physical Review B - Condensed Matter and Materials Physics*, 73(3):035215, 2006.

[285] A. F. Wright and N. A. Modine. Comparison of Two Methods for Circumventing the Coulomb Divergence in Supercell Calculations for Charged Point Defects. *Physical Review B - Condensed Matter and Materials Physics*, 74(23):235209, 2006.

[286] C. Persson, Y. J. Zhao, S. Lany, and A. Zunger. *n*-Type Doping of $CuInSe_2$ and $CuGaSe_2$. *Physical Review B - Condensed Matter and Materials Physics*, 72(3):035211, 2005.

[287] D. B. Laks, C. G. Van de Walle, G. F. Neumark, P. E. Blöchl, and S. T. Pantelides. Native Defects and Self-Compensation in ZnSe. *Physical Review B*, 45(19):10965–10978, 1992.

[288] T. Mattila and A. Zunger. Deep Electronic Gap Levels Induced by Isovalent P and As Impurities in GaN. *Physical Review B*, 58(3):1367–1373, 1998.

[289] G. Kresse and J. Hafner. *Ab initio* Molecular Dynamics for Open-Shell Transition Metals. *Physical Review B*, 48(17):13115–13118, 1993.

[290] G. Kresse and J. Furthmüller. Efficient Iterative Schemes for *ab initio* Total-Energy Calculations using a Plane-Wave Basis Set. *Physical Review B*, 54(16):11169–11186, 1996.

[291] J. D. Gale and A. L. Rohl. The General Utility Lattice Program (GULP). *Molecular Simulation*, 29(5):291–341, 2003.

[292] G. Kresse and J. Furthmüller. Efficiency of ab-initio Total Energy Calculations for Metals and Semiconductors using a Plane-Wave basis set. *Computational Materials Science*, 6(1):15–50, 1996.

[293] J. He and C. Franchini. Screened Hybrid Functional Applied to $3d^0 \rightarrow 3d^8$ Transition-Metal Perovskites La$M$O$_3$ ($M$ = Sc-Cu): Influence of the Exchange Mixing Parameter on the Structural, Electronic, and Magnetic Properties. *Physical Review B*, 86:235117, 2012.

[294] F. A. Kröger. *The Chemistry of Imperfect Crystals: Imperfection Chemistry of Crystalline Solids*. North-Holland Pub. Co, $3^{rd}$ edition, 1974.

[295] S. T. Murphy and N. D. M. Hine. Anisotropic Charge Screening and Supercell Size Convergence of Defect Formation Energies. *Physical Review B - Condensed Matter and Materials Physics*, 87(9):094111, mar 2013.

[296] J. Buckeridge, D. O. Scanlon, A. Walsh, and C. R. A. Catlow. Automated Procedure to Determine the Thermodynamic Stability of a Material and the Range of Chemical Potentials Necessary for its Formation Relative to Competing Phases and Compounds. *Computer Physics Communications*, 185(1):330–338, 2014.

[297] B. S. Thomas, N. A. Marks, and B. D. Begg. Defects and Threshold Displacement Energies in $SrTiO_3$ Perovskite using Atomistic Computer Simulations. *Nuclear Instruments and Methods in Physics Research, Section B: Beam Interactions with Materials and Atoms*, 254(2):211–218, 2007.

[298] A. A. Sokol, A. Walsh, and C. R. A. Catlow. Oxygen Interstitial Structures in Close-Packed Metal Oxides. *Chemical Physics Letters*, 492(1-3):44–48, 2010.

[299] M. M. Kuklja, Y. A. Mastrikov, B. Jansang, and E. A. Kotomin. The Intrinsic Defects, Disordering, and Structural Stability of $Ba_xSr_{1-x}Co_yFe_{1-y}O_{3-\delta}$ Perovskite Solid Solutions. *The Journal of Physical Chemistry C*, 116(35):18605–18611, 2012.

[300] M. S. Palmer, M. Neurock, M. M. Olken. Periodic Density Functional Theory Study of Methane Activation over $La_2O_3$: Activity of $O^{2-}$, $O^{-}$, $O_2{}^{2-}$, Oxygen Point Defect, and $Sr^{2+}$-Doped Surface Sites. *Journal of the American Chemical Society*, 124(28):8452–8461, 2002.

[301] K. M. Ervin, I. Anusiewicz, P. Skurski, J. Simons, and W. C. Lineberger. The Only Stable State of $O^{2-}$ is the X $^2\Pi_g$ Ground State and it (still!) has an Adiabatic Electron Detachment Energy of 0.45 eV. *Journal of Physical Chemistry A*, 107(41):8521–8529, 2003.

[302] J. C. Ruiz-Morales, J. Canales-Vzquez, C. Savaniu, D. Marrero-Lpez, W. Zhou, J. T. S. Irvine. Disruption of Extended Defects in Solid Oxide Fuel Cell Anodes for Methane Oxidation. *Journal of Physical Chemistry A*, 107(41):8521–8529, 2003.

[303] Sourceforge Page for sc-fermi. https://sourceforge.net/projects/ sc-fermi/.

[304] Github Page for sc-fermi. https://github.com/jbuckeridge/scfermi.

[305] K. Reuter and M. Scheffler. Composition, Structure and Stability of $RuO_2$ (110) as a Function of Oxygen Pressure. *Physical Review B*, 65:035406, 2001.

[306] D. R. Stull and H. Prophet. *JANAF Thermochemical Tables*. $2^{nd}$ ed. U.S. Dept. of Commerce, National Bureau of Standards, Washington DC, 1971.

[307] K.T. Jacob and R. Ranjani. Thermodynamic Properties of $LaFeO_{3-\delta}$ and $LaFe_{12}O_{19}$. *Materials Science and Engineering: B*, 176(7):559–566, 2011.

[308] M. Yashima and T. Tsuji. Structural Investigation of the Cubic Perovskite-Type Doped Lanthanum Cobaltite $La_{0.6}Sr_{0.4}CoO_{3-\delta}$ at 1531K: Possible Diffusion Path of Oxygen Ions in an Electrode Material. *Journal of Applied Crystallography*, 40(6):1166–1168, 2007.

[309] A. Banerjee, N. Adams, J. Simons, and R. Shepard. Search for Stationary Points on Surfaces. *The Journal of Physical Chemistry*, 89(1):52–57, 1985.

[310] G. Mills, H. Jonsson, and G. K. Scgenter. Reversible Work Transition State Theory: Application to Dissociative Adsorption of Hydrogen. *Surface Science*, 324:305–337, 1995.

[311] G. Henkelman, B. P. Uberuaga, and H. Jónsson. Climbing Image Nudged Elastic Band Method for Finding Saddle Points and Minimum Energy Paths. *Journal of Chemical Physics*, 113(22):9901–9904, 2000.

[312] D. Sheppard, R. Terrell, and G. Henkelman. Optimization Methods for Finding Minimum Energy Paths. *Journal of Chemical Physics*, 128(13):134106, 2008.

[313] M. S. Khan, M. S. Islam, and D. R. Bates. Dopant Substitution and Ion Migration in the $LaGaO_3$-Based Oxygen Ion Conductor. *The Journal of Physical Chemistry B*, 102(17):3099–3104, 1998.

[314] P. Brix and G. Herzberg. The Dissociation Energy of Oxygen. *The Journal of Chemical Physics*, 21(796):2240, 1953.

[315] F. H. Taylor, J. Buckeridge, and C. R. A. Catlow. Defects and Oxide Ion Migration in the Solid Oxide Fuel Cell Cathode Material $LaFeO_3$. *Chemistry of Materials*, 28(22):8210–8220, 2016.

[316] B. S. Youmbi and F. Calvayrac. Structure of CoO (001) Surface from DFT+U Calculations. *Surface Science*, 621:1–6, 2014.

[317] A. L. Dalverny, J. S. Filhol, F. Lemoigno, and M. L. Doublet. Interplay between Magnetic and Orbital Ordering in the Strongly Correlated Cobalt Oxide: A DFT+$U$ Study. *Journal of Physical Chemistry C*, 114(49):21750–21756, 2010.

[318] A. Floris, S. De Gironcoli, E. K. U. Gross, and M. Cococcioni. Vibrational Properties of MnO and NiO from DFT+$U$-Based Density Functional Perturbation Theory. *Physical Review B - Condensed Matter and Materials Physics*, 84:161102, 2011.

[319] K. Sebbari, J. Roques, C. Domain, and E. Simoni. Uranyl Ion Interaction at the Water/NiO(100) Interface: A Predictive Investigation by First-Principles Molecular Dynamic Simulations. *Journal of Chemical Physics*, 137:164701, 2012.

[320] M. Forti, P. Alonso, P. Gargano, and G. Rubiolo. Transition Metals Monoxides. An LDA+U Study. *Procedia Materials Science*, 1:230–234, 2012.

[321] D. Novoselov, Dm. M. Korotin, and V. I. Anisimov. Hellmann-Feynman Forces within the DFT+*U* in Wannier Functions Basis. *Journal of Physics: Condensed Matter*, 27:325602, 2015.

[322] Z. Yang, Q. Wang, and S. Wei. The Synergistic effects of the $CuCeO_2$ (111) Catalysts on the Adsorption and Dissociation of Water Molecules. *Physical Chemistry Chemical Physics*, 13(20):9363–9373, 2011.

[323] C. E. Ekuma, V. I. Anisimov, J. Moreno, and M. Jarrell. Electronic Structure and Spectra of CuO. *European Physical Journal B*, 87:23, 2014.

[324] M. Nolan and S. D. Elliott. The p-type Conduction Mechanism in $Cu_2O$: A First Principles Study. *Physical Chemistry Chemical Physics*, 8(45):5350–5358, 2006.

[325] D. K. Kanan, J. A. Keith, and E. A. Carter. Water Adsorption on MnO: ZnO (001) From Single Molecules to Bilayer Coverage. *Surface Science*, 617:218–224, 2013.

[326] M. C. Toroker and E. A. Carter. Transition Metal Oxide Alloys as Potential Solar Energy Conversion Materials. *Journal of Materials Chemistry A*, 1(7):2474–2484, 2013.

[327] R. Grau-Crespo, S. Hamad, C. R. A. Catlow, and N. H. de Leeuw. Symmetry-Adapted Configurational Modelling of Fractional Site Occupancy in Solids. *Journal of Physics: Condensed Matter*, 19:256201, 2007.

[328] R. D. Shannon. Revised Effective Ionic Radii and Systematic Studies of Interatomic Distances in Halides and Chalcogenides. *Acta Crystallographica Section A*, 32(5):751–767, 1976.

[329] J. N. Kuhn and U. S. Ozkan. Surface Properties of Sr- and Co-Doped $LaFeO_3$. *Journal of Catalysis*, 253(1):200–211, 2008.

[330] G. V. Lewis and C. R.A. Catlow. Defect Studies of Doped and undoped Barium Titanate using Computer Simulation Techniques. *Journal of Physics and Chemistry of Solids*, 47(1):89–97, 1986.

[331] M. V. Patrakeev, J. A. Bahteeva, E. B. Mitberg, I. A. Leonidov, V. L. Kozhevnikov, and K. R. Poeppelmeier. Electron/Hole and Ion Transport in $La_{1-x}Sr_xFeO_{3-\delta}$. *Journal of Solid State Chemistry*, 172(1):219–231, 2003.

[332] S. Ghosh and S. Dasgupta. Synthesis, Characterization and Properties of Nanocrystalline Perovskite Cathode Materials. *Materials Science-Poland*, 28(2):427–438, 2010.

[333] R. Kungas, A. S. Yu, J. Levine, J.-M. Vohs, and R. J. Gorte. An Investigation of Oxygen Reduction Kinetics in LSF Electrodes. *Journal of the Electrochemical Society*, 160(2):F205–F211, 2013.

[334] B. Timurkutluk, C. Timurkutluk, M. D. Mat, and Y. Kaplan. Development of High-Performance Anode Supported Solid Oxide Fuel Cell. *International Journal of Energy Research*, 36(15):1383–1387, 2012.

[335] V. M. Goldschmidt. Die Gesetze der Krystallochemie. *Die Naturwissenschaften*, 14(21):477–485, 1926.

[336] B. Hu, K. Guo, M. Li, Y. Li, and C. Xia. Effect of SDC Grain Size on the Oxygen Incorporation at the LSCF-SDC-Gas Three-Phase Boundary. *Journal of The Electrochemical Society*, 163(3):F190–F195, 2016.

[337] S. Liu, Q. Liu, and J.-L. Luo. The Excellence of La(Sr)Fe(Ni)$O_3$ as an Active and Efficient Cathode for Direct $CO_2$ Electrochemical Reduction at Elevated Temperatures. *Journal of Materials Chemistry A*, 5:2673–2680, 2017.

[338] G. Zhu, X. Fang, C. Xia, and X. Liu. Preparation and Electrical Properties of $La_{0.4}Sr_{0.6}Ni_{0.2}Fe_{0.8}O_3$ using a Glycine Nitrate Process. *Ceramics International*, 31(1):115–119, 2005.

[339] R. Chiba, F. Yoshimura, and Y. Sakurai. An Investigation of $LaNi_{1-x}Fe_xO_3$ as a Cathode Material for Solid Oxide Fuel Cells. *Solid State Ionics*, 124(3):281–288, 1999.

[340] V. V. Kharton, A. P. Viskup, E. N. Naumovich, and V. N. Tikhonovich. Oxygen Permeability of $LaFe_{1-x}Ni_xO_{3-d}$ Solid Solutions. *Materials Research Bulletin*, 34(8):1311–1317, 1999.

[341] M. I. Díez-García and R. Gómez. Metal Doping to Enhance the Photoelectrochemical Behavior of $LaFeO_3$ Photocathodes. *ChemSusChem*, 10:1–8, 2017.

[342] M. Kuhn, S. Hashimoto, K. Sato, K. Yashiro, and J. Mizusaki. Thermo-Chemical Lattice Expansion in $La_{0.6}Sr_{0.4}Co_{1-y}Fe_yO_{3-\delta}$. *Solid State Ionics*, 241:12–16, 2013.

[343] V. V. Sereda, D. S. Tsvetkov, I. L. Ivanov, and A. Y. Zuev. Oxygen Non-stoichiometry, Defect Structure and Related Properties of $LaNi_{0.6}Fe_{0.4}O_{3-\delta}$. *Journal of Materials Chemistry A*, 3:6028–6037, 2015.

[344] E. Niwa and T. Hashimoto. Dependence of Thermal Expansion of $LaNi_{0.6}Fe_{0.4}O_{3-\delta}$ and $La_{0.6}Sr_{0.4}Co_{0.2}Fe_{0.8}O_{3-\delta}$ on Oxygen Partial Pressure. *Solid State Ionics*, 285:187–194, 2016.

[345] L. Gan, Q. Zhong, X. Zhao, Y. Song, and Y. Bu. Structural and Electrochemical Properties of B-Site Mg-Doped $La_{0.7}Sr_{0.3}MnO_{3-\delta}$ Perovskite Cathodes

for Intermediate Temperature Solid Oxide Fuel Cells. *Journal of Alloys and Compounds*, 655:99–105, 2016.

[346] K. A. Stoerzinger, R. Comes, S. R. Spurgeon, S. Thevuthasan, K. Ihm, E. J. Crumlin, and S. A. Chambers. Influence of $LaFeO_3$ Surface Termination on Water Reactivity. *Journal of Physical Chemistry Letters*, 8(5):1038–1043, 2017.